TU Delft

Delft University of Technology

In-situ interfacial approaches on chemisorption and stability of buried metal oxide-polymer interfaces

Fockaert, L.I.

DOI
10.4233/uuid:34e0eb58-9ba4-4fa3-9f25-e91c136b97f7

Publication date
2020

Document Version
Final published version

Citation (APA)
Fockaert, L. I. (2020). *In-situ interfacial approaches on chemisorption and stability of buried metal oxide-polymer interfaces*. [Dissertation (TU Delft), Delft University of Technology].
https://doi.org/10.4233/uuid:34e0eb58-9ba4-4fa3-9f25-e91c136b97f7

Important note
To cite this publication, please use the final published version (if applicable).
Please check the document version above.

Copyright
Other than for strictly personal use, it is not permitted to download, forward or distribute the text or part of it, without the consent of the author(s) and/or copyright holder(s), unless the work is under an open content license such as Creative Commons.

Takedown policy
Please contact us and provide details if you believe this document breaches copyrights.
We will remove access to the work immediately and investigate your claim.

This work is downloaded from Delft University of Technology.
For technical reasons the number of authors shown on this cover page is limited to a maximum of 10.

In-situ interfacial approaches on chemisorption and stability of buried metal oxide-polymer interfaces

PhD thesis

Laura-Lynn Irena Fockaert

This research was carried out under project number F81.3.13509 in the framework of the Partnership Program of the Materials innovation institute M2i (www.m2i.nl) and the Foundation for Fundamental Research on Matter (FOM), which is part of the Netherlands Organisation for Scientific Research NWO (www.nwo.nl).

This research was performed in Delft University of Technology,
Department of Materials Science and Engineering
Mekelweg 2, 2628 CD Delft
The Netherlands

The cover represents the importance of a fundamental understanding of buried metal oxide – polymer interfaces for durable corrosion protection of widely used metal structures.

In-situ interfacial approaches on chemisorption and stability of buried metal oxide-polymer interfaces

Proefschrift

Ter verkrijging van de graad van doctor
aan de Technische Universiteit Delft,
op gezag van de Rector Magnificus, Prof. Dr. Ir. T.H.J.J. van der Hagen,
voorzitter van het College voor promoties,
in het openbaar te verdedigen op
Donderdag 24 september 2020 om 12:30 uur

door

Laura-Lynn Irena FOCKAERT
Master of Science in Industrial Engineering Chemistry
Universiteit Antwerpen, Belgium
Geboren te Wilrijk, België

Dit proefschrift is goedgekeurd door de promotoren:

Prof. dr. ir. J.M.C. Mol

Prof. dr. ir. H. Terryn

Samenstelling promotiecommissie bestaat uit:

Rector Magnificus	Voorzitter
Prof. dr. ir. J.M.C. Mol	Technische Universiteit Delft, promotor
Prof. dr. ir. H. Terryn	Vrije Universiteit Brussel/Technische Universiteit Delft, promotor

Onafhankelijke leden:

Prof. dr. ir. M. Olivier	Université de Mons (Belgium)
Prof. dr. ir. A. Hubin	Vrije Universiteit Brussel (Belgium)
Prof. dr. H. Bakker	Universiteit van Amsterdam
Dr. ir. B. Boelen	Tata Steel IJmuiden B.V., IJmuiden
Prof. dr. ir. J. Sietsma	Technische Universiteit Delft
Prof. dr. J. Dik	Technische Universiteit Delft, reservelid

Keywords: Zr/Ti-based conversion coatings, metal-polymer interfaces, model molecules, zinc, aluminium, magnesium, coil coating, galvanized steel, polyester polyurethane coatings, molecular spectroscopy.

ISBN: 978-94-6366-309-0

Copyright © 2020 by L.I. Fockaert

All rights reserved. No part of the material protected by this copyright notice may be reproduced of utilized in any form or by any means, electronic or mechanical, including photocopying, recording or by any information storage and retrieval system, without permission from the author.

Printed by Universitas

An electronic version of this dissertation is available at: http//repository.tudelft.nl/.

Table of content

Summary	vi
Samenvatting	viii
List of abbreviations	x
Chapter 1: Introduction	1
Chapter 2: Literature review	9
Chapter 3: Zr/Ti-based conversion treatments	41
Chapter 4: Molecule interactions	75
Chapter 5: Chemisorption of coil coat primers	111
Chapter 6: Interfacial stability coil coat primers	129
Chapter 7: Validation ATR-FTIR as in-situ interfacial sensitive technique	143
Chapter 8: Conclusions	175
Appendix	195
Acknowledgements	198
List of publications	200
Curriculum Vitae	202

Summary

Until today, interfacial bond formation and degradation between polymer coatings and metal substrates is still far from fully understood, whilst it is a limiting factor for the durability of metal-polymer hybrid systems.

To improve the corrosion resistance and adhesion properties of metal substrates, a chemical surface treatment is applied prior to painting. However, due to ecological and health related issues, traditional well established surface treatments containing hexavalent chromate or high phosphate loads are being replaced by a new generation of ecologically-justified surface treatments. This comes with the need of gaining fundamental insights on the impact of substrate and pretreatment variations on the (chemical) adhesion of polymers to guarantee the lifetime of newly developed metal-polymer hybrid systems. A challenge in this regard is the hardly accessible buried interface, which until today requires the use of model systems when using non-destructive surface sensitive techniques. Yet, industrial metal-polymer hybrid systems are typically highly heterogeneous, creating a distinct gap between model and industrial systems.

This dissertation aims to close this gap starting from simplified model systems to which complexity is gradually added. This has been done using the thin organic film approach on one hand, and the thin (thermally vaporized) metal substrate approach on the other hand, allowing non-destructive access of the metal-polymer interface from the polymer side and metal side, respectively. Complementary use of both approaches allows systematically comparison of model systems to industrially relevant paint and metal substrates.

The first part of this dissertation discusses the effect of substrate heterogeneities on the formation of a conversion oxide layer. The growing interest of implementing lightweight metals in prepainted structures, for example in carbodies and zinc coatings used for galvanizing lead to the use of pure zinc, aluminium and magnesium as model substrates. This evidenced varying conversion kinetics with thermally vaporized magnesium growing ten times thicker conversion oxides compared to zinc, while aluminium was shown to be only partially covered and thus the least efficient under the defined conversion conditions. Next to conversion kinetics, also (de)hydroxylation equilibria were shown to strongly relate to the native metal oxide properties, affecting final hydroxide densities.

The second part of this dissertation investigates metal-molecule interactions using functionalized model molecules, with selected functionalities representative for polyester polyurethane coil coats. A direct correlation was established between initial metal hydroxide fractions and interfacial bond density. This demonstrated that surface hydroxides act as a bonding site for the chemisorption of organic compounds. On the other hand, the type of interfacial bond was associated to the oxide's acid-base properties. It was evidenced that zirconium-and titanium-treatments increase the acidic

nature of the respective metal oxides, thereby altering the ratio of competitive interfacial interactions.

The third part of this dissertation aims to validate the chemisorption mechanisms using model molecules to industrially relevant polyester primer used for coil coating. This required modelling of the metal substrate to access the buried metal-paint interface. Using this thin substrate approach, polyester primers were shown to form interfacial carboxylate bonds validating the chemisorption mechanisms observed using model compounds. However, whereas model ester-functionalized compounds were found to coordinate in a bridging bidentate mode, polyester primer coordinated in a monodentate coordination, which was attributed to steric hindrance of the macromolecular polymer chains. In addition to the polyester resin also the melamine-based crosslinker was shown to interact with the metal substrates, which highlights the increased complexity of interfacial phenomena at metal–paint interfaces.

Subsequently, interfacial bond formation and degradation was followed in-situ during exposure to an aqueous environment with an initial neutral pH value. This demonstrated that interfacial bond degradation was associated to the susceptibility of the metal substrate to corrosion under the exposed conditions. As such, interfacial bond degradation was delayed in following order: magnesium < zinc < aluminium. Furthermore, it was shown that zirconium-treatment of magnesium and zinc, significantly delayed interfacial bond degradation which was attributed to the passivation of the respective oxides. Consequently, in addition to the type of interfacial bonds, also the activity of the metal oxide has a predominant role on the interfacial stability.

The final chapter of this dissertation presents two case studies to highlight the strengths and limitations of ATR-FTIR as interface-sensitive tool. The first case investigates the interfacial sensitivity of ATR-FTIR by performing a comparative study with the inherently surface sensitive technique vibrational summed frequency generation (SFG). The second case focusses on the integrated EIS-ATR-FTIR setup as in situ tool to simultaneously study chemisorption mechanisms and corrosion resistance. This demonstrates that in situ ATR-FTIR in Kretschmann configuration is a highly valuable tool for molecular studies at buried metal (oxide) – polymer interfaces during immersion in aqueous media.

Samenvatting

Tot op vandaag bestaat er nog steeds veel onduidelijkheid over de vorming en afbraak van moleculaire interacties aan het metaal oxide-polymeer grenslak, terwijl het een beperkende factor is voor de duurzaamheid van metaal-polymeer hybride systemen.

Om de corrosieweerstand en hechtingseigenschappen van het metaaloppervlak te verbeteren wordt deze vaak chemisch behandeld alvorens de verflaag aan te brengen. Echter omwille van ecologische en gezondheid gerelateerde problemen die geassocieerd worden met traditionele voorbehandelingen, die typisch zeswaardig chroom of hoge fosfaatconcentraties bevatten, worden zij momenteel vervangen door een nieuwe generatie ecologisch verantwoorde voorbehandelingen. Om de levensduur van recent ontwikkelde metaal-polymeer hybride systemen te garanderen, is er een urgente nood aan fundamentele inzichten in de effecten van substraat en voorbehandelingen variaties op de chemische hechting van polymeren. De uitdaging hierin bestaat erin om het verborgen grensvlak op een niet-destructieve manier te bereiken met oppervlakte gevoelige technieken. Hiervoor zijn we tot op vandaag nog steeds afhankelijk van modelsystemen. Echter, industriële metaal-polymeer systemen zijn typisch erg heterogeen waardoor de afstand tussen model en industriële systemen tot op vandaag nog steeds erg groot is.

Deze dissertatie beoogt deze afstand te verkleinen door een fundamentele studie op te bouwen, startende vanuit vereenvoudigde modelsystemen waarvan de complexiteit systematisch verhoogd wordt. Langs de ene kant trachten we het metaal-polymeer grensvlak te bereiken langs de polymeerzijde, door gebruik te maken van een organisch modelsysteem, en langs de andere kant trachten we hetzelfde grensvlak te bereiken langs de metaalzijde gebruik makend van model-metaalsubstraten. Door beide methoden complementair toe te passen, kunnen modelsystemen systematisch vergeleken worden met industrieel relevante metaal substraten en verfsystemen.

Het eerste deel van de thesis beschrijft de impact van substraat heterogeniteit op de vorming van conversielagen. De groeiende interesse in het implementeren van lichtgewicht metalen in geverfde toepassingen zoals auto's en gegalvaniseerd staal, leidde tot het gebruik van puur zink, aluminium en magnesium als gedefinieerde modelsubstraten. Hieruit volgde een verschillende conversie kinetiek voor de betreffende metalen die thermisch opgedampt werden als modelsubstraat, waarbij magnesium een 10 keer dikkere conversielaag groeit dan zink, en waarbij aluminium slechts gedeeltelijk bedekt wordt door een conversielaag en dus het minst effectief werd bevonden onder de gedefinieerde conversie condities. Naast de conversiekinetiek, bleek ook het (de)hydroxylatie evenwicht sterk afhankelijk te zijn van de initiële metaaloxide eigenschappen.

Het tweede deel van de dissertatie bestudeert metaal-molecuul interacties aan de hand van gefunctionaliseerde modelmoleculen. De functionaliteit van deze modelmoleculen werd

geselecteerd op basis van de functionele groepen aanwezig in polyester polyurethaan coil coats die verantwoordelijk worden geacht voor de hechting met het metaal substraat. Deze studie toont aan dat hydroxylgroepen op het metaaloxide oppervlak dienst doen als hechtingsplaats voor deze functionele groepen (esters en amiden). Daardoor is de hydroxidefractie rechtstreeks gerelateerd aan de hoeveelheid bindingen die worden gevormd aan het grensvlak. Anderzijds, het type binding dat gevormd word is afhankelijk van de zuur-base eigenschappen van het oxide. Het zuurkarakter van de metaaloxiden werd bovendien verhoogd door zircoon- en titaan-gebaseerde voorbehandelingen, waardoor de verhouding van competitieve grensvlakinteracties met zowel ester- als amide-groepen verschuift na chemische voorbehandeling.

Het derde deel van de dissertatie beoogt de chemisorptiemechanismen bekomen voor modelmoleculen te valideren voor industrieel relevante verfsystemen. Dit vereist het gebruik van modelmetaalsubstraten om het grensvlak langs de metaalzijde te bereiken. Een gelijkaardig hechtingsmechanisme kon zo aangetoond worden voor polyester primers. Naast de estergroepen eigen aan het polyester resin, blijkt ook de melamine-gebaseerde crosslinker interacties te vertonen met het metaal oxide oppervlak. Dit benadrukt de toenemende complexiteit van metaal-verf grensvlakken.

Vervolgens werd de (ont)hechting in-situ gevolgd tijdens het onderdompelen van het metaal-polymeer systeem in waterig milieu bij neutrale pH waarden. Dit toonde aan dat de afbraak van bindingen aan het grensvlak gerelateerd waren aan de gevoeligheid van metaal oxiden voor corrosie, welke afneemt in volgende volgorde: magnesium < zink < aluminium. Verder werd er aangetoond dat een zircoon-gebaseerde voorbehandeling actieve substraten zoals magnesium en zink passiveert, wat de afbraak van bindingen aan het grensvlak vertraagt. Bijgevolg kan men dus besluiten dat naast het type bindingen ook de activiteit van het metaaloxide een bepalende rol heeft voor de stabiliteit aan het grensvlak.

Het laatste deel van deze dissertatie beschrijft twee casestudies die de sterktes en beperkingen van ATR-FTIR benadrukken. De eerste case bestudeert de grensvlakgevoeligheid van ATR-FTIR aan de hand van een vergelijkende studie met de inherent oppervlaktegevoelige techniek vibrational summed frequency generation (SFG). De tweede case focust op de geïntegreerde EIS – ATR-FTIR setup als in situ tool om gelijktijdig chemisorptiemechanismen en corrosieweerstand te beoordelen. Dit toont aan dat situ ATR-FTIR in Kretschmann configuratie een zeer waardevolle oppervlaktegevoelige techniek is om moleculaire fenomenen aan het verborgen metaal(oxide) – polymeer grensvlakken te bestuderen en dit in situ tijdens onderdompeling in waterig milieu.

Abbreviations

2,5-PDCA	2,5-pyridinedicarboxylic acid
3-MSA	3-methylsalicylic acid
AES	Auger electron spectroscopy
ATR	Attenuated total reflection
BB	Bridging Bidentate
BE	Binding Energy
CA	Contact Angle
CB	Chelating bidentate
CE	Counter electrode
DFT	Density Functional Theory
DMS	Dimethylsuccinate
EC	Electrochemical cell
EIS	Electrochemical Impedance Spectroscopy
FA	Fumaric acid
FE-AES	Field Emmision Auger Electron Spectroscopy
FWHM	Full width Half Maximum
GI	Galvanized Iron
HB	Hydrogen bonding
HDG	Hot dip galvanized steel
IEP	Isoelectric point
IRE	Internal Reflection Element
IRRAS	Infrared Reflection – Absorption Spectroscopy
MOF	Metal Organic Framework
MZ	Magizinc®
OCP	Open Circuit Potential
PAA	Polyacrylic acid
PAW	Projector Augmented Wave
PDP	Potnetiodynamic polarisation measurements
PE	Polyester
PVA	Polyvinyl alcohol
PVD	Physical Vapor Deposition
PVP	Polyvinyl pyrrolidone
RE	Reference electrode
SFE	Surface Free Energy
SFG	Sum Frequency Generation
SS	Sodium salicylate
THF	Tetrahydrofuran
ToF-SIMS	Time of Flight – Secundary Ion Mass Spectroscopy
TiCC	Titanium-based Conversion Coating
VASP	Vienna Ab Initio Simulation Package
vdW	van der Waals
VIS	Visible light
WE	Working Electrode
XC	Exchange-Correlation
XPS	X-ray photoelectron Spectroscopy
ZrCC	Zirconium-based Conversion Coating

Chapter 1: Introduction

1.1. Motivation

Prepainted metal is a popular material in the building and construction industry, but also the automobile industry appreciates the many benefits of prepainted metal. Unlike other building materials, such as cement, wood and brick, prepainted metal can be recycled without loss of quality, durability or aesthetical appeal and this even for multiple times.[1] As a result 95 % of the prepainted metal used in buildings is being recycled, making it a very sustainable choice of material.[1] In the 1980's European-based coil coating companies began producing textured prepainted metal products, the look of traditional building materials such as brick, stone and wood could be recreated. Since then, prepainted metal is knowing a growing trend, which is forecast to maintain in the next decade.[2]

Figure 1.1: Examples of coil coat as roofing- and cladding products.[3]

Coil coating is a highly efficient way to apply surface treatments and paint finishes and is therefore very cost-effective. This process consists of multiple steps, including cleaning, pretreatment, i.e. chemical conversion coating and two paint sections, one for primer and one for top coat application.

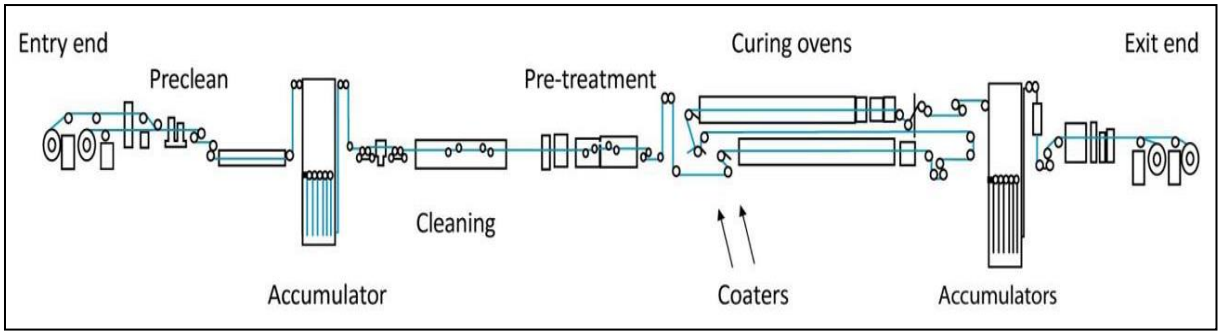

Figure 1.2: Multiple steps taken during the coil coating process.

With the appropriate surface treatment, prepainted roofing and cladding products can be amazingly durable. However, due to recent restrictions on the use of well-established treatments such as phosphating and hexavalent chrome passivation, a new generation of surface treatments are being

developed. Zirconium and/or titanium-based fluoroacid treatments are currently gaining more attention since they offer both improved corrosion resistance and paint adhesion.[4] However, whereas the corrosion resistance of zirconium- and titanium-based conversion coatings are extensively described, insights in their bonding properties and this on a molecular level are largely lacking. These lack of insights relate to the well-known difficulties of non-destructively probing metal-paint interfaces. Furthermore, next to new developments in surface treatment, also the base metal, typically hot dipped galvanized steel, continuously develops.[5–8] Conventional galvanized steel substrates concern steel substrates coated with a homogeneous zinc layer, in this thesis referred to as GI. However, zinc alloy coatings containing magnesium and aluminium additions are gaining more attentions because of their excellent corrosion resistance properties allowing the use of thinner coatings with respect to traditional zinc coatings.[9] TataSteel produces galvanized steel sheets with a zinc-aluminium-magnesium coating named Magizinc®, in this thesis referred to as MZ. These developments resulting in heterogeneous and multi-metal substrates poses a number of new challenges. Although different oxides exist at the surface of such multi-metal substrates, all are lead through the very same industrial coil coating process raising questions on the long term durability of newly designed metal-polymer hybrid systems.

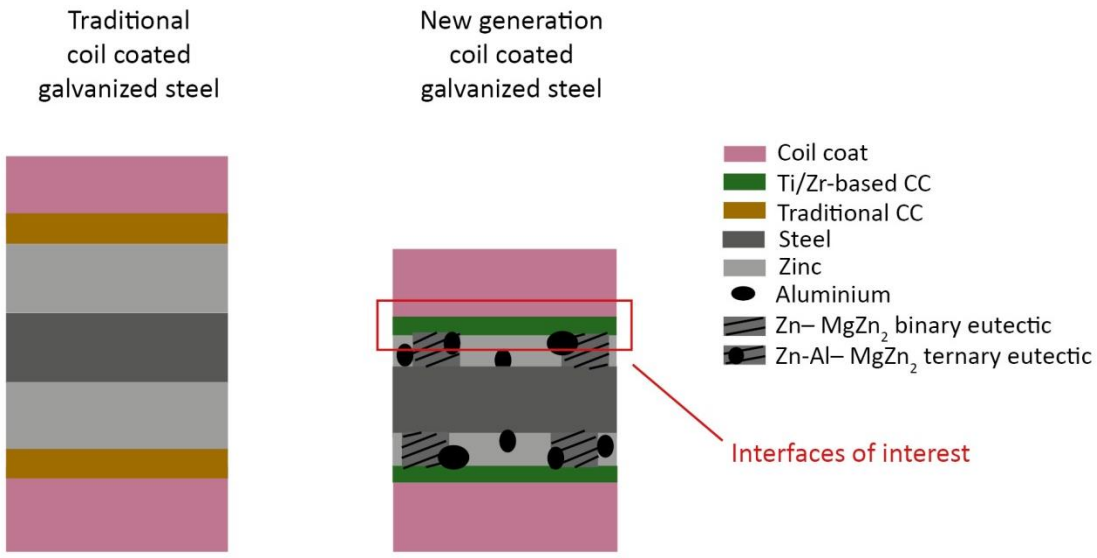

Figure 1.3: Traditional and new generation coil coated galvanized steel.

Until today, developing conversion coatings as well as organic coatings was much more based on trial and error than on science. Yet, the latter becomes inevitably more crucial due to more strict regulations and increasing performance requirements. A fundamental understanding of the relation between metal oxide physicochemical properties and its bonding affinity and stability towards organic coatings would allow for more efficient development of a new generation of chemical

conversion coatings. Consequently, there is an increasing need for thorough insights on interfacial bond formation and degradation mechanisms. However, whereas destructive methodologies on adhesion and corrosion resistance measurements are well established. This is not the case for non-destructive methodologies which aims to access the buried metal-polymer interface chemistry and this on a molecular level. In addition, since the durability of metal-polymer hybrid systems are determined by its resistance to interfacial bond degradation in the presence of water and ions, there is a need of studying metal-polymer interfaces in-situ during exposure to an aqueous environment.

1.2. Research aim

This thesis aims to develop a methodology that: (1) provides non-destructive access to the buried interface, (2) has a high surface sensitivity elucidating the interfacial chemistry on a molecular level and (3) which allows to in-situ to follow interfacial bond formation and degradation.

Using such non-destructive in-situ interfacial methodology, this thesis aims to (partially) answer following open research questions.

On the effect of substrate heterogeneities:

- *What is the effect of substrate heterogeneity on conversion coating formation?*
- *What is the role of metal oxide acid-base properties on chemisorption mechanisms?*
- *What is the role of surface hydroxides on the chemisorption mechanism?*
- *Which interface parameters are responsible for the stability of interfacial bonds established at (conversion treated) metal oxide-paint interfaces exposed to an aqueous environment?*
- *How do thermally vaporized model substrates used for the thin substrate approach correlate to industrially relevant substrates?*

On the effect of conversion bath composition:

- *What is the effect of conversion bath composition on the conversion layer build-up?*
- *What is the effect of fluoacid cation (Zr-and Ti) on adhesion performance?*
- *What is the effect of organic compounds added to conversion bath to adhesion performance?*

On the effect of paint composition and curing:

- *How do model organic components used for the model molecule and thin film approach correlate to industrially relevant paint formulations?*
- *How does curing alter the interfacial properties?*

On the development of a non-destructive in-situ interfacial sensitive tool:

- *What is the importance of the use of complementary tools?*

- *To which degree can attenuated total reflection – Fourier transform infrared spectroscopy (ATR-FTIR) in Kretschmann configuration be considered as an interfacial sensitive technique?*

1.3. Approach

1.3.1 Definition of metal substrates

The complicated microstructure of zinc alloyed coatings used for galvanizing increase the system complexity hindering a straightforward mechanistic study. Therefore, this study starts with separating the metal oxides occurring at galvanized steel surfaces, i.e. zinc, aluminium and magnesium oxide.

The main challenge of studying buried metal-polymer interfaces are the high thicknesses of industrially relevant metal substrates and polymer coatings. Because of these high thickness, they fully absorb X-rays or infrared radiation before reaching the metal-polymer interface, hindering the use conventional surface sensitive techniques. Therefore, until today the application of thin films with a thickness in the nanoscale remains a prerequisite for non-destructive access of the buried metal-polymer interface. This thin film approach can be employed from the metal side using thermally evaporated metal films with applied thicknesses between 20-80 nm allowing the use of spectroscopic techniques such as attenuated total reflection – Fourier transform infrared spectroscopy (ATR-FTIR) and sum frequency generation (SFG). Nevertheless, it can be expected that the oxide's nature and thus its bonding properties considerably varies between thermally vaporized metal films (model substrates) and thicker metal sheets (bulk substrates). Therefore, a comparative study between thermally vaporized model substrates and thicker metal substrates has been conducted. Polished metal sheets with a high purity grade of zinc, aluminium and magnesium (bulk substrates) have been used as an intermediate step between thermally vaporized model metal substrates and industrial galvanized steel substrates (GI and MZ), as illustrated in figure 1.4. For this approach, reaching the metal-polymer interface form the polymer side, a thin organic coating is required allowing the use surface sensitive techniques such as X-ray photonelectron spectroscopy (XPS).

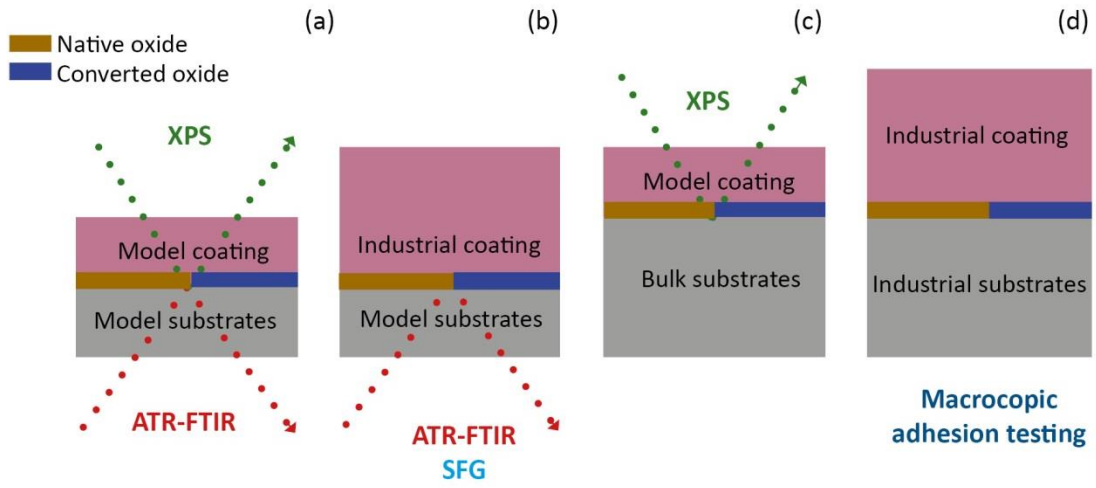

Figure 1.4: Bridging fundamental science with industrially applied metal-polymer hybrid systems.

1.3.2 Definition of conversion bath

The formation of zirconium- and titanium-based conversion film formation on these multi-metal substrates have been characterized both in-situ and ex-situ. Initially, a commercial zirconium-based conversion solution has been used, containing hexafluorozirconic acid, phosphates and polyacrylate. However, the multi-component composition of commercial conversion coatings complicate the subsequent bonding studies due to the high share of interface variables. Therefore, model conversion solutions have been defined to characterize the bonding properties of zirconium- and titanium conversion coatings without additives. After studying the role of metal oxide cations (Zn, Al, Mg, Zr, Ti), commonly used organic additives have been added to the zirconium-and titanium-based conversion solutions to study their effect on the chemisorption of organic compounds and their stability in aqueous environment

1.3.3 Definition of the polymer coating

Due to the multicomponent composition of industrial coatings the resulting spectra become very complex and information-rich and thus hard to interpret. As a consequence, chemical interfacial interactions have been unravelled using model compounds with a well-defined chemistry even when the interface has been approached from the metal side. As such monomeric molecules with carboxylic acid, ester and amide functionalities has been defined representative for polyester polyurethane primers. In addition, a comparative study using aliphatic and aromatic carboxylic acid compounds elaborates on the contribution of π-electrons at interfacial interactions. Subsequently, the unravelled chemisorption mechanisms using model compounds are being translated to industrial multi-component coating, i.e. a primer with polyester-based resin and melamine-based crosslinker. Upon characterizing the chemisorption of the polyester coil coat in dry conditions, the metal-polymer

hybrid system will be exposed to an aqueous environment to further determine the stability of the established interfacial bonds. This stepwise approach is illustrated in figure 1.5.

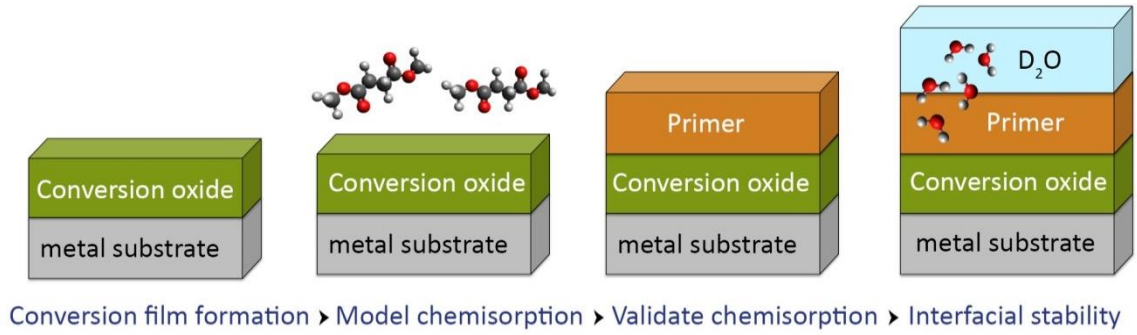

Figure 1.5: Research steps taken in the proposed research approach.

1.4. Thesis outline

Figure 1.6 illustrates the structure of this thesis. The industrial relevance of this work and a general introduction are given in chapter 1. Chapter 2 provides an extensive literature review on the corrosion properties of newly developed galvanized steel substrates, fluoro acid-based treatments as a promising chrome(VI)-free pretreatments and state-of-the-art methodologies for studying buried metal-polymer interfaces. Subsequently, the experimental work is presented in chapter 3-7. Because the published articles related to this thesis systematically describe conversion film formation, chemisorption mechanisms and interfacial stability, there has been opted to disassemble the published articles accordingly to maintain a structure as illustrated in figure 1.5. Chapter 3, describes the conversion film formation of multi-metal model evaporated and bulk substrates, i.e. zinc, aluminium and magnesium with a high purity grade (> 99.9 %) and industrially relevant galvanized steel substrates, i.e. GI and MZ. First a commercially available zirconium-based conversion system has been characterized to demonstrate its complexity, after which model conversion solutions have been defined based on hexafluorozirconic and -titanic acid. Chapter 4 unravels chemisorption mechanisms at the respective (converted) metal substrates using model monomeric compounds with functionalized groups representative for polyester polyurethane primers. Subsequently, the elucidated chemisorption mechanisms are validated using realistic paint formulations in chapter 5. The bonds established in dry conditions as described in chapter 5 are than exposed to aqueous media to determine their stability as given in chapter 6. Finally, chapter 7 covers the strengths and limitations of ATR-FTIR as interfacial sensitive technique. The conclusions and further perspectives of this current work are summarized in chapter 8. The numbers given between brackets in the thesis outline illustrated in figure 1.6 refer to the articles where parts of the concerning chapter are being published.

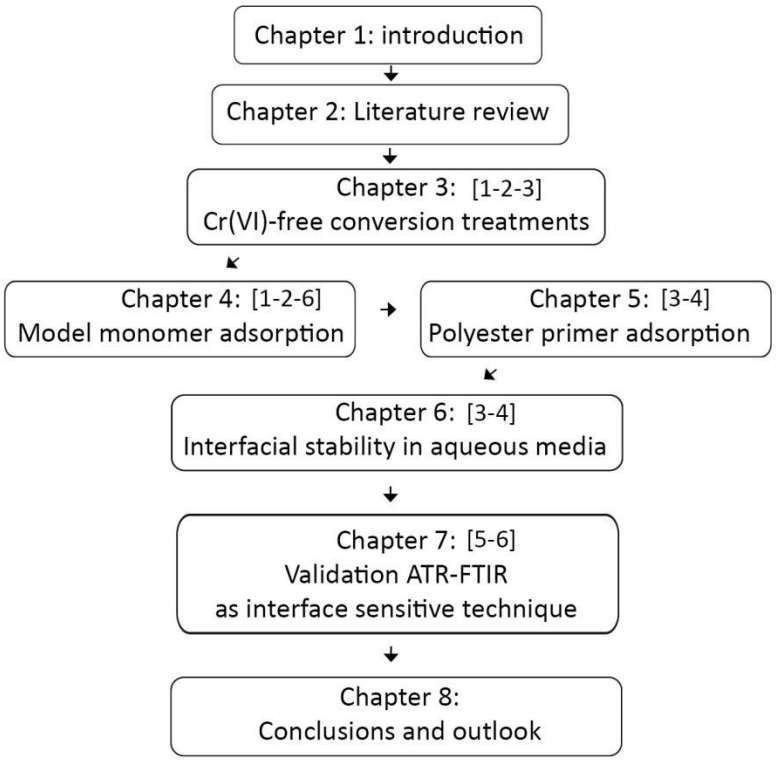

Figure 1.6: Thesis outline

Articles referring to this thesis:

[1] L. I. Fockaert, P. Taheri, S. T. Abrahami, B. Boelen, H. Terryn, J. M. C. Mol, Zirconium-based conversion film formation on zinc, aluminium and magnesium oxides and their interactions with functionalized molecules. *Applied Surface Science*, 423 **(2017)** 817–828.

[2] L.I. Fockaert, S. Pletincx, D. Ganzinga-Jurg, B. Boelen, T. Hauffman, H. Terryn, J. M. C. Mol, Chemisorption of polyester coatings on zirconium-based conversion coated multi-metal substrates and their stability in aqueous environment, *Applied Surface Science*, 508 **(2020)** 144771-144781.

[3] L. I. Fockaert, M. V. E. Ankora, J. P. B. Van Dam, S. Pletincx, A. Yilmaz, B. Boelen, T. Hauffman, Y. Garcia-Gonzalez, H. Terryn, J. M. C. Mol, Effect of organic additives in fluoacid-based Ti and Zr-treatments for galvanized steel on the stability of a polymer coated interface, *Progress in Organic Coatings,* 146 **(2020)** 105738.

Erratum to 'Effect of organic additives in fluoacid-based Ti and Zr-treatments for galvanized steel on the stability of a polymer coated interface.' *Progress in Organic Coatings*, **(2020)** 105902.

[4] L.I. Fockaert, S. Pletincx, D. Ganzinga-Jurg, B. Boelen, T. Hauffman, H. Terryn, J. M. C. Mol, Chemisorption of polyester coatings on zirconium-based conversion coated multi-metal substrates and their stability in aqueous environment, *Applied Surface Science*, 508 **(2020)** 144771-144781.

[5] L.I. Fockaert, D. Ganzinga-Jurg, J. Versluis, B. Boelen, H.J. Bakker, H. Terryn, J.M.C. Mol, Studying chemisorption at metal-polymer interfaces by complementary use of attenuated total reflection – Fourier transform infrared spectroscopy (ATR-FTIR) in the Kretschmann geometry and visible-infrared

sum-frequency generation spectroscopy (SFG), *Journal of Physical Chemistry C,* 124, 13 **(2020)** 7127-7138.

[6] L. I. Fockaert, T. Würger, R. Unbehau, B. Boelen, R. H. Meißner, S. V. Lamaka, M. L. Zheludkevich, H. Terryn, J. M. C. Mol, ATR-FTIR in Kretschmann configuration integrated with electrochemical cell as in-situ interfacial sensitive tool to study corrosion inhibitors for magnesium substrates, *Electrochimica Acta*, 345 **(2020)** 136166.

References

(1) European coil coating Association (ecca). Ecca Sustainibility Report. 2014.

(2) Grand View Research. Market Research Report, U.S. Coil Coated Steel Market Size, Share and Trends Analysis Report 2019-2025. 2019, p 114.

(3) TataSteel Colorcoat Urban®.

(4) Milošev, I.; Frankel, G. S. Review—Conversion Coatings Based on Zirconium and/or Titanium. *J. Electrochem. Soc.* **2018**, *165* (3), C127–C144.

(5) Elvins, J.; Spittle, J. A.; Sullivan, J. H.; Worsley, D. A. The Effect of Magnesium Additions on the Microstructure and Cut Edge Corrosion Resistance of Zinc Aluminium Alloy Galvanised Steel. *Corros. Sci.* **2008**, *50* (6), 1650–1658.

(6) Sullivan, J.; Mehraban, S.; Elvins, J. In Situ Monitoring of the Microstructural Corrosion Mechanisms of Zinc-Magnesium-Aluminium Alloys Using Time Lapse Microscopy. *Corros. Sci.* **2011**, *53* (6), 2208–2215.

(7) Davies, J. L.; Glover, C. F.; Van de Langkruis, J.; Zoestbergen, E.; Williams, G. The Effect of Mg Concentration on the Resistance of PVD Zn-Mg Coatings to Corrosion Driven Organic Coating Delamination. *Corros. Sci.* **2015**, *100*, 607–618.

(8) Zoestbergen, E.; Langkruis, J. Van De; Maalman, T. F. J.; Batyrev, E. Influence of Diffusion on the Coating Adhesion of Zinc-Magnesium Thin Films onto Steel. *Surf. Coat. Technol.* **2017**, *309*, 904–910.

(9) Thierry, D.; Persson, D.; Le Bozec, N. *Atmospheric Corrosion of Zinc and Zinc Alloyed Coated Steel*; Elsevier, 2018.

Chapter 2: Literature review

To guarantee the lifetime of newly developed metal-polymer hybrid systems, there is an urgent need to gain fundamental insights on the impact of substrate and pretreatment variations on the (chemical) adhesion of coil coat primers. The existing lack of knowledge on metal paint interfaces relates to the difficulty of studying buried interfaces. Different methodologies have been developed in the past to overcome this challenge. For non-destructive research simplification of reality remains a prerequisite. However, with newly developed multi-substrates, as well as multi-component paint systems, there remains a gap between model and realistic systems. Moreover, a new generation of Cr(VI)-free surface treatments arises. Fundamental knowledge on the relation of oxide properties and paint adhesion would allow more efficient developments within chemical treatments. This chapter aims to describe innovations within galvanizing, Cr(VI)-free conversion treatments as well as the state-of-the-art methodologies currently used to study buried metal-polymer.

2.1 Introduction

The need for thinner, weight-saving zinc coatings together with the aim of conserving limited natural zinc resources, creates a significant industrial interest in the reduction of the amount of zinc used in galvanized steel. The best balance between adhesion quality, corrosion performance and cost was determined for an aluminium-magnesium-zinc alloy.[1] In order to further improve the durability of galvanized steel a protective polymer coating can be applied. Coil coating represents the most efficient, reliable and environmentally friendly means of applying a high quality paint finish to metal surfaces for the building industry. This process includes i.e. a cleaning-, pretreatment- and a paint section, determining the final quality and durability of the polymer-metal hybrid system. Alterations in metal oxide chemistry and morphology, induced by varying types of galvanized steel, greatly influence subsequent pretreatment processes[2,3] and final interfacial metal-polymer bonding integrity.[4] To establish a stable metal-polymer adhesion a chemical conversion treatment is applied on the metal surface. Traditional conversion coatings based on phosphate and hexavalent chromate are associated to different health and environmental issues. As a result a new generation of surface treatments based on non-regulated metals (Zr, Ti) and with a reduced phosphate load arises. However, the traditional surface treatments have been used during the past 60 years, proving their long term effectiveness and self-healing properties in the case of hexavalent chromate.[5,6] Although the new generation conversion processes are associated to lower energy consumption and waste disposal, their long term effects are not yet fully determined. Moreover, the effect of substrate variations on conversion film formation remains underexposed. Acquiring a correlation between initial metal oxide and final conversion oxide physicochemical properties is important to understand the consequences for subsequent corrosion resistance and paint adhesion.[7] Whereas the corrosion resistance of zirconium- and titanium-treatments is relatively well described,[8–13] its effect on the chemisorption of polymer coatings remains far from fully understood. A major reason for this lack of knowledge relates to the well-known difficulties of studying buried interfaces.[14] In addition, a high portion of interface variables in each separate layer of the metal-polymer hybrid system, i.e. metal substrate heterogeneities, multi-component conversion solutions and multi-component paint formulations hinder a straightforward mechanistic study. This chapter provides a literature review on development in galvanizing, zirconium-based conversion treatments and state-of-the-art methodologies to study buried metal-polymer interfaces.

2.2 Zinc and zinc-alloyed coated steel

The application of zinc and zinc alloyed coatings on steel is one of the commercially most important processing techniques used to protect steel components exposed to corrosive environments.[15] The

first usage of zinc in construction dates from 79 AD,[16] hence its capability to protect iron and steel from corrosion has long been known. Today, more than 13 million tons of zinc are produced annually word wide of which more than half is used for galvanizing.[16] The most common technique used to apply a zinc coating is the hot-dip (HDG) in a molten zinc bath, which results in a thick zinc coat. Other ways are continuous sheet galvanizing, spraying or electro-galvanizing, which results in approximately 10 times thinner zinc layers compared to HDG, what makes them less suited for outdoor use. This work focusses on two types of hot-dip galvanized steel sheets. Conventionally hot-dip galvanized steel (GI) resulting in a homogeneous zinc coat and a zinc-aluminium-magnesium coat (MZ). Their properties will be briefly discussed in the following paragraphs.

2.2.1 Hot-dip galvanized steel (GI) with low aluminium additions (<1 %)

GI results from dipping steel into a molten zinc bath with low additions of aluminium. Aluminium levels of more than 0.005 wt. % form a $Fe_2Al_5Zn_X$ inhibiting layer at the iron-zinc interface suppressing the formation of brittle Fe-Zn phases.[17] This compact and hence ductile inhibiting layer acts as a barrier to preventing the diffusion of Fe and Zn atoms forming other alloy layers and allows the coated sheet to be formed into many complexes without loss of coating adhesion.[17] In addition, a continuous Al_2O_3 layer is formed on the zinc coating surface. This surface layer of aluminium improves the reflectivity of the surface, but is known to be detrimental for paint adhesion. Consequently, prior to coil coating surface aluminium will be removed, typically by an alkaline cleaning step.

2.2.2 Magizinc (MZ) with additions of aluminium (1.6 %) and magnesium (1.6 %)

Zinc coatings add corrosion resistance to steel by offering barrier and sacrificial corrosion protection. Therefore, the durability of the protective zinc film is mainly determined by its thickness.[17] A lot of work has been done towards achieving thinner weight-saving coatings with comparable or an even better performance than the traditional GI. This in order to optimize process costs as well as conserving limited natural resources and reducing energy consumption and carbon emissions. Different types of zinc alloys have shown to fulfill these requirements without reducing corrosion resistance.[3–10] Additions of small amounts of magnesium have shown to provide two to four times longer corrosion protection than the standard zinc alloy.[21] However, the addition of magnesium limits the adhesion to steel.[22] This effect can be solved by adding aluminium to the alloy, at least equaling the level of magnesium, which at the same time offers the possibility of further improvements in corrosion protection.[1] Numerous studies describe the formation of compact protective corrosion products on zinc alloyed coatings.[3–10] The atmospheric corrosion rate of galvanized steel is governed by oxygen reduction which is often limited by diffusion through a layer

of corrosion products. Therefore, together with the eutectic microstructure, which retards the corrosion progress, the nature and stability of the corrosion products is considered as the main mechanism responsible for the enhanced corrosion performance.[23] The presence of ZnO is often associated with elevated corrosion rates since it accelerates the electron transfer from zinc to adsorbed oxygen molecule. The formation of this undesired corrosion product is hindered by zinc-aluminium-magnesium alloyed coatings, which corrosion products have lower electric conductivity inhibiting the rate-controlling oxygen reduction reaction.[24] This was confirmed by scanning Kelvin probes experiments, which showed that the oxygen reduction efficiency significantly decreased due to the presence of aluminium and even more strongly by the presence of magnesium.[24] Impedance measurements revealed that the capacity of the double electric layer decreases significantly with the content of magnesium and aluminium, which was ascribed to a decreasing porosity of the corrosion products.[24] The presence of magnesium hinders the formation soluble hydroxide, carbonate or sulfate complexes by pH buffering or by consumption of the excess anions. The continuous ability of magnesium corrosion products to neutralize hydroxide ions at the cathodes reduces the surface alkalinity allowing the formation of insoluble zinc hydroxyl chloride simonkolleite ($Zn_5(OH)_8Cl_2$-H_2O).[21,25] This stabilization effect of Mg^{2+} occurs in an initial corrosion stage, whereafter in an advanced stage, the dissolution of aluminium starts in neutral or alkaline conditions. In neutral conditions Al^{3+} is formed when zinc rich phases are sufficiently consumed to allow an increase of the electrochemical potential. The presence of Al^{3+} results in formation of Zn-Al and or Mg-Al layered double hydroxide (LDH).[23,26] The chemical composition of LDH can be described as: $M(II)_XM(III)_Y(A-)_M(OH)_N.zH_2O$ with M(II) = Mg^{2+} or Zn^{2+}, M(III) = Al^{3+} and A^- = CO_3^{2-}, Cl^- or SO_4^{2-}.[26] The dissolution of magnesium and aluminium controls the pH and has a buffering effect which prevents the formation of regions with very high pH. This reduces (or prevent) the formation of ZnO and extensive zinc dissolution in alkaline areas at the cathodic sites.[27] Instead magnesium and aluminium will precipitate on the surface slowing down the cathodic process and as a consequence also retard the anodic dissolution of the Zn–$MgZn_2$ phases.[27] Mg/Al LDH is formed in larger amounts compared to Zn/Al LDH implying a preferential dissolution of magnesium in the initial stages of the corrosion.[27] The formation of LDH on aluminium containing alloys has been reported to show a 4-6 times lower mass loss than GI, however ZnMg did not contain LDH and performed even better with up to 10-fold lower weight loss compared to zinc.[18,19] The contribution of Mg ions on the formation of different corrosion products is thus very complex and is still a subject for further investigations.[28] The presence of LDH on corroded coatings might be a consequence of high pH at cathodic sites, leading to the dissolution of aluminium.[29] The relative content of LDH in corrosion products then correlates to the aggressiveness of exposure conditions, specifically to a chloride load. Harsh conditions (acid pH, alkaline pH, extreme salt concentrations) can cause misleading conclusion as compared to real live

situations. Therefore recent publications described electrolytes based upon a statistical study of natural rainwater composition respecting the ratio of the various species while maintaining a total dissolved salt content equivalent to standard corrosion testing electrolytes.[23,29,30] Those publications revealed that LDH formation was delayed during rainwater tests, suggesting an overestimated anticorrosion performance in accelerated tests. Moreover the weight loss of both GI and zinc-magnesium alloys in rainwater was higher than in modified rainwater, indicating that the reality is more complex and other possible effects of NH^{4+} and HCO^{3-} on the corrosion mechanisms such as modification of the intrinsic anodic reactivity should be considered.[29]

However, the chemical nature of the protective layer was not uniquely identified. Basic zinc salts such as zinc hydroxyl chloride (=simonkolleite)[18], Al-rich oxide layers[31], layered double hydroxides[23,25,27], hydrozincite[19] and other carbonate compounds are described corrosion products. The variation of the reported results relates to the highly heterogeneous microstructure of the alloyed coating as well as the various chemical environments used to study corrosion. The $ZnAl_2Mg_2$ coating has a multiphase structure with a Zn– $MgZn_2$ binary eutectic and Zn dendrites. In addition, there are also zones of ternary eutectic Zn–Al–$MgZn_2$ and Al-dendrites, these phases are illustrated in figure 2.1.[32] This heterogeneity hinders a straightforward mechanistic study on the correlation of the different oxides and their physicochemical properties to their bonding properties and the stability of metal-polymer hybrid interfaces when water is being introduced.

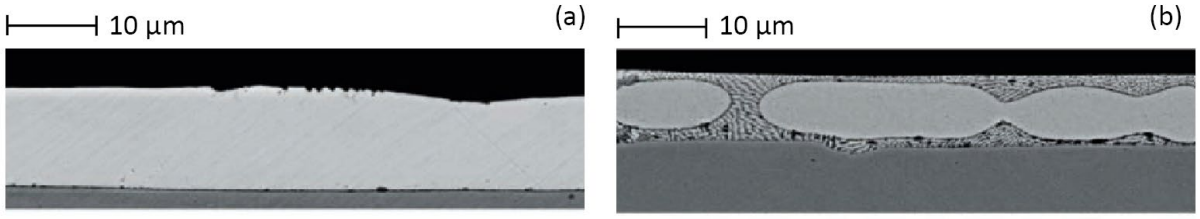

Figure 2.1: Crossection profile of microstructure zinc coatings on (a) GI and (b) MZ.[32]

2.3 Cr(VI)-free surface treatments

2.3.1 titanium- and zirconium-based conversion film formation

Recent restrictions on the use of carcinogenic hexavalent chromium, as well as ecological concerns on the use of heavy loads of phosphate lead to the development of a new generation of surface treatments. Currently, zirconium- and/or titanium-treatments are considered as viable alternatives since they improve both corrosion resistance[8–13] and paint adhesion[7,33–36] and this on both ferrous and non-ferrous substrates.[37] Fluorides present in the conversion solution activate the metal oxide removing natural metal (hydr)oxides by anodic dissolution.[38] The requirement for fluoride attack depends on the nature and thus the electrochemical activity of the native oxide.[39] During the anodic dissolution of native metal (hydr)oxides cathodic counter reactions are taking place on local cathodes

which lead to local alkalinization and thus the precipitation of zirconium- and titanium oxides.[2,40–43] Consequently, zirconium and titanium-based conversion are pH-based as well as electrochemical-based processess.[39–45]

Tetravalent elements are soluble only within narrow acidity ranges and the hydroxides $M(OH)_4$ are too polarized to be stable.[46] Consequently, because of their high formal charge, Ti and Zr cations hydrolyse to hydrated oxides.[46,47] In the case of titanium oxide, spontaneous dehydration via oxolation reactions leads to TiO_2 which crystal structure (rutile or anatase) depends on the acidic and temperature conditions.[39,46,48] Conversely, the high coordination number of zirconium ($N_{Zr} = 8$ vs $N_{Ti} = 6$) and resulting geometry (associated with its larger ionic radius) does not allow the formation of compact condensation products.[47] Instead, amorphous polymeric structures are being formed, also known as oxyhydroxides.[46–50] Literature on precipitation of Zr(VI)- and Ti(VI)-oxides from fluoroacid solutions are very scarce. Verdier *et al.* showed that during the conversion of AM60 magnesium alloy, titanium occurred only in its oxide form (TiO_2), whereas zirconium, depending on the solution composition, was found as oxide (ZrO_2), oxyhydroxide ($ZrO_{2-x}OH_{2x}$) and hydroxyfluoride.[48] This confirms the formation of amorphous zirconium oxyhydroxide phases, which have been reported to have variable compositions depending on the experimental conditions.[47] As such, the pH, Zr concentration, temperature and presence of anions in the conversion solution determine the equilibrium between competitive olation (leading to Zr-OH-Zr bonds) and oxolation (leading to Zr-O-Zr bonds) reactions.[46,47] Finally, when forming solid phases, OH groups can be replaced by anions, which effect diminishes with increasing pH.[47]

Although the conversion mechanism is reported to be similar for different substrates.[42] Deposition kinetics and thus lateral and in-depth elemental composition highly depends on the fluorine concentration, presence of additives to the conversion solution and the nature of native oxide.[2,3] The previous paragraph already discussed the ability of magnesium to neutralize hydroxide ions at the cathodes present at the MZ surface, which may delay the precipitation of zirconium and titanium oxides. On the other hand, the various phases appearing at the MZ surface increase the electrochemical activity compared to GI. Consequently, variations in electrochemical activity and local pH effects at GI and MZ surfaces are expected to affect the kinetics of conversion film formation and thus the thickness and elemental distribution both lateral and in-depth.[42] Lostak reported that Zn-rich phases are more noble than Al-rich phases, while both are nobler than Mg-rich phases.[43] Additionally, he showed that the deposition of zirconium-based conversion coating on Zn-Al-Mg alloys preferentially starts on Zn-rich cathodes. The simultaneous dissolution of Mg- and to a lesser extent Al-rich phases enriched the metallic phases with Zn. Upon, longer immersion times, precipitation of the zirconium-based conversion coating also takes place on Mg-rich phases, followed by complete coverage of the alloy surface.[43]

2.3.2 Barrier and bonding properties titanium- and zirconium-based conversion films

It is well accepted that the preferred deposition of zirconium oxide layers occurs on and around intermetallic particles.[40–42] The coverage of these surface heterogeneities are reported to reduce potential differences and thus cathodic activity, which is one explanation of improved corrosion resistance by zirconium- and titanium-treatments. Additionally, zirconium-based conversion coatings have been reported to reduce the corrosion current density on aluminium alloys,[38,51,52] galvanized steel[12,53] and steel substrates[9,11,34] acting as a barrier coating. These barrier properties can be further improved by adding inorganic and or organic compounds to the conversion bath. Typical inorganic additives are metallic cations (Cu, Ni) in the form of phosphates or sulphates.[54,55] Whereas the metallic cations act as nucleation sites enhancing precipitation of the conversion layer[42], barrier properties are enhanced by their anionic counterparts. Next to adding corrosion resistance conversion coatings are expected to improve bonding properties to an organic layer. Improved paint adhesion has been ascribed to altered oxide physicochemical properties upon zirconium-treatment. Increased surface roughness,[56] surface free energies,[9,57] electron donor properties[45,58] and altered hydroxide fractions[7,45] have shown to enhance chemical interactions with an organic layer. Moreover, scanning Kelvin probe studies revealed a lowered potential difference at the delamination front reducing the delamination rate.[59] However, the impact of organic additives is less described. There are various reasons to add polymeric compounds to the conversion solution. Among others, they are supposed to improve conversion coating homogeneity, as well as enhance bonding properties to both the underlying substrate and overlaying paint layer.[60–62] Common water soluble polymeric compounds found in patents to be added to conversion treatments are polyacrylic acid (PAA), polyvinyl alcohol (PVA) and polyvinyl pyrrolidone (PVP).[61–65] It has been reported that polymeric additives are more effective in a zirconium- than in a titanium-based coating due to the ability of zirconium to act as a crosslinking agent.[60] Deck *et al.* reported that the addition of polymeric additives improves both stability and corrosion resistance of zirconium- and titanium-treatment of aluminium, with polyacryl amide performing better than polyacrylic acid.[60] Smit et al, investigated the effect of polyacrylic and tannic acid added to the titanium-treatment of aluminium-manganese alloys and confirmed the corrosion resistance to be improved significantly due to organic additives.[51] However, longer immersion in NaCl solutions leads to selective dissolution of the polymer film resulting in worse corrosion protection performances than those obtained after titanium-treatment without organic additives.[51] Since the majority of the work on zirconium- and titanium-treatments focusses on corrosion resistance and macroscopic adhesion testing, fundamental insights on the bonding properties of zirconium- and titanium coatings are largely missing. Yet similarities can be found in literature describing metal-organic frameworks (MOFs).[66] MOFs are metal ions coordinated to organic ligands forming one, two-or three dimensional structures, mostly containing divalent

transition metal cations.[66] However, there is a high interest in increasing the charge of the metal cation to strengthen the cation-ligand bond and thus its chemical stability (especially in the presence of water).[66] Ti(IV) is considered as a highly attractive, yet challenging cation due to its high polarizing power resulting in fast and spontaneous precipitation of TiO_2.[66] Zr(IV) on the other hand, has shown to be a noticeable exception for tetravalent cations based MOFs.[67] The high affinity between Zr(IV) and carboxylate oxygen atoms gives stable Zr-MOFs in organic solvents, water and acidic aqueous solutions. In alkaline aqueous solutions they are found to be less stable due to replacement of carboxylate groups by OH^- anions.[67] Although such coordination chemistry cannot fully be translated to metal oxide – polymer interactions, higher bonding properties of zirconium than titanium oxide can be hypothesized from this.

2.3.3 The role of surface hydroxide fractions on conversion film formation

Different studies reported that the deposition kinetics and elemental distribution (lateral and in-depth) strongly depend on the microstructure and chemistry of the substrate surface.[3,7,39–41,43] In-situ ATR-FTIR combined with OCP measurements elucidated the critical importance of the initial hydroxide fraction on the zirconium deposition rate and final surface chemistry.[45] As such, high hydroxide fractions were shown to encourage the zirconium deposition, whereas lower hydroxide fractions favours surface hydroxylation what retards the zirconium deposition as depicted in scheme 2.2[45] This competitive surface hydroxylation has shown to retard the zirconium deposition of zinc [3] and AA6014 [2].

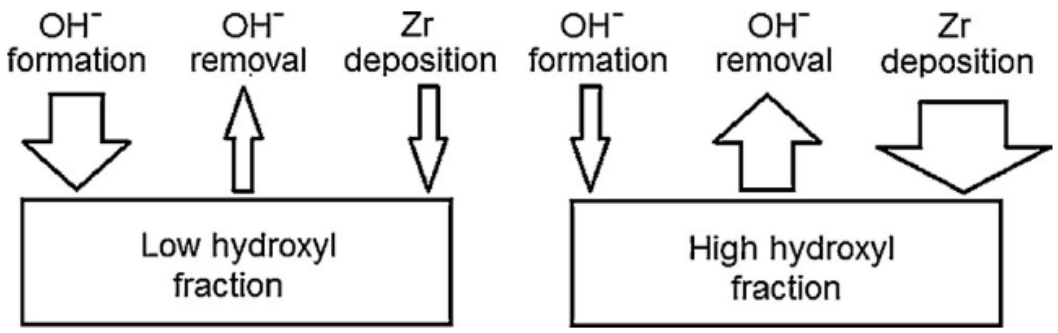

Figure 2.2: Schematic sketch of the conversion process kinetics versus the initial hydroxyl fraction. The arrow widths indicate the process kinetics qualitatively.[45]

In accordance to the work of Taheri et al.[45], on pure zinc substrates, Cerezo et al.[2], confirmed the determining role of surface hydroxide fractions during zirconium-based conversion of aluminium alloys. However, the resulting surface chemistry is shown to be highly substrate dependent. Low hydroxylated aluminium alloys result in a less developed zirconium film which contains more aluminium(hydr)oxides.[2] On the other hand, higher amounts of zinc impurities occur within the

zirconium film when zinc is highly hydroxylated.[45] This phenomenon, shown in figure 2.3, demonstrates the importance of a fundamental interface parameter study to gain insights in the zirconium oxide deposition on multi-metal substrates.

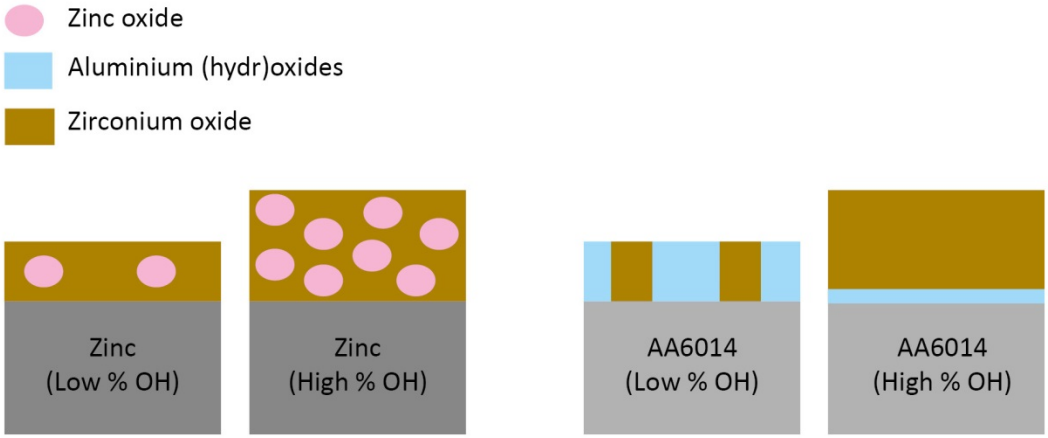

Figure 2.3: schematic presentation of the effect of initial surface hydroxide fractions on zinc[45] and aluminium alloy 6014[2] substrates on the final zirconium-converted oxide composition.

2.4 The chemistry of polyester-polyurethane primers relevant for coil coating

Polyester/polyurethane primers are widely used as in coil coating and therefore the coating of interest for this current research.[75,76] The final coating properties strongly depend on the nature of the resin components. Aromatic isocyanates result in higher rates of cross-linking and curing, but these resins are susceptible to color retention due to sunlight exposure.[75] Conversely, aliphatic isocyanates lead to lower rates of cross-linking and curing and are therefore better resistance to yellowing and chalking.[75] Although polyester polyurethanes are highly cross-linked resins when cured, they are not suitable for immersion service.[76] However, they have excellent heat stability, adhesive properties and oil resistance, making them highly suitable as primer. Additionally, the lower manufacturing cost has made widespread application of polyester type PU coatings.[76] These resins are formed by reaction of a polyisocyanate with free hydroxyl groups in polyols such as acrylics, epoxies, polyesters, polyethers and vinyls,[76] as demonstrated in figure 2.4.

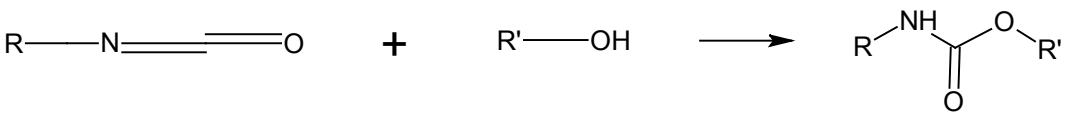

Figure 2.4: Reaction of a polyisocyanate and an alcohol forming polyurethane resin.

Polyesters polyols are formed during the reaction of diacid with an excess diol, as seen in figure 2.5. Despite the vulnerability of polyester polyols to gradually hydrolyse to their former carboxylic acid

and alcohol, they are generally preferred for harder coatings with better weather resistance.[76] The in-situ formation of carboxylic acid catalyses further ester hydrolysis, accounting for an significant reduction of average molar mass.[76] Therefore, to slow down deterioration of mechanical properties during prolong exposure to humid atmosphere acid scavengers are typically added to suppress this autocatalytic effect.[76]

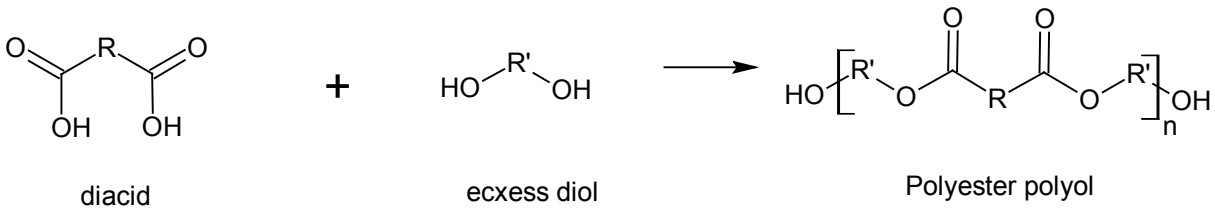

Figure 2.5: Preparation of polyester polyol with diacid and excess diol.

Polyester resins for coating applications are usually prepared with both aromatic and aliphatic dibasic acids.[77] The excess acid and alcohol compounds in the polyester resin is indicated by the acid- and OH-value which is obtained by titration. The polyester primer formulation used in this current work is given in table 2.1. Two types of coil coat formulations have been used, i.e. a white pigmented primer and a transparent clearcoat. Both coatings are crosslinked with a melamine-based crosslinker, which crosslinking reaction takes place between terminal CH_3 groups of the highly methylated melamine-based crosslinker and OH-groups of the highly hydroxylated polyesters as illustrated in figure 2.6. [78]

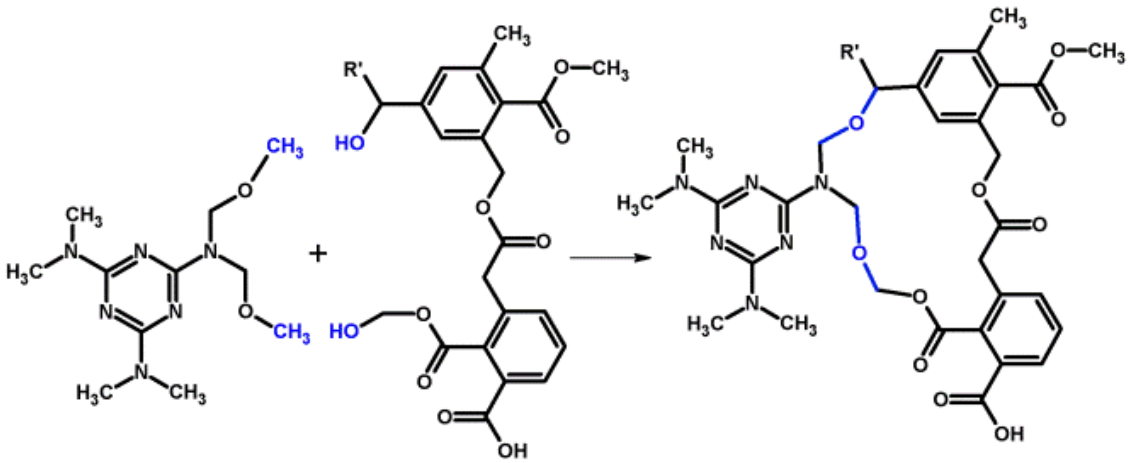

Figure 2.6: Crosslinking reaction between highly hydroxylated polyester resin and highly methylated melamine-based crosslinker.

The multi-component coil coat formulation given in table 2.1, indicates the high complexity of industrially relevant paint systems. As a result, the use of vibrational tools lead to information rich interfacial spectra hindering a straightforward mechanistic study. Moreover, the high absorptive properties of both paint and metal substrate hinder direct access to the buried metal-paint interface

using conventional surface sensitive techniques such as XPS and ToF-SIMS. Therefore, major insights in metal-polymer chemisorption reactions result from model systems.[45,79–84] Different methodologies for studying chemisorption mechanisms are discussed below. Moreover, a literature review on chemisorption mechanisms reported on zinc, aluminium and magnesium oxide is given in the following paragraphs.

Table 2.1 Polyester primer and clearcoat formulation

Compound	**Quantity primer (wt. %)**	**Quantity Clearcoat (wt. %)**	**Function**	**Chemistry + properties**
Dynapol LH 820-16 /55%	61.1	70.2	Polyester resin	Saturated, medium molecular (MM 5000 g/mol), linear hydroxylated co-polyester resin. T_G = 60°C, (acid value of 2 mg KOH /g and an OH-value of 20 mg KOH /g)
Aerosil 200	0.4	0.0	Thicking agent	SiO_2, Hydrophilic fumed silica, surface area 200 m^2/g
Kronos 2360	11.1	0.0	Pigment white	Rutile TiO_2
Cymel 303	4.8	5.5	Crosslinker	Highly methylated-monomeric melamine-based crosslinker (methoxy methyl functional sites)
Dynapol Catalyst 1203	1.8	2.1	Catalyst for crosslinker	Non-ionic blocked sulfonic acid catalyst for aminoplast crosslinking
Deuteron MK	1.1	0.0	Matting agent	Methylediaminomethylether
Resiflow FL2	0.4	0.0	Flow control agent	polyacrylate
Solvent Naphta 200	9.6	11.0	Solvent	Aromatic solvent
Butyl diglycol	4.0	4.6	Solvent	$HO\text{-}(CH_2)_2\text{-}O\text{-}(CH_2)_2\text{-}(CH_2)_3CH_3$
Butyl glycol	5.8	6.6	Solvent	$CH_3\text{-}(CH_2)_3\text{-}O\text{-}CH_2\text{-}OH$

2.5 Studying chemisorption mechanisms at buried metal-polymer interfaces

Most chemisorption studies at metal oxide surfaces focus on simplified organic compounds representative for components present in paint formulations.[45,79–82] The use of monomeric compounds gives a high freedom of selecting chemical functionalities of interest. Three functional groups relevant for polyester polyurethane primers will be discussed in terms of their bonding affinity to metal oxides. The first functionality are carboxylic acids which originate from the excess acid compounds used for the in-situ synthesis of polyester resin. Subsequently, chemisorption mechanisms reported for ester- and amide-functionalized molecules representative for polyurethane

primers will be discussed. Thereafter, the thin film and thin substrate approach are being described allowing the study of more complex metal substrate and polymer systems, respectively.

2.5.1 Model molecule approach (XPS, IRRAS, ATR-FTIR)

2.5.1.1 Carboxylic acids

Carboxylic acids are known to coordinate to metal cations upon deprotonation forming metal carboxylate bonds.[81,85–90] Various coordination modes ranging from ionic to covalent are reported, of which the latter can be subdivided into monodentate, bridging bidentate and chelating coordination as illustrated in figure 2.7.[85] The transition from ionic to covalent carboxylate bonds has geometric consequences which are reflected in the two C-O lengths.[91,92] A commonly used strategy to study the coordination of metal carboxylates is by determining the separation between asymmetric and symmetric carboxylate infrared peak position ($\Delta\nu_{as\text{-}s}$) using vibrational tool such as IRRAS or ATR-FTIR.[85–87,93,94] The separation values obtained for the metal carboxylate complexes ($\Delta\nu_{COO\text{-}M}$) are compared to those specific to the respective ionic carboxylate salt ($\Delta\nu_{COO\text{-}}$). Larger separation values ($\Delta\nu_{COO\text{-}M} > \Delta\nu_{COO\text{-}}$) are correlated to monodentate complexes, similar separation values ($\Delta\nu_{COOMe} \approx \Delta\nu_{COO\text{-}}$) are associated to bridging bidentate complexes, whereas significantly smaller separation values ($\Delta\nu_{COO\text{-}M} < \Delta\nu_{COO\text{-}}$) are attributed to chelating carboxylate complexes.[85–87,94] However, in addition to the comparative study with salt complexes (mostly sodium carboxylate), commonly accepted guide values are reported, since band separations are generally > 200 cm^{-1} for monodentate coordination, 140-180 cm^{-1} for bridging bidentate coordination and 40-100 cm^{-1} for chelating coordination.[86,87] Using this vibrational approach, bridging bidentate carboxylate bond formation has been reported for succinic acid and myristic acid at variously treated zinc oxide surfaces.[95] However, CH_2 deformation vibrations are known to occur in the same infrared frequency region as symmetric carboxylate stretch vibration, which hinders straightforward determination of the separation value. To avoid interference by CH_2 in the carboxylate infrared region, deuterated succinic acid has been used.[90] Nevertheless, the peak shape attributes to symmetric carboxylate stretching vibrations remained highly asymmetric, which was associated to differences in electronic polarizability of aluminium cations depending on their environment.[90] Also De Wit et al., observed different aluminium-succinate coordination modes, i.e. bridging bidentate and monodentate coordination.[96] It was demonstrated that the portion of monodentate coordination increased with increasing surface hydroxide fractions.[96] As described in the previous paragraph, surface hydroxide act as bonding site and were thus shown to determine the amount of carboxylate bond formation but in addition also promotes a two-end adsorption with dicarboxylic acids.[95,97] Furthermore, dicarboxylates chemisorbed by a two-end adsorption have shown to be more stable in an aqueous environment than monofuntional carboxylates.[90]

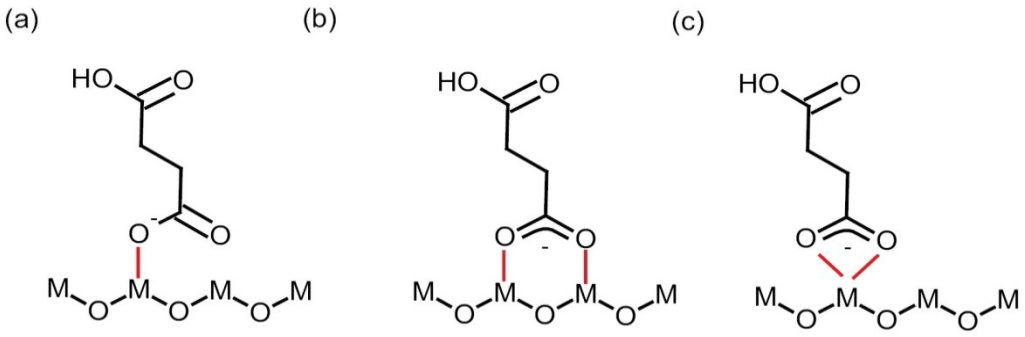

Figure 2.7: One-end carboxylate bond formation at metal oxide surface with M, being the metal cation (a) monodentate, (b) bridging bidentate and (c) chelating carboxylate coordination.

Sodium carboxylate is considered as an obvious example of an ionic carboxylate bond. However, for other metal carboxylate bonds, the terminology of ionic and covalent metal carboxylate bonds have been used interchangeably.[7,85,98] In addition, a third terminology, i.e. polar covalent bond is used for cases were the bonds are not 100 % covalent or ionic, but a mixture of both.[99] The nature of the metal-carboxylate bond is important in terms of stability in an aqueous environment. This because ionic bonds are more readily replaced by water than covalent bonds.[100] Yet, quantifying the ionic and covalent nature of metal carboxylate bonds is challenging. Due to the stronger nature of covalent bonds compared to ionic ones, a quantitative relationship has been proposed by Chen et al, correlating the shift of asymmetric carboxylate bands ($vCOO^-_{as}$) with the degree of ionic character of the metal-carboxylate bond.[101] This lead to the introduction of percentage of ionic bonding (PIB) given by equation 2.1, with vC=O representing the IR-frequency for carbonyl bonds in the protonated acid (COOH) and $v_{as}COO^-$ (M and Na) representing the IR-frequency of the asymmetric carboxylate stretching vibration of the deprotonated acid coordinated to metal cations or in its ionic form repsectively.[101]

$$PIB\ (\%) = \frac{\nu C{=}O - \nu_{as}COO^-(M)}{\nu C{=}O - \nu_{as}COO^-(Na)} \qquad (2.1)$$

Hocking et al, attempted to measure metal-oxygen bond covalency from changes in C-O bond lengths which was correlated to the delocalisation of the carboxylate ligand.[91,92] For these structural measurements, carboxylate C-O bond lengths were extracted from the Cambridge structural Database, containing more than 40 000 crystal structures with carboxylate groups.[91,92] This lead to the conclusions that elemental centres with electronegativity closest to that of oxygen (N, P, C) exhibit the largest loss of carboxylate resonance and thus the greatest covalency.[91] Furthermore, covalency was shown to increase with oxidation state (II < III < IV) and decreases with coordination

number.[92] The amount of covalent nature in metal carboxylate bonds as proposed by Hocking et al, equals 20 % for magnesium, between 10 and 30 % for zinc, and 50 % for aluminium.[92] Therefore, a higher bonding strength as well as resistance against water is expected for aluminium compared to zinc and magnesium. For comparison, the amount of covalent character in phosphor-carboxylate complexes situates around 80%. Consequently, phosphate-based surface treatments are expected to contribute to carboxylate bond strength and stability. Similar, tetravalent cations (Zr and Ti) are also expected to increase carboxylate bond strength and thus its resistivity against water.

2.5.1.2 Amides

Amide-functionalized molecules are representative for functional groups present in polyurethane coatings.[71,102–104] Polyurethanes are formed by reaction of a polyisocyanate with free hydroxyl groups in polyols, which results in amide and ester functionalized polymer chains. Contrary to carboxylic acid groups, amide and esters are known as non-ionisable. Moreover, amides are stable and thus rather unreactive because the electrophilicity of the amide oxygen is reduced by nitrogen sharing his free electron pair.[105] This explains the good chemical and weathering resistance properties of polyurethane coatings. However, those inert properties might be disadvantageous for adhesion.

The occurrence of two different electrophilic atoms, i.e. nitrogen and oxygen, increases the possible metal-amide bonding mechanisms. For the interaction of N,N'-dimethylsuccinamide with iron oxide it has been proposed that the chemisorption occurs through the amide nitrogen atom.[71,102] On the other hand, N,N'-dimethylsuccinamide was shown to donate electrons through its oxygen lone pair to aluminium oxide hydroxide end groups establishing hydrogen bonds.[103,104] Hence, the bonding site, i.e. metal hydroxide or metal cation and thus the chemisorption mechanisms is expected to correlate to the metal oxide physicochemical properties.

It should be mentioned that the majority of the chemisorption studies concerning amide-functionalized molecules are based on the results of one technique, commonly IRRAS[102,103] or XPS[71,104]. FTIR is particularly sensitive for carbonyl (C=O) bond vibration and therefore suitable for chemisorption studies with carboxylic molecules. The tendency for changes in electronic structure and inter- and intramolecular hydrogen bonding induces large shifts in vibration energy. Studying the susceptibility to hydrogen bonding, or carboxylate formation by means of XPS is less straightforward. This because of its high surface sensitivity, what leads to contributions of adsorbed ambient carbon contamination in the C1s and O1s XPS peaks. However, amide-functionalized molecules contain a nitrogen hetero-atom, which binding energy gives unique information on the interfacial dipole and thus the type of interaction with metal oxides. Barthés-Labrouse and Mercier proposed an approach to quantify Bronsted and Lewis acid-base interactions by deconvoluting the N 1s XPS peak.[106,107]

Bronsted interactions on one hand concern a proton exchange from the metal hydroxide ion towards the amide-functionalized molecule. As a result the metal oxide becomes negatively charged, whereas the amide-functional group becomes positively charged. The positive charge is energetically more favourable on the nitrogen atom than the oxygen atom. As a consequence, an ionic Bronsted bond is being established between the amide nitrogen atom and metal oxide. A second bonding mechanism concerns Lewis acid-base interactions, where the electron-rich oxygen atom donates electrons to metal oxide cations. Since the amide-functionalized molecule becomes partially positive charged and the metal oxide partially negative, the resulting shift of the N1s XPS peak will be smaller for Lewis acid-base interactions compared to ionic Bronsted interactions, as illustrated in figure 2.8.[71,104]

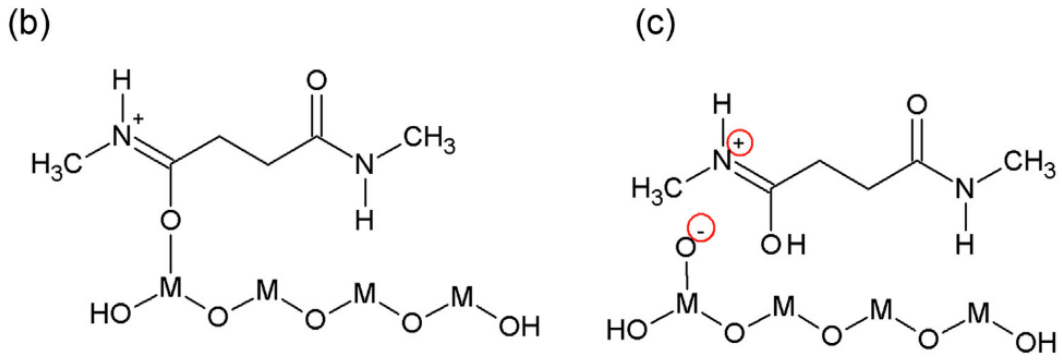

Figure 2.8: Chemisorption reactions of amide-functionalized molecules at a metal oxide surface (a) Lewis acid-base interaction, (b) Bronsted interaction.

2.5.1.3 Esters

Various chemisorption mechanisms have been reported for ester-functionalized molecules. Most commonly reported are the saponification reactions resulting in metal carboxylate complexes by a two-step mechanism.[108–110] During the first step, the ester group is being hydrolysed to more reactive carboxylic acid groups. Whereas in a second step, the carboxylic acid is being deprotonated allowing the formation of metal-carboxylate bonds.[111] Divalent metal cations have shown to be able to catalyse ester hydrolysis reactions which have extensively been studied for Zn^{2+}, Cu^{2+}, Ni^{2} and Co^{2+}.[108–110] However, this saponification reaction was not consistently observed questioning the possibility of bond cleavage under mild conditions.[80,89,112] Instead, Lewis acid-base bonding has been propsed with the ester carbonyl oxygen acting as electron donor and the aluminium hydroxyls as electron acceptor, establishing a hydrogen bond.[79,94] This was evidenced by the downward shift of the v(C=O) carbonyl stretching band in the FTIR spectrum.[79,94] The susceptibility of ester-functionalized monomeric compounds to hydrolysis is thus part of an ongoing debate. The tendency to hydrolyse ester groups is expected to depend on the metal (hydr)oxide acid-base properties and thus the tendency of metal oxides to donate hydroxide groups to hydrolyse the esters to carboxylic

acids. Moreover, the cation plays a determining role as they may catalyse hydrolysis reactions by chelating to the ester-groups. For optimal conditions for cation catalysed ester hydrolysis reactions, the organic compounds should have a poor leaving group and a steric functional group to promote chelation of the metal ion to the leaving group oxygen and not to the carboxyl oxygen.[110]

The requirement for cations to chelate to specific functional groups to induce the desired reaction is more readily fulfilled when using small molecules. This because monomeric compounds sense a high degree of rotational freedom. Because of this, unravelled chemisorption mechanisms may not be fully representative for polymer coatings. Moreover, monomeric compounds can be more susceptible to decomposition, either due to metal oxide catalysis or by the high dose of ion or X-ray bombardment.[113,114] To take this into account, the thin film approach is described in the following paragraph.

2.5.2 Thin-film approach (XPS, IRRAS, ATR-FTIR)

Next to the use of functionalized monomeric compounds, the chemisorption of industrially–relevant paints is often mimicked using the thin-film approach. For this approach, model polymer films are applied by solvent evaporation forming a nanolayer, which still allows the use of surface sensitive techniques (XPS, ToF-SIMS, IRRAS, etc.) while offering more similarities with the mobility and thus reactivity of functional groups embedded in polymeric chains as in the case of industrially-relevant paint systems. One point of attention is the potential competition with solvent adsorption as shown by Pletincx et al.[115] Moreover, similar to the model molecule approach, the use of surface sensitive techniques when using the thin film approach, unavoidable also detects adsorbed adventitious carbon contamination, which may interfere with the signal specific to the organic compound of interest. This carbon contamination is typically formed immediately upon exposure of the oxide surface to the atmosphere and might block potential surface bonding sites.[40]

Frequently applied polymeric compounds are polyacrylic acid (PAA)[98,100,116] and polymethyl methacrylate (PMMA).[82,117–120] Leadley and Watts studied metal oxide - polymethylmethacrylate (PMMA) interfaces performing XPS analysis.[79] Similar to ester-functionalized molecules two different chemisorption mechanisms have been demonstrated. Acidic metal oxides, such as silicon, interact with PMMA by hydrogen bonding. Whereas amphoteric substrates, such as iron and aluminium oxide, hydrolyse PMMA forming interfacial carboxylate bonds.[79] PMMA hydrolysis resulting in aluminium-carboxylate bonds was also evidenced by other authors using solid state NMR.[119,121] Tannenbaum, et al.[118], reported the importance of water as a mediating agent in the chemisorption of PMMA to aluminium oxide. Hydrolysing the ester group forming carboxylic acids was believed not

to be sufficient to establish chemical bonding at the aluminium oxide surface. A subsequent intermediate step, being the dissociation of acid to carboxylate anions in the presence of water, was considered as a requirement for chemisorption to occur.[118] Pletincx et al.[82] supported this statement using near-ambient XPS, ToF-SIMS and ATR-FTIR in Kretschmann geometry. More water at the interface was shown to lead to more ionic bond formation with PAA.[82] dependent.[7,42,45] It becomes clear that the majority of thin film studies have been conducted on aluminium oxide, whereas those on zinc and magnesium oxide are more limited. Based on a comparative study on the deformation behaviour of PAA-metal oxides (Zn, Al, Mg and Ca). PAA- zinc and aluminium- oxide composites were shown to behave as elastic brittle materials.[100] Their tensile strength partially reduced during submersion in water, but elastic-brittle behaviour was maintained. Conversely, PAA-calcium and magnesium oxide composites changed to elastically soft materials when saturated with water, which was explained by weakening of the metal-carboxylate bonds associated to the different nature of the carboxylate bonds.[100] Whereas magnesium and calcium oxide formed ionic polyacrylate salts with a highly ionic nature, zinc and aluminium oxide were shown to form a bridging bidentate or chelating carboxylate coordination with a higher covalent character. The differences in ionic/covalent ratio of the interfacial PAA-metal oxide bond was considered as the main cause for different mechanical behaviour in aqueous media.[100]

2.5.3. Thin substrate approach (ATR-FTIR and SFG)

The use of simplified organic compounds (functionalized-monomers or thin film approach) has thus shown to be highly useful for revealing chemisorption mechanisms.[14] However, hitherto, these insights have not been validated on industrially relevant paints, which are typically multicomponent systems containing crosslinkers, curing agents, matting agents, fillers, binders, corrosion-inhibiting pigments, etc. As a result, its chemical composition is complex hindering straightforward chemisorption studies. Next to the well-known difficulties of studying buried interfaces, this is one of the reasons why molecular studies on metal-paint interfaces are limited. Obviously, the effect of adhesion promotors on interfacial properties cannot be neglected. In particular silanes play an important role in the chemical interaction of paints with metal oxides.[122] Another component that affect the interfacial strength are crosslinkers and more specifically, the degree of crosslinking. Too much crosslinking can make the polymer system too rigid hindering dissipation. On the other hand, less crosslinked polymers are more elastic, so when performing the pull-off test they may deform before the interface breaks.[123] Moreover, in case of a not fully crosslinked polymer system a higher amount of functional groups will be available to interact with the metal substrate.[124] Next to the amount of crosslinkers, also curing is assumed to have an impact on the interfacial properties. Chemical interactions at the metal-polymer interface are expected to take place already before

curing.[125] However, curing can change the interface significantly. For instance, it has been reported that curing can relieve polymeric constraints leading to a lower steric hindrance and a stronger metal-polymer bonding.[126] Conformational variations as well as improved hydrolysis and metal-bond formation due to curing at elevated temperatures have also been reported for silane primer films on aluminium.[122] It becomes increasingly clear that adhesion properties are not only a result of resin chemistry. In addition, also disbondment phenomena of painted metal substrates result from an interplay of multiple compounds present in the complex paint formulation.[14,127,128] Öhman et al.[129] integrated attenuated total reflection – Fourier transform infrared spectroscopy (ATR-FTIR) with an electrochemical cell (EC), allowing simultaneous electrochemical and molecular characterization of the metal-polymer hybrid system during exposure to electrolyte. Using the integrated ATR-FTIR – EC-setup, it was demonstrated that the character of water in epoxy films differs from the water within the siloxane network.[130] Moreover, in-situ ATR-FTIR studies lead to insights in water transport and polymer swelling phenomena, as well as corrosion processes at the buried interfaces.[84,127,129–131] Later, Taheri et al. adopted the in-situ ATR-FTIR approach to study buried metal-polymer interfaces, demonstrating increased polymer stability due to curing, which not only increased barrier properties but also the interfacial stability of carboxylic polymer – zinc oxide interface.[128] The growth of water bands in the ATR-FTIR spectra were correlated to the polymer stability against water. A correlation between water uptake of the coating and initial surface hydroxide fractions and thus interfacial bonding density was demonstrated.[128] The importance of surface hydroxides for interfacial bond formation with carboxylic polymers was also evidenced by Pletincx, et al.[98], who showed initial increase of carboxylate bonds between PMMA and aluminium oxide when water was introduced at the interface. However, in-situ real-time monitoring of interfacial carboxylate bond degradation by means of ATR-FTIR is experimentally hindered by the strong OH-bending modes of water which occur at similar IR-frequencies as the carboxylate bonds of interest. Moreover, the role of zirconium-based conversion treatments on interfacial bond formation and degradation with industrially relevant paints has not yet been described. The main reason for this is the high complexity of commercial conversion systems containing inorganic and organic additives which increases the surface chemistry complexity The high share of interface parameters at realistic metal (oxide)-polymer hybrid systems hinders straightforward interpretation of bonding properties at these metal (oxide)-polymer hybrid interfaces.

It is clear that the study of industrially relevant metal (oxide)-paint interfaces are complicated by the high share of interfacial parameters. Another key-factor in the lack of knowledge on interfacial metal (oxide)-paint interface are the high absorptive properties of both paint layer and metal substrate, hindering the non-destructive use of common surface sensitive techniques.

By applying model metal films with thicknesses ranging in the nanometer scale IR-light transparency is maintained which allows the use of vibrational tools to reach the metal oxide – polymer interface from the model metal side. Currently, two spectroscopic techniques are used interchangeably to elucidate molecular interactions at the buried polymer-metal (oxide) interfaces. Presumably the most accessible and user-friendly spectroscopic tool is ATR-FTIR in the Kretschmann geometry.[4,59,127] In the Kretschmann geometry, a nanolayered metal (oxide) film, transparent for the IR-beam, is brought in direct contact with an internal reflection element (IRE). Upon reflection from the internal surface of the IRE, an evanescent wave is created and projected orthogonally into the sample as illustrated in figure 2.9. The charges in the evanescent wave create an electric field that extends into the coating were a second wave, i.e. the polariton, is generated reducing the intensity of reflected light.[10] A fraction of the energy of the evanescent wave is absorbed by the sample, the reflected radiation is returned to the detector. The true depth of this evanescent wave passing the nanolayered metal film into the polymer coating is an ongoing debate.[132] It is known that some transition metals are capable of inducing an enhancement-effect in the Kretschmann configuration, also known as surface enhanced infrared adsorption (SEIRA).[133,134] Due to this enhancement, vibration modes in the first monolayer (within 5 nm) directly attached to the surface are 10-1000 times more intense compared to measurements without metal.[133,134] Two mechanisms are supposed to contribute to the total enhancement; the electromagnetic (EM) and chemical mechanism (CM). The first mechanism only occurs on discontinuous films, typically thinner than 10 nm.[133] The second mechanism relates to chemical effects, such as charge-transfer interactions between adsorbate and metal. Vibrational modes with dipole changes perpendicular to the metal surface are preferentially enhanced.[134] Although some transition metals are capable of inducing such an enhancement effect, they have rarely been studied. This because the enhancement is more significant on noble metals.[134] Consequently, ATR-FTIR with reported probing depths from 100 nm to several µm is not a surface sensitive technique.[135136] Yet, it is frequently used to gain metal-polymer interfacial information.[4,59,84,126–128] The majority of ATR-FTIR Kretschmann studies use monolayered model coatings. This because of the high level of control on chemical behaviour. Yet, it also eliminates the discussion on interfacial sensitivity, as there is no interfering bulk signal. When making the step from model molecules to industrial coatings, the thickness of the applied organic layers shifts from the nanoscale to the microscale, which raises the ongoing debate on the interfacial sensitivity of ATR-FTIR.

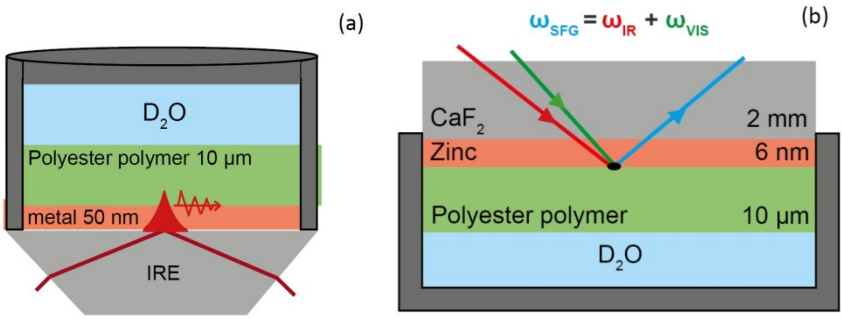

Figure 2.9: in-situ spectroscopic tools with different interfacial sensitivity: (a) ATR-FTIR and (b) SFG.

Contrary, the second order non-linear spectroscopic tool; visible-infrared sum-frequency generation spectroscopy (SFG) is able to probe the true interface with sub-monolayer sensitivity and selectivity.[137,138] Because SFG is a second order non-linear technique it requires symmetry breaking. The SFG signal generation is therefore absent in the centrosymmetric media, which is the case for most of the materials in bulk. By definition sample symmetry is broken at surfaces and interfaces. Its surface and interface selectivity makes SFG a highly valuable tool for studying interfaces. However, existing literature on the use of SFG on metal-polymer interfaces are still rather limited.[139] Most likely this relates to the complex setup, as well as experimental limitations on the use of SFG in the mid-IR region. Because of these experimental limitations, existing literature mainly focusses on the O-H and C-H stretch region, i.e. 3800 – 2400 cm-1.[137,140] In addition, efforts had to be taken to differentiate the SFG signal at the metal-polymer interface from those of the polymer-air interface.[138,141–143] Nowadays, the SFG setup becomes more user-friendly. Moreover, recent developments in laser technology opened up the mid-IR region up to 1200 cm^{-1} for SFG studies[144,145], giving access to the vibrational modes of carboxylic groups such as carbonyl (C=O) stretch vibrations and carboxylate (COO^-) stretch vibrations. Gained access to this head group region offers SFG the opportunity to become a valuable tool in a broad range of research fields.

2.6 Conclusions

The nature of oxides on the two types of galvanized steel substrates, i.e. GI and MZ, are highly different. It is reported that magnesium acts as a pH buffer, continuously neutralizing hydroxide ions at the cathodes, which prevents the formation of regions with very high pH. Since, zirconium- and titanium-based conversion film formation are pH based processes, this is expected to affect their precipitation from aqueous solution. Furthermore, the formation of zirconium- and titanium-based conversion films are also determined by the electrochemical activity of the native metal oxides. The coexistence of multiple phases with different electrochemical activity at the surface of MZ substrates, is therefore expected to enhance the formation of zirconium- and titanium-based conversion coatings. Next to variations in the base metal oxides, also considerable variations exists in

the physicochemical properties of titanium and zirconium oxide. As such titanium oxide is most acidic, resulting in a lower coordination number leading to different precipitation products. Furthermore, it has been described that the native metal oxide properties determine the conversion oxide precipitation rate as well as its oxide chemistry, and more specifically its hydroxide fraction. The latter is known to act as a key parameter in the bonding mechanisms of organic compounds. Hence, it becomes increasingly clear that the different nature of native metal oxide greatly influences the conversion oxide physicochemical properties and therefore thus also its bonding properties towards organic coatings. Because of this there is a crucial need to gain more fundamental insights on the relation between metal oxide physicochemical properties and the chemisorption of organic coatings. However, such approach offering in-situ molecular interfacial information of buried metal-polymer interfaces in a non-destructive manner is not yet available. As a consequence, the use of model systems remains a prerequisite. Studying the chemisorption of organic model compounds has shown to result in important fundamental insights in interfacial interactions. The main advantages of using monomeric molecules are the high freedom of selecting molecular structures and the access to surface sensitive techniques, such as XPS, ToF-SIMS and IRRAS. Possible pitfalls associated to the use of monomeric compounds are the higher sensitivity for catalytic and chelating effects which require a high degree of rotational freedom, which makes them not always highly representative for large polymer chains. Because of this, the thin film approach was introduced using model polymers, which chains approaches the steric behaviour of realistic resins. These model polymers are typically applied by solvent evaporation resulting in a monolayer or maximum couple of monolayers of a polymeric compound. Consequently, the resulting thin films, which are in the order of nanometres, still allow the use of surface sensitive techniques. A point of attention when using surface sensitive techniques relates to their sensitivity for ambient carbon contamination which may block potential surface bonding sites. In addition, also competitive solvent adsorption can hinder straightforward interpretation of chemisorption mechanisms of the organic compound of interest. As an alternative ATR-FTIR in the Kretschmann configuration has been proposed as a valuable tool to access buried metal-polymer interfaces by applying thin IR-transparent metal films. The resulting invert configuration (i.e. interface access through metal side) allows the use of realistic paint systems applied with thicknesses in the µm-range. Furthermore, it offers the possibility to integrate an electrochemical cell on top of the polymer coated substrates providing in-situ interfacial molecular information during exposure to an aqueous environment. These advantages open the way to many research questions regarding buried metal-polymer interfaces. Yet, the surface sensitivity of this technique is still an ongoing debate. On the other hand, SFG is considered as an inherent interface sensitive tool. Yet, due to its unfamiliarity, not very frequently used for studying buried metal-polymer interfaces.

References

(1) Sullivan, J.; Mehraban, S.; Elvins, J. In Situ Monitoring of the Microstructural Corrosion Mechanisms of Zinc-Magnesium-Aluminium Alloys Using Time Lapse Microscopy. *Corros. Sci.* **2011**, *53* (6), 2208–2215.

(2) Cerezo, J.; Taheri, P.; Vandendael, I.; Posner, R.; Lill, K.; de Wit, J. H. W.; Mol, J. M. C.; Terryn, H. Influence of Surface Hydroxyls on the Formation of Zr-Based Conversion Coatings on AA6014 Aluminum Alloy. *Surf. Coatings Technol.* **2014**, *254*, 277–283.

(3) Taheri, P.; Laha, P.; Terryn, H.; Mol, J. M. C. An in Situ Study of Zirconium-Based Conversion Treatment on Zinc Surfaces. *Appl. Surf. Sci.* **2015**, *356*, 837–843.

(4) Taheri, P.; Terryn, H.; Mol, J. M. C. Studying Interfacial Bonding at Buried Polymer–Zinc Interfaces. *Prog. Org. Coatings* **2015**, *89*, 323–331.

(5) Deck, P. D.; Reichgott, D. W. Characterization of Chromium-Free No-Rinse Prepaint Coatings on Aluminium and Galvanized Steel. *Met. Finish.* **1992**, No. September, 29–35.

(6) Hughes, A. E. *Conversion Coatings*; Elsevier Inc., 2018.

(7) Taheri, P.; Lill, K.; De Wit, J. H. W.; Mol, J. M. C.; Terryn, H. Effects of Zinc Surface Acid-Based Properties on Formation Mechanisms and Interfacial Bonding Properties of Zirconium-Based Conversion Layers. *J. Phys. Chem. C* **2012**, *116* (15), 8426–8436.

(8) Yoganandan, G.; Pradeep Premkumar, K.; Balaraju, J. N. Evaluation of Corrosion Resistance and Self-Healing Behavior of Zirconium-Cerium Conversion Coating Developed on AA2024 Alloy. *Surf. Coatings Technol.* **2015**, *270*, 249–258.

(9) Khun, N. W.; Frankel, G. S. Composition and Corrosion Protection of Hexafluorozirconic Acid Treatment on Steel. *Mater. Corros.* **2015**, *66* (11), 1215–1222.

(10) Ardelean, H.; Frateur, I.; Marcus, P. Corrosion Protection of Magnesium Alloys by Cerium, Zirconium and Niobium-Based Conversion Coatings. *Corros. Sci.* **2008**, *50* (7), 1907–1918.

(11) Ghanbari, A.; Attar, M. M. Influence of Phosphate Ion on the Morphology, Adhesion Strength, and Corrosion Performance of Zirconium-Based Surface Treatment. *J. Coatings Technol. Res.* **2015**.

(12) Pareja, R. R.; Ibáñez, R. L.; Martín, F.; Leinen, D. Corrosion Behaviour of Zirconia Barrier Coatings on Galvanized Steel. *Surf. Coat. Technol.* **2006**, *200*, 6606–6610.

(13) Fedrizzi, L.; Rodriguez, F. .; Rossi, S.; Deflorian, F.; Di Maggio, R. The Use of Electrochemical Techniques to Study the Corrosion Behaviour of Organic Coatings on Steel Pretreated with Sol–Gel Zirconia Films. *Electrochim. Acta* **2001**, *46*, 3715–3724.

(14) Pletincx, S.; Fockaert, L. L. I.; Mol, J. M. C.; Hauffman, T.; Herman, T. Probing the Formation and Degradation of Chemical Interactions from Model Molecule / Metal Oxide to Buried

Polymer / Metal Oxide Interfaces. *npj Mater. Degrad.* **2019**, *3* (23), 1–12.

(15) Kutz, M. *Handbook of Environmental Degradation of Materials*; William Andrew Pub, 2005.

(16) American Galvanizers Association http://www.galvanizeit.org/.

(17) Marder, A. R. The Metallurgy of Zinc-Coated Steel. *Prog. Mater. Sci.* **2000**, *45*, 191–271.

(18) Prosek, T.; Nazarov, A.; Bexell, U.; Thierry, D.; Serak, J. Corrosion Mechanism of Model Zinc-Magnesium Alloys in Atmospheric Conditions. *Corros. Sci.* **2008**, *50* (8), 2216–2231.

(19) Prosek, T.; Persson, D.; Stoulil, J.; Thierry, D. Composition of Corrosion Products Formed on Zn–Mg, Zn–Al and Zn–Al–Mg Coatings in Model Atmospheric Conditions. *Corros. Sci.* **2014**, *86*, 231–238.

(20) Prosek, T.; Nazarov, A.; Thierry, D. Role of Steel and Zinc Coating Thickness in Cut Edge Corrosion of Coil Coated Materials in Atmospheric Weathering Conditions; Part 2: Field Data and Model. *Prog. Org. Coatings* **2016**, *101*, 45–50.

(21) Hosking, N. C.; Ström, M. A.; Shipway, P. H.; Rudd, C. D. Corrosion Resistance of Zinc-Magnesium Coated Steel. *Corros. Sci.* **2007**, *49* (9), 3669–3695.

(22) Zoestbergen, E.; Langkruis, J. Van De; Maalman, T. F. J.; Batyrev, E. Influence of Diffusion on the Coating Adhesion of Zinc-Magnesium Thin Films onto Steel. *Surf. Coat. Technol.* **2017**, *309*, 904–910.

(23) Salgueiro Azevedo, M.; Allély, C.; Ogle, K.; Volovitch, P. Corrosion Mechanisms of Zn(Mg,Al) Coated Steel: The Effect of HCO3− and NH4+ Ions on the Intrinsic Reactivity of the Coating. *Electrochim. Acta* **2015**, *153*, 159–169.

(24) Stoulil, J.; Prosek, T.; Nazarov, A.; Oswald, J.; Kriz, P.; Thierry, D. Electrochemical Properties of Corrosion Products Formed on Zn-Mg , Zn-Al and Zn-Al-Mg Coatings in Model Atmospheric Conditions. *Mater. Corros.* **2015**, *66* (8), 777–782.

(25) Volovitch, P.; Allely, C.; Ogle, K. Understanding Corrosion via Corrosion Product Characterization: I. Case Study of the Role of Mg Alloying in Zn–Mg Coating on Steel. *Corros. Sci.* **2009**, *51* (6), 1251–1262.

(26) Volovitch, P.; Vu, T. N.; All??ly, C.; Abdel Aal, A.; Ogle, K. Understanding Corrosion via Corrosion Product Characterization: II. Role of Alloying Elements in Improving the Corrosion Resistance of Zn-Al-Mg Coatings on Steel. *Corros. Sci.* **2011**, *53* (8), 2437–2445.

(27) Persson, D.; Thierry, D.; Lebozec, N.; Prosek, T. In Situ Infrared Reflection Spectroscopy Studies of the Initial Atmospheric Corrosion of Zn – Al – Mg Coated Steel. *Corros. Sci.* **2013**, *72*, 54–63.

(28) Thierry, D.; Persson, D.; Le Bozec, N. *Atmospheric Corrosion of Zinc and Zinc Alloyed Coated Steel*; Elsevier, 2018.

(29) Salgueiro Azevedo, M.; Allély, C.; Ogle, K.; Volovitch, P. Corrosion Mechanisms of Zn(Mg, Al)

Coated Steel in Accelerated Tests and Natural Exposure: 1. The Role of Electrolyte Composition in the Nature of Corrosion Products and Relative Corrosion Rate. *Corros. Sci.* **2015**, *90*, 472–481.

(30) Salgueiro Azevedo, M.; Allély, C.; Ogle, K.; Volovitch, P. Corrosion Mechanisms of Zn(Mg,Al) Coated Steel: 2. The Effect of Mg and Al Alloying on the Formation and Properties of Corrosion Products in Different Electrolytes. *Corros. Sci.* **2015**, *90*, 482–490.

(31) Schuerz, S.; Fleischanderl, M.; Luckeneder, G. H.; Preis, K.; Haunschmied, T.; Mori, G.; Kneissl, A. C. Corrosion Behaviour of Zn-Al-Mg Coated Steel Sheet in Sodium Chloride-Containing Environment. *Corros. Sci.* **2009**, *51* (10), 2355–2363.

(32) Landschoot, N.; Dane, C.; Bleeker, R.; Vlot, M. Zinc-Magnesium Coated Hot Dip Galvanised Steel. *Materials (Basel).* **2013**, *115* (4), 1–8.

(33) Sharifi Golru, S.; Attar, M. M.; Ramezanzadeh, B. Effects of Surface Treatment of Aluminium Alloy 1050 on the Adhesion and Anticorrosion Properties of the Epoxy Coating. *Appl. Surf. Sci.* **2015**, *345*.

(34) Asemani, H. R.; Ahmadi, P.; Sarabi, A. A.; Eivaz Mohammadloo, H. Effect of Zirconium Conversion Coating: Adhesion and Anti-Corrosion Properties of Epoxy Organic Coating Containing Zinc Aluminum Polyphosphate (ZAPP) Pigment on Carbon Mild Steel. *Prog. Org. Coatings* **2016**, *94*, 18–27.

(35) Ghanbari, A.; Attar, M. M. Surface Free Energy Characterization and Adhesion Performance of Mild Steel Treated Based on Zirconium Conversion Coating: A Comparative Study. *Surf. Coatings Technol.* **2014**, *246*, 26–33.

(36) Mohammadloo, H. E.; Sarabi, A. A.; Hosseini, R. M.; Sarayloo, M.; Sameie, H.; Salimi, R. A Comprehensive Study of the Green Hexafluorozirconic Acid-Based Conversion Coating. *Prog. Org. Coatings* **2014**, *77* (2), 322–330.

(37) Milošev, I.; Frankel, G. S. Review—Conversion Coatings Based on Zirconium and/or Titanium. *J. Electrochem. Soc.* **2018**, *165* (3), C127–C144.

(38) Fedrizzi, L.; Deflorian, F.; Bonora, P. L. Corrosion Behaviour of Fluotitanate Pretreated and Painted Aluminium Sheets. *Electrochim. Acta* **1997**, *42* (6), 969–978.

(39) Verdier, S.; van der Laak, N.; Dalard, F.; Metson, J.; Delalande, S. An Electrochemical and SEM Study of the Mechanism of Formation, Morphology, and Composition of Titanium or Zirconium Fluoride-Based Coatings. *Surf. Coatings Technol.* **2006**, *200* (9), 2955–2964.

(40) Nordlien, J. H.; Walmsley, J. C.; Østerberg, H.; Nisancioglu, K. Formation of a Zirconium-Titanium Based Conversion Layer on AA 6060 Aluminium. *Surf. Coatings Technol.* **2002**, *153* (1), 72–78.

(41) Andreatta, F.; Turco, a.; de Graeve, I.; Terryn, H.; de Wit, J. H. W.; Fedrizzi, L. SKPFM and SEM

Study of the Deposition Mechanism of Zr/Ti Based Pre-Treatment on AA6016 Aluminum Alloy. *Surf. Coatings Technol.* **2007**, *201* (18), 7668–7685.

(42) Cerezo, J.; Vandendael, I.; Posner, R.; Lill, K.; de Wit, J. H. W.; Mol, J. M. C.; Terryn, H. Initiation and Growth of Modified Zr-Based Conversion Coatings on Multi-Metal Surfaces. *Surf. Coatings Technol.* **2013**, *236*, 284–289.

(43) Lostak, T.; Maljusch, A.; Klink, B.; Krebs, S.; Kimpel, M.; Flock, J.; Schulz, S.; Schuhmann, W. Zr-Based Conversion Layer on Zn-Al-Mg Alloy Coated Steel Sheets: Insights into the Formation Mechanism. *Electrochim. Acta* **2014**, *137*, 65–74.

(44) Lunder, O.; Simensen, C.; Yu, Y.; Nisancioglu, K. Formation and Characterisation of Ti-Zr Based Conversion Layers on AA6060 Aluminium. *Surf. Coatings Technol.* **2004**, *184* (2–3), 278–290.

(45) Fockaert, L. I.; Taheri, P.; Abrahami, S. T.; Boelen, B.; Terryn, H.; Mol, J. M. C. Zirconium-Based Conversion Film Formation on Zinc, Aluminium and Magnesium Oxides and Their Interactions with Functionalized Molecules. *Appl. Surf. Sci.* **2017**, *423*, 817–828.

(46) Jolivet, J.; Henry, M.; Livage, J.; Bescher, E. *Metal Oxide Chemistry and Synthesis - From Solution to Solid State*, 3th editio.; John Wiley & Sons, Inc, 2000.

(47) Brown, P. L.; Curti, E.; Grambow, B.; Ekberg, C. Chemical Thermodynamics of Zirconium. **2008**, 1–512.

(48) Verdier, S.; Delalande, S.; Van Der Laak, N.; Metson, J.; Dalard, F. Monochromatized X-Ray Photoelectron Spectroscopy of the AM60 Magnesium Alloy Surface after Treatments in Fluoride-Based Ti and Zr Solutions. *Surf. Interface Anal.* **2005**, *37* (5), 509–516.

(49) Clearfield, A. The Mechanism of Hydrolytic Polymerization of Zirconyl Solutions. *J. Mater. Res.* **2016**, *5* (1), 161–162.

(50) Gao, Y.; Masuda, Y.; Ohta, H.; Koumoto, K. Room-Temperature Preparation of ZrO2 Precursor Thin Film in an Aqueous Peroxozirconium-Complex Solution. *Chem. Mater.* **2004**, 2615–2622.

(51) Smit, M. A.; Hunter, J. A.; Sharman, J. D. B.; Scamans, G. M.; Sykes, J. M. Effect of Organic Additives on the Performance of Titanium-Based Conversion Coatings. *Corros. Sci.* **2003**, *45* (9), 1903–1920.

(52) Golru, S. S.; Attar, M. M.; Ramezanzadeh, B. Morphological Analysis and Corrosion Performance of Zirconium Based Conversion Coating on the Aluminum Alloy 1050. *J. Ind. Eng. Chem.* **2015**, *24*, 233–244.

(53) Guan, Y.; Liu, J.; Yan, C. Novel Ti/Zr Based Non-Chromium Chemical Conversion Coating for the Corrosion Protection of Electrogalvanized Steel. *Int. J. Electrochem. Sci.* **2011**, *6*, 4853–4867.

(54) Andreatta, F.; Lanzutti, A.; Paussa, L.; Fedrizzi, L. Addition of Phosphates or Copper Nitrate in a Fluotitanate Conversion Coating Containing a Silane Coupling Agent for Aluminium Alloy. *Prog. Org. Coatings* **2014**, *77* (12), 2107–2115.

(55) Lostak, T.; Krebs, S.; Maljusch, A.; Gothe, T.; Giza, M.; Kimpel, M.; Flock, J.; Schulz, S. Formation and Characterization of Fe3+ /Cu2+ Modified Zirconium Oxide Conversion Layers on Zinc Alloy Coated Steel Sheets. *Electrochim. Acta* **2013**, *112*, 14–23.

(56) Khun, N. W.; Frankel, G. S. Effects of Surface Roughness , Texture and Polymer Degradation on Cathodic Delamination of Epoxy Coated Steel Samples. *Corros. Sci.* **2013**, *67*, 152–160.

(57) Golru, S. S.; Attar, M. M.; Ramezanzadeh, B. Effects of Surface Treatment of Aluminium Alloy 1050 on the Adhesion and Anticorrosion Properties of the Epoxy Coating. *Appl. Surf. Sci.* **2015**, *345*, 360–368.

(58) Ghanbari, A.; Attar, M. M. The Effect of Zirconium-Based Surface Treatment on the Cathodic Disbonding Resistance of Epoxy Coated Mild Steel. *Appl. Surf. Sci.* **2014**, *316*, 429–434.

(59) Sababi, M.; Terryn, H.; Mol, J. M. C. The Influence of a Zr-Based Conversion Treatment on Interfacial Bonding Strength and Stability of Epoxy Coated Carbon Steel. *Prog. Org. Coatings* **2017**, *105*, 29–36.

(60) Deck, P. D.; Moon, M.; Sujdak, R. J. Investigation of Fluoacid Based Conversion Coatings on Aluminum. *Prog. Org. Coatings* **1998**, *34*, 39–48.

(61) Faigen, H. L. Method for Treating Metal Surfaces with Compositions Comprising Zirconium and a Polymer. 3912548, 1975.

(62) Karmaschek, U.; Mady, R. Chromium-Free Process for the No-Rinse Treatment of Aluminium and Its Alloys and Aqueous Bath Solution Suitable for This Process. 5868872, 1999.

(63) Fristad, W. E.; Liang, J.; Kelly, T. S. Coating Composition. US7063735B, 2006.

(64) Sander, Lothar, S.; Musingo, E. M.; Neill, W. J. Composition and Method for Non-Chromate Coating of Aluminium. 4921552, 1990.

(65) Wichelhaus, W.; Schenzie, B.; Quellhorst, H. Methos for Providing Metal Surfaces with Protection against Corrosion. 0150524A1, 2003.

(66) Assi, H.; Mouchaham, G.; Steunou, N.; Devic, T.; Serre, C. Titanium Coordination Compounds : From Discrete Metal Complexes to Metal – Organic Frameworks. *Chem. Soc. Rev.* **2017**, *46*, 3431–3452.

(67) Bai, Y.; Dou, Y.; Xie, L.; Rutledge, W.; Li, J.; Zhou, H. Zr-Based Metal–Organic Frameworks: Design, Synthesis, Structure, and Applications. *Chem. Soc. Rev.* **2016**, *45*, 2327–2367.

(68) McCafferty, E.; Wightman, J. P. Determination of the Concentration of Surface Hydroxyl Groups on Metal Oxide Films by a Quantitative XPS Method. *Surf. Interface Anal.* **1998**, *26* (8), 549–564.

(69) Smith, G. C. Evaluation of a Simple Correction for the Hydrocarbon Contamination Layer in Quantitative Surface Analysis by XPS. *J. Electron Spectros. Relat. Phenomena* **2005**, *148*, 21–28.

(70) Abrahami, S. T.; Hauffman, T.; De Kok, J. M. M.; Mol, J. M. C.; Terryn, H. XPS Analysis of the Surface Chemistry and Interfacial Bonding of Barrier-Type Cr(VI)-Free Anodic Oxides. *J. Phys. Chem. C* **2015**, *119* (34), 19967–19975.

(71) Wielant, J.; Hauffman, T.; Blajiev, O.; Hausbrand, R.; Terryn, H. Influence of the Iron Oxide Acid-Base Properties on the Chemisorption of Model Epoxy Compounds Studied by XPS. *J. Phys. Chem. C* **2007**, *111* (35), 13177–13184.

(72) Hauffman, T.; Blajiev, O.; Snauwaert, J.; van Haesendonck, C.; Hubin, A.; Terryn, H. Study of the Self-Assembling of n -Octylphosphonic Acid Layers on Aluminum Oxide. *Langmuir* **2008**, *24* (5), 13450–13456.

(73) Nefedov, V. *X-Ray Photoelectron Spectroscopy of Solid Surfaces*; Taylor & Francis, 1988.

(74) Tanuma, S.; Powell, C. J.; Penn, D. R. Proposed Formula for Electron Inelastic Mean Free Paths Based on Calculations for 31 Materials. *Surf. Sci. Lett.* **1987**, *192*, 849–857.

(75) Buchheit, R. G. *Corrosion Resistant Coatings and Paints*, Second Edi.; Elsevier Inc., 2005.

(76) Chattopadhyay, D. K.; Raju, K. V. S. N. Structural Engineering of Polyurethane Coatings for High Performance Applications. *Prog. Polym. Sci.* **2007**, *32* (3), 352–418.

(77) Awasthi, S.; Agarwal, D. Preparation and Characterisation of Polyurethane Coatings Based on Polyester Polyol. *Pigment Resin Technol.* **2010**, *39* (4), 208–213.

(78) Wilson, R. C.; Pfohl, W. F. Study of Cross-Linking Reactions of Melamine r Formaldehyde Resin with Hydroxyl Functional Polyester by Generalized 2-D Infrared Spectroscopy. *Vib. Spectrosc.* **2000**, *23*, 13–22.

(79) Leadley, S. R.; Watts, J. F. The Use of Monochromated XPS to Evaluate Acid- Base Interactions at the PMMA/Oxidised Metal Interface. *J. Adhes.* **1997**, *60*, 175–196.

(80) Brand, J. Van Den; Blajiev, O.; Beentjes, P. C. J.; Terryn, H.; Wit, J. H. W. De. Interaction of Ester Functional Groups with Aluminum Oxide Surfaces Studied Using Infrared Reflection Absorption Spectroscopy. *Langmuir* **2004**, *20*, 6318–6326.

(81) Taheri, P.; Wielant, J.; Hauffman, T.; Flores, J. R.; Hannour, F.; Wit, J. H. W. De; Mol, J. M. C.; Terryn, H. A Comparison of the Interfacial Bonding Properties of Carboxylic Acid Functional Groups on Zinc and Iron Substrates. *Electrochim. Acta* **2011**, *56* (4), 1904–1911.

(82) Pletincx, S.; Marcoen, K.; Trotochaud, L.; Fockaert, L.-L.; Mol, J. M. C.; Head, A. R.; Karslioğlu, O.; Bluhm, H.; Terryn, H.; Hauffman, T. Unravelling the Chemical Influence of Water on the PMMA/Aluminum Oxide Hybrid Interface In Situ. *Sci. Rep.* **2017**, *7* (1), 13341.

(83) Öhman, M. *Development of ATR-FTIR Kretschmann Spectroscopy for In Situ Studies of Metal/Polymer Interfaces: And Its Intergration with EIS for Exposure to Corrosive Conditions*; 2010.

(84) Öhman, M.; Persson, D.; Leygraf, C. In Situ ATR-FTIR Studies of the Aluminium / Polymer

Interface upon Exposure to Water and Electrolyte. *Prog. Org. Coatings* **2006**, *57*, 78–88.

(85) Zelenak, V.; Vargova, Z.; Györyova, K. Correlation of Infrared Spectra of Zinc(II) Carboxylates with Their Structures. *Spectrochim. Acta - Part A Mol. Biomol. Spectrosc.* **2007**, *66* (2), 262–272.

(86) Tackett, J. E. FT-IR Characterization of Metal Acetates in Aqueous Solution. *Appl. Spectrosc.* **1989**, *43* (3), 483–489.

(87) Dobson, K. D.; Mcquillan, A. J. In Situ Infrared Spectroscopic Analysis of the Adsorption of Aliphatic Carboxylic Acids to TiO2, ZrO2, Al2O3, and Ta2O5 from Aqueous Solutions. *Spectrochim. Acta - Part A Mol. Biomol. Spectrosc.* **1999**, *55*, 1395–1405.

(88) Dobson, K. D.; McQuillan, A. J. In Situ Infrared Spectroscopic Analysis of the Adsorption of Aromatic Carboxylic Acids to TiO2, ZrO2, Al2O3, and Ta2O5 from Aqueous Solutions. *Spectrochim. Acta - Part A Mol. Biomol. Spectrosc.* **2000**, *56* (3), 557–565.

(89) Beentjes, P. C. J.; Van den Brand, J.; De Wit, J. H. W. Interaction of Ester and Acid Groups Containing Organic Compounds with Iron Oxide Surfaces. *J. Adhes. Sci. Technol..* **2006**, *20* (1), 1–18.

(90) van den Brand, J.; Blajiev, O.; Beentjes, P. C. J.; Terryn, H.; de Wit, J. H. W. Interaction of Anhydride and Carboxylic Acid Compounds with Aluminum Oxide Surfaces Studied Using Infrared Reflection Absorption Spectroscopy. *Langmuir* **2004**, *20* (15), 6308–6317.

(91) Hocking, R. K.; Hambley, T. W. Structural Measure of Metal-Ligand Covalency from the Bonding in Carboxylate Ligands. *Inorg. Chem.* **2003**, *42* (9), 2833–2835.

(92) Hocking, R. K.; Hambley, T. W. Structural Measures of Element-Oxygen Bond Covalency from the Changes to the Delocalisation of the Carboxylate Ligand. *Dalt. Trans.* **2005**, 969–978.

(93) Deacon, G. B.; Phillips, R. J. Relationships Between the Carbon-Oxygen Stretching Frequencies of Carboxylato Complexes and the Type of Carboxylate Coordination. *Rev. Chem.* **1980**, *33*, 227–250.

(94) Deacon, G. B.; Huber, F.; Phillips, R. J. Diagnosis of the Nature of Carboxylate Coordination from the Direction of Shifts of Carbon-Oxygen Stretching Frequencies. *Inorganica Chim. Acta* **1985**, *104*, 41–45.

(95) Taheri, P.; Hauffman, T.; Mol, J. M. C.; Flores, J. R.; Hannour, F.; De Wit, J. H. W.; Terryn, H. Molecular Interactions of Electroadsorbed Carboxylic Acid and Succinic Anhydride Monomers on Zinc Surfaces. *J. Phys. Chem. C* **2011**, *115* (34), 17054–17067.

(96) Wit, F. M. De; Mol, J. M. C.; Terryn, H.; Wit, J. H. W. De; Mol, J. M. C.; Terryn, H.; Influence, J. H. W. D. W. T. The Influence of Chemical Pre-Treatment and Magnesium Surface Enrichment on Bonding of Succinic Acid Molecules to Aluminium Alloy The Influence of Chemical Pre-Treatment and Magnesium Surface Enrichment on Bonding of Succinic Acid Molecules. *J.*

Adhes. Sci. Technol. **2008**, *22*, 1089–1104.

(97) Giannakoudakis, D.; Mitchell, J.; Bandosz, T. J. Reactive Adsorption of Mustard Gas Surrogate on Zirconium (Hydr)Oxide/Graphite Oxide Composites: The Role of Surface and Chemical Features. *J. Mater. Chem. A* **2015**, *4*, 1008–1019.

(98) Pletincx, S.; Trotochaud, L.; Fockaert, L.-L.; Mol, J. M. C.; Head, A. R.; Karslıoğlu, O.; Bluhm, H.; Terryn, H.; Hauffman, T. In Situ Characterization of the Initial Effect of Water on Molecular Interactions at the Interface of Organic/Inorganic Hybrid Systems. *Sci. Rep.* **2017**, *7*, 45123.

(99) Crabtree, R. H. *The Organometallic Chemistry of the Transition Metals*, sixth.; John Wiley & Sons, Inc, 2014.

(100) Hu, H.; Saniger, J. M.; Castaño, V. M. Deformation Behavior of Polyacrylic Acid-Metal Oxide Composites in Water. *Mater. Lett.* **1993**, *16* (4), 200–205.

(101) Chen, J. P.; Hong, L.; Wu, S.; Wang, L. Elucidation of Interactions between Metal Ions and Ca Alginate-Based Ion-Exchange Resin by Spectroscopic Analysis and Modeling Simulation. *Langmuir* **2002**, *18* (24), 9413–9421.

(102) Taheri, P.; Terryn, H.; Mol, J. M. C. An in Situ Study of Amine and Amide Molecular Interaction on Fe Surfaces. *Appl. Surf. Sci.* **2015**, *354*, 242–249.

(103) Van Den Brand, J. On the Adhesion between Aluminium and Polymers, Delft Univeristy of Technology, 2004.

(104) Salgin, B.; Özkanat, Ö.; Mol, J. M. C.; Terryn, H.; Rohwerder, M. Role of Surface Oxide Properties on the Aluminum/Epoxy Interfacial Bonding. *J. Phys. Chem. C* **2013**, *117* (9), 4480–4487.

(105) Henry, C. R. Surface Studies of Supported Model Catalysts. *Surface Science Reports*. 1998, pp 231–325.

(106) Barthés-Labrousse, M. G. Acid-Base Characterisation of Flat Oxide-Covered Metal Surfaces. *Vacuum* **2002**, *67* (3–4), 385–392.

(107) Mercier, D.; Rouchaud, J. C.; Barthés-Labrousse, M. G. Interaction of Amines with Native Aluminium Oxide Layers in Non-Aqueous Environment: Application to the Understanding of the Formation of Epoxy-Amine/Metal Interphases. *Appl. Surf. Sci.* **2008**, *254* (20), 6495–6503.

(108) Fife, T. H.; Przystas, T. J. Divalent Metal Ion Catalysis in the Hydrolysis of Esters of Picolinic Acid. Metal Ion Promoted Hydroxide Ion and Water Catalyzed Reactions. *J. Am. Chem. Soc.* **1985**, *107* (4), 1041–1047.

(109) Fife, T. H.; Pujari, M. P. Divalent Metal Ion Catalysis in the Hydrolysis of Phosphomonoesters. Hydrolysis of 2-(1,10-Phenantrolyl)Phosphate. *J. Am. Chem. Soc.* **1988**, *110* (23), 7790–7797.

(110) Fife, T. H.; Przystas, T. J. Transition-State Effects in the Divalent Metal Ion Catalyzed Hydrolysis of Esters. Hydrolysis of 2-Pyridylmethyl Hydrogen Phthalate. *J. Am. Chem. Soc.* **1980**, *102* (24),

7297–7300.

(111) De Wit, F. M.; Özkanat, Ö.; Mol, J. M. C.; Terryn, H.; De Wit, J. H. W. The Influence of Pre-Treatments of Aluminium Alloys on Bonding of PET Coatings. *Surf. Interface Anal.* **2010**, *42* (4), 316–320.

(112) Strålin, A.; Hjertberg, T. A FTIR Study of Interfacial Interactions between Ethylene Copolymers and Hydrated Aluminium Surfaces. *J. Adhes. Sci. Technol.* **1992**, *6* (11), 1233–1250.

(113) Vohs, J. M.; Barteau, M. A. Reaction Pathways and Intermediates in the Decomposition of Acetic and Propionic Acids on the Polar Surfaces of Zinc Oxide. *Surf. Sci.* **1988**, *201*, 481–502.

(114) Gervasini, A.; Auroux, A. Acidity and Basicity of Metal Oxide Surfaces II. Determination by Catalytic Decomposition of Isopropanol. *J. Catal.* **1991**, *131* (1), 190–198.

(115) Pletincx, S.; Fockaert, L. I.; Meeusen, M.; Mol, J. M. C.; Terryn, H.; Hau, T. In Situ Methanol Adsorption on Aluminum Oxide Monitored by a Combined ORP-EIS and ATR-FTIR Kretschmann Setup. *J. Phys. Chem. C 2018,* **2018**, *122*, 21963–21973.

(116) Liufu, S.; Xiao, H.; Li, Y. Adsorption of Poly(Acrylic Acid) onto the Surface of Titanium Dioxide and the Colloidal Stability of Aqueous Suspension. *J. Colloid Interface Sci.* **2005**, *281* (1), 155–163.

(117) Berquier, J. M.; Arribart, H. Attenuated Total Reflection Fourier Transform Infrared Spectroscopy Study of Poly(Methyl Methacrylate) Adsorption on a Silica Thin Film: Polymer/Surface Interactions. *Langmuir* **1998**, *14* (13), 3716–3719.

(118) Tannenbaum, R.; King, S.; Lecy, J.; Tirrell, M.; Potts, L. Infrared Study of the Kinetics and Mechanism of Adsorption of Acrylic Polymers on Alumina Surfaces. *Langmuir* **2004**, *20* (11), 4507–4514.

(119) Konstadinidis, K.; Thakkar, B.; Chakraborty, A.; Potts, L. W.; Tannenbaum, R.; Tirrell, M.; Evans, J. F. Segment Level Chemistry and Chain Conformation in the Reactive Adsorption of Poly(Methylmethacrylate) on Aluminum Oxide Surfaces. *Langmuir* **1992**, *8* (5), 1307–1317.

(120) Brinkhuis, R.; Schouten, A. Thin-Film Behavior of Poly (Methyl Methacrylates). 2. An FT-IR Study of Langmuir-Blodgett Films of Isotactic PMMA. *Macromolecules* **1991**, *24*, 1496–1504.

(121) Papirer, E.; Perrin, J. M.; Nanse, G.; Fioux, P. Adsorption of Poly (Methylmethacrylate) on an [Alpha] Alumina: Evidence of Formation of Surface Carboxylate Bonds. *Eur. Polym. J.* **1994**, *30* (8), 985–991.

(122) Abel, M.; Watts, J. F.; Digby, R. P.; Watts, J. F.; Digby, R. P.; Influence, T. H. E.; Abel, M.; Watts, J. F.; Digby, R. P. The Influence of Process Parameters on the Interfacial Chemistry of γ -GPS on Aluminium: A Review. *J. Adhes.* **2004**, *80*, 291–312.

(123) Abbott, S. *Adhesion Science: Principles and Practice*; DEStech Publications, Inc, 2015.

(124) Papaj, E. A.; Mills, D. J.; Jamali, S. S. Effect of Hardener Variation on Protective Properties of

Polyurethane Coating. *Prog. Org. Coatings* **2014**, *77* (12), 2086–2090.

(125) Perruchot, C.; Watts, J. F.; Lowe, C.; Beamson, G. Characterisation of the Curing Temperature Effects on Polyester Systems by Angle-Resolved XPS (ARXPS). *Int. J. Adhes. Adhes.* **2003**, *23*, 101–113.

(126) Taheri, P.; Flores, J. R.; Hannour, F.; De Wit, J. H. W.; Terryn, H.; Mol, J. M. C. In Situ Study of Buried Interfacial Bonding Mechanisms of Carboxylic Polymers on Zn Surfaces. *J. Phys. Chem. C* **2013**, *117* (7), 3374–3382.

(127) Öhman, M.; Persson, D. ATR-FTIR Kretschmann Spectroscopy for Interfacial Studies of a Hidden Aluminum Surface Coated with a Silane Film and Epoxy I. Characterization by IRRAS and ATR-FTIR. *Surf. Interface Anal.* **2012**, *44* (2), 133–143.

(128) Taheri, P.; De Wit, J. H. W.; Terryn, H.; Mol, J. M. C. In Situ Study of Buried Metal-Polymer Interfaces Exposed to an Aqueous Solution by an Integrated ATR-FTIR and Electrochemical Impedance Spectroscopy System. *J. Phys. Chem. C* **2013**, *117* (40), 20826–20832.

(129) Öhman, M.; Persson, D. An Integrated in Situ ATR-FTIR and EIS Set-up to Study Buried Metal – Polymer Interfaces Exposed to an Electrolyte Solution. *Electrochim. Acta* **2007**, *52*, 5159–5171.

(130) Öhman, M.; Persson, D. ATR-FTIR Kretschmann Spectroscopy for Interfacial Studies of a Hidden Aluminum Surface Coated with a Silane Film and Epoxy II . Analysis by Integrated ATR-FTIR and EIS during Exposure to Electrolyte with Complementary Studies by in Situ ATR-FTIR and in Si. *Surf. Interface Anal.* **2012**, *44*, 105–113.

(131) Öhman, M.; Persson, D.; Jacobsson, D. In Situ Studies of Conversion Coated Zinc / Polymer Surfaces during Exposure to Corrosive Conditions. *Prog. Org. Coatings* **2011**, *70*, 16–22.

(132) Mangolini, F.; Rossi, A. *Attenuated Total Reflection-Fourier Transform Infrared Spetroscopy: A Powerful Tool for Investigating Polymer Surfaces and Interfaces*; 2014.

(133) Osawa, M. *Near-Field Optics and Surface Plasmon Polaritons; Surface-Enhanced Infrared Absorption*, 1st ed.; Kawata, S., Ed.; Springer-Verlag Berlin Heidelberg, 2001; Vol. 81.

(134) Osawa, M.; Ataka, K.; Yoshii, K.; Nishikawa, Y. Surface-Enhanced Infrared Spectroscopy: The Origin of the Absorption Enhancement and Band Selection Rule in the Infrared Spectra of Molecules Adsorbed on Fine Metal Particles. *Appl. Spectrosc.* **1993**, *47* (9), 1497–1502.

(135) Harrick, N. J. Study of Physics and Chemistry of Surfaces from Frustrated Total Internal Reflections. *Phys. Rev. Lett.* **1960**, *4* (5), 224–226.

(136) Ishida, K. P.; Griffiths, P. R. Theoretical and Experimental Investigation of Internal Reflection at Thin Copper Films Exposed to Aqueous Solutions. *Anal. Chem.* **1994**, *66* (4), 522–530.

(137) Lu, X.; Shephard, N.; Han, J.; Xue, G.; Chen, Z. Probing Molecular Structures of Polymer/Metal Interfaces by Sum Frequency Generation Vibrational Spectroscopy. *Macromolecules* **2008**,

8770–8777.

(138) Lu, X.; Xue, G.; Wang, X.; Han, J.; Han, X.; Hankett, J.; Li, D.; Chen, Z. Directly Probing Molecular Ordering at the Buried Polymer/Metal Interface 2: Using P-Polarized Input Beams. *Macromolecules* **2012**, *45* (15), 6087–6094.

(139) Myers, J. N.; Chen, Z. Polymer Molecular Behaviors at Buried Polymer/Metal and Polymer/Polymer Interfaces and Their Relations to Adhesion in Packaging. *J. Adhes.* **2017**, *93* (13), 1081–1103.

(140) Zhang, C.; Hankett, J.; Chen, Z. Molecular Level Understanding of Adhesion Mechanisms at the Epoxy / Polymer Interfaces. **2012**.

(141) Lu, X.; Shephard, N.; Han, J.; Xue, G.; Chen, Z. Probing Molecular Structures of Polymer/Metal Interfaces by Sum Frequency Generation Vibrational Spectroscopy. *Macromolecules* **2008**, *41*, 8770–8777.

(142) Israelachvili, J.; Min, Y.; Akbulut, M.; Alig, A.; Carver, G.; Greene, W.; Kristiansen, K.; Meyer, E.; Pesika, N.; Rosenberg, K.; et al. Recent Advances in the Surface Forces Apparatus (SFA) Technique. *Reports Prog. Phys.* **2010**, *73* (3), 036601.

(143) Myers, J. N.; Chen, Z. Polymer Molecular Behaviors at Buried Polymer/Metal and Polymer/Polymer Interfaces and Their Relations to Adhesion in Packaging. *J. Adhes.* **2016**, *8464* (July), 1–23.

(144) Johnson, C. M.; Tyrode, E.; Baldelli, S.; Rutland, M. W.; Leygraf, C. A Vibrational Sum Frequency Spectroscopy Study of the Liquid - Gas Interface of Acetic Acid - Water Mixtures : 1 . Surface Speciation. *J. Phys. Chem. B* **2005**, *109*, 321–328.

(145) Myers, J. N.; Chen, Z. Surface Plasma Treatment Effects on the Molecular Structure at Polyimide / Air and Buried Polyimide / Epoxy Interfaces. **2015**, *26*, 449–454.

Chapter 3 : Zr/Ti-based conversion treatments

Zirconium- and titanium-based conversion treatments are currently being used as environmentally viable alternative for chromate- and phosphate- based conversion treatments. However, due to substrate variations on one hand, and the multi-component conversion bath composition on the other hand, conversion film formation is not yet fully understood.

This chapter describes the effect of different oxides occurring at galvanized steel surfaces, fluoroacid cation (i.e. zirconium and titanium) and organic additives on the conversion film formation. The high variety of interface variables requires a systematic approach starting from simplified systems to which complexity is gradually added.

As such, the zirconium-treatment of zinc, aluminium and magnesium oxides have been studied *in-situ* using ATR-FTIR in a Kretschmann geometry. This set-up was coupled to an electrochemical cell, correlating physico-chemical surface properties to precipitation kinetics as well as the protective nature of the converted oxide layer. The conversion kinetics obtained by in-situ studies of thermally vaporized multi-metal substrates were in accordance with those obtained by ex-situ XPS and AES studies on polished metal sheets. However, different (de)hydroxylation equilibria were noted for model and industrially relevant substrates. This was attributed to the different nature of the native oxides and thus their different activity in the respective conversion solution. Nevertheless, GI and MZ were shown to be equivalent in terms of conversion layer composition, surface hydroxide fractions and surface free energy.

3.1 Introduction

The formation of zirconium- and titanium-based conversion coatings is known to highly depend on the nature and thus the activity of the metal oxide.[1–7] Not only the kinetics and thus final layer thickness, but also surface chemistry correlates to the initial oxide physicochemical properties as discussed in section 2.3.[7,8] It is well-known that zirconium- and titanium conversion coatings result from a pH-based and electrochemical based mechanism. The electrochemical mechanism is mainly determined by substrate heterogeneities creating local anodes and cathodes.[5] Conversely, the activity of the oxide layer and its surface hydroxide fractions have shown to play a predominant role in the pH-based mechanism.[7,8] Because many interfacial factors can affect the conversion film formation, a straightforward mechanistic study is hindered by the complex surface chemistry of magnesium-aluminium-zinc alloys (MZ). Therefore, pure model metal substrates have been defined to allow a fundamental interface parameter study. As such, pure zinc, aluminium and magnesium have been thermally vaporized (20-50 nm) on internal reflection elements (IRE) for in-situ ATR-FTIR studies by means of physical vapor deposition (PVD). This way, oxide evolution can be followed in-situ during conversion.[7,9] Moreover, integrating an electrochemical cell in the ATR-FTIR setup provides additional information on the dynamic equilibrium between anodic and cathodic reactions and the evolution of conductive properties of the oxide layer during conversion.[1,7] Complementary to this, AES depth profiles have been collected on polished bulk metal sheets (1.0 mm) to evaluate the in-depth elemental distribution and conversion layer thickness.

Section 3.3.1 describes the in-situ zirconium-based conversion of thermally vaporized zinc, aluminium and magnesium substrates using the integrated ATR-FTIR – EC setup. Furthermore, ex-situ surface analysis has been performed on zirconium-treated polished metal sheets (1.0 mm) to describe the lateral and in-depth elemental distribution of the converted oxide layers. For these studies a commercial conversion system (Mavom CC1742) has been used, which in addition to hexafluorozirconic acid (H_2ZrF_6) also contains inorganic (phosphates) and organic (poly acrylic acid) additives increasing the conversion coating complexity. It becomes clear that the interchangeable use of bulk and thermally vaporized substrates together with the use of a commercial conversion system increases the variables having impact on conversion film formation. Consequently, a good parameter control is crucial for a fundamental understanding of the bonding properties of conversion oxides. Therefore, 3.3.2 continues the study using a model conversion solutions without any additives. Furthermore, surface analysis has been performed consistently on thermally vaporized substrates. This way, the obtained surface chemistry can directly be correlated to chemisorption studies performed using ATR-FTIR as described in the following chapters. Subsequently, section 3.3.3 presents a comparative study on zirconium-treatment of thermally vaporized and polished bulk

metal substrates. To further bridge the gap with industrially relevant systems, section 3.3.4 discusses the zirconium- and titanium-treatment of hot-dip galvanized substrate GI and MZ substrates. Finally, section 3.3.5 presents a comparative study on the bonding properties of zirconium- and titanium-treated GI and MZ substrates with and without organic additives. For this study model conversion solutions have been prepared based on hexafluorozirconic acid (H_2ZrF_6) and hexafluorotitanic acid (H_2TiF_6) to which commonly used organic additives, i.e. poly acrylic acid (PAA), poly vinylalcohol (PVA) and poly vinylpyrrolidone (PVP) are added. The surface free energy of variously treated GI and MZ substrates have been determined using the OWRK method by means of contact angle measurements.

3.2 Experimental

3.2.1 Materials and chemicals

Section 3.3.1: For the ex-situ studies (XPS and AES) 1.0 mm thick metal sheets (zinc foil: Goodfellow, 99.95% - aluminium foil: Goodfellow, 99.999% - magnesium foil: Alfa Aesar, 99.9%) were polished to 1 µm diamond paste grade. Subsequently, the samples were generously rinsed with aceton and ultrasonically cleaned with ethanol for 15 min. For the *in-situ* study, metal films (20nm) were deposited on a germanium internal reflection element (PIKE Technologies, 60°) by means of a high-vacuum Balzers BAE 250 evaporation system. The high purity metal sheets used for the ex-situ studies were used as source material for physical vapour deposition. Hexafluorozirconic acid solution with a low phosphate contribution and polyacrylic acid (PAA) additives (MAVOM, CC1742) was diluted to 20 g/L and brought to pH 4 with 0.1M NaOH. The conversion was conducted at room temperature for 90 seconds, where after the samples were generously rinsed with demineralized water and dried with pressed air.

Section 3.3.2 and 3.3.3: The metal substrates used were similar to those described for section 3.3.1. For the ex-situ studies, the high purity metal sheets were polished to 1 µm diamond paste grade. Subsequently, the samples were generously rinsed with aceton and ultrasonically cleaned with ethanol for 15 min. For the *in-situ* study, metal films (20nm) were deposited on a germanium internal reflection element (PIKE Technologies, 60°) by means of a high-vacuum evaporation system (VCM 600 Standard Vacuum Thermal Evaporator, Norm Electronics). Zirconium-treatment was conducted using hexafluorozirconic acid (Sigma-Aldrich Chemistry) diluted to 0.01 M and brought to pH 4 with 0.1 M NaOH. Aluminium and zinc coated IREs were dipped in conversion solution at room temperature for 60 seconds, whereas the exposure time of magnesium coated IRE to the conversion solution was limited to 10 seconds, due to the high reactivity of the thermally vaporized magnesium

film. Bulk substrates were dipped in the conversion solution for 90 seconds. Subsequently, the samples were generously rinsed with demineralized water and dried with pressurized air.

Section 3.3.4 and 3.3.5: Hot-dip galvanized steel (GI and MZ) sheets with a thickness of 0.4 mm were sourced from Tata Steel IJmuiden B. V. They were ultrasonically cleaned in acetone and ethanol both for 10 minutes. This was followed with an alkaline cleaning step at elevated temperature (60 °C) to remove surface aluminium, which results from the galvanizing process.[10] Therefore, the samples (50 x 50 mm) were immersed for 30 seconds in 1 M NaOH adjusted to pH 12 using concentrated phosphoric acid, after which they were rinsed using demineralized water and dried with compressed air. To investigate the effect of the cation (Zr vs Ti) and organic additives, model conversion treatments were prepared. Hexafluorozirconic acid, 50 wt% in H_2O (Sigma-Aldrich Chemistry) and hexafluorotitanic acid, 60wt% in H_2O (SigmaAldrich Chemistry) were diluted to 0.01 M. The pH was adjusted to 4 using 1 M NaOH. GI and MZ were dipped in the conversion solution for 90 seconds, after which they were abundantly rinsed with demineralised water and dried with pressurized air. The polymer additives investigated as potential adhesion enhancers were polyvinyl alcohol (PVA) molecular weight 145 000 (Sigma-Aldrich Chemistry), polyvinylpyrrolidone (PVP) molecular weight 360 000 (Sigma-Aldrich Chemistry) and polyacrylic acid (PAA) molecular weight 150 000 (Sigma-Aldrich Chemistry). They were added to the fluoroacid solutions with a concentration of 0.1 g/L. To dissolve the polymers, stirring at elevated temperatures was required. PVA and PAA were fully dissolved after 30 min stirring at 70°C, PVP required a higher temperature and was dissolved after 12 hours stirring at 80 °C.

3.2.2 Attenuated Total Reflection (ATR)-FTIR setup coupled to an electrochemical cell to in-situ study the formation of conversion oxide layer

The spectro-electrochemical cell was mounted on a VeeMAX III multi-purpose reflection accessory with ATR specifications from PIKE Technologies. The FTIR apparatus used was a Thermo-Nicolet Nexus equipped with a liquid-nitrogen cooled mercury-cadmium-telluride A detector and a nitrogen-purged measurement chamber. The incident infrared light was reflected off the surface at 80° to the surface normal. In order to reduce dominant water signals during in-situ conversion studies, infrared backgrounds were collected from native metal oxides exposed to demineralized water. Infrared spectra were taken every 10 seconds during zirconium-based conversion and averaged from 5 cycles with a resolution of 4 cm^{-1}. An electrochemical cell (Pike Technologies) was mounted on the VeeMAX III multi-purpose reflection accessory. Open circuit potential (OCP) measurements were conducted simultaneously in a conventional three-electrode cell using an SI1286 Electrochemical Interface Solartron Potentiostat. The reference was a silver/ silver chloride electrode. A platinum gaze was

utilized as counter electrode. The deposited metal layer was used as the working electrode. A graphical representation of the integrated ATR-FTIR- EC setup is given in figure 3.1.

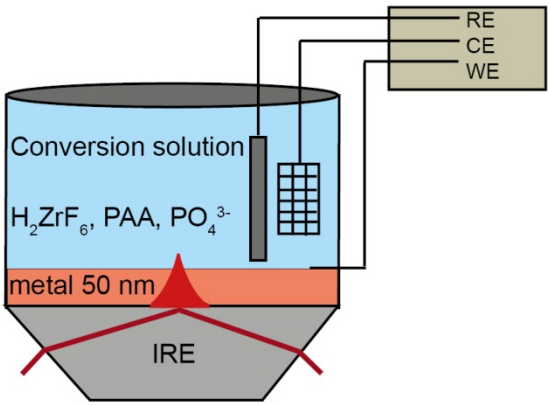

Figure 3.1: ATR-FTIR setup coupled to an electrochemical cell for in-situ spectro-electrochemical measurements during conversion of metal oxide.

3.2.3 Auger Electron Spectroscopy (AES)

AES measurements described in section 3.3.1 were performed using a PHI 650(SAM) with a LaB_6 cathode and a cylindrical mirror analyzer (CMA). A primary electron beam of 9 keV and an emission current of 50 nA were applied on 0.30 mm^2 of the sample surface at 30 degrees incident angle. Elemental depth profiles were obtained using a PHI 04-303 ion gun at 3 keV argon ions with emission current of 20 mA and an argon pressure in the sputter gun of 10 mPa. The sputter surface was 2x2 mm and argon ions impinged the surface at 50 degrees to its normal. From the sputter profile of 20 nm SiO_2 on Si, a sputter velocity of 10 nm/min. was assumed for SiO_2. Atomic concentrations in AES were determined using the sensitivity factors provided by the manufacturer. It is known that materials characterized by lower densities are preferentially sputtered at higher velocities. This relation is described in equation 3.1, were the sputter velocity, S (Å/min.) is proportional to the sputtering yield Y (atom/ion), the ion beam current density, J (μA/cm^2) and atomic or molecular weight of the target, A (g), and inversely proportional to the materials density, d (g/cm^3) [11].

$$S = Y\,(0{,}06\,JA)/d \qquad (3.1)$$

Obtained sputter times were converted to sputter depths using the sputter ratios of Al_2O_3 and ZnO versus SiO_2 experimentally determined by Bear[12]. Table 1 presents the materials under investigation with their respective densities[13] and the sputter ratios versus SiO_2. It was assumed that the sputter velocities of materials with similar density (MgO ≈ Al_2O_3 and ZrO_2 ≈ ZnO) are comparable. The heterogeneity of the oxide layer was not taken into account for the conversion to sputter depth. The reproducibility was verified by triplication of the measurements. AES data was analysed with PHI Multipak software (V9.1.0.9).

Field Emission Auger Electron Spectroscopy (FE-AES) described in section 3.3.2 and 3.3.4 were performed using a JEOL JAMP9500F FE-AES spectrometer, employing an electron beam of 10 keV and 10.6 nA at an angle of incidence of 30°. The utilized magnification was x3000 for zirconium-treated aluminium, x10 000 for zirconium-treated magnesium and x20 000 for zirconium-treated zinc. This resulted in mapping areas of approximately 35 x 35 µm for aluminium, 12 x 12 µm for magnesium and 6 x 6 µm for zinc. The utilized magnification was 12220 x for zirconium-treated GI and 20000 x for titanium-treated GI. This resulted in mapping areas of approximately 9x9 µm for zirconium-treated GI and 6x6 µm for titanium-treated GI. The data was extracted and processed using the JEOL Image Investigator V1.04 software.

3.2.4 X-ray photo-electron spectroscopy (XPS)

XPS spectra discussed in section 3.3.1, 3.3.4 and 3.3.5 were collected using a PHI5600 photoelectron spectrometer (Physical Electronics) with an Al Kα monochromatic X-ray source (1486.71 eV of photons) from a spot diameter of 800 µm using pass energy of 23.5 eV and step size 0.1 eV. The irradiation power was 150 W. The vacuum in the analysis chamber was approximately 8×10^{-9} Torr during measurements and measurements were performed with take-off angles of 45° with respect to the sample surface. XPS spectra discussed in sections 3.3.2 and 3.3.3 were collected using a PHI-5000 Versaprobe II (Physical Electronics) utilizing an Al Kα monochromatic X-ray source (1486.71 eV photon energy) with a spot diameter of 100 µm to measure surface compositions up to ca. 10 nm in depth. The irradiation power of the X-ray beam was 25 W. The kinetic energy of the photoelectrons was measured with a take-off angle of 45°. The vacuum in the analysis chamber was better than 1 x 10^{-9} Torr. Survey scans were recorded with a pass energy of 187.85 eV and energy step size of 0.1 eV. The reproducibility was verified by triplication of the measurements. XPS data was analysed with PHI Multipak software (V9.1.0.9). Before curve fitting, the energy scale of the XPS spectra was calibrated relative to the binding energy of adventitious hydrocarbons (C-C/C-H) in the C 1s peak at 284.8 eV. Curve fitting was done after a Shirley-type background removal, using mixed Gaussian − Lorentzian shapes.

3.2.5 Contact angle measurements (CA)

Contact Angle Measurements: Contact angle measurements of variously treated GI and MZ were performed using a OneAttension Theta Lite optical tensiometer (Biolin Scientific). Milli-Q water, ethylene glycol and diiodomethane were the liquids used to calculate dispersive and polar parts of the surface free energy (SFE). The procedure involved placing a drop of liquid with a volume of 1.5 µL on the surface of the sample, whereafter wetting force data were recorded for 10 seconds starting from the moment of liquid contact. The contact angle at the metal-liquid-air interface obtained after

10 seconds of contact with the solid substrate is presented in this work. Surface free energies were calculated based on the OWRK method using the OneAttension software. This software does not allow for standard deviation calculations. Yet, the reproducibility was verified by at least three measurements per liquid and substrate of which the average contact angle value for each liquid/substrate was used for calculating the SFE. For this reason presented SFE values are shown without error bars.

3.3 Results

3.3.1 Zirconium oxide film formation on model metal substrates using commercial conversion systems

3.3.1.1 In-situ spectro-electrochemical ATR-FTIR – OCP study

The oxide conversion kinetics of thermally vaporized aluminium, zinc and magnesium using a commercial zirconium-based conversion solution with phosphate load is studied *in-situ* using ATR-FTIR coupled with an electrochemical cell. The ATR-FTIR spectra during zirconium-based conversion of aluminium is presented in figure 3.2 (a). Two strong vibration bands at 570 and 1080 cm^{-1} are assigned symmetric and asymmetric to P-O stretches vibrations respectively,[14,15] although the latter also contains contributions of aluminium (hydr)oxide.[16] Their instantaneous presence, indicates the rapid formation of aluminium phosphate. The band positioned at 631 cm^{-1} is assigned to OH-F deformation vibrations,[17] whereas the weak band positioned at 728 cm^{-1} relates to Zr-O stretching vibrations,[18,19] representative for zirconium oxide precipitation. The in-situ ATR-FTIR spectra during zirconium-based conversion of zinc are shown in figure 3.2 (b). Similar to aluminium, peaks at 568 and 979 cm^{-1} demonstrate the instantaneous formation of zinc phosphate at initial conversion times, whereas the peak at 736 cm^{-1} is attributed to Zr-O stretching vibrations.[18] Contrary to the P-O stretching vibrations, the Zr-O peak area is shown to increase progressively during prolonged conversion times. Similarly, also the peak positioned at 639 cm^{-1}, associated to OH-F deformation vibrations, slightly increases with conversion time. The ATR-FTIR spectra during zirconium-based conversion of magnesium are demonstrated in figure 3.2 (c). A simultaneous growth of the peaks at 626 cm^{-1} and 716 cm^{-1}, illustrate rapid zirconium- fluoride and oxide formation. However, upon prolonged conversion times the respective peak areas turn negative. In addition, also the peaks positioned at 3276 and 846 cm^{-1} attributed to Mg-OH and Mg-O vibrations turn negative implying magnesium (hydr)oxide dissolution.[20] Consequently, thermally vaporized magnesium is shown to be unstable in the acid conversion solution (pH 4).

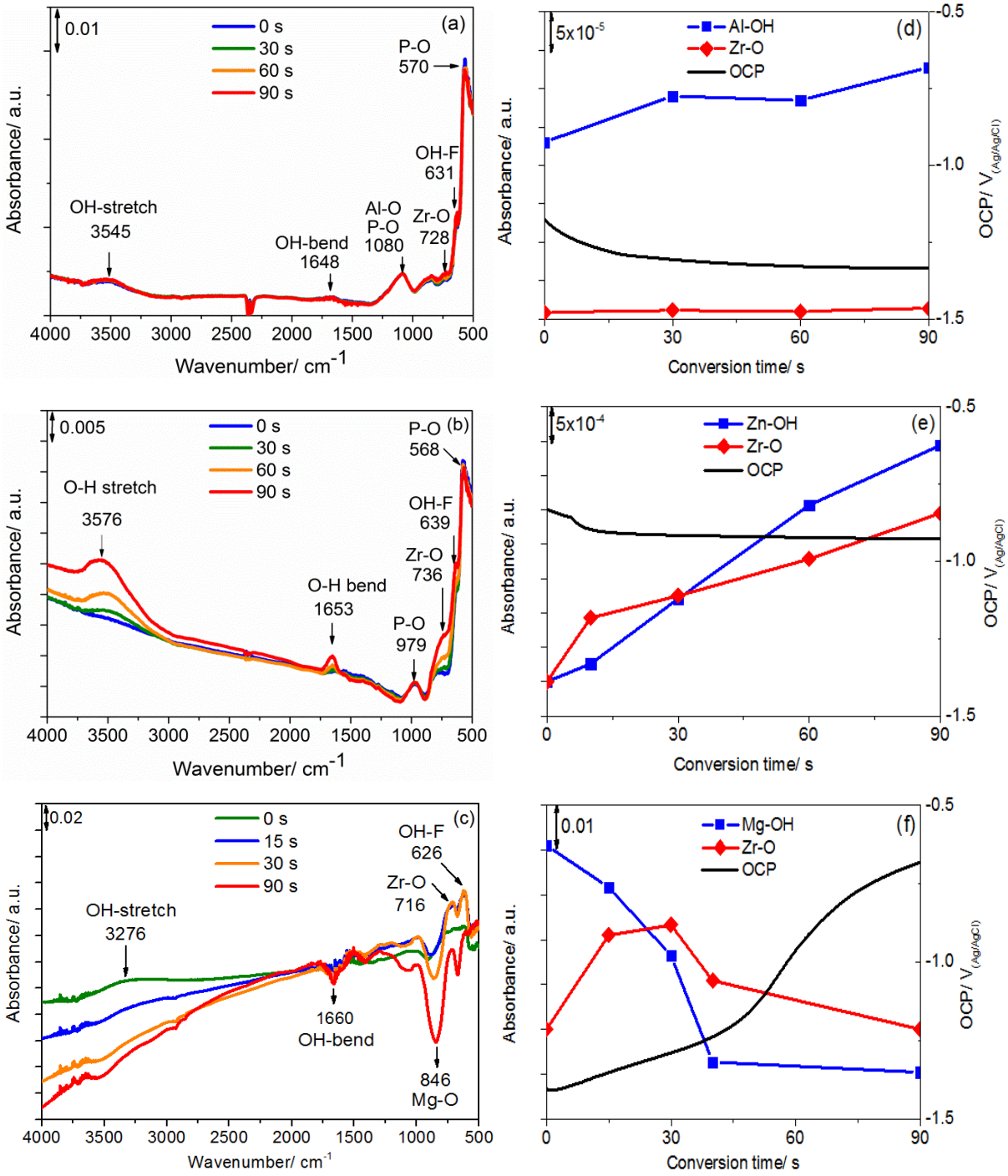

Figure 3.2: in-situ ATR-FTIR spectra obtained during zirconium-based conversion treatment of (a) aluminium, (b) zinc and c) magnesium oxide and the quantified peak areas for M-OH and Zr-O bonds scaled on the primary Y-axes and the corresponding OCP response scaled on the secondary Y-axes for (c) aluminium, (b) zinc and (c) magnesium oxide.

Furthermore, figure 3.2 shows OH stretch bands positioned at 3545, 3576 and 3276 cm^{-} during conversion of aluminium, zinc and magnesium, respectively. Although the IR signal of water has been

implemented in the background which was collected during immersion of the native metal oxides in water. No unambiguous statement on the evolution of metal hydroxide groups can be made based on this OH-stretch band. This because the presence of interfacial water, indicated by small OH-bending signals at 1640 cm^{-1} also contributes to the OH-stretching band. Yet, the evolving OH-stretching band area, demonstrated in figure 3.3 indicates that OH groups are involved in conversion reactions. This because the signal of bulk water is expected to remain constant over time. The OH-stretch band might relate to surface hydroxylation reactions resulting in metal and/or zirconium hydroxide formation. While also the in-situ generation of water as a result of the interaction between removed hydroxide anions and the excess protons in the acid conversion solution might contribute to the OH-stretch peak area. Hence, both hydroxide formation and removal reactions are expected to affect the OH-stretch peak area.

Figures 3.2 (d-f) scales the Zr-O and OH-stretch peak area evolution during conversion on the primary Y-axis and the simultaneously obtained OCP response on the secondary Y-axis. The OCP response during conversion of aluminium is shown in figure 3.2 (d). The observed OCP decay is associated to natural oxide dissolution caused by free fluorides present in the conversion solution.[7,8] Thinning of the natural oxide layer alters the oxide electronic properties, reducing the OCP. The absence of a cathodic OCP shift indicates that zirconium oxide deposition on aluminium is limited, as the formation of a compact stable oxide would shift the OCP to more positive values. This hypothesis is supported by the limited increase in Zr-O peak area indicating a low precipitation rate. Analogous behaviour is observed during the conversion of zinc, shown in figure 3.2 (e). Yet, the final OCP reduction is smaller compared to those observed on aluminium. After 7 seconds of conversion the OCP of zinc reduced by 50 mV, which is 50 % of the final OCP drop. The OCP of aluminium shows a total reduction of 200 mV. The smaller OCP decay on zinc can be related to a higher zirconium deposition rate. This is supported by the increasing Zr-O peak area. On both aluminium and zinc oxide, the anodic OCP shift is associated to the growth of OH-stretch band. In section 2.3.3, it has been described that zirconium deposition kinetics strongly relates to the equilibrium between surface hydroxide removal and formation.[7] Whereas metal substrates with high initial hydroxide fractions favour hydroxide removal and consequently fast zirconium deposition, poorly hydroxylated substrates tend to shift the equilibrium more to hydroxide formation. This concurrent surface hydroxylation has shown to retard the zirconium deposition of zinc and AA6014.[7,8] The competition between surface hydroxylation and zirconium deposition might explain the absence of a cathodic OCP shift for aluminium and zinc. It is thus suggested that the increased OH-stretch band area observed during conversion of aluminium and zinc, as illustrated in figure 3.3 (a) and (b), respectively, is attributed to the formation of a metal hydroxide film. Therefore, despite its high sensitivity for water, ATR-FTIR is suggested to be able to elucidate metal hydroxide evolution

reactions in aqueous media. Meanwhile, figure 3.2 (f) indicates a cathodic OCP shift during the conversion of magnesium oxide. The substantial increase of OCP suggests the formation of a thick oxide layer during the zirconium-based conversion, which is supported by the growth of the Zr-O peak at 716 cm^{-1} observed in the FTIR spectra in figure 3.2 (c). The high activity of magnesium in the acid conversion solution is shown to be challenging to in-situ monitor the zirconium oxide deposition on by means of ATR-FTIR. Hence, the Zr-O peak area, illustrated in figure 3.2 (f), is expected to be lower than the actual zirconium concentration in the converted oxide layer, due to the interference of the negative Mg-O peak.

Finally, it should be noted that the absorbance scale varies for the different metal substrates. This is related to the optical properties of the respective metal oxides. Therefore, the absorbance intensity cannot be directly compared between the different metal oxides.

3.3.1.2 Ex-situ surface characterization, lateral and in-depth elemental distribution

Whereas the in-situ study described in section 3.3.1.1. describes thermally vaporized metal substrates, the ex-situ elemental surface characterization of zirconium-treated aluminium, zinc and magnesium substrates discussed in this section have been conducted on polished metal sheets. The elements identified in the XPS survey scan, not shown, are expressed in atomic percentages using the relative sensitivity factors provided by the manufacturer. Figure 3.3 (a) presents the carbon (C), oxygen (O) and fluorine (F) concentrations at the zirconium-treated surfaces. Because the oxygen concentration is highly dominant with respect to the other elements, the metallic compounds of interests are presented using an enlarged scale, as shown in figure 3.3 (b). Although the physicochemical properties of the native oxides and thus their conversion kinetics are expected to vary compared to the thermally vaporized substrates described in section 3.3.1.1, a similar trend for zirconium oxide deposition is observed, with increasing zirconium concentrations in following order Al < Mg < Zn. Moreover, XPS surface analysis demonstrate higher phosphate concentrations on zirconium-treated aluminium and zinc substrates, whereas zirconium-treated magnesium substrate is characterized by the highest fluoride concentration.

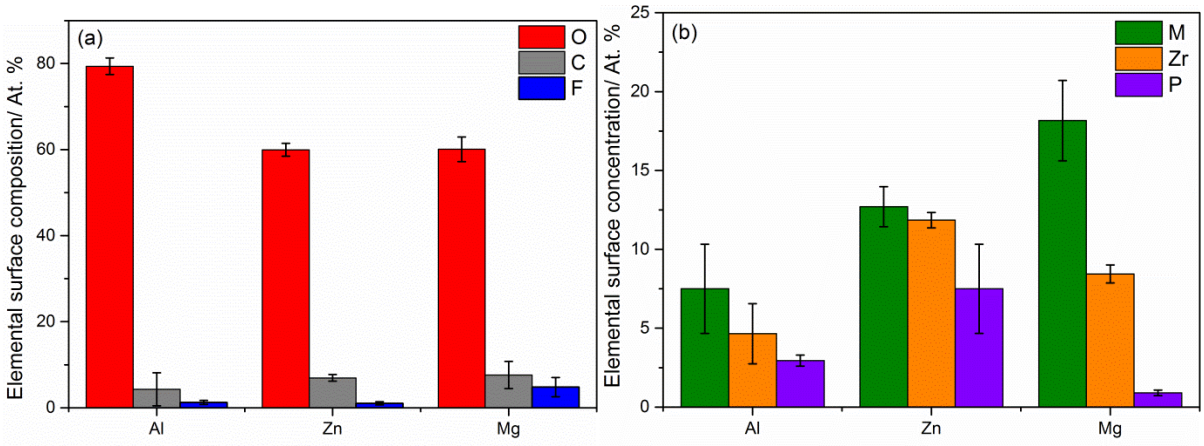

Figure 3.3: XPS elemental surface analysis of zirconium-treated aluminium, zinc and magnesium substrates (a) carbon, oxygen and fluorine concentrations, (b) metal, zirconium and phosphor concentration on an enlarged scale.

It has been demonstrated that the zirconium-based conversion kinetics strongly depends on the metal oxide physicochemical properties. In order to indicate the final conversion oxide thickness, Auger electron spectroscopy depth profiling has been performed after a 90 seconds dip in the zirconium-based conversion solution. The resulting AES depth profiles of zirconium-treated aluminium are shown in figure 3.4 (a). This demonstrates simultaneous evolution of zirconium and phosphor, which both rapidly reach the baseline, i.e. after 0.5 min of argon sputtering. On the other hand, figure 3.4 (b) demonstrates that longer sputter times are required to penetrate the zirconium oxide layer on zinc, i.e. 1.5 min. Phosphor and zirconium does not show analogous precipitation rates during the conversion of zinc. Since the phosphor signal reaches the baseline after 0.5 min of sputtering, phosphates are shown to be concentrated at the outer surface of the conversion film, which is in accordance with the ATR-FTIR data shown in figure 3.2 (b). Moreover, figure 3.4 (c) illustrates the in-depth elemental distribution of zirconium-treated magnesium. The high sputter times required to penetrate the zirconium oxide layer, i.e. more than 30 minutes suggest extreme high precipitation rates on magnesium oxide. These high precipitation rates are expected to correlate to the basic nature of magnesium oxide having an isoelectric point of 12, compared to 8 and 9 for aluminium and zinc oxide.[21] The alkaline nature of magnesium oxide, together with its highly active oxide enhances the efficiency of fluoride attack, which explains the high precipitation rate.

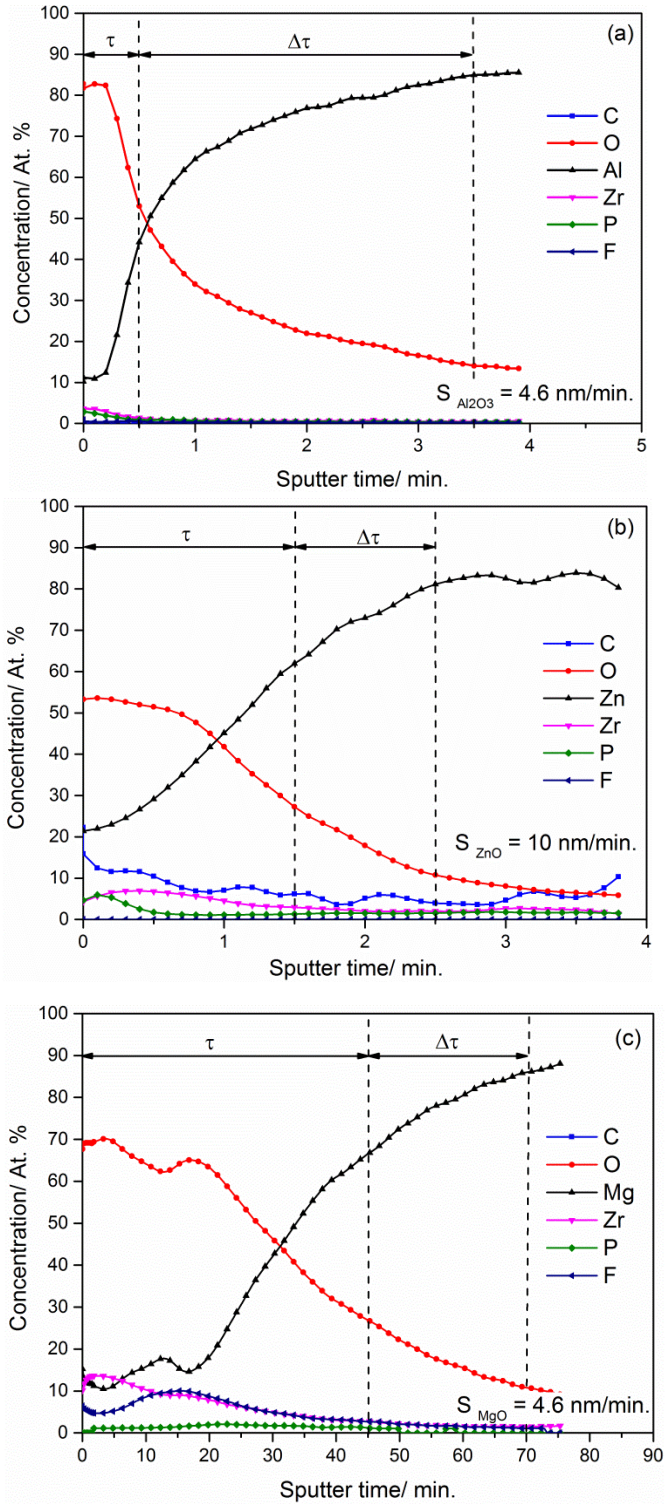

Figure 3.4. AES sputter depth profiles of zirconium-based converted (a) aluminium oxide (b) zinc oxide and (c) magnesium oxide.

The atomic concentration of zirconium at the surface obtained by AES analysis varies from 4 at.% on aluminium, 6 at.% on zinc and 9 at.% on magnesium, which slightly deviates from the concentrations

observed by XPS, i.e. 4, 12 and 8 %, on aluminium, zinc and magnesium respectively. These variations in surface zirconium concentration are associated to the different surface sensitivity of the respective techniques, with AES being most surface sensitive. Whereas the AES signal result from a depth smaller than 5 nm, XPS has a typical measuring depth of 3-10 nm.[22] Additionally, it can be seen that zirconium oxide coexists with metal oxide at the surface. With increasing sputter time, zirconium tends to decrease to zero at.% whereas oxygen is still largely present in the layer. The further declining oxygen concentration together with increasing metal concentrations suggests the presence of an intermediate metal oxide layer between the mixed zirconium/metal oxide film and the bulk metal. In order to determine the thickness of the top (τ) and intermediate (Δτ) oxide layer, the obtained sputter times are converted to sputter depths based on Bear's constant as described in the experimental section. The resulting sputter velocities (S), which are related to the specimen densities are estimated to be 10 nm/ min. for ZnO and 4.6 nm/ min. for Al_2O_3 and MgO. The top layer thickness (τ) results from the sputter time required to reduce zirconium to the base line level. The sputter velocity for this mixed zirconium/metal oxide layer is considered equal to pure metal oxide, ignoring the oxide heterogeneity. The interfacial metal oxide layer (Δτ) is determined by subtracting the thickness of the top layer from those of the total oxide thickness, as illustrated in figure 3.4. The latter is determined with the sputter time indicating a constant metal concentration. The estimated oxide thicknesses are presented in figure 3.5. For the top layer (τ), a thickness of approximately 15 nm, 2 nm and 180 nm has determined on zinc, aluminium and magnesium, respectively. Due to the heterogeneity of the top layer, the calculation gives only an estimation of the oxide thickness. Nevertheless, this gives a good semi-quantitative indication and allows the comparison of the different metal oxides. Moreover, the estimated thicknesses are in accordance with the observations of the growth kinetics obtained by in-situ ATR-FTIR studies. The zirconium conversion film formation kinetics on thermally vaporized and polished metal sheets are thus shown to be comparable.

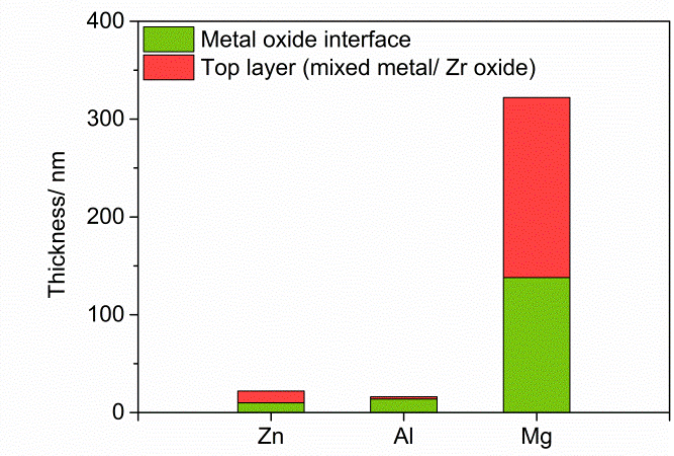

Figure 3.5: Estimated thickness of zirconium top layer and interfacial metal oxide layer on zinc, aluminium and magnesium based on argon sputtering.

3.3.2 Zirconium- treatment of thermally evaporated metal substrates using a model conversion solution without additives

The previous sections; 3.3.1 and 3.3.2, describe the conversion characteristics of model metal substrates using a commercial zirconium-based conversion solution. Its multicomponent composition, containing inorganic and organic additives, are considered as challenging for mechanistic interfacial chemisorption and stability studies of buried metal-polymer interfaces. Therefore, there has been opted to define a model conversion solution to reduce the complexity of the converted oxide surfaces enabling mechanistic interfacial studies as described in chapters 4-6.

3.3.2.1 XPS elemental surface characterization

Thermally vaporized metallic layers were characterized using XPS analysis. Survey scans elucidated carbon, oxygen and metal signals on the native oxides. After zirconium-treatment, also zirconium and fluoride were traced on all converted oxide layers. An example of the survey scan for zirconium-treated zinc is presented in figure 3.6.

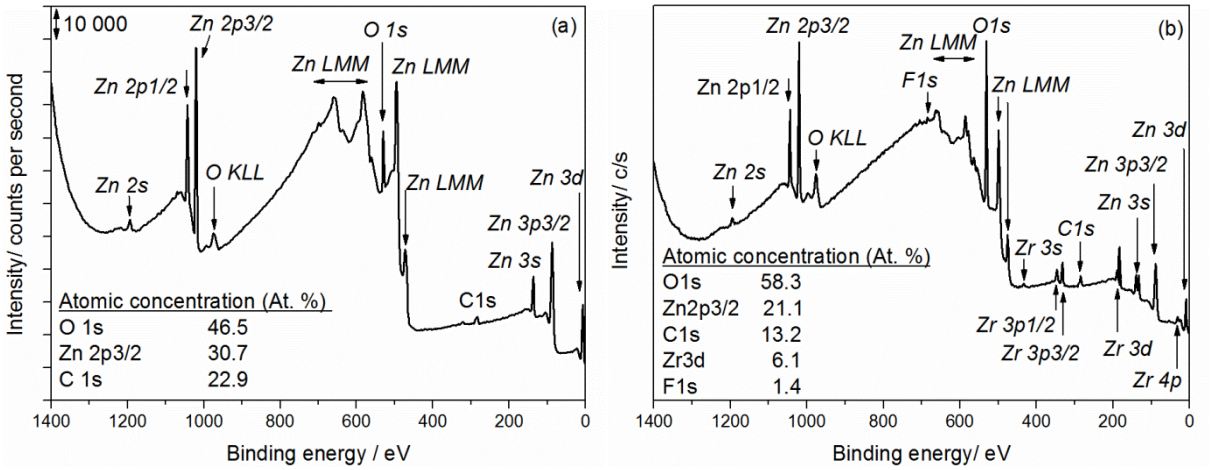

Figure 3.6: Survey scan and the resulting elemental concentration of (a) native zinc oxide and (b) zirconium-treated zinc oxide.

The elements identified in the survey scan are expressed in atomic percentages using the relative sensitivity factors provided by the manufacturer. The resulting elemental surface composition is illustrated in figure 3.7 (a-b). Figure 3.7 (a) compares the carbon (C), oxygen (O) and metal (M) contributions at the surface before (Native) and after (ZrCC) zirconium-treatment. This illustrates an increase in surface oxygen concentration after zirconium-treatment of zinc, aluminium and magnesium, while surface carbon and metal concentrations are being reduced. The reduction of surface carbon is attributed to the removal of ambient carbon contamination, resulting in a cleaner surface. The reduction of surface metal concentrations relates to the deposition of zirconium oxide. The atomic concentrations of zirconium (Zr), metal (M) and fluor (F) after zirconium-treatment (ZrCC)

are illustrated in figure 3.7 (b). Significant variations in metal concentrations are being observed after zirconium-treatment of zinc (22 At. %), aluminium (14 At. %) and magnesium (8 At. %). Whereas more or less constant concentrations of zirconium oxide (ca 7 At. %) are being observed. The indication of metal oxides may refer to metal impurities existing in the zirconium oxide layer, or to the formation of a homogeneous zirconium oxide layer, with a thickness thinner than 10 nm, being the maximum sampling depth of XPS measurements. Surface concentrations of fluorides are minor (1-2 At. %) in case of zinc and magnesium and reach approximately 5 At.% in case of converted aluminium. This is in line with reported stability constants for fluoride complexes, which are reported to increase in following order; Zn^{2+} (K = 0.8-1), Mg^{2+}(K = 1.3), Al^{3+} (K = 6-7).[23]

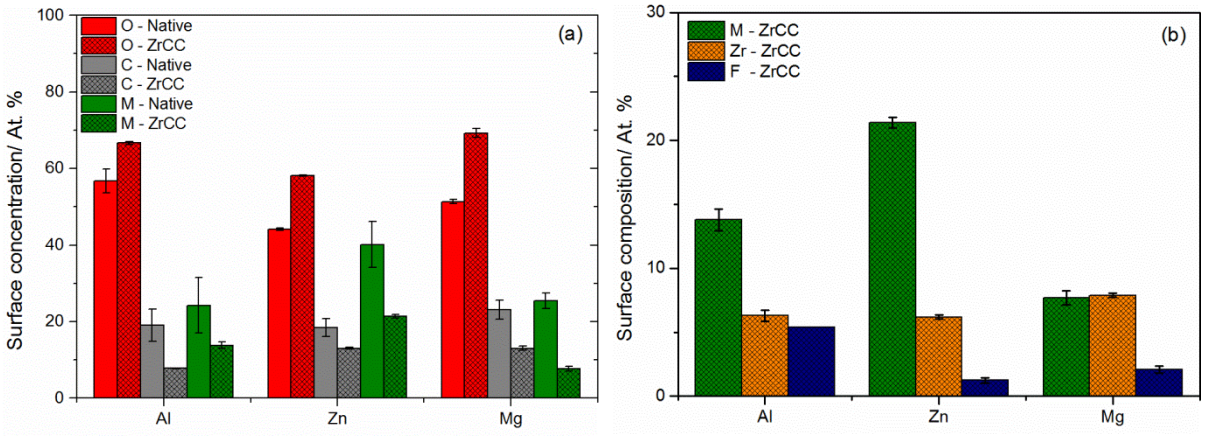

Fig. 3.7: Elemental surface composition (a) relative surface contributions oxygen, carbon and metal (Zn, Al, Mg) on native oxides (Native) and zirconium-treated (ZrCC) PVD substrates, (b) relative surface contributions of metal, zirconium and fluoride on zirconium-treated PVD substrates.

3.3.2.2. FE-AES elemental surface mappings

FE-AES mappings, shown in figure 3.8, were performed to evaluate the lateral elemental distribution of the converted oxide layers. The white squares implemented in the FE-AES mappings define a 5 x 5 µm area demonstrating homogeneous lateral elemental distribution in the micrometer scale. Since molecular interfacial interactions take place on the nanometer scale, homogeneity of the converted oxide layers is thus shown to exist on a higher order of magnitude. Notable intensities of both aluminium and zirconium, given in figure 3.8 (a) and (b) respectively, indicate a mixed conversion oxide with aluminium and zirconium oxide coexisting at the outer surface. On the other hand, minor intensities of zinc and magnesium, shown in figure 3.8 (c) and (e), together with the higher intensities observed for zirconium, given in figure 3.8 (d) and (f), demonstrate that the outer surface of zirconium-treated zinc and magnesium oxide solely exists of zirconium oxide. As a result, molecular interactions on zirconium-treated zinc and magnesium substrates are taking place with zirconium

oxide, whereas in case of zirconium-treated aluminium molecular interactions can take place on both aluminium and zirconium oxide.

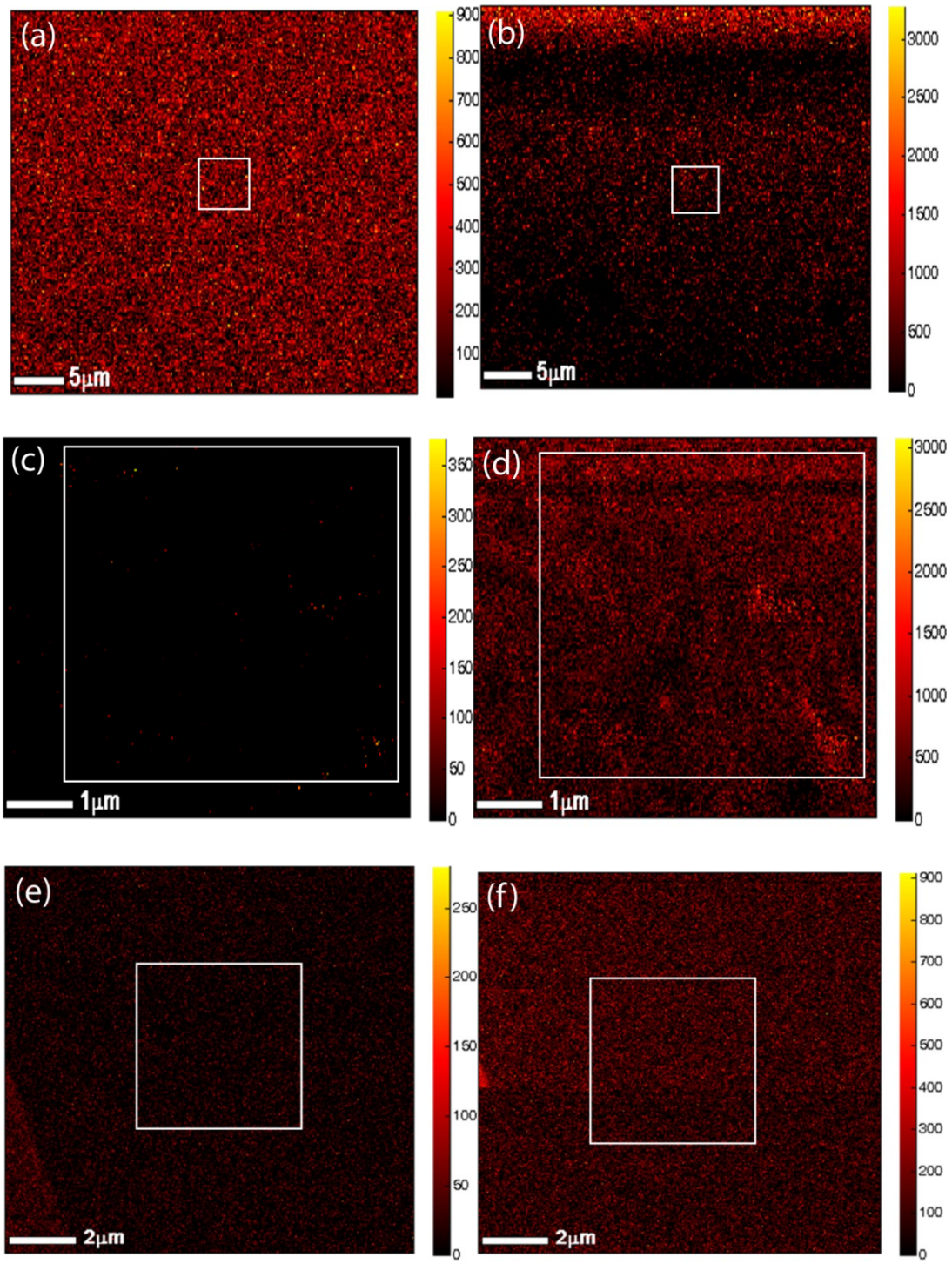

Figure 3.8: FE-AES mappings obtained after zirconium-treatment, (a) aluminium and (b) zirconium distribution after conversion of aluminium, (c) zinc and (d) zirconium distribution after conversion of zinc, (e) magnesium and (f) zirconium distribution after conversion of magnesium.

Based on the obtained FE-AES mappings, a graphical representation of the converted oxides is given in figure 3.9. It should be noted that oxide thickness variations are not taken into account in figure 3.9. Yet, since the elemental surface composition obtained by XPS (given in figure 3.7) indicates the presence of zinc and magnesium, whereas these appear to be absent at the outer zirconium oxide surface according to FE-AES mappings, the respective zirconium oxide layers are expected to be homogeneous with a thickness between 3 and 10 nm This because the sampling depth for XPS is known to be 3-10 nm for AlKα radiation.[22]

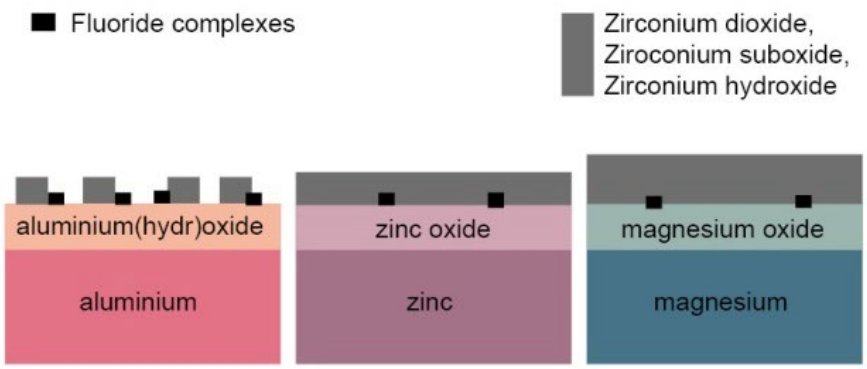

Fig. 3.9: Graphical presentation oxide composition after zirconium-treatment.

3.3.2.3 Quantification surface hydroxide densities

The formation of a zirconium–based conversion layer is known to be a pH-based reaction in equilibrium with surface OH densities.[7] Because metal hydroxides are known to be important binding sites for molecule interactions, their densities are being evaluated using O1s XPS analysis. Normalised high resolution XPS O 1s peaks before and after chemical conversion are shown in figure 3.10 (a-c). The O^{2-} component specific to metal oxide, is positioned at 529.9 eV ± 0.3 eV.[24] Similar binding energies are expected in case of ZnO, Al_2O_3, MgO and ZrO_2. Therefore, no distinction can be made between metal and zirconium oxide based on the O 1s XPS peak. A second component, OH^- specific to metal hydroxide contributions is positioned at 531.5 ± 0.2 eV.[24] It is evidenced that the O^{2-} component reduces relative to OH^- component after zirconium-treatment indicating increased hydroxide densities at the metal surface after conversion. A third component assigned to chemisorbed water is positioned at 532.6 ± 0.3 eV.[24] By deconvoluting the O 1s XPS peak into its subcomponents, surface hydroxide fractions before and after zirconium-treatment can be estimated. A detailed description of the calculation of surface hydroxide fractions based on the methodology approached by McCafferty and Wightman[25] can be found in the appendix on page 195.

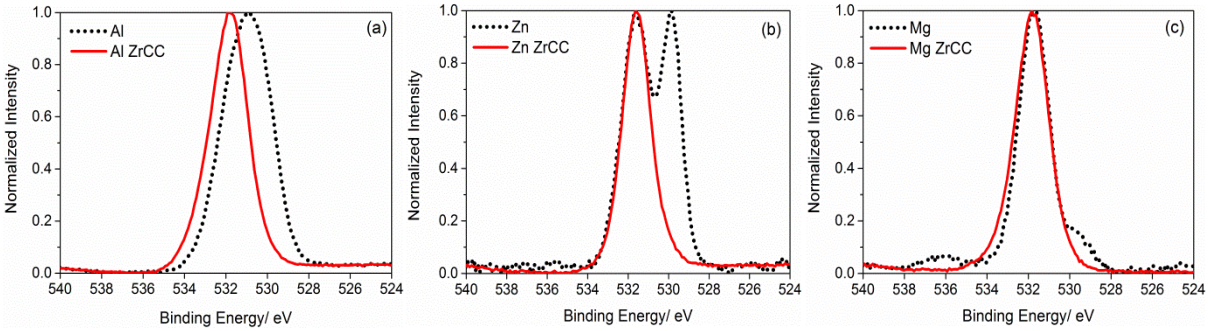

Figure 3.10: High resolution O1s XPS peak before and after zirconium-treatment of (a) aluminium, (b) zinc and (c) magnesium.

Figure 3.11 illustrates the estimated hydroxide fractions of native and zirconium-treated zinc, aluminium and magnesium oxide. It can be seen that zirconium-treatment results in a substantial increase of surface hydroxide fraction varying between 80 and 90 %. The high hydroxide coverages, nearly saturating the surface, likely relates to the active oxides of thermally vaporized films. Because of this, the fluoride concentration of the conversion solution is rather high resulting in aggressive dissolution of the native oxide.[5] High rates of accompanying oxygen reduction reactions cause local alkalinisation which is held responsible for the precipitation of zirconium dioxide.[41,49] Yet, because of the high kinetics, accumulating hydroxides are expected to be incorporated in the precipitated zirconium oxide layer, as illustrated by the estimated hydroxide fractions in figure 3.11.[7,8]

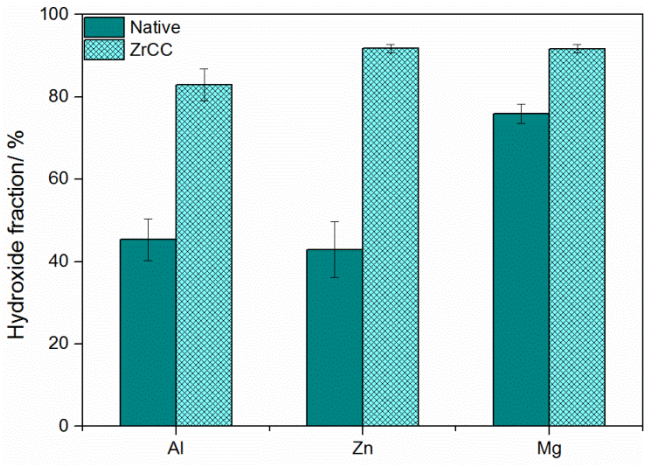

Figure 3.11: Calculated hydroxide fractions before (native) and after (ZrCC) zirconium-treatment.

3.3.3 Comparative study zirconium-treatment thermally vaporized and bulk substrates

3.3.3.1 XPS surface characterization

Higher Zr/M ratios are being observed on converted bulk substrates, shown in figure 3.12 (b), compared to converted PVD substrates, shown in figure 3.12 (a). These reduced metal contributions at the converted bulk substrates are suggested to result from thicker zirconium oxide layers.[27] Higher

fluoride concentrations observed on bulk zinc and magnesium might relate to the lowered activity of the native zinc and magnesium oxides requiring more fluoride attack, and thus explaining their accumulation at the converted surface.

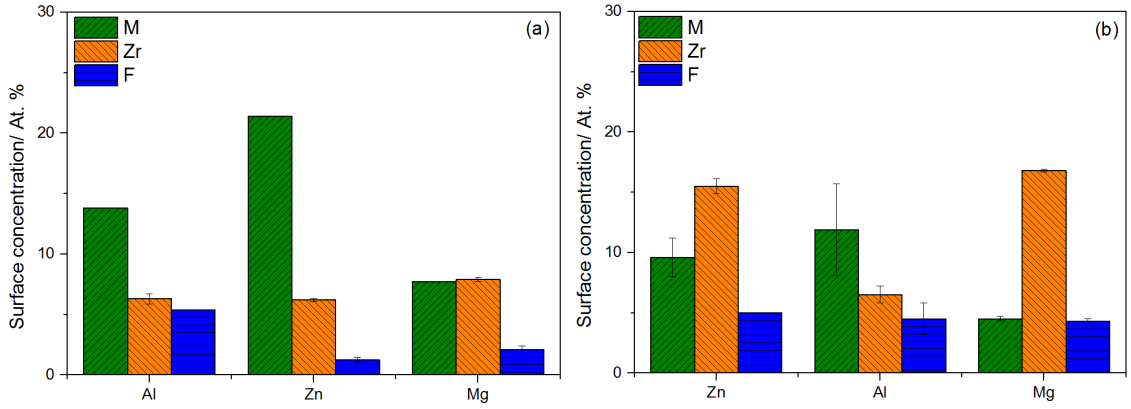

Figure 3.12: Elemental surface composition of zirconium-treated (a) PVD and (b) bulk substrates.

Figure 3.13 shows high-resolution O 1s prior and after zirconium-treatment, suggesting altered surface hydroxide concentrations upon conversion. Due to the varying O 1s peak shapes, associated to variations in hydroxide (OH^-) and metal oxide (O^{2-}) subpeak areas positioned at different binding energies, variations in surface hydroxide fractions are expected.[25]

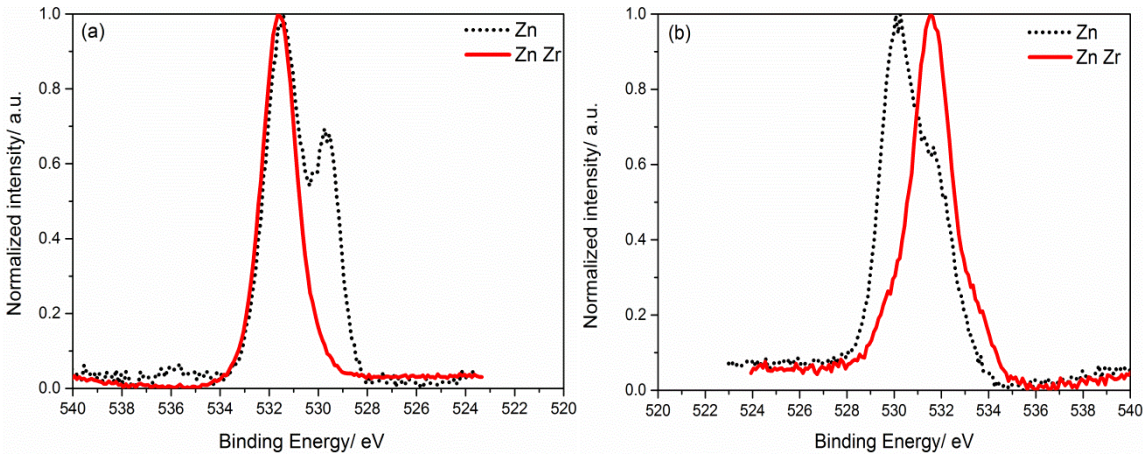

Figure 3.13: High-resolution O 1s XPS peak of (a) PVD and (b) bulk substrates prior and after zirconium-treatment.

O 1s curve fitting allows the quantification of surface hydroxide fractions, which has been done using the approach proposed by McCafferty and Wightman.[25] This approach represents the metal oxide film as a multilayer system consisting of an overlayer of adsorbed organic contamination covering the hydroxylated metal oxide of interest. The presence of carbon contamination attenuates the XPS signals of the underlying signal. Moreover, carboxylic acid species (C-O, COO^-, COOH) also contribute

to the hydroxide subpeak in the O 1s XPS peak. Therefore, there is a need to correct for this overestimation of hydroxides, which is done by C 1s and O 1s XPS peak deconvolution. Following centered peak positions have been used for C 1s deconvolution: C-C/C-H 284.7 ± 0.1 eV, C-O 286.2 ± 0.3 eV, COO^- 288.5 ± 0.4 eV and 289.5 ± 0.3 eV. The O 1s peak has been fitted using following centered peak positions: O^{2-} 529.9 ± 0.3, OH^- 531.5 ± 0.2 and H_2O 532.6 ± 0.3. All subpeaks had a FWHM of 1.5 eV. The resulting peak areas of the C 1s subpeaks are given in table 3.1.

Table 3.1: C-C/C-H, C-O, COO^- and O-C=O peak areas (%) and their standard deviations prior and after Dimethylsuccinate (DMS) adsorption on thermally vaporized and polished metal sheet‡ substrates.

	C-C/C-H		**C-O**		**COO-**		**O-C=O**	
	Area	**(%)**	**Area**	**(%)**	**BE**	**(%)**	**BE**	**(%)**
Zn	58	± 3	5	± 1	20	± 3	17	± 0
Zn DMS	41	± 0	10	± 1	25	± 0	25	± 0
Zn‡	80	± 3	7	± 1	9	± 2	5	± 2
Zn DMS‡	71	± 3	10	± 1	13	± 2	7	± 1
Zn ZrCC	68	± 1	14	± 1	10	± 1	9	± 1
Zn ZrCC DMS	52	± 7	18	± 5	15	± 1	15	± 1
Zn ZrCC‡	57	± 11	19	± 10	8	± 4	17	± 3
Zn ZrCC DMS‡	40	± 3	28	± 2	19	± 1	13	± 2
Mg	35	± 1	4	± 1	46	± 3	14	± 3
Mg DMS	55	± 6	10	± 2	17	± 4	17	± 4
Mg‡	52	± 10	14	± 10	13	± 2	21	± 2
Mg DMS‡	60	± 11	14	± 9	14	± 1	11	± 6
Mg ZrCC	56	± 1	24	± 0	11	± 1	8	± 2
Mg ZrCC DMS	55	± 2	22	± 1	12	± 1	12	± 1
Mg ZrCC‡	53	± 5	17	± 4	8	± 1	21	± 2
Mg ZrCC DMS‡	63	± 4	19	± 1	15	± 1	4	± 1
Al	50	± 6	20	± 0	19	± 1	11	± 8
Al DMS	33	± 17	20	± 1	17	± 0	17	± 0
Al‡	71	± 0	13	± 0	10	± 1	22	± 3
Al DMS‡	73	± 0	8	± 0	12	± 2	8	± 2
Al ZrCC	42	± 0	28	± 0	22	± 1	8	± 0
Al ZrCC DMS	61	± 7	23	± 5	8	± 1	8	± 1
Al ZrCC‡	63	± 1	12	± 1	11	± 0	8	± 3
Al ZrCC DMS‡	68	± 4	12	± 1	15	± 1	5	± 4

Estimated surface hydroxide fractions on zirconium-based converted PVD and bulk substrates are presented in figure 3.14 (a) and (b) respectively. The equations used for calculating surface hydroxide fractions according to the approach of McCafferty and Wightman[25] are given in the appendix on page 195.

A substantial increase of surface hydroxide fractions is demonstrated after zirconium-based treatment of PVD substrates, whereas bulk substrates are characterized by reduced hydroxide fractions after zirconium-based treatment. Since initial hydroxide fractions are comparable, varying between 40 and 60 %, this opposite trend must be related to the initial oxide properties rather than initial hydroxide density. It can be expected that on nanolayered metallic substrates, such as PVD substrates (20-50 nm) fluoride action is more aggressive compared to bulk (1.0 mm) substrates. Therefore, more rapid oxide dissolution with accompanying cathodic reactions are expected, which must result in higher near surface pH compared to bulk substrates, where surface reactions are expected to occur at a lower rate. Consequently, it is not surprising that accumulating hydroxides resulting from oxygen reduction reactions are largely incorporated in the converted oxide layer of PVD substrates. Earlier work showed that zirconium oxide deposition is in equilibrium with surface hydroxide removal and formation.[7,8] When hydroxylation becomes more prominent, as in case of PVD substrates, zirconium oxide deposition is expected to be less efficient. Conversely, when the hydroxide removal rate is higher than hydroxylation rate as in case of bulk substrates, zirconium oxide deposition becomes more efficient.[7,8] This is in line with the zirconium oxide thickness which were suggested to be higher on bulk substrates.

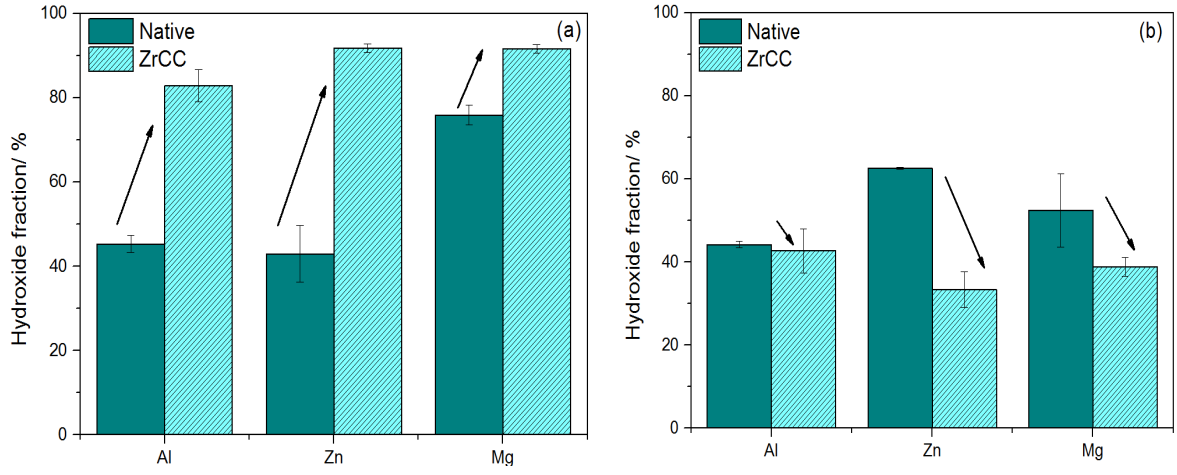

Figure 3.14: Calculated surface hydroxide fractions on (a) PVD and (b) bulk substrates obtained using the approach of McCafferty and Wightman[25].

3.3.4 Comparative study on zirconium- and titanium-treatment of GI and MZ

3.3.4.1 Elemental surface analysis

The formation of a zirconium- and titanium-based conversion film on GI and MZ was studied using XPS. The survey spectrum of untreated GI, presented in figure 3.15 (a), includes XPS peaks for oxygen, zinc, aluminium and carbon. The presence of aluminium on untreated GI indicate that the

applied alkaline cleaning procedure does not remove all surface aluminium. However, subsequent zirconium- and titanium-treatment efficiently removes remaining surface concentrations of aluminium, as demonstrated in figure 3.15 (b) and (c). Based on the zirconium-based conversion mechanism proposed by Lostak et al.,[4] it is suggested that the zinc matrix is more noble compared to the aluminium impurities. Hence, these aluminium impurities are being dissolved, while zirconium oxide precipitates covering the galvanized steel surface. Furthermore, zirconium, titanium and fluoride XPS peaks were detected in the relevant oxides.

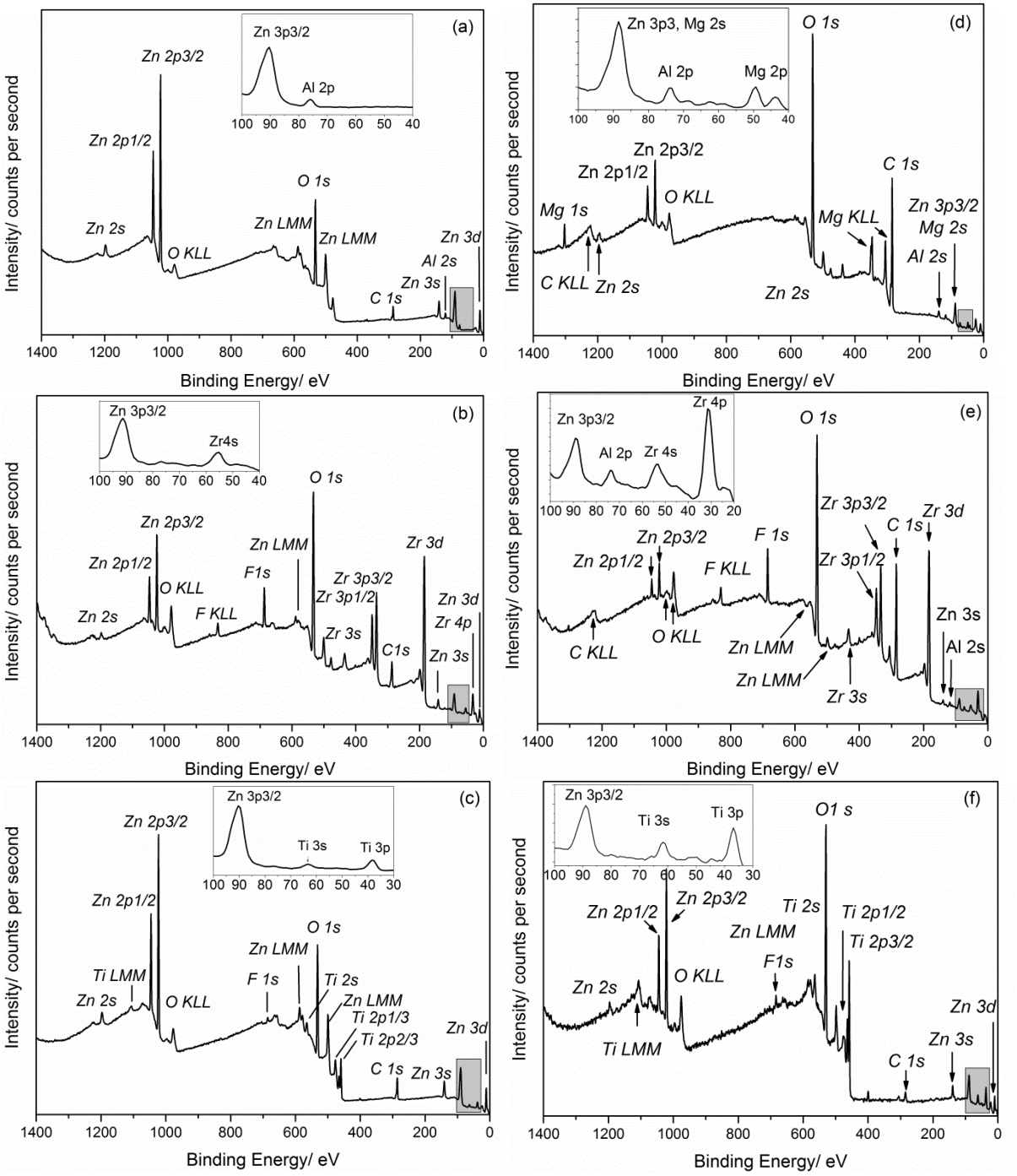

Figure 3.15: XPS survey scans of (a) untreated GI, (b) zirconium-treated GI, (c) titanium-treated GI, (d) untreated MZ, (e) zirconium-treated MZ and (f) titanium-treated MZ.

The elements traced in the XPS survey scans were converted to atomic percentages using the sensitivity factors (S) provided by the manufacturer[28] and summarized in figure 3.16. It is known that the overlayer of ambient carbon contaminants attenuates signals from the underlying surface.[29] As a consequence, carbon and oxygen signals are predominant. Therefore, elemental carbon (C), oxygen (O) and fluorine (F) concentrations are given in figure 3.16 (a) and (b) for variously treated GI and MZ respectively. Whereas the metal concentrations are given on an enlarged scale in figure 3.16 (c) and (d) for variously treated GI and MZ, respectively. From figure 3.16 (a) and (b) it can be seen that higher surface concentrations of fluorides are observed upon zirconium-treatment as compared to titanium-treatment and this on both GI and MZ. Furthermore, higher zinc concentrations are noted upon titanium-treatment of GI and MZ compared to zirconium-treatment as illustrated in figure 3. 16 (c) and (d).

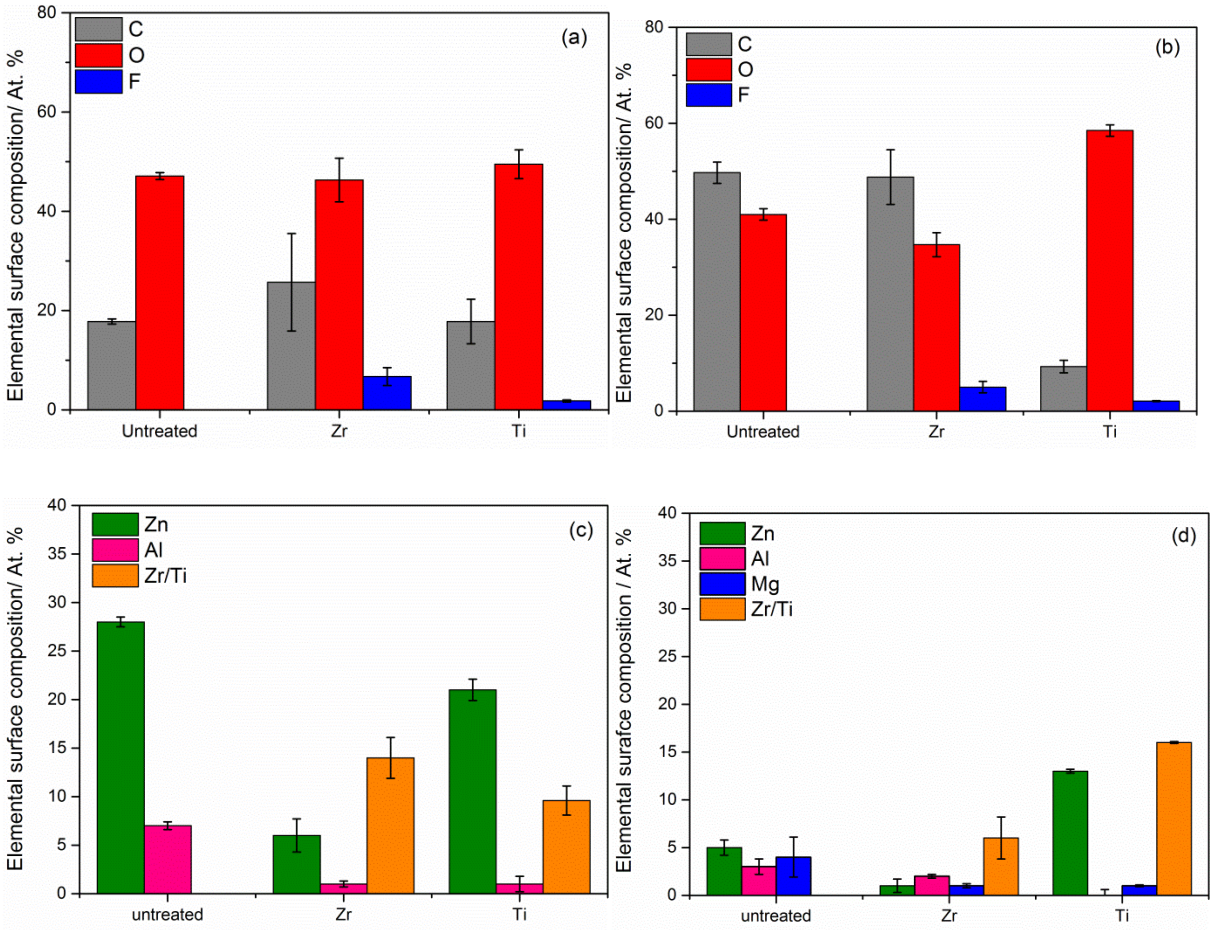

Figure 3.16: Carbon, oxygen and fluoride contributions at the surface as a function of conversion treatment of (a) GI and (b) MZ, and metal contributions; zinc, aluminium, magnesium, zirconium and titanium as a function conversion treatment of (c) GI and (d) MZ.

Figure 3.16 (d) illustrates more or less equal (ca. 5 At. %) concentrations of zinc, aluminium and magnesium at the untreated MZ surface. Whereas zirconium- and titanium-treatment of MZ significantly reduces surface aluminium and magnesium concentrations due to preferential dissolution of these oxides. This observation is in line with the deposition mechanism of zirconium-based conversion coatings proposed by Lostak et al.[4], who suggested that zinc-rich phases are local cathodes and thus act as initial nucleation sites for zirconium oxide precipitation, whereas aluminium and magnesium-rich phases undergo anodic dissolution leading to surface enrichment with zinc. As a result 6.0 ± 2.2 At. % zirconium has been determined on MZ compared to 14.0 ± 2.1 At. % in the case of GI. Conversely, 16.0 ± 0.5 At. % titanium has been determined on MZ compared to 9.6 ± 1.5 At. % in the case of GI. Therefore, it is suggested that zirconium-treatment is more efficient on GI, whereas titanium-treatment is suggested to be more efficient on MZ.

To study the lateral elemental distribution of the converted GI substrates FE-AES mappings were performed. Figure 3.17 (a) and (b) demonstrate the lateral zinc and zirconium distribution of zirconium-treated GI. Due to the absence of a Zn 2p3/2 signal in figure 3.17 (a), a homogeneous coverage of zirconium oxide is derived for zirconium-treated GI. Conversely, figure 3.17 (c) evidences a homogeneous distribution of zinc at the titanium-treated GI surface, indicating that both zinc and titanium coexist at the titanium-treated GI surface.

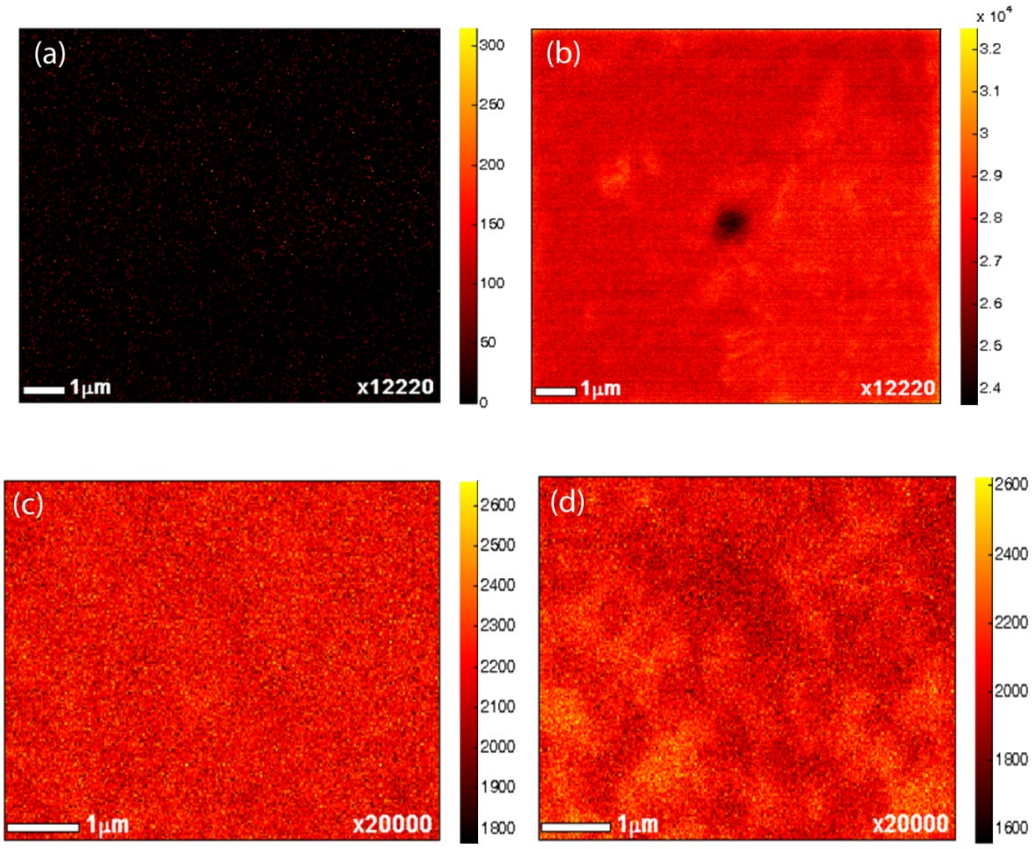

Figure 3.17: FE-AES elemental mappings of zirconium-treated GI with (a) zinc and (b) zirconium mappings and titanium-treated GI with (c) zinc and (d) titanium mappings.

Based on the XPS and AES surface analysis results presented in figure 3.16 and 3.17, GI and MZ are suggested to be equivalent in terms of conversion oxide build-up. A graphical representation of the zirconium- and titanium conversion oxide layer build-up is shown in figure 3.18 (a) and (b), respectively.

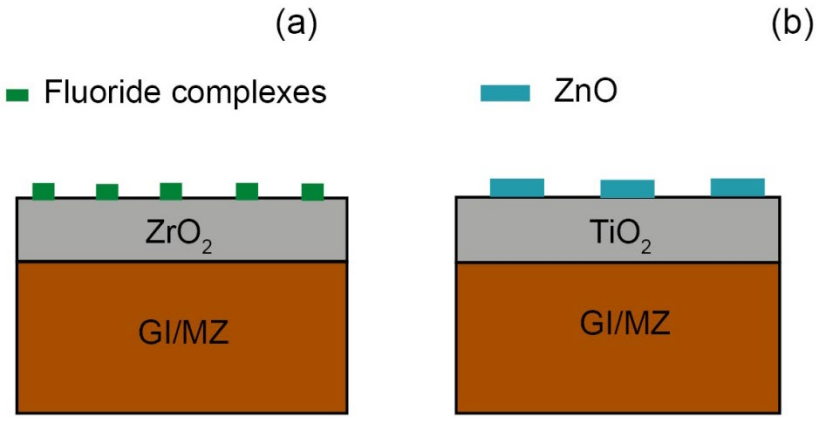

Fig. 3.18: Equivalent behaviour of GI and MZ upon (a) zirconium-treatment and (b) titanium treatment

Figure 3.19 illustrates the high resolution O 1s XPS of variously treated GI and MZ containing contributions of both metal oxide (530.2 ± 0.2 eV) and hydroxide (531.6 ± 0.2 eV).[25] On both GI and MZ the contribution of metal oxide (O^{2-}) significantly increases after both zirconium- and titanium-treatment. Yet, the growth of metal oxide subpeak is predominant for titanium-treated substrates. It is proposed that the higher portion of metal oxide (O^{2-}) to the oxygen O 1s XPS peaks originates from the higher valence number of Zr (IV) and Ti (IV) compared to Zn (II), Mg (II) and Al (III), raising the oxygen atoms in the converted oxide structures. Based on O 1s peak fitting the surface hydroxide fractions have been quantified using the approach proposed by McCafferty and Wightman.[30] Following fitting parameters were defined, all with a FWHM of 1.5 eV: C-C/C-H 284.7 ± 0.1 eV, C-O 286.2 ± 0.3 eV, COO^- 288.5 ± 0.4 eV and 289.5 ± 0.3 eV. The O 1s peak has been fitted using following centred peak positions: O^{2-} 529.9 ± 0.3 eV, OH^- 531.5 ± 0.2 eV and H_2O 532.6 ± 0.3 eV.

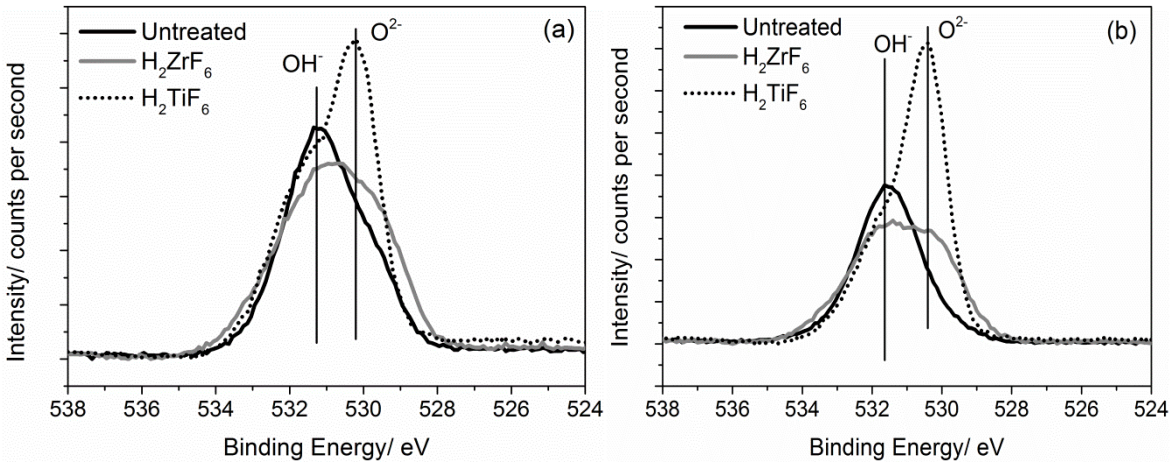

Figure 3.19: O 1s XPS peak prior and after conversion treatment of (a) GI and (b) MZ.

The resulting hydroxide fractions are presented in figure 3.20. It is apparent that the initial hydroxide fraction on MZ (77 ± 3 %) is higher compared to GI (56 ± 3%). These relatively high hydroxide fractions might originate from the alkaline cleaning step prior to conversion. Nevertheless upon conversion treatment the surface hydroxide fractions significantly decline. This trend is in line with those observed on bulk substrates and inversely correlated to the increased hydroxide fractions observed on thermally vaporized substrates. Therefore it is strongly recommended to be thoughtful when extrapolating results obtained for model systems to industrially relevant substrates. This current work proposes ATR-FTIR and XPS as two highly complementary techniques, enabling to reduce the gap between model and industrially relevant substrates.

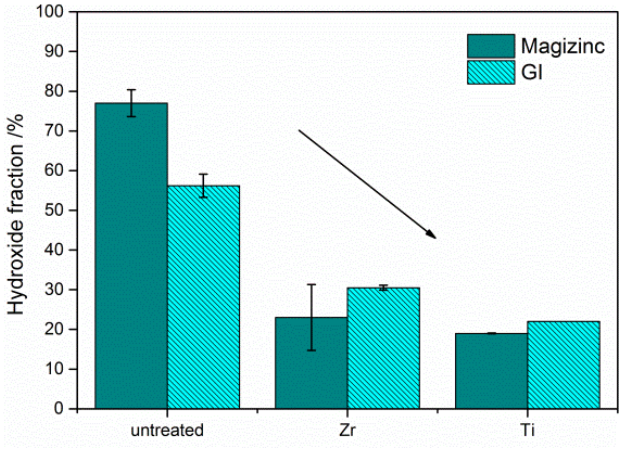

Figure 3.20: Calculated surface hydroxide fraction on GI and MZ as a function of conversion treatment.

3.3.5 Contact angle studies on the surface free energy upon conversion with organic additives

The effect of zirconium- and titanium-treatment on wettability is investigated using contact angle measurements. Figure 3.21 demonstrates measured contact angles using ultrapure water on

variously treated GI. Clearly, wetting behaviour is improved after conversion treatment, with the best performance obtained after zirconium-treatment of GI.

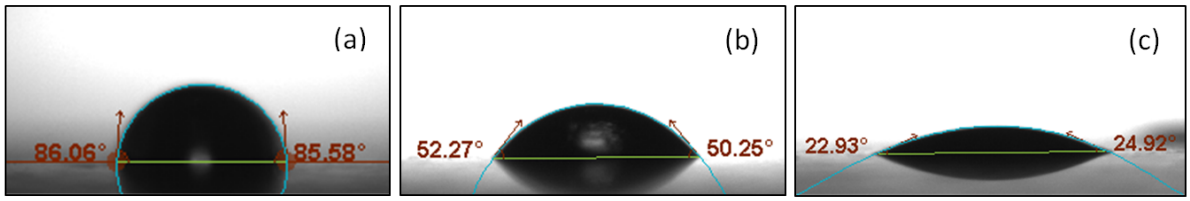

Figure 3.21: Measured contact angle of water on (a) untreated GI, (b) titanium-treated GI and (c) zirconium-treated GI.

Determination of the contact angle using minimum two liquids with known surface energy (γ_L) allow to determine the surface free energy of the metal (γ_S) and solid-liquid interfacial surface energy (γ_{SL}) using Young's equation, described in equation 3.2.

$$\gamma_s = \gamma_L cos\theta + \gamma_{SL} \qquad (3.2)$$

The cohesion between atoms and molecules, reflected in the surface free energy of a solid (and surface tension of a liquid) can be explained by different types of interfacial interactions which depend on the properties of both measured substrate and liquid. Equation 3.3 illustrates that these interfacial interactions, defined as dispersion (γ_s^d), polar (γ_s^p), hydrogen (γ_s^h), induction (γ_s^i), acid-base (γ_s^{ab}) and other remaining interfacial interactions (γ_s^0), can be considered as independent components, which sum results in the total free surface energy of a substance (γ_S).

$$\gamma_s = \gamma_s^d + \gamma_s^p + \gamma_s^h + \gamma_s^i + \gamma_s^{ab} + \gamma_s^0 \qquad (3.3)$$

Fowkes[31] investigated mainly dispersive interactions, which he related to London interactions arising from electron dipole fluctuations. Owen and Wendt[32] continued Fowkes approach, stating that all component except for dispersive components contributing to the total surface free energy can be considered polar, as stated in the OWRK equation 3.4.

$$\gamma_s = \gamma_s^p + \gamma_s^d \qquad (3.4)$$

If combined with Young's equation, given in equation 3.2, two unknown components remain, being, γ_s^d and γ_s^p. Therefore, minimum two liquids with known dispersive and polar components are required to solve equation 3.4. To calculate the contribution of polar and dispersive components to the overall surface energy, three liquids have been used to measure the contact angle, being ultrapure water (W), ethylene glycol (EG) and diiodomethane (DIM). Their surface tension (γ_L) polar forces (γ_l^p) and dispersive forces (γ_l^d) are summarized in table 3.2.

Table 3.2: Surface tension values (expressed in mN/m) of the liquids used in this study [33]

Liquid	Surface tension (γ_l),	dispersive forces (γ_l^d)	polar forces (γ_l^p)
water	72.8	21.8	51.0
Ethylene glycol	48.2	31.5	16.7
diiodomethane	50.8	50.8	0.7

Minimum 4 measurements have been conducted for each liquid, which average contact angle values and standard deviations are listed in table 3.3.

Table 3.3 Contact angle values (°) measured using water (W), ethyleneglycol (EG) and diiodomethane (DIM), and the resulting surface free energies (SFE) calculates according the OWRK method, total SFE (γ^{tot}), dispersive part of the SFE (γ^{d}) and polar part of the SFE (γ^{p}).

Substrate	W (°)	EG (°)	DIM (°)	γ^{tot} (mN/m)	γ^{d} (mN/m)	γ^{p} (mN/m)
GI	83 ± 4	61 ± 3	47 ± 5	36.7	34.4	2.2
GI Ti	43 ± 8	40 ± 8	43 ± 1	54.5	32.6	21.9
GI Ti PAA	13 ± 6	17 ± 11	33 ± 1	65.3	37.2	28.0
GI Ti PVA	48 ± 7	34 ± 4	31 ± 6	54.2	39.6	14.6
GI Ti PVP	63 ± 8	31 ± 6	39 ± 3	48.2	38.4	9.8
GI Zr	18 ± 7	31 ± 6	30 ± 11	63.0	37.7	25.3
GI Zr PAA	13 ± 2	11 ± 5	13 ± 5	67.7	43.0	24.6
GI Zr PVA	15 ± 5	19 ± 11	20 ± 4	66.2	41.3	25.0
GI Zr PVP	52 ± 13	55 ± 8	45 ± 6	46.0	31.6	14.3
MZ	89 ± 6	69 ± 2	56 ± 6	32.1	30.0	2.1
MZ Ti	47 ± 12	37 ± 8	37 ± 6	52.9	36.9	16.0
MZ Ti PAA	24 ± 2	29 ± 3	31 ± 2	61.8	37.6	24.2
MZ Ti PVA	87 ± 4	57 ± 11	45 ± 5	38.2	36.3	1.8
MZ Ti PVP	24 ± 10	32 ± 10	42 ± 9	38.1	37.1	1.0
MZ Zr	25 ± 6	36 ± 7	28 ± 5	61.0	38.3	22.8
MZ Zr PAA	47 ± 8	67 ± 15	53 ± 5	43.7	26.2	17.6
MZ Zr PVA	34 ± 4	52 ± 4	31 ± 8	54.7	35.9	18.8
MZ Zr PVP	45 ± 5	37 ± 7	33 ± 4	54.3	38.2	16.1

The resulting surface free energies obtained using the OWRK method of zirconium-treated GI and MZ substrates are presented in figure 3.22. The total surface free energy (γ^{tot}) includes both dispersive (γ^{d}) and polar contributions (γ^{p}). The former reflects van der Waals and London interactions, whereas the latter represents acid-base and hydrogen interactions.[31,32] The calculated surface free energies of zirconium-treated GI and MZ are given in figure 3.22 (a) and (b), whereas those of titanium-treated GI and MZ are given in figure 3.22 (c) and (d), respectively. It is evidenced that the polar forces (2.2 and 2.1 mN/m for untreated GI and MZ) increase with a factor ten upon zirconium- (25.3 and 22.8 mN/m) and titanium-treatment (21.9 and 16.0 mN/m). Furthermore, it can be seen that dispersive forces (35.0 ± 3.3 mN/m) remain more or less equal upon the various conversion treatments. The

significant increase in polar forces is associated with the high valence number of Zr(IV) and Ti(IV) increasing the surface oxide polarizing power and thus its chemical activity.[34] The polymeric compounds added to the zirconium-based conversion solution do not greatly alter the polar surface forces. Contrary, the addition of PAA to titanium-based conversion solution increases the polar forces, whereas PVA and PVP additions significantly reduce the chemical polarity. GI and MZ can thus be considered as equivalent in terms of surface free energy.

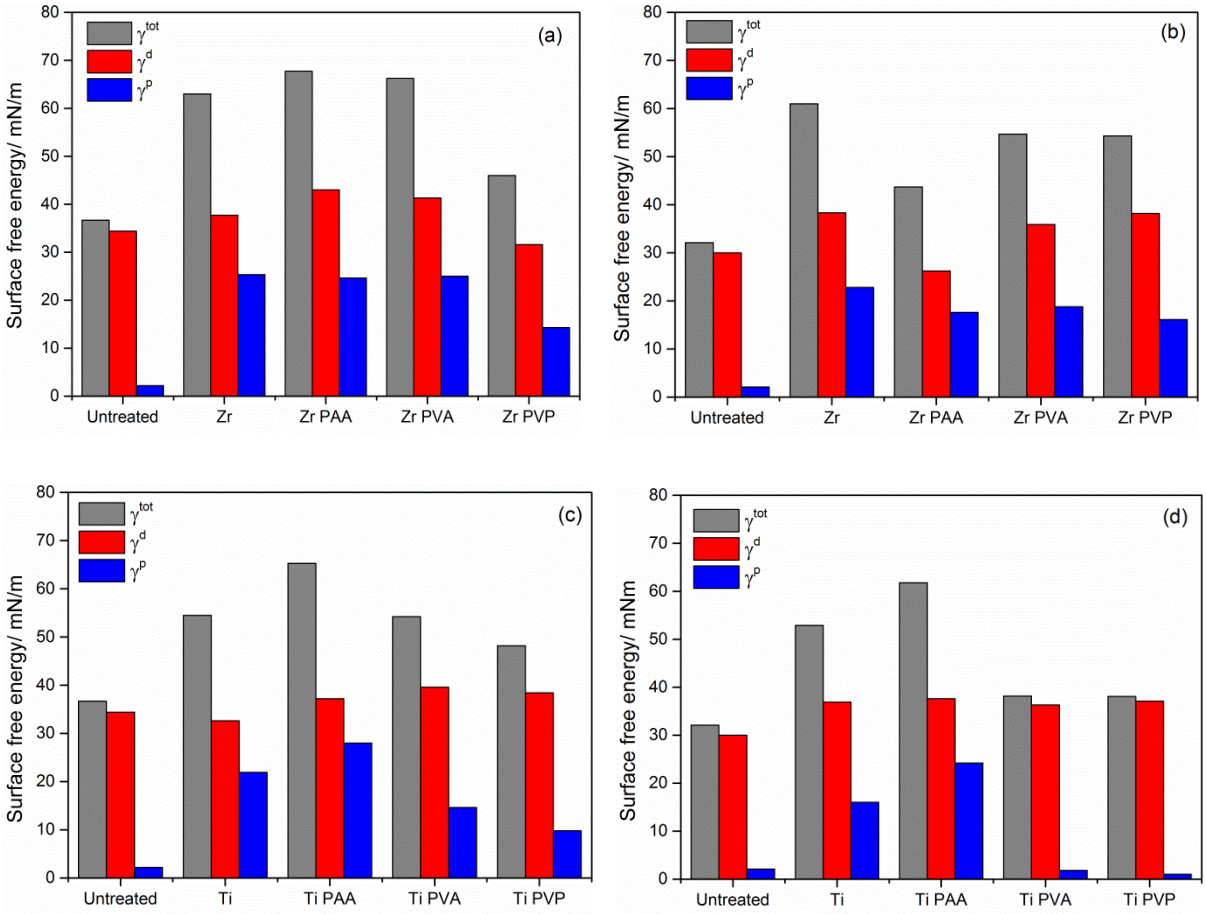

Figure 3.22: Surface free energies of (a) zirconium-treated GI, (b) zirconium-treated MZ, (c) titanium-treated GI and (d) titanium-treated MZ.

It is suggested that the limited impact of organic additives on the surface free energy of zirconium-treated GI relates to the tendency of zirconium to precipitate as an amorphous oxyhydroxide inducing crosslinking reactions with the polymeric compounds.[35] This is expected to result in entanglement of the additives within the zirconium oxide layer.[36,37] On the other hand, titanium oxide is thermodynamically stable in a crystalline oxide structure and does not show these crosslinking capacities.[38] As a result, separated layers of titanium oxide covered by a polymeric films are expected, which may explain the higher impact of organic compounds on the surface free energy of titanium-treated GI. The considerable reduction of surface free energy in the case of PVA and PVP

additions to the titanium-treatment suggest that the polar groups of these polymer chains are oriented towards the titanium oxide, whereas the carbon backbone is orientated towards the outer surface reducing the polar surface forces.

The proposed oxide structures are given in figure 3.23. Although the crosslinking capacities of zirconium, as well as the different nature of precipitation products when comparing zirconium- and titanium oxide have been frequently reported.[35–38] Experimental validation of the entanglement of organic additives in the conversion oxide structures is highly challenging. This because the precipitated oxide layers are rather thin (25-50 nm). Dominating mixing effects during depth profiling might induce preferential sputtering, which affects the shape of the depth profile.[39] Therefore, acquired sputter profiles will be hard to interpret which is further complicated by the coexistence of carbon signal associated to ambient contamination.[12,39] Especially, small fatty acids strongly adsorb to metal oxide surfaces upon immediate contact to atmospheric environment, which hinders unambiguous assignment of carbon signal to the respective organic additives.[40,41]

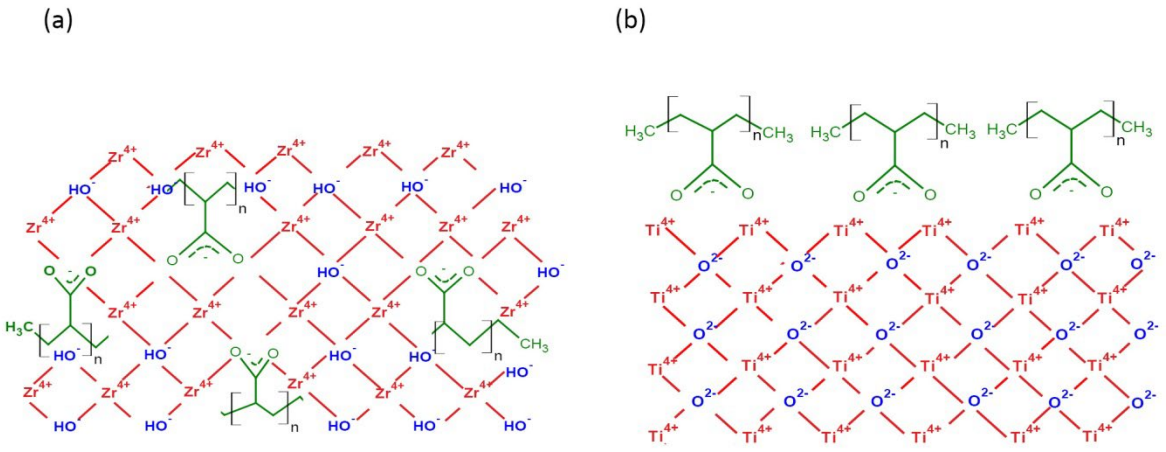

Figure 3.23: Proposed conversion oxide structures containg PAA as organic additive, (a) PAA crosslinked in amorphous zirconium-oxide strucure, (b) PAA as covering layer on top of crystaline titanium oxide structure.

3.4 Conclusions

The integrated ATR-FTIR – EC setup allowed for the in-situ evaluation of precipitation kinetics of phosphates, fluorides and hydroxides and zirconium oxide. The multi-metal approach, studying pure aluminium, zinc and magnesium substrates, evidenced increased conversion kinetics in the following order aluminium < zinc < magnesium. The lower activity on aluminium substrates was attributed to its protective native oxide layer at the conversion conditions used (pH 4). Consequently, despite its high sensitivity for water, ATR-FTIR was shown to be a highly valuable tool for in-situ conversion

studies. In addition, simultaneously obtained OCP informed on the protective nature of the converted oxide layer, as a lower conductive oxide properties shifts the OCP to more positive values indicative for a protective film formation.

The conversion kinetics obtained by in-situ ATR-FTIR studies of thermally vaporized multi-metal substrates were in accordance with those obtained by ex-situ XPS and AES studies on polished metal sheets. The latter confirmed that zirconium oxide precipitation is most effective on magnesium, forming a zirconium oxide layer approximately 10 times thicker than zinc, whereas the zirconium oxide precipitation on aluminium is very slow and can be considered as not fully covering the metal oxide. However, a striking difference was noted between surface hydroxide fractions, when comparing thermally vaporized model substrates with polished bulk substrates. Both ATR-FTIR and XPS analysis evidenced obvious surface hydroxylation in the case of thermally vaporized multi-metal substrates, whereas polished multi-metal sheets were shown to dehydroxylate upon conversion treatment. This was observed for zinc, aluminium and magnesium sheets, as well as for GI and MZ and this both upon zirconium- and titanium-treatment. Different hydroxide equilibria for model and industrially relevant substrates were attributed to the different nature of the native oxides and thus their different activity in the respective conversion solution.

Further characterization of zirconium- and titanium-treated GI and MZ substrates demonstrated a significant increase of surface free energy upon conversion. This was attributed to altered polar forces, which increased by a factor ten upon conversion treatment. The addition of organic additives to zirconium-treatment did not further affect the surface energy. However, when these organic additives were added to the titanium-treatment, the surface free energy was shown to slightly increase in the case of PAA, and a severe reduction of surface free energy was noted in the case of PVP and PVA. This was the case on both GI and MZ. Consequently, converted GI and MZ are considered to be equivalent in terms of surface free energy. The limited impact of organic additives on the surface free energy of zirconium-treated substrates was associated to its crosslinking capacities resulting in an entanglement of the polymeric compounds in the zirconium oxide structure. On the other hand, titanium does not possesses these crosslinking capacities, which means that the polymeric compounds form an additional layer on top of the titanium oxide layer, explaining its higher impact on the surface free energy.

References

(1) Cerezo, J.; Vandendael, I.; Posner, R.; Lill, K.; de Wit, J. H. W.; Mol, J. M. C.; Terryn, H. Initiation and Growth of Modified Zr-Based Conversion Coatings on Multi-Metal Surfaces. *Surf. Coatings Technol.* **2013**, *236*, 284–289.

(2) Nordlien, J. H.; Walmsley, J. C.; Østerberg, H.; Nisancioglu, K. Formation of a Zirconium-Titanium Based Conversion Layer on AA 6060 Aluminium. *Surf. Coatings Technol.* **2002**, *153* (1), 72–78.

(3) Taheri, P.; Lill, K.; De Wit, J. H. W.; Mol, J. M. C.; Terryn, H. Effects of Zinc Surface Acid-Based Properties on Formation Mechanisms and Interfacial Bonding Properties of Zirconium-Based Conversion Layers. *J. Phys. Chem. C* **2012**, *116* (15), 8426–8436.

(4) Lostak, T.; Maljusch, A.; Klink, B.; Krebs, S.; Kimpel, M.; Flock, J.; Schulz, S.; Schuhmann, W. Zr-Based Conversion Layer on Zn-Al-Mg Alloy Coated Steel Sheets: Insights into the Formation Mechanism. *Electrochim. Acta* **2014**, *137*, 65–74.

(5) Verdier, S.; van der Laak, N.; Dalard, F.; Metson, J.; Delalande, S. An Electrochemical and SEM Study of the Mechanism of Formation, Morphology, and Composition of Titanium or Zirconium Fluoride-Based Coatings. *Surf. Coatings Technol.* **2006**, *200* (9), 2955–2964.

(6) Andreatta, F.; Turco, a.; de Graeve, I.; Terryn, H.; de Wit, J. H. W.; Fedrizzi, L. SKPFM and SEM Study of the Deposition Mechanism of Zr/Ti Based Pre-Treatment on AA6016 Aluminum Alloy. *Surf. Coatings Technol.* **2007**, *201* (18), 7668–7685.

(7) Taheri, P.; Laha, P.; Terryn, H.; Mol, J. M. C. An in Situ Study of Zirconium-Based Conversion Treatment on Zinc Surfaces. *Appl. Surf. Sci.* **2015**, *356*, 837–843.

(8) Cerezo, J.; Taheri, P.; Vandendael, I.; Posner, R.; Lill, K.; de Wit, J. H. W.; Mol, J. M. C.; Terryn, H. Influence of Surface Hydroxyls on the Formation of Zr-Based Conversion Coatings on AA6014 Aluminum Alloy. *Surf. Coatings Technol.* **2014**, *254*, 277–283.

(9) Öhman, M.; Persson, D.; Jacobsson, D. In Situ Studies of Conversion Coated Zinc / Polymer Surfaces during Exposure to Corrosive Conditions. *Prog. Org. Coatings* **2011**, *70*, 16–22.

(10) Fink, N.; Wilson, B.; Grundmeier, G. Formation of Ultra-Thin Amorphous Conversion Films on Zinc Alloy Coatings: Part 1. Composition and Reactivity of Native Oxides on ZnAl (0.05%) Coatings. *Electrochim. Acta* **2006**, *51* (14), 2956–2963.

(11) Veisfeld, N.; Geller, J. D. Ion Sputtering Yield Measurements for Submicrometer Thin Films. *J. Vac. Sci. Technol. A* **1988**, *6* (3), 2077–2081.

(12) Baer, D. R. et al. Comparison of the Sputter Rates of Oxide Films Relative to the Sputter Rate of SiO2. *J. Vac. Sci. Technol. A Vacuum, Surfaces, Film.* **2010**, *28* (5), 1060.

(13) Haynes, W. M. Physical Constants of Inorganic Compounds List of Abbreviations. *CRC Handb.*

Chem. physics, 94th Ed. **2013**, *94*, 4.43-4.101.

(14) Efimov, A. M. IR Fundamental Spectra and Structure of Pyrophosphate Glasses along the 2ZnO·P2O5–2Me2O·P2O5 Join (Me: Na and Li). *J. Non. Cryst. Solids* **1997**, *209* (3), 209–226.

(15) Yaguchi, M.; Uchida, T.; Motobayashi, K.; Osawa, M. Speciation of Adsorbed Phosphate at Gold Electrodes: A Combined Surface-Enhanced Infrared Absorption Spectroscopy and DFT Study. *J. Phys. Chem. Lett.* **2016**, *7* (16), 3097–3102.

(16) Ahern, A. M.; Schwartz, P. R.; Shaffer, L. A. Characterization of Conversion-Coated Aluminum Using Fourir Transform Infrared and Raman Spectroscopies. *Appl. Spectrosc.* **1992**, *46* (9), 1412–1419.

(17) Guan, Y.; Liu, J.; Yan, C. Novel Ti/Zr Based Non-Chromium Chemical Conversion Coating for the Corrosion Protection of Electrogalvanized Steel. *Int. J. Electrochem. Sci.* **2011**, *6*, 4853–4867.

(18) Fernandez Lopez, E.; Sanchez Escribano, V.; Panizza, M.; Carnasciali, M. M.; Busca, G. Vibrational and Electronic Spectroscopic Properties of Zirconia Powders. *J. Mater. Chem.* **2001**, *11* (7), 1891–1897.

(19) Chinchamalatpure, V. R.; Chore, S. M.; Patil, S. S. Synthesis and Electrical Characterization of ZrO 2 Thin Films on Si (100). *J. Mod. Phys.* **2012**, *2012* (January), 69–73.

(20) Hanna, R. Infrared Properties of Magnesium Oxide. *J. Am. Ceram. Soc.* **1965**, *48* (7), 376–380.

(21) Kosmulski, M. Isoelectric Points and Points of Zero Charge of Metal (Hydr) Oxides : 50 Years after Parks ' Review. *Adv. Colloid Interface Sci.* **2016**, *238*, 1–61.

(22) Powell, C. J.; Jablonski, A.; Tilinin, I. S.; Tanuma, S.; Penn, D. R. Surface Sensitivity of X-Ray Photoelectron Spectroscopy. *J. Electron Spectros. Relat. Phenomena* **1999**, *98–99*, 1–15.

(23) Bond, A. M.; Hefter, G. T. *Critical Survey of Stability Constants and Related Thermodynamic Data of Fluoride Complexes in Aqueous Solution*; Oxford; New York: Pergamon Press, 1980.

(24) Abrahami, S. T.; Hauffman, T.; De Kok, J. M. M.; Mol, J. M. C.; Terryn, H. XPS Analysis of the Surface Chemistry and Interfacial Bonding of Barrier-Type Cr(VI)-Free Anodic Oxides. *J. Phys. Chem. C* **2015**, *119* (34), 19967–19975.

(25) McCafferty, E.; Wightman, J. P. Determination of the Concentration of Surface Hydroxyl Groups on Metal Oxide Films by a Quantitative XPS Method. *Surf. Interface Anal.* **1998**, *26* (8), 549–564.

(26) Lunder, O.; Simensen, C.; Yu, Y.; Nisancioglu, K. Formation and Characterisation of Ti-Zr Based Conversion Layers on AA6060 Aluminium. *Surf. Coatings Technol.* **2004**, *184* (2–3), 278–290.

(27) Fockaert, L. I.; Taheri, P.; Abrahami, S. T.; Boelen, B.; Terryn, H.; Mol, J. M. C. Zirconium-Based Conversion Film Formation on Zinc, Aluminium and Magnesium Oxides and Their Interactions with Functionalized Molecules. *Appl. Surf. Sci.* **2017**, *423*, 817–828.

(28) Wagner, C. D.; Raymond, R. H.; Gale, L. H. Empirical Atomic Sensitivity Factors for Quantitative

Analysis by Electron Spectroscopy for Chemical Analysis. *Surf. Interface Anal.* **1981**, *3* (5), 211–225.

(29) Smith, G. C. Evaluation of a Simple Correction for the Hydrocarbon Contamination Layer in Quantitative Surface Analysis by XPS. *J. Electron Spectros. Relat. Phenomena* **2005**, *148*, 21–28.

(30) McCafferty, E.; Wightman, J. P. Determination of the Acid Base Properties of Metal Oxide Films and of Polymers by Contact Angle Measurements. *J. Adhes. Sci. Technol.* **2000**, *13* (12), 149–170.

(31) Fowkes, F. M. Attractive Forces at Interfaces. *Ind. Eng. Chem.* **1964**, *5*, 40–52.

(32) Owens, D. K.; Wendt, R. C. Estimation of the Surface Free Energy of Polymers. *J. Appl. Polym. Sci.* **1969**, *13*, 1741–1747.

(33) Janczuk, B.; Wojcik, W.; Zdziennicka, A. Determination of the Components of the Surface Tension of Some Liquids from Interfacial Liquid-Liquid Tension Measurements. *J. Colloid Interface Sci.* **1993**, *157*, 384–393.

(34) Assi, H.; Mouchaham, G.; Steunou, N.; Devic, T.; Serre, C. Titanium Coordination Compounds : From Discrete Metal Complexes to Metal – Organic Frameworks. *Chem. Soc. Rev.* **2017**, *46*, 3431–3452.

(35) Brown, P. L.; Curti, E.; Grambow, B.; Ekberg, C. Chemical Thermodynamics of Zirconium. **2008**, 1–512.

(36) Verdier, S.; Delalande, S.; Van Der Laak, N.; Metson, J.; Dalard, F. Monochromatized X-Ray Photoelectron Spectroscopy of the AM60 Magnesium Alloy Surface after Treatments in Fluoride-Based Ti and Zr Solutions. *Surf. Interface Anal.* **2005**, *37* (5), 509–516.

(37) Deck, P. D.; Moon, M.; Sujdak, R. J. Investigation of Fluoacid Based Conversion Coatings on Aluminum. *Prog. Org. Coatings* **1998**, *34*, 39–48.

(38) Jolivet, J.; Henry, M.; Livage, J.; Bescher, E. *Metal Oxide Chemistry and Synthesis - From Solution to Solid State*, 3th editio.; John Wiley & Sons, Inc, 2000.

(39) Hofmann, S.; Zhou, G.; Kovac, J.; Drev, S.; Lian, S. Y.; Lin, B.; Liu, Y.; Wang, J. Y. Preferential Sputtering Effects in Depth Profiling of Multilayers with SIMS, XPS and AES. *Appl. Surf. Sci.* **2019**, *483* (November 2018), 140–155.

(40) Deacon, G. B.; Huber, F.; Phillips, R. J. Diagnosis of the Nature of Carboxylate Coordination from the Direction of Shifts of Carbon-Oxygen Stretching Frequencies. *Inorganica Chim. Acta* **1985**, *104*, 41–45.

(41) Deacon, G. B.; Phillips, R. J. Relationships Between the Carbon-Oxygen Stretching Frequencies of Carboxylato Complexes and the Type of Carboxylate Coordination. *Rev. Chem.* **1980**, *33*, 227–250.

Chapter 4 : Molecule interactions

Polyester/polyurethane resins are widely applied in can and coil coating, packaging, automotive paints and industrial paints. Yet their multicomponent properties hinder straightforward insights in interfacial metal-polymer interactions. Therefore, this chapter is dedicated to unravelling chemisorption mechanisms of functionalized model molecules. Carboxylic acids, esters and amides have been selected based on the functionalities occurring in paint resins which are held responsible for chemical interactions with the metal substrate. Combining XPS and ATR-FTIR, it was shown that multiple interactions are taking place at the interface, for which the oxide's acid-base properties have a determining role. Furthermore, it was shown that zirconium-treatment increases the acidic character of metal oxides, thereby altering the ratio of competing interfacial reaction mechanisms.

4.1 Introduction

Coil coated galvanized steel is frequently used in outdoor applications, mainly in the building sector for roof and cladding purposes. For durable use a high resistance against dry, wet and corrosive paint delamination is desired. As introduced in chapter 3, there is an industrial need to understand the effect of zirconium-treatments on paint adhesion. However, difficulties in studying chemisorption mechanisms at paint-metal interfaces are associated to the high absorptive character of both paint and metal substrate resulting in a buried interface.[1] Moreover, complex multicomponent paint formulations hinder a straightforward interpretation of interfacial chemisorption mechanisms of the industrial paint/engineering metal system. Therefore, to gain fundamental insights in metal-polymer interactions, it is crucial to simplify the polymer chemistry.[1] One way to elucidate molecular interactions at the polymer-metal interface is by mimicking the functional groups in polymer coatings using monomer molecules.[2–4] In the case of industrially relevant polyester polyurethane resins, which are frequently used for coil coating, ester- and amide-functional groups are held responsible for chemisorption at the metal oxide surface. In addition, because these polyester polyurethane resins are commonly synthesised in-situ, a portion of unreacted carboxylic acid groups remains present in the paint formulation. The chemisorption of carboxylic acids on aluminium[5–8], zinc[9–11] and zirconium oxide[12,13] surfaces have extensively been studied. As a result it is widely accepted that carboxylic acids form metal carboxylate complexes upon deprotonation. Furthermore, it has been evidenced that surface hydroxide groups were involved in the chemisorption mechanism.[6,10,14] Because of this increased bonding properties were demonstrated for zirconium-treated zinc substrates, which were shown to have higher hydroxide fractions than native zinc oxide.[14] Altered surface hydroxide fractions are also reported for zirconium-treated aluminium substrates.[15] However, detailed chemisorption studies on zirconium-treated aluminium substrates have not yet been reported. Also the literature on chemisorption of carboxylic acids on native magnesium oxides is highly limited[16–18] and non-existing in case of zirconium-treated magnesium oxide. The reason for this lack of literature regarding magnesium carboxylate interactions might relate to the ionic nature of magnesium carboxylate complexes, which are typically weaker compared to metal carboxylate bonds with a higher covalent character.[16] Moreover, the high activity of magnesium in aqueous environment is considered to be problematic for stable magnesium-carboxylate bond formation in aqueous media. Section 4.3.1 aims to describe the in-situ chemisorption of carboxylic acid on magnesium oxide in aqueous media and the stability of the resulting carboxylate complexes. Section, 4.3.2, concerns, the chemisorption of ester-functionalized compounds on native as well as zirconium-treated aluminium, zinc and magnesium oxide. The main research question in this regard is the catalytic nature of the respective oxides to induce bond cleavage of the ester-group forming the more reactive carboxylic

acid. Finally, section 4.3.3 describes chemisorption of amide-functionalized molecules on native and zirconium-treated aluminium, zinc and magnesium oxide. It is known that amide-functionalities are stable because the electrophilicity of the amide oxygen is reduced by nitrogen sharing his free electron pair. Gaining more fundamental knowledge on their chemisorption mechanisms allows to optimize the conditions for maximum chemisorption.

4.2 Experimental

4.2.1 Materials and chemicals

4.2.1.1 Carboxylic acid study

Carboxylic acid solutions containing 0.05 M 2,5-pyridinedicarboxylic acid (>98%, Sigma-Aldrich Chemie GmbH),3-methylsalicylic acid (99%, Sigma-Aldrich Chemie GmbH), sodium salicylate (> 99.5 %, Sigma-Aldrich Chemie GmbH) and fumaric acid (98%, Alfa Aesar) were prepared in demineralized water. The pH of the inhibitor solutions was adjusted to pH 7 +/- 0.3 using 1 M NaOH. Magnesium films with a thickness of approximately 20 nm were thermally vaporized (PVD) on germanium internal reflection elements (PIKE Technologies, 60°) by means of a high-vacuum evaporation system (VCM 600 Standard Vacuum Thermal Evaporator, Norm Electronics). The source material for the PVD substrates was resublimed pure Mg (a by-product during Mg sintering process), which composition is shown in table 4.1. The high purity of the magnesium source used together with the low melting point of magnesium compared to the impurities present in the source material are expected to result in magnesium films with a level of impurities significantly lower than that in the source material.

Table 4.1: Elemental composition of high purity magnesium used in this work as a source of PVD.

Element	**Al**	**Ca**	**Cu**	**Be**	**Fe**	**Mn**	**Ni**	**Si**	**Zn**	**Zr**	**Mg**
Impurity level, ppm	<100	14	5	0.2	12	73	10	7	21	25	99,97%

4.2.1.2 Ester study

50 nm zinc (Goodfellow, 99.95%), aluminium (Johnson Matthey, 99.99%) and magnesium (Alfa Aesar, 99.9%) were deposited on germanium internal reflection elements (IRE) by means of a high-vacuum evaporation system (VCM 600 Standard Vacuum Thermal Evaporator, Norm Electronics). Zirconium-based conversion was conducted using hexafluorozirconic acid (Sigma-Aldrich Chemistry) diluted to 0.01 M and brought to pH 4 with 0.1 M NaOH. The metallic coated IREs were dipped in conversion solution at room temperature for 90 seconds, where after the samples were generously rinsed with demineralized water and dried with pressurized air. Monomer studies were performed using 0.1 wt%

dimethylsuccinate (Sigma-Aldrich Chemistry) dissolved in tetrahydrofuran (THF). The metal substrates were placed in solution for 30 minutes, dried in air and measured with ATR-FTIR before (combination physisorbed and chemisorbed dimethylsuccinate) and after rinsing with pure THF (mainly chemisorbed dimethylsuccinate).

4.2.1.3 Amide study

For the ex-situ XPS measurements 1.0 mm thick metal sheets (zinc foil: Goodfellow, 99.95% - aluminium foil: Goodfellow, 99.999% - magnesium foil: Alfa Aesar, 99.9%) were polished to 1µm diamond paste grade. Subsequently, the samples were generously rinsed with aceton and ultrasonically cleaned with ethanol for 15 min. For the *in-situ* study, metal films (20nm) were deposited on a germanium internal reflection element (PIKE Technologies, 60°) by means of a high-vacuum Balzers BAE 250 evaporation system. Hexafluorozirconic acid solution with a low phosphate contribution (MAVOM, CC1742) was diluted to 20 g/L and brought to pH 4 with 0.1M NaOH. The conversion was conducted at room temperature for 90 seconds, where after the samples were generously rinsed with demineralized water and dried with pressed air. Interfacial molecular interactions were studied using N,N'-dimethylsuccinamide (Sigma-Aldrich Chemistry). The metal substrates were placed in THF solution containing 0.1 wt% N,N'-dimethylsuccinamide molecules. After 30 minutes, the metal substrates were abundantly rinsed with pure tetrahydrofuran (THF) solution, in order to remove non-adsorbed molecules.

4.2.2 Techniques

4.2.2.1 Attenuated total reflection – Fourier transform infrared spectroscopy (ATR-FTIR) in Kretschmann configuration

The FTIR apparatus was a Thermo-Nicolet Nexus equipped with a liquid-nitrogen cooled mercury-cadmium-telluride (MCT-A) detector and a nitrogen-purged measurement chamber with a Veemax III single reflection ATR accessory. Germanium internal reflection elements (PIKE Technologies) were used with a fixed face angle of 60 degrees. IR-light was configured with an incident set angle of 80 degrees. A precision manual polarizer (PIKE) was mounted on the Veemax III and set to 90° for p-polarized and 0° for s-polarized IR-light. The control of the spectra acquisition and incident angles was managed by the OMNIC 8.1 software package (ThermoElectron Corporation, Madison, WI).

Prior to the in-situ chemisorption study of carboxylic acids, infrared backgrounds were obtained of magnesium coated germanium internal reflection elements immersed in demineralized water. Subsequently, demineralized water was quickly replaced by the inhibitor-containing solution for in-situ ATR-FTIR measurements. Infrared spectra were collected every 3 seconds and averaged from 16 cycles with a resolution of 4 cm^{-1}. For the amide-and ester chemisorption studies infrared

backgrounds were obtained from the metallic coated IREs, after zirconium-based treatment when applicable. Infrared spectra were averaged from 128 cycles with a resolution of 4 cm^{-1}.

4.2.2.2 Density functional theory (DFT) computations

DFT computations were performed using the plane-wave code Vienna Ab Initio Simulation Package (VASP)[19–22] with the projector augmented wave (PAW) method. As van der Waals (vdW) interactions may have a significant impact on the adsorption energies of organic molecules[23], the exchange-correlation (XC) functional optB88-vdW[24–27] was employed for all DFT calculations in this study. This functional, which belongs to the group of van der Waals density functionals (vdW-DF), accounts for dispersion interactions by including a non-local correlation part in the exchange-correlation energy instead of using external input parameters. Still, some approximations are assumed, such as that the vdW interactions are considered to be pairwise additive. By optimizing the correlation part of the original vdW-DF by Langreth, Lundqvist and colleagues[28], Klimeš et al. introduced the "opt" functionals[24,25], which have been successfully applied to numerous systems[29–36]. Particularly, the optB88-vdW functional is considered to represent well the subtle energetic contributions of weak interactions in the adsorption of organic molecules.[37–39]

All computations were performed using a 4×4×1 Γ-centered grid of *k*-points.[40] The plane-wave expansion was limited by a cutoff energy of 520 eV. During the relaxation process, the atomic positions were allowed to adjust until the Hellmann–Feynman forces were less than 5 meV $Å^{-1}$. For the relaxation process, the systems were pre-converged using the conjugate gradient algorithm; subsequently a quasi-Newton algorithm was employed, which is efficient close to a minimum. In a third computation step, the structure was investigated statically to obtain more accurate total energies via the tetrahedron method with Blöchl corrections[41].

The MgO/$Mg(OH)_2$ interface was modeled using a slab of five MgO(100) layers in a 2×2 surface cell. With respect to the number of carboxyl groups within the adsorbed inhibitor molecules, hydrogen atoms were co-adsorbed accordingly on the oxygen sites of the MgO(100) surface, resulting in a partially hydroxylated surface – representing the start of the passivation layer formation – and leaving the deprotonated inhibitor molecule to adsorb. Atoms in the two bottom layers were kept fixed in their bulk-like positions, whereas the remaining layers were free to relax, thus being able to respond to occurring forces due to adsorption or surface effects. A vacuum region of around 20 Å was added above the surface slab in order to avoid interaction between periodic images.[42] A dipole correction was applied to compensate for slab asymmetry.[43,44] The binding energies E_{B} of the adsorbed inhibitor molecules on the partially hydroxylated MgO(100) surface were determined as

the difference between total energies of the educts, $E_{\mathrm{adsorbate,gas}}$ and $E_{\mathrm{substrate}}$, as well as the total energy of the product, $E_{\mathrm{subs+ads}}$:

$$E_{\mathrm{B}} = E_{\mathrm{adsorbate,gas}} + E_{\mathrm{substrate}} - E_{\mathrm{subs+ads}}$$

Hence, for $E_B > 0$ the corresponding adsorption structure is energetically favorable and vice versa, assuming negative total energies.

4.2.2.3 X-ray photo-electron spectroscopy (XPS)

High-resolution XPS spectra of chemisorbed amide-functionalized molecules were collected using a PHI5600 photoelectron spectrometer (Physical Electronics) with an Al Kα monochromatic X-ray source (1486.71 eV of photons). The vacuum in the analysis chamber was approximately 9×10^{-9} Torr during measurements. High-resolution scans of the N 1s XPS peaks were recorded from a spot diameter of 0.8 mm using pass energy of 23.5 eV and step size 0.1 eV. Measurements were performed with take-off angles of 45° with respect to the sample surface.

XPS measurements of chemisorbed ester-functionalized molecules were done with a PHI-5000 Versaprobe II (Physical Electronics) utilizing an Al Kα monochromatic X-ray source (1486.71 eV photon energy) with a spot diameter of 100 μm to measure surface compositions up to ca. 10 nm in depth. The irradiation power of the X-ray beam was 25 W. The kinetic energy of the photoelectrons was measured with a take-off angle of 45°. The vacuum in the analysis chamber was better than 1 x 10^{-9} Torr. Survey scans were recorded with a pass energy of 187.85 eV and energy step size of 0.1 eV. High resolution scans of O 1s and C 1s peaks were obtained with a pass energy of 23.5 eV and 0.05 eV energy step size. Dual beam charge neutralization was utilized to compensate potential charging effects.

The XPS data of both chemisorbed amide- and ester-functionalized molecules was analyzed with PHI Multipak software (V9.5 and V9.8, respectively). The reproducibility was verified by triplication of the measurements. Before curve fitting, the energy scale of the XPS spectra was calibrated relative to the binding energy of adventitious hydrocarbons (C C/C H) in the C 1 s peak at 284.8 eV. The peak shape is a mixed Gaussian-Lorentzian, with a Shirley type background.

4.3 Results

4.3.1 Carboxylic acids

4.3.1.1 In-situ ATR-FTIR kinetic study of magnesium in demineralized water without organic inhibitors

Figure 4.1 presents the dynamic behaviour of magnesium in demineralized water without organic compounds. Broad bands at 3378 and 1670 cm^{-1}, specific to O-H stretching and bending modes illustrate the hydration of the surface during immersion in water. Furthermore, the higher wavenumber region is characterized by a sharp negative peak at 3700 cm^{-1} attributed to brucite, $Mg(OH)_2$.[45] The sharpness of this characteristic peak relates to the absence of hydrogen bonds in this compound[46], whereas its negative intensity relative to the background (collected prior to immersion) relates to the conversion of brucite into species of which the hydroxide ions are involved in hydrogen bonds.[46] Meanwhile, additional vibrational bands appear at 1176 and 860 cm^{-1} consistent with the deformation of H_2O or OH^-.[47] Although all aqueous solutions are initially neutral, anodic dissolution reactions accompanied with cathodic oxygen reduction reactions generating hydroxide anions thereby locally increasing the pH to 10.5.[48] Due to this instant local pH increase, rapid formation of $Mg(OH)_2$ is expected within seconds upon adding an aqueous electrolyte.[48] In addition to the formation of a hydroxylation layer, two new peaks at 1382 and 1530 cm^{-1} arise upon prolonged immersion in demineralised water. The growth of these peaks is assigned to the formation of magnesium carbonate complexes originating from the presence of ambient CO_2 dissolved in the aqueous solution.[45] In figure 4.1 (b) the quantified peak areas of the Mg-OH peak at 1176 cm^{-1} and the summed peak area of the carbonate peaks positioned at 1530 and 1382 cm^{-1} are plotted as a function of immersion time. From these plots it is seen that native magnesium oxide rapidly hydroxylates upon immersion in demineralized water, reaching their maximum intensity after 1.2 minutes, where after they decline again. Meanwhile carbonate peaks assigned to magnesium carbonate complexes are being formed. However, their reducing peak intensities upon prolonged submersion illustrate that neither the magnesium hydroxide layer, nor the magnesium carbonate layer are stable in the aqueous environment. The poor stability of hydroxide layers formed during immersion of magnesium in neutral aqueous environment has been reported previously.[49]

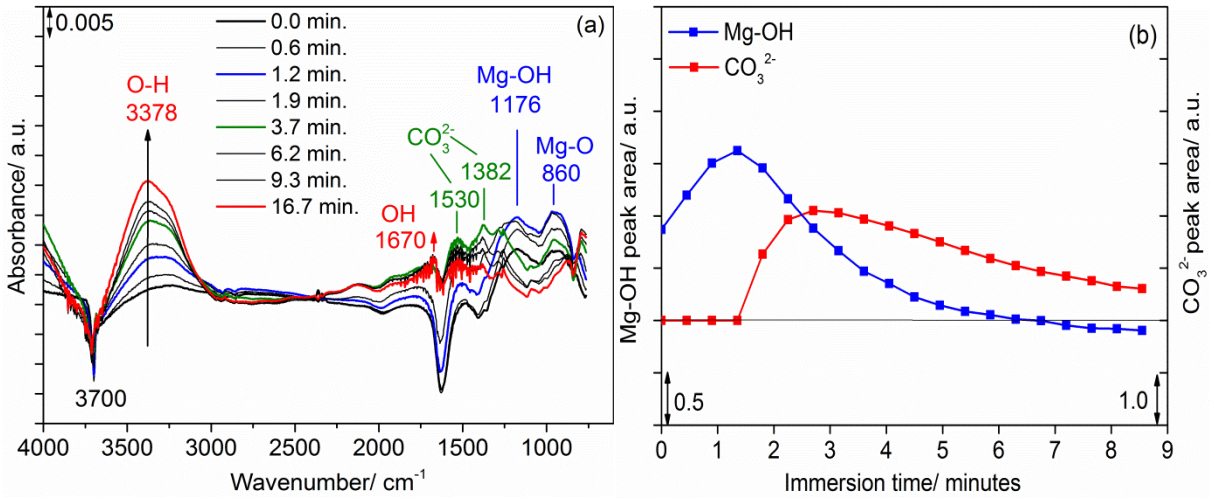

Figure 4.1: (a) in-situ ATR-FTIR spectra of magnesium exposed to demineralized water, (b) quantified Mg-OH and CO_3^{2-} peak areas as a function of immersion time.

4.3.1.2 In situ ATR-FTIR adsorption study of carboxylic corrosion inhibitors on magnesium

In situ ATR-FTIR measurements of magnesium during immersion in aqueous solution without organic inhibitors elucidated the occurrence of two phenomena at the magnesium surface, being surface hydroxylation and carbonation processes. To further investigate the effect of carboxylic acids in the aqueous solution, in-situ ATR-FTIR measurements have been performed using p- and s-polarized IR-light. The use of p-polarized light (90°) probes molecular vibrations with their transition dipole moment perpendicular to the surface, whereas s-polarized light (0°) probes molecular vibrations with their transition dipole moment in plane with the surface.

In-situ ATR-FTIR spectra of 2,5-pyridinedicarboxylate, 3-methylsalicylate and sodium salicylate obtained using p-polarized IR-light are shown in figure 4.2 (a-c) respectively. Spectral features are limited to negative bands characteristic for species present in the background. Therefore, chemisorption of these aromatic compounds could not be monitored using p-polarized IR-light. On the other hand, fumarate, presented in figure 4.2 (d), clearly demonstrates two distinct peaks positioned at 1570 and 1366 cm^{-1} attributed to asymmetric and symmetric carboxylate bonds respectively. The separation of both peaks by 181 cm^{-1} suggests a bridging bidentate carboxylate coordination. Additionally, their high sensitivity for p-polarized IR-light indicates that carboxylate bonds are highly oriented perpendicular to the magnesium oxide surface.

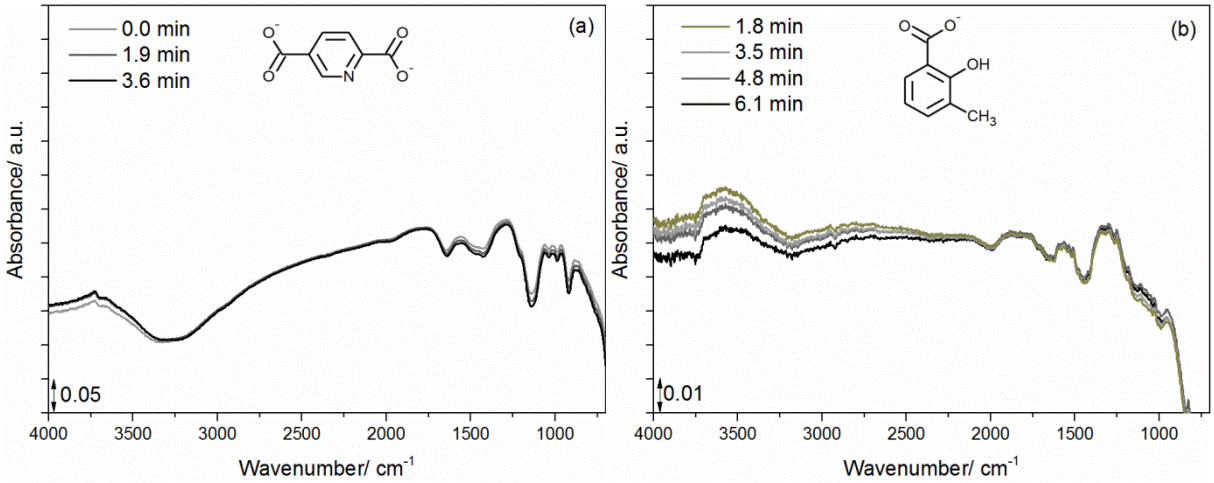

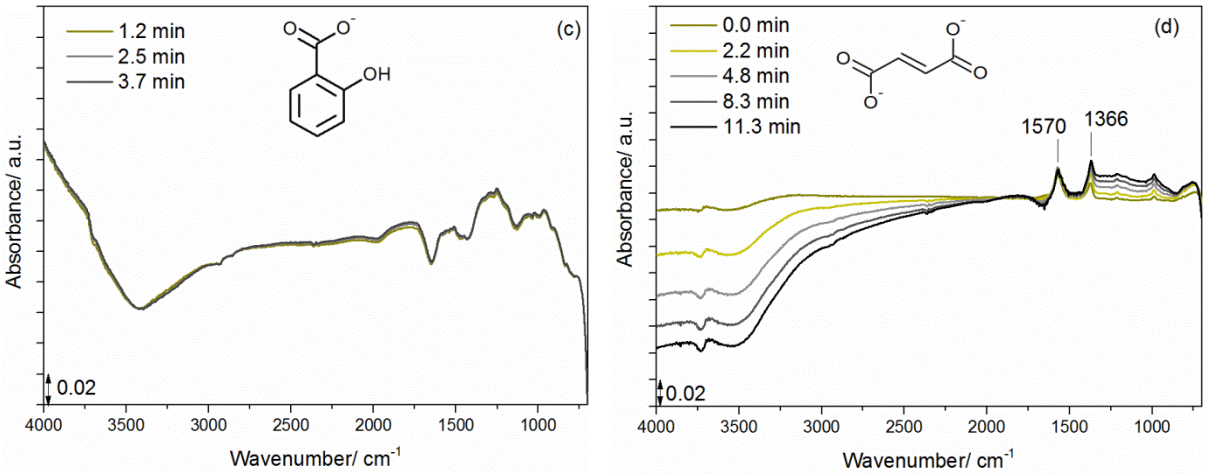

Figure 4.2: p-polarized ATR-FTIR spectra of magnesium during immersion in inhibitor solutions containing (a) 2,5-pyridine-dicarboxylate, (b) 3-methylsalicylate, (c) sodium salicylate and (d) fumarate.

In-situ ATR-FTIR spectra of 2,5-pyridinedicarboxylate, 3-methylsalicylate and sodium salicylate obtained using s-polarized IR-light are shown in figure 4.3 (a-c) respectively. For 2,5-pyridinedicarboxylate and salicylate hydroxylation (indicated in blue) followed by carboxylation (indicated in red) is observed using s-polarized light, which is similar to the trends observed in 4.1 during immersion in demineralized water. This illustrates that the hydroxylated surface is not stable in the respective solutions. On the other hand, in-situ ATR-FTIR adsorption spectra of 3-methylsalicylate, shown in figure 4.3 (b), demonstrates simultaneous hydroxylation and carboxylation. Both processes are shown to be stable confirming the capability of 3-methylsalicylate to stabilize formed hydroxide layers. Next to carboxylate peaks, also aromatic ring vibrations (indicated in green) are excited using s-polarized IR-light. This together with the absence of vibrational bonds using p-polarized IR-light, indicates that aromatic compounds are oriented in plane with the $MgO/Mg(OH)_2$ surface. The in plane orientation observed for aromatic compounds suggest that strong interactions are taking place between metal oxide and π-electrons of the aromatic ring.[50] Conversely, chemisorption of fumarate is not elucidated using s-polarized IR-light, which confirms the highly oriented bridging bidentate coordination perpendicular to the magnesium oxide surface.

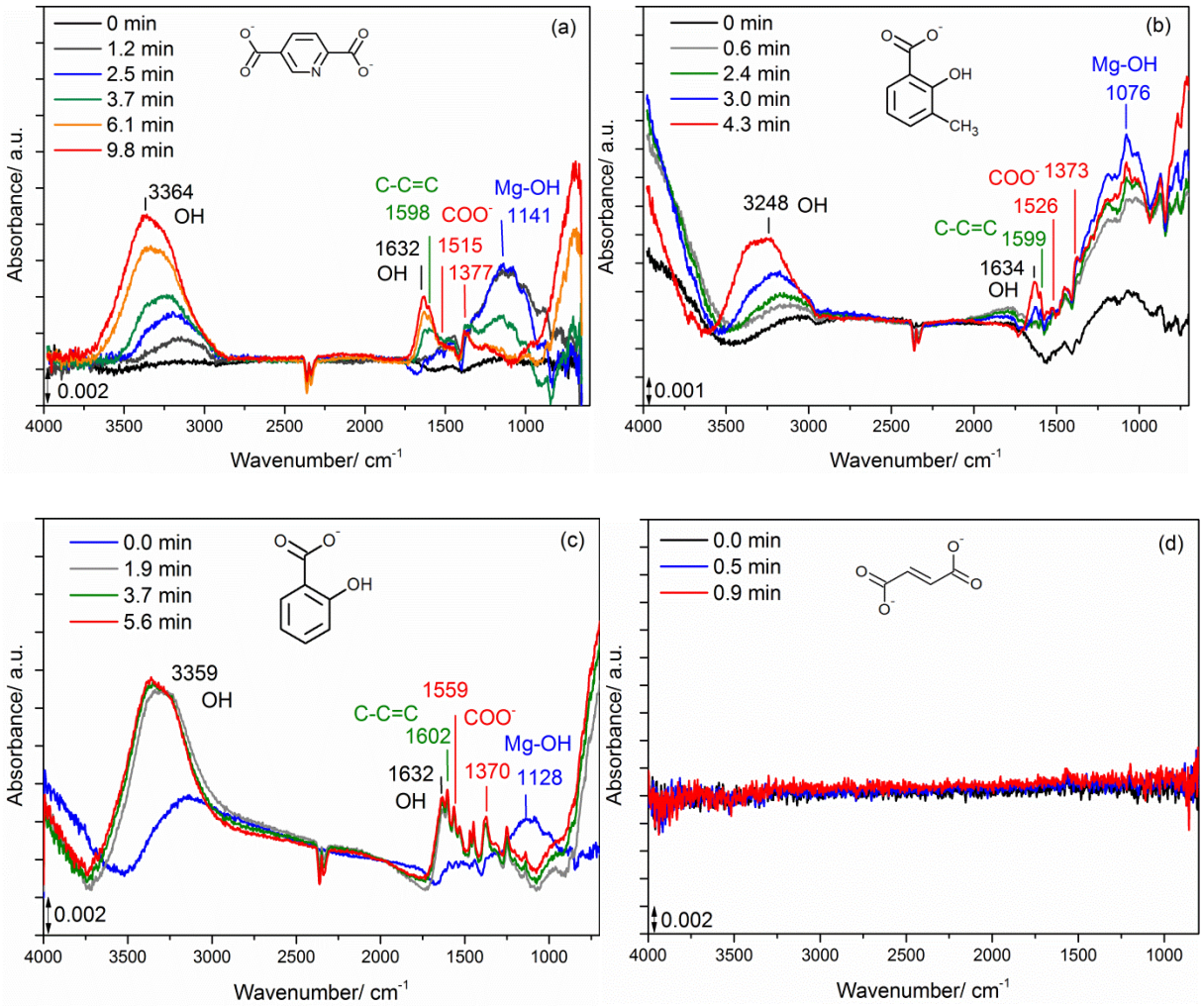

Figure 4.3: s-polarized ATR-FTIR spectra of magnesium during immersion in inhibitor solutions containing (a) 2,5-pyridine-dicarboxylate, (b) 3-methylsalicylate, (c) sodium salicylate and (d) fumarate.

Using polarized IR-light, ATR-FTIR revealed two adsorption orientations distinguishing aliphatic from aromatic structures. Figure 4.4 (a) depicts fumarate with its hydrocarbon backbone in plane with the magnesium (hydr)oxide surface but with a transition dipole of the carboxylate bonds perpendicular to the substrate explaining its sensitivity for p-polarized IR-light. Conversely, 2,5-pyridinedicarboxylate, presented in figure 4.4 (b), shows an orientation of both the molecule backbone with aromatic ring as well as the transition dipole moment of the carboxylate bonds in plane with the magnesium (hydr)oxide surface. In line with their sensitivity for s-polarized IR-light, the latter representation is assumed to also apply for salicylate and 3-methylsalicylate. The graphical representation given in figure 4.4 also illustrates why surface hydroxylation processes are more obvious in FTIR spectra using s-polarized IR-light compared to p-polarized IR-light as shown in figures 4.3 and 4.2, respectively.

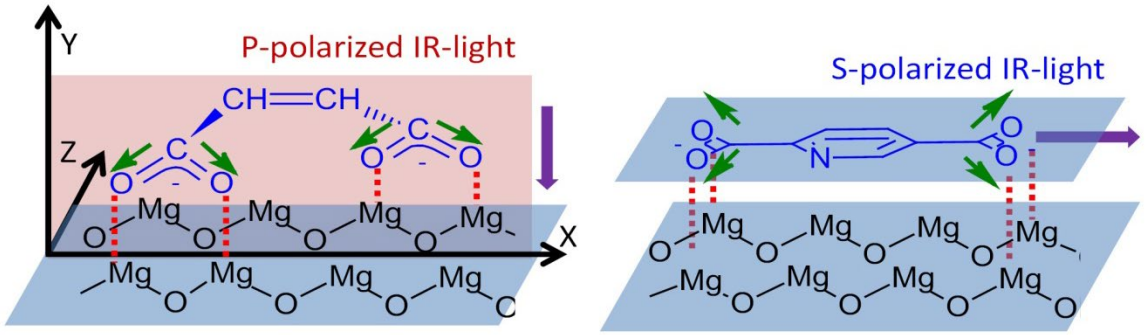

Figure 4.4: Graphical representation transition dipole moments carboxylates bonds and the corresponding polarized IR-light beams used to probe them; (left) fumarate, (right) 2,5-pyridinedicarboxylate.

3.1.3.4 Adsorption study using DFT calculations

For a more comprehensive understanding of the adsorption behavior of the investigated inhibitor molecules at the MgO/$Mg(OH)_2$ interface, density functional theory (DFT) computations were performed. Figure 4.5, presents two orientations (upright and flat) of the molecular symmetry plane perpendicular and in plane with the magnesium (hydr)oxide surface. From the obtained adsorption energies, preferential orientation of the molecules in plane (flat) with the partially hydroxylated MgO (100) surface is demonstrated for a surface coverage θ = 0.25 monolayers (ML). The highest adsorption energy is obtained for 2,5-pyridine dicarboxylic acid. However, due to a varying number of co-adsorbed hydrogen atoms, adsorption energies from inhibitors yielding different numbers of carboxylate groups are not directly comparable. Yet, comparing dicarboxylic acids; 2,5-pyridinedicarboxylate (E_{ads} = 2.92 eV) and fumarate (E_{ads} = 2.26 eV) and the monocarboxylic acids; 3-methylsalicylate (E_{ads} = 2.73 eV) and salicylate (E_{ads} = 2.36 eV) reveals that molecular structures with additional hetero-atoms (nitrogen atom or hydroxyl groups respectively) increase the adsorption energy. As a consequence, it is expected that also hetero-atoms are involved in the interaction with magnesium (hydr)oxide.

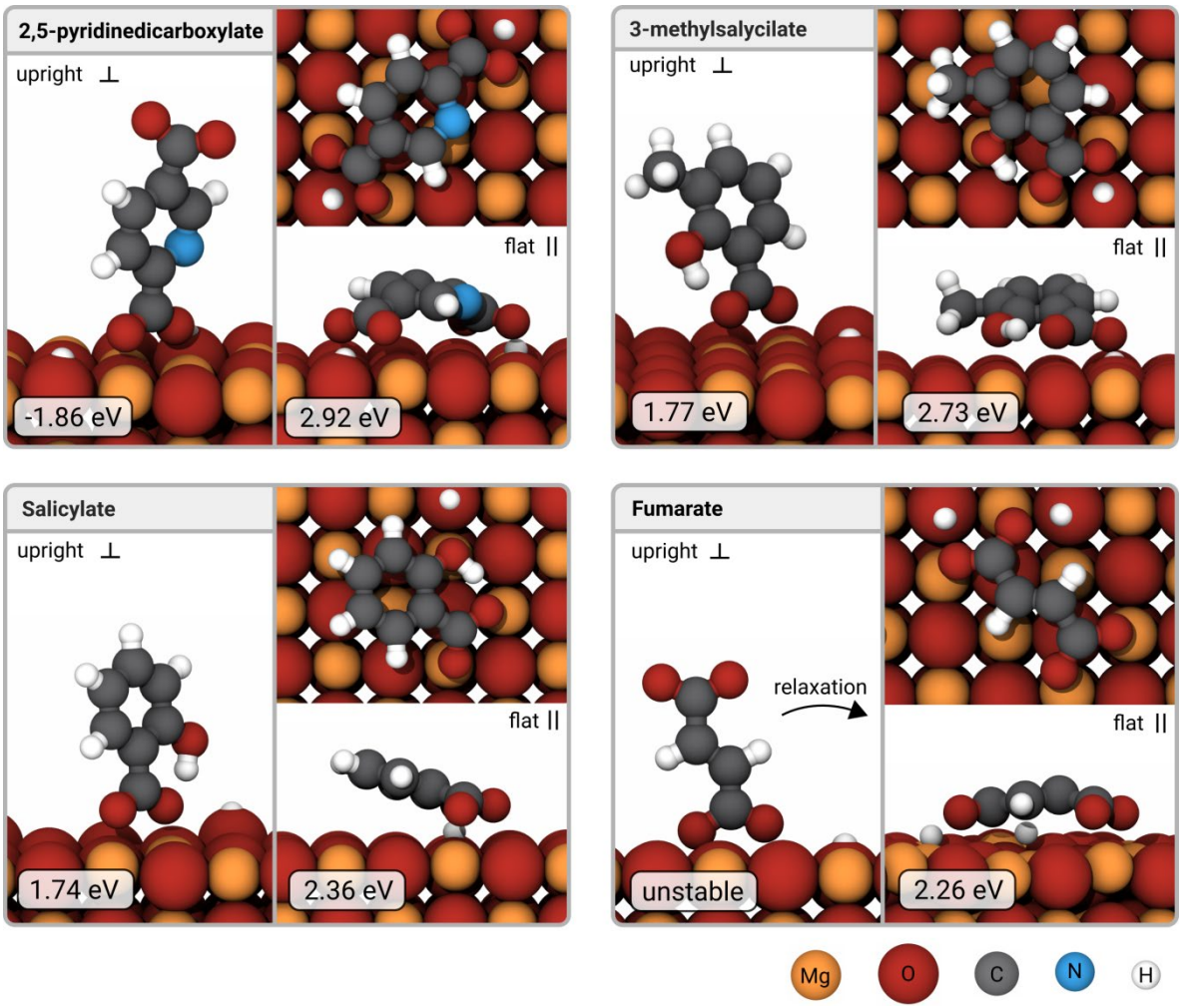

Figure 4.5: The DFT-computed adsorption structures of the investigated inhibitor molecules including their respective adsorption energies on the partially hydroxylated MgO(100) surface for a coverage θ = 0.25 ML. The structures are categorized into upright and flat, according to the orientation of the molecular symmetry plane relative to the substrate.

4.3.2 Esters

4.3.2.1 ATR-FTIR study of ester-functionalized monomer chemisorption: dimethylsuccinate

ATR-FTIR studies of dimethylsuccinate molecules dissolved in THF (0.1 wt%) were performed on chemically inert germanium internal reflection elements (IRE). Figure 4.6 illustrates the FTIR spectrum of bulk dimethylsuccinate obtained in the absence of a metallic oxide layer. The sharp peak at 1743 cm^{-1} is characteristic for the carbonyl (C=O) stretching vibration. The peaks at 1456 cm^{-1} and 1363 cm^{-1} are assigned to CH_2 and CH_3 bonds respectively.[51] The multiple bands in the 1200 cm^{-1} region correspond to C-O-C vibrations.[51]

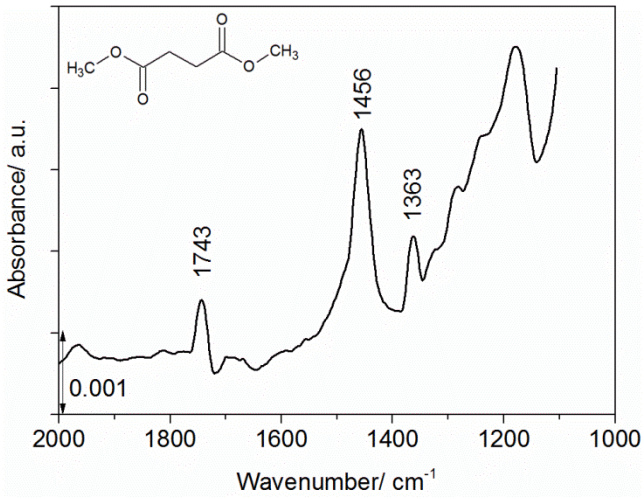

Figure 4.6: ATR-FTIR reference spectrum of non-interacting dimethylsuccinate applied on germanium IRE by THF solvent evaporation.

The three metals under investigation (Zn, Al and Mg) were deposited on germanium internal reflection elements by means of physical vapour deposition and immersed for 30 minutes in THF containing 0.1 wt% dimethylsuccinate molecules. After immersion the oxides were dried by solvent evaporation and analysed using ATR-FTIR. The resulting spectra, shown in figure 4.7 (a), are associated to a combination of chemisorbed, physisorbed and possibly some non-interacting molecules. The subsequent rinsing step with pure THF solvent is supposed to remove those non- and weakly interacting dimethylsuccinate molecules. Therefore, the resulting spectra presented in figure 4.7 (b) represent strongly interacted dimethylsuccinate.

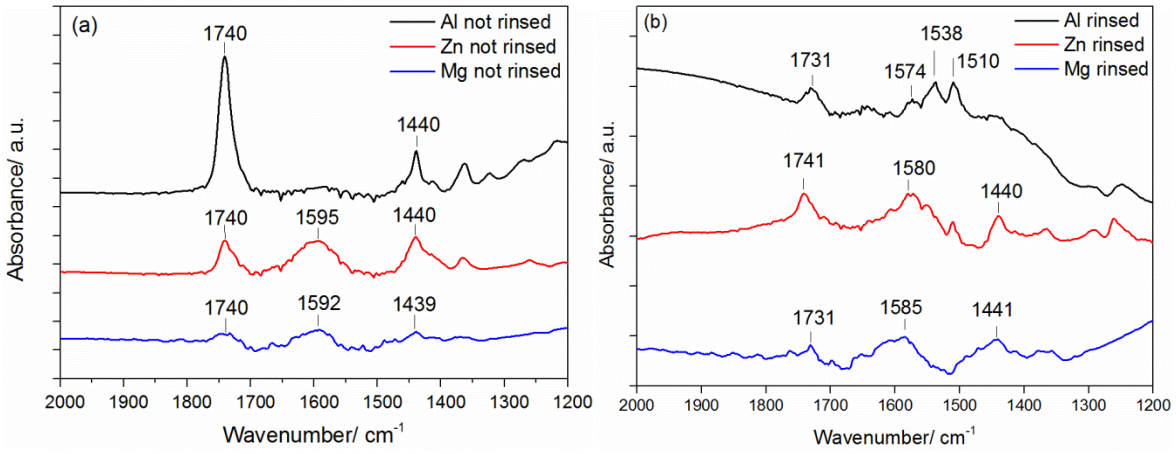

Figure 4.7: Adsorption dimethylsuccinate molecules onto native metal oxides (a) combination of physisorbed and chemisorbed molecules before THF solvent rinsing (b) chemisorbed dimethylsuccinate molecules which resisted THF solvent rinsing.

Figure 4.7 (b) evidences a reduced IR-frequency for carbonyl (C=O) peak in the presence of aluminium oxide (1731 cm^{-1}) compared to non-interacted dimethylsuccinate (1743 cm^{-1}) shown in figure 4.6 This shifts towards lower wavenumbers is associated to the involvement of carbonyl (C=O) oxygen atom in hydrogen bonds.[52,53] A similar shift can be seen for magnesium oxide. However, because of the low intensity of the carbonyl (C=O) peak which is in the order of the noise level, the establishment of interfacial hydrogen bonds are assumed to be negligible on magnesium oxide surface.

Furthermore, compared to the ATR-FTIR spectrum of bulk dimethylsuccinate (figure 4.6) an additional peak arises in the 1650-1500 cm^{-1} region in the presence of a metal film. The appearance of this additional peak is assigned to asymmetric carboxylate stretch vibrations and thus suggests the formation of carboxylate bonds upon interaction with the metal oxides under investigation.[54] The formed metal-carboxylate complexes are shown to be resistant to solvent rinsing, as illustrated by the remaining asymmetric carboxylate peak in figure 4.7 (b).

Since carboxylate bonds originate from carboxylic acid species, the ester-groups of dimethylsuccinate are shown to hydrolyse in the presence of metal (hydr)oxide.[55] Hence, a two-step chemisorption mechanism is proposed, involving ester hydrolysis forming carboxylic acids followed by a deprotonation reaction giving carboxylate anion species, as illustrated in figure 4.8.

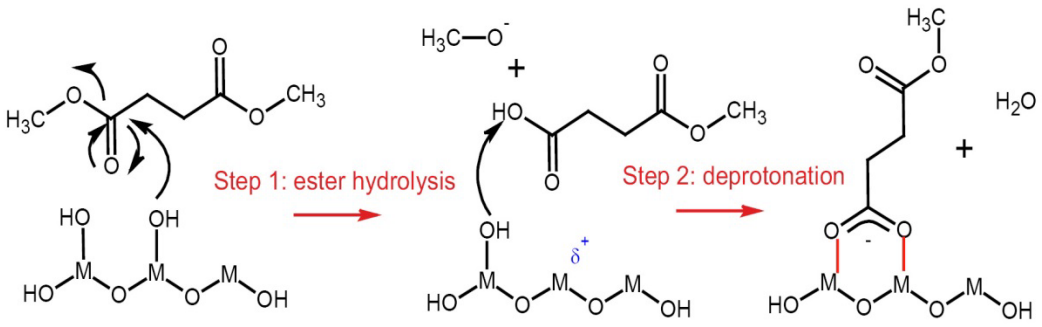

Figure 4.8: Proposed chemisorption mechanism for dimethylsuccinate resulting in interfacial metal carboxylate bond formation.

Variable asymmetric carboxylate (COO^-_{as}) peak positions depending on the interacting metal cation are being observed in figure 4.7 (b). For aluminium, zinc and magnesium oxide, maximum asymmetric carboxylate peak intensities are noted at 1538, 1580 and 1585 cm^{-1}, respectively. Based on reported isoelectric points (IEP) for aluminium, zinc and magnesium oxide (8, 9 and 12 respectively)[56], the increasing asymmetric carboxylate peak position can be associated to the increasing alkaline nature of the metal oxide. It has been reported that higher IR-frequencies for the asymmetric carboxylate stretching mode are associated to higher carboxylate bond strengths.[57,58]

Hence, the carboxylate bond strength is suggested to increase with increasing IEP (Al < Zn < Mg). In addition, figure 4.7 illustrates a very small carbonyl (C=O) peak intensity at the magnesium oxide surface, which suggests a two-end chemisorption as illustrated in figure 4.9 (c).

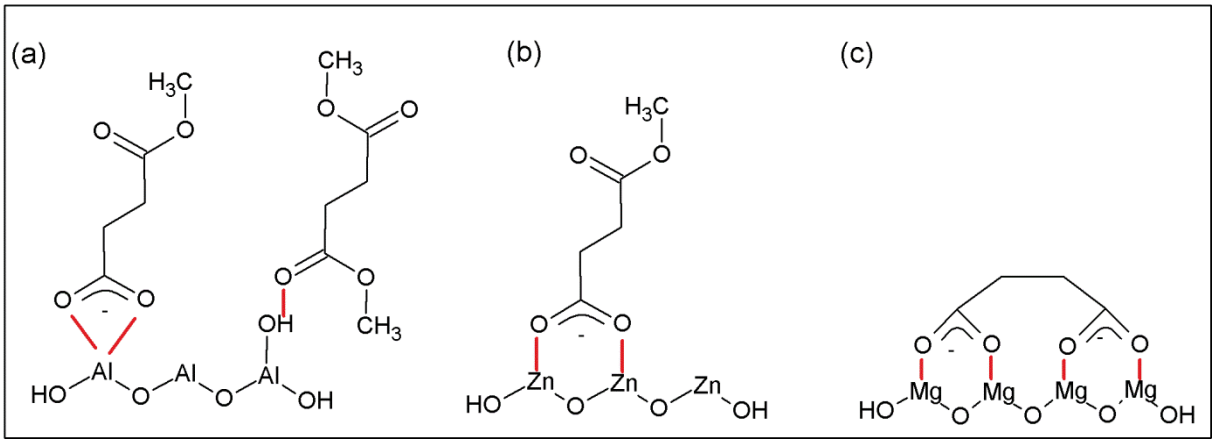

Figure 4.9: Coordination modes of chemisorbed dimethylsuccinate on (a) aluminium, (b) zinc and (c) magnesium oxide interpreted from ATR-FTIR data.

Subsequently, the effect of zirconium-treatment on the chemisorption mechanism of dimethylsuccinate molecules is investigated. The same procedure was repeated for the three metal substrates after a 90 seconds dip in H_2ZrF_6 0.01 M (pH 4). The resulting spectra before and after rinsing physisorbed molecules with THF are presented in figure 4.10 (a) and (b) respectively. Figure 4.10 (a) points out that also after zirconium-treatment, interfacial carboxylate bonds are being formed on all three metal substrates. After washing off weakly interacting molecules, carboxylate bonds remain present, demonstrating the stability of the chemical interfacial bonds. Remarkable is the absence of carbonyl bonds at the magnesium surface, suggesting that dimethylsuccinate is fully hydrolysed and coordinated to zirconium converted magnesium in a two-end adsorption mode as demonstrated in figure 4.9.

The IR-frequencies for carbonyl (C=O), asymmetric carboxylate (COO^-_{as}) and symmetric carboxylate (COO^-_{s}) bonds observed after rinsing, given in figures 4.7 (b) and 4.10 (b) are summarized in table 4.2. It can be seen that the carbonyl (C=O) peak on both zinc and aluminium shifts towards lower wavenumbers, indicating its involvement in hydrogen bonds. A larger shift of the carbonyl peak is observed for both native aluminium oxide (12 cm^{-1}) and zirconium-treated aluminium oxide (11 cm^{-1}) compared to that for native zinc (2 cm^{-1}) and zirconium-treated zinc oxide (6 cm^{-1}). The increased shift of the carbonyl peak after zirconium-treatment suggests that zirconium oxide increases the hydrogen bonding properties, resulting in stronger H-bond interactions.

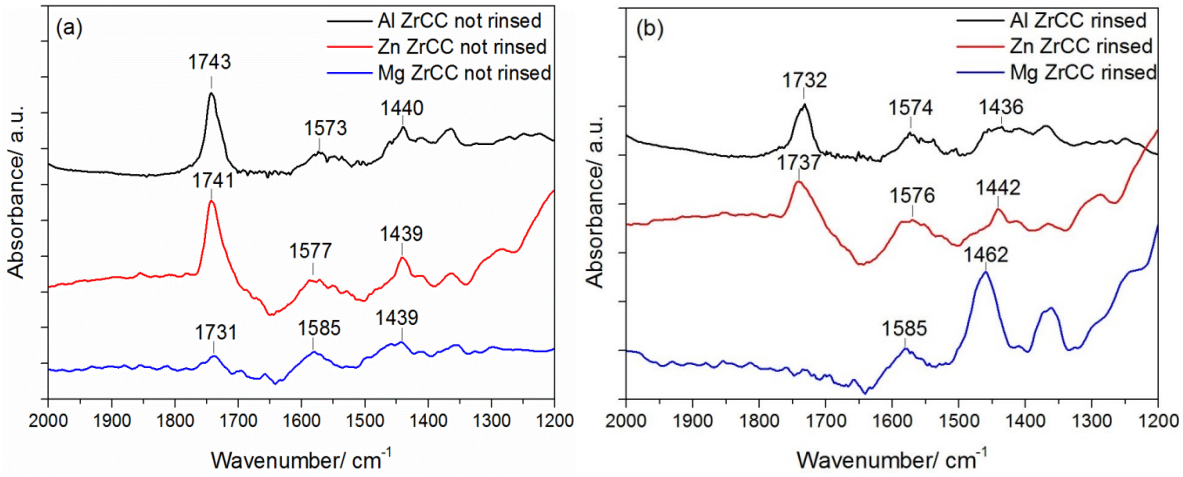

Figure 4.10: Adsorption dimethylsuccinate molecules onto zirconium-treated metal oxides (a) combination of weakly and strongly interacting molecules before THF solvent rinsing (b) strongly interacting dimethylsuccinate molecules resistant to THF solvent rinsing.

Furthermore, table 4.2 summarizes the observed asymmetric and symmetric carboxylate peak separation values, which are typically indicative for the coordination mode. A minor shift of the separation values ($\Delta\nu_{as\text{-}s}$) for adsorbed dimethylsuccinate species compared to the succinate ion indicates the formation of a bridging bidentate surface complex.[9,12] Separation values significantly smaller than these observed for succinate ion suggest chelating bidentate coordination.[9,12] Separation values of 157 cm^{-1} are reported for succinate ions.[12] Hence, a bridging bidentate coordination is proposed to be formed on all metal oxides studied. Only native aluminium oxide gives a significantly lower separation value, which suggests the formation of chelating complexes. It is evidenced from the ATR-FTIR spectra in figures 4.7 and 4.10 that carboxylate peaks are subjected to band broadening, which is a general feature of adsorbed carboxylate species.[12] Therefore, it cannot be excluded that a combination of bridging and chelating bidentate coordination exist at the respective oxide surfaces.

Table 4.2: IR-frequencies of observed carbonyl and carboxylate stretching vibrations after rinsing weakly interacted dimethylsuccinate molecules using THF solvent rinsing and the respective coordination modes; Hydrogen bond (HB), Chelating bidentate (CB), Bridging bidentate (BB). (*Succinate ion reference value[12])

	vC=O (cm^{-1})	**$vCOO^-_{(as)}$ (cm^{-1})**	**$vCOO^-_{(s)}$ (cm^{-1})**	**$\Delta\nu_{as\text{-}s}$ (cm^{-1})**	**Coordination**
Blanc	1743	-	-	157*	-
Al	1731	1538	1440	98	HB + CB
Zn	1741	1580	1440	140	BB
Mg	(1731)	1585	1441	144	BB

Al Zr	1732	1574	1436	138	HB + BB
Zn Zr	1737	1576	1438	138	HB + BB
Mg Zr	-	1585	1462	123	BB

The lower asymmetric carboxylate peak position and thus its lower separation value observed on aluminium can be associated to its higher acidic character. Moreover, it is obvious that zirconium-treatment reduces the IR-frequency of the asymmetric carboxylate stretch vibrations. As a result also its separation value reduced. Earlier, a direct correlation between high metal oxide IEP values and high carboxylate IR-frequencies has been evidenced. From this, an increasing carboxylate bond strength was derived for Mg > Zn > Al. Combining this observation with the reported highly ionic nature of magnesium carboxylate complexes compared to zinc and aluminium carboxylate complexes. It is suggested that the reduced asymmetric carboxylate peak position and it resulting lower separation value can be interpreted as an increased covalent character of the established carboxylate bonds upon zirconium-treatment. Consequently, zirconium-treatment increases the acidic nature of the metal oxide, thereby enhancing H-bonding interactions, as well as increasing the covalent nature of established carboxylate bonds. To summarize, two chemisorption mechanisms have been evidenced using ATR-FTIR in Kretschmann geometry. Both hydrogen-bonding and carboxylate bond formation were shown to depend on the metal-oxide acid-base properties. As such aluminium oxide demonstrated the highest tendency for hydrogen bonding. This is not surprising as its high positive charge (+III) is distributed on a relatively small ionic radius (Al 68 pm, Zn 88 pm, Mg 86 pm)[59,60] making aluminium cations most acidic. The high positive charge of aluminium cations strengthen the Al-OH bonds with hydroxide end-groups. This Al-OH bond strength is further enhanced by electron donation from the electron-rich carbonyl oxygen atom. Moreover, the electron donation by carbonyl oxygen atoms satisfied the desire of acidic aluminium cations for electrons resulting in strong interfacial hydrogen bonds between aluminium hydroxide and dimethylsuccinate carbonyl groups as illustrated in figure 4.11. On the other hand, more basic metal cations have less strong metal-hydroxide bonds. As a result they are characterized by a higher ability to donate these hydroxide end-groups, making them available for ester hydrolysis or carboxylic acid deprotonation as demonstrated in figures 4.8 and 4.9. Furthermore, it has been suggested that the higher basic nature increases the ionic nature of the carboxylate bond. Whereas zirconium-treatments reduces the basic nature, resulting in a stronger H-bond formation as well as increasing the covalent nature of the carboxylate bond.

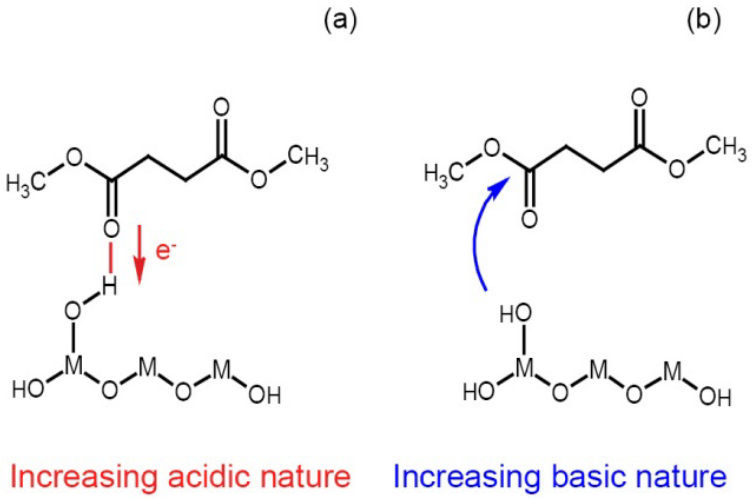

Figure 4.11: The determining role of metal oxide acid-base properties on the preferred chemisorption mechanism (a) increased acidic nature enhancing hydrogen bonding, (b) increased basic nature enhancing carboxylate bond formation.

4.3.2.2 XPS study of ester-functionalized monomer chemisorption: dimethylsuccinate

XPS surface analysis demonstrated increased hydroxide fractions after zirconium- treatment which act as binding sites for both hydrogen interaction as well as ester-hydrolysis reactions. Nevertheless, no unambiguous statement can be made on the increased quantity of interfacial bonds due to zirconium-treatment based on the ATR-FTIR results. This because the IR-absorptive properties of the metal oxides as well as small variations in layer thickness hinder direct comparison of ATR-FTIR peak intensities between different oxides. A quantitative approach to determine the amount of interfacial carboxylate bonds will be discussed in the following paragraph. Figure 4.12 presents the C 1s signal of native zinc oxide before and after dimethylsuccinate (DMS) adsorption. A chemical shift of oxygen bonded carbon towards lower binding energies suggests an increase in surface carboxylate species (COO^-) which has a characteristic binding energy at 288.5 eV.[6,55] All converted metal oxides exhibit such a chemical shift, suggesting increased portion of carboxylate species after dimethylsuccinate adsorption, which is in line with the observations obtained by ATR-FTIR.

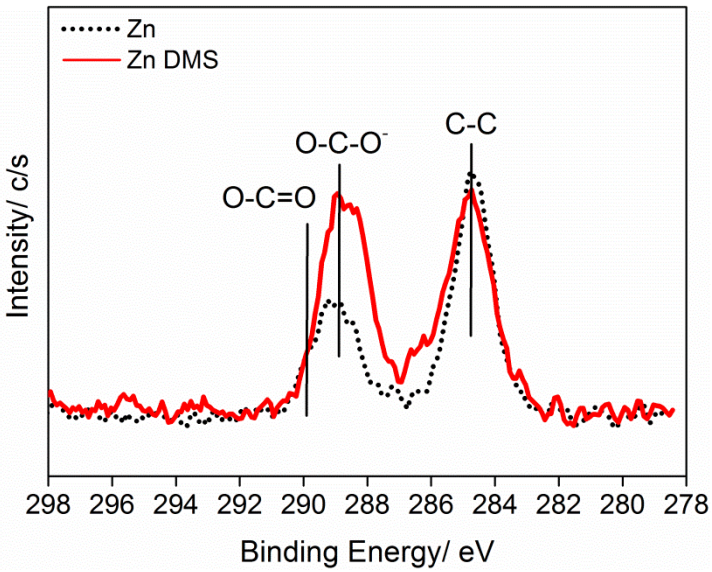

Figure 4.12: High resolution C 1s carbon peak before and after dimethylsuccinate adsorption on native zinc oxide.

The carbon signal resulting from the ambient contamination overlayer, could be deconvoluted into following subpeaks; C-C/C-H, C-O, COO^-, O-C=O , as discussed in section 2.4.2. A similar approach, validated by Pletincx et al.[6,55], has been applied on native and zirconium-treated metal oxides after dimethyl succinate adsorption to quantify the amount of carboxylate species on the respective oxide surfaces. The centred binding energy (BE) positions of the C 1s subcomponents are defined as followed: C-C/C-H (284.7 ± 0.1 eV), C-O (286.0 ± 0.4 eV), O-C=O (289.6 ± 0.3 eV) and the final component of interest COO^- (288.6 ± 0.2). All subcomponents were fitted using a FWHM of 1.5 ± 0.1 eV. The resulting subpeak areas prior and after dimethylsuccinate adsorption are normalized versus the total C 1s peak area, which results are shown in table 4.3.

Table 4.3: Deconvoluted C1s subpeak areas expressed versus the total C 1s peak area (%)

Sample	**C-C/C-H Area/ %**	**C-O Area/ %**	**O-C=O Area/ %**	**COO- Area/ %**	**X^2**
Zn	58.3 ± 3.1	5.0 ± 0.6	20.1 ± 2.8	16.6 ± 0.2	1.16
Zn DMS	40.9 ± 0.3	9.6 ± 0.6	24.7 ± 0.4	24.7 ± 0.4	1.07
Zn ZrCC	67.7 ± 1.2	13.9 ± 1.5	9.8 ± 1.0	8.6 ± 1.2	1.21
Zn ZrCC DMS	51.5 ± 7.4	18.1 ± 5.4	15.2 ± 1.0	15.2 ± 1.0	1.38
Mg	35.4 ± 0.8	3.8 ± 0.7	46.5 ± 2.9	14.3 ± 2.8	1.85
Mg DMS	55.2 ± 6.5	10.3 ± 1.5	17.3 ± 4.0	17.3 ± 4.0	2.89
Mg ZrCC	56.1 ± 1.0	24.4 ± 0.1	11.3 ± 0.9	8.2 ± 2.0	1.69
Mg ZrCC DMS	54.6 ± 2.2	21.8 ± 0.7	11.8 ± 1.5	11.8 ± 1.5	2.83
Al	50.2 ± 5.6	19.6 ± 0.1	19.3 ± 0.9	11.0 ± 4.6	4.08
Al DMS	33.1 ± 17.2	20.4 ± 0.7	17.4 ± 0.0	17.4 ± 0.0	2.4

Al ZrCC	42.0 ± 0.2	27.7 ± 0.3	21.8 ± 0.8	8.5 ± 0.4	1.54
Al ZrCC DMS	60.6 ± 6.8	23.1 ± 4.9	8.2 ± 0.9	8.2 ± 0.9	2.74

The quantified carboxylate (COO^-) subpeak areas before and after dimethylsuccinate chemisorption, presented in table 4.3, are summarized in figure 4.13. This evidences that zirconium-treatment does not increase the amount of adsorbed carboxylate species compared to native oxides. Subtracting quantified carboxylate species obtained before adsorption (bare) from those obtained after dimethylsuccinate adsorption (DMS) gives the net increase in carboxylate species indicated by the vertical grey arrows in figure 4.13.

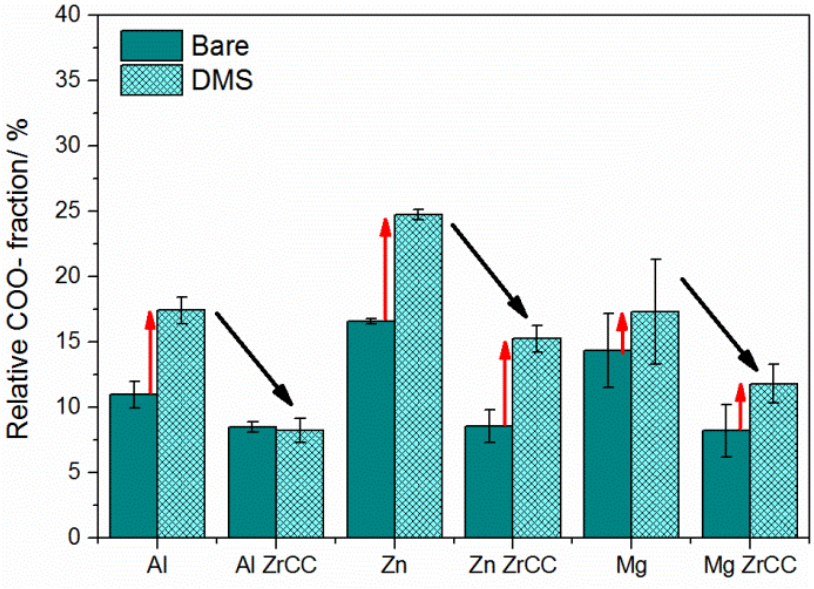

Figure 4.13: Relative COO^- fractions (%) at metal oxide surface before (bare) and after (DMS) dimethylsuccinate adsorption.

This net increase of carboxylate species is shown to remain equal after zirconium-treatment of zinc and magnesium and reduces after zirconium-treated aluminium. However, it is expected that during adsorption ambient carbon contaminants are being replaced. Therefore, this net increase underestimates the amount of established interfacial carboxylate bonds. When comparing the total amount of carboxylate species after dimethylsuccinate adsorption a significant reduction is being observed after zirconium-treatment, indicated by the black arrows in figure 4.13. It was demonstrated that zirconium-treatment of thermally vaporized metal films results in highly hydroxylated surfaces. Although surface hydroxides are a requirement for carboxylate bond formation with dimethylsuccinate molecules due to the hydrolysis intermediate step, overhydroxylation might hinder accessibility of Lewis acid bonding sites for adsorption. Two reasons for such a poisoning effect have been described by Bjelopavlic et al.[61] Firstly, the Lewis acidity of the surface, related to the excess positive charge of metal cations, may become neutralized by the

presence of negatively charged hydroxyl groups. Secondly, the cations (Lewis acid sites) are physically buried due to neighbouring hydroxide groups (Bronsted acid sites), as illustrated in figure 4.14. In that case, Lewis acid sites exist in holes, which may be sterically inaccessible for bridging bidentate carboxylate bond formation. Under these circumstances, it is expected that the establishment of interfacial bonds on Bronsted acid sites, being the formation of hydrogen bonds between dimethylsuccinate oxygen atom and zirconium hydroxide proton, becomes more favourable, as illustrated in figure 4.14. This was also indicated by ATR-FTIR, since the ester carbonyl peak shift towards lower wavenumbers after zirconium-treatment of zinc, indicating increased affinity for hydrogen bonding after zirconium-treatment. Hence, tuning the surface hydroxides density, to meet requirements for carboxylate anion formation by ester hydrolysis and deprotonation without poisoning Lewis acid sites is suggested to be crucial for maximum interfacial carboxylate bond formation.

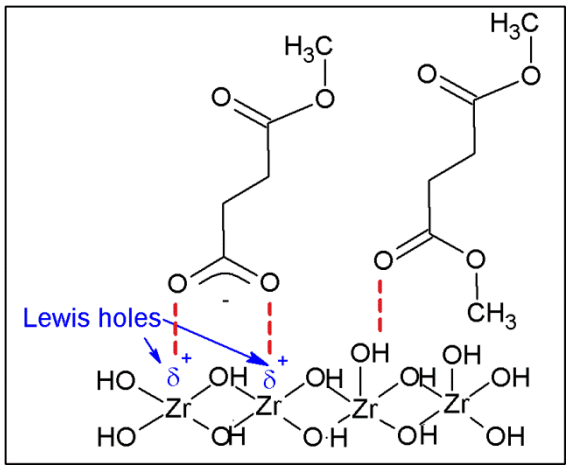

Figure 4.14: Structural presentation of Lewis acid sites, sterically poisoned by surrounding Bronsted acid bonding sites on highly hydroxylated zirconium oxide.

4.3.2.3 Comparative XPS study on the interfacial carboxylate bond density of thermally vaporized and bulk substrates

ATR-FTIR in Kretschmann configuration has shown to provide valuable information regarding the role of oxide acid-base properties on the interfacial chemisorption mechanisms. Nevertheless, this technique requires the use of model metal substrates (thermally vaporized nanolayers) which rises the relevance of the obtained information for industrial metal-polyester hybrid systems. Whereas 4.3.2.2 focussed on the complementary of ATR-FTIR and XPS using model substrates. This current section continues interfacial XPS studies using industrially relevant bulk substrates to further investigate the correlation between surface hydroxide fractions and the interfacial carboxylate bond density. Similar to the work presented in 4.3.2.2, C 1s XPS peaks were obtained after chemisorption of dimlethymlsuccinate. Deconvolution of the C 1s peak lead to the quantification of COO^-

contributing to the overall C 1s XPS peak, which results (Bulk) are presented in figure 4.15. The PVD results shown in figure 4.15 are identical to the DMS results shown in figure 4.13, associated to the COO- fractions obtained after DMS adsorption on thermally vaporized substrates. When comparing the COO- fractions on native PVD substrates (Zn, Al, Mg) with those on zirconium-treated PVD substrates (Zn Zr, Al Zr, Mg Zr) no significant increase in COO- fraction can be seen after zirconium-treatment. However, when comparing native bulk substrates with zirconium-treated bulk substrates the net increase in COO^- bonds is obvious. This confirms the hypothesis proposed in 4.3.2.2 stating that although hydroxides are required for carboxylate bond formation with ester-functionalized molecules, saturation of the respective surface by hydroxide groups might hinder its chemisorption. Nevertheless, zirconium-treatment is shown to enhance chemisorption, when overhydroxylation is avoided. It is suggested that the high oxidation state of zirconium results in strong Lewis acid sites being highly oxophilic.[62] Therefore, the amount of chemisorption is shown to be predominantly determined by the metal oxide acid-base properties.

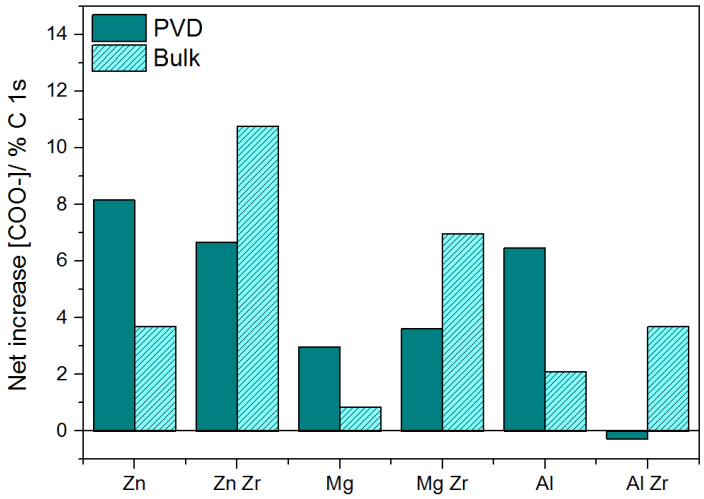

Figure 4.15: Relative COO^- fractions (%) upon dimethylsuccinate adsorption at thermally vaporized (PVD) substrates and polished metal sheets with high purity grade (Bulk) .

4.3.3 Amides

4.3.3.1 FTIR study of amide-functionalized monomer chemisorption: N,N'-dimethylsuccin amide

Figure 4.16 presents the reference FTIR spectra of non-adsorbed N,N'-dimethylsuccinamide molecules remaining on a bare IRE after solvent evaporation. The sharp intense peak positioned at 1634 cm^{-1} represents amide carbonyl (C=O) stretch vibrations and is frequently referred to as amide I peak. In addition, the two peaks at 3305 and 1557 cm^{-1}, are assigned to NH stretch and a combination of NH bend and C-N stretch vibrations, respectively. The latter is typically referred to as amide II peak. Additionally, the peak positioned at 1415 cm^{-1} can be attributed to C-CH_2-C bending vibrations.[51]

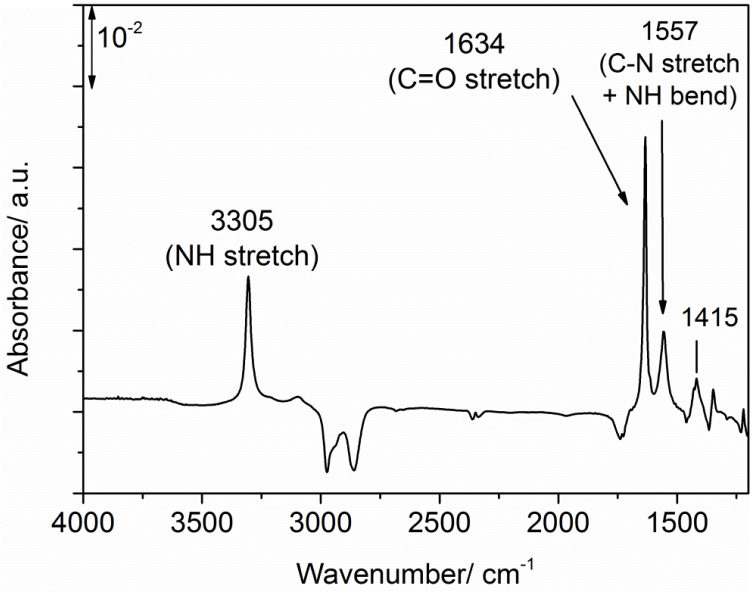

Figure 4.16: ATR-FTIR reference spectrum of non-interacting N,N'-dimethylsuccinamide applied on germanium IRE by THF solvent evaporation.

The ATR-FTIR spectra obtained upon chemisorption of N,N'-dimethylsuccinamide on native and zirconium-treated (ZrCC) aluminium, zinc and magnesium oxide are given in figure 4.17 (a-c). The presented spectral features are obtained upon THF solvent rinsing and thus represents strongly interaction molecules. Significant peak shifts can be observed compared to non-interacted N,N'-dimethylsuccinamide molecules. Table 4.4 summarizes the observed amide I (C=O) and amide II (C-N/N-H) peak positions.

Table 4.4: Amide I and II peak position of N,N'-dimethylsuccinamide upon interaction with native and zirconium-treated multi-metal substrates

	Amide I (C=O)	**Amide II (C-N/N-H)**
Reference	1634	1557
Al	1640	1550
Al ZrCC	1649	1543
Zn	-	1577
Zn ZrCC	1649	1579
Mg	1653	1563
Mg ZrCC	1650	1577

It is well-described that the amide I and amide II peaks are anti-correlated.[63,64] Therefore, interactions strengthen the C=O double bond will weaken the C-N bond. As a consequence, when the amide carbonyl peak shift to higher IR-frequencies, an inverse shift of the C-N/N-H peak to lower IR-frequencies is expected. Such shift of the amide I carbonyl (C=O) peak towards higher IR-frequencies

is seen upon interaction with all native and zirconium-treated metal oxides. Yet, only native and zirconium-treated aluminium oxide demonstrate an opposite shift of the amide II peak to lower IR-frequencies. Conversely, in the case of native and zirconium-treated zinc and magnesium oxide a shift of amide II peak to higher IR-frequencies is noted. Simultaneously, a second peak between 1400-1490 arises. This additional peak may be interpreted as the shift of C-N/N-H peak to lower wavenumbers. Yet, the observed shift would be rather large, since, amide II peak is typically not as sensitive for shifts as the amide I peak.[63] A second hypothesis on the amide II shift to higher IR-frequencies might be related to simultaneous interactions with both amide oxygen and nitrogen atom, strengthening both the C-N and C=O bonds. Furthermore, figure 4.17 (b) demonstrates the loss of an amide I peak (C=O) at the zinc oxide surface. This might be attributed to a loss of double bond character upon interaction Nevertheless, it becomes clear that no unambiguous statement on the chemisorption mechanism of amide-functionalized molecules at the metal oxide surfaces can be made. To provide additional information on the chemisorption of N,N'-dimethylsuccinamide XPS analysis has been performed.

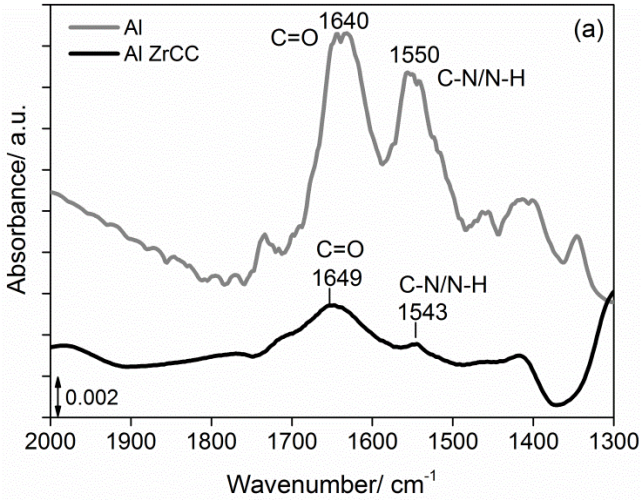

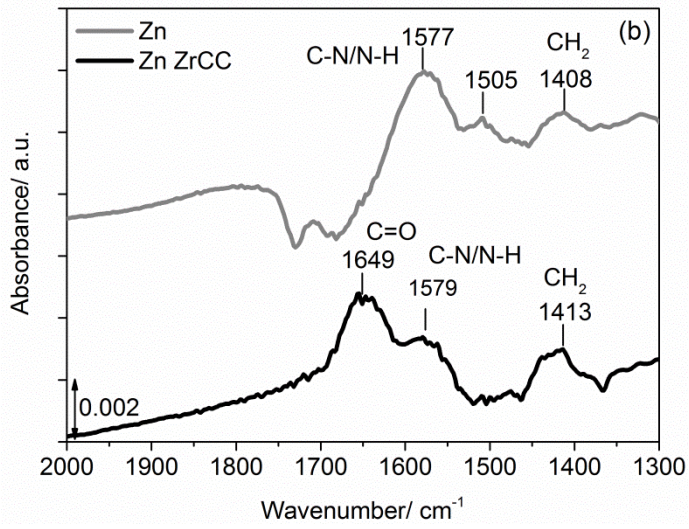

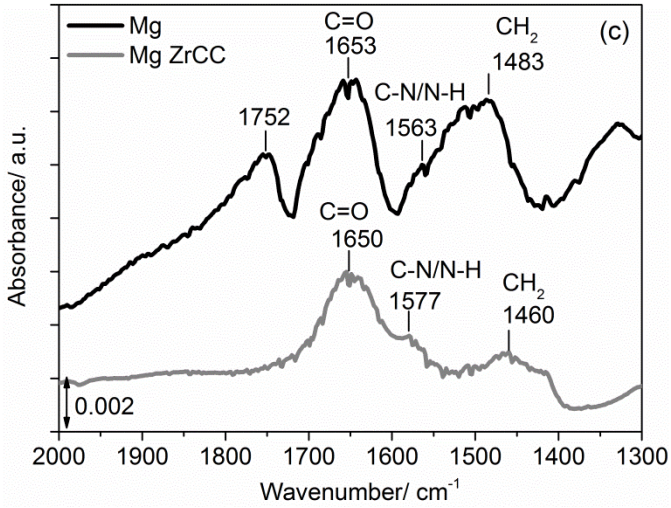

Figure 4.17: ATR-FTIR spectra of strongly interacting N,N'-dimethylsuccinamide molecules resistant to THF solvent rinsing on native and zirconium-treated (a) aluminium, (b) zinc and (c) magnesium oxide.

4.3.3.1 XPS study of amide-functionalized monomer chemisorption: N,N'-dimethylsuccin amide

Figure 4.18 (a) and (b) presents the XPS survey spectrum obtained after adsorption of N,N'-dimethylsuccinamide on native and zirconium-treated zinc oxide, respectively. Of special interest is the N 1s XPS peak since deconvolution of this peak in its subpeaks offers information on the different binding modes of nitrogen. Both native and zirconium-treated substrates reveal the presence of a N 1s XPS peak confirming the chemisorption of N,N'-dimethylsuccinamide.

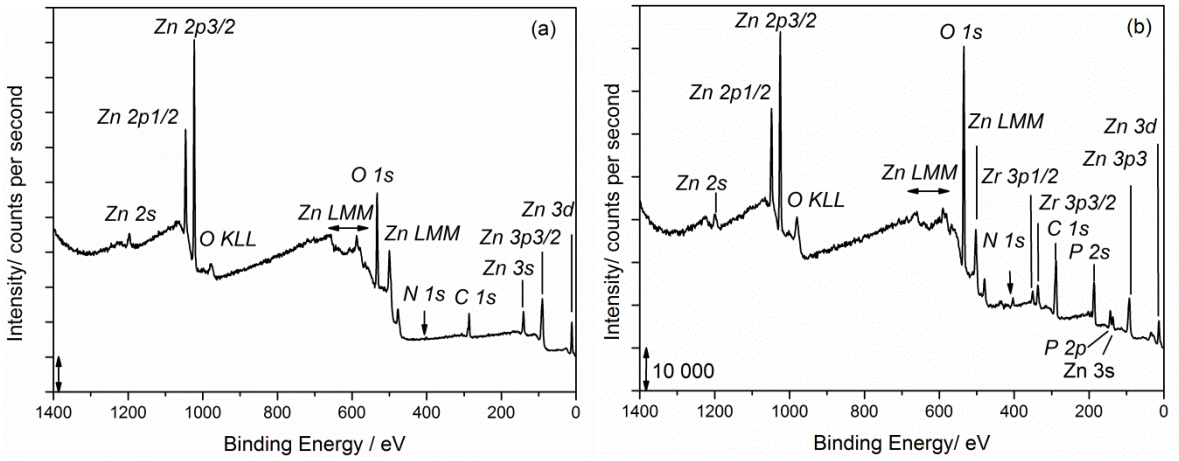

Fig. 4.18: XPS survey scan after 30 min. N,N'-dimethylsuccinamide adsorption on (a) native and (b) zirconium-treated zinc oxide.

The binding energy, the shift versus non-adsorbed N,N'-dimethylsuccinamide molecules and the full-width half maximum (FWHM) values of the N 1s high-resolution XPS peaks are represented in table 4.5. The shift in BE and increased FWHM indicates that all metal substrates under investigation interact with N,N'-dimethylsuccinamide through the amide nitrogen atom. Increased FWHM values

upon chemisorption suggests the contribution of multiple types of interactions to the N 1s signal after adsorption.

Table 4.5: N 1s XPS peak parameters associated to N,N'-dimethylsuccinamide chemisorbed at various metal oxide surfaces.

Substrate	BE/ eV	Shift/ eV	FWHM/ eV
None	399.1 ± 0.1	-	1.7 ± 0.1
Al	400.1 ± 0.2	1.0	3.1 ± 0.9
Al ZrCC	400.3 ± 0.2	1.2	3.0 ± 0.2
Zn	400.0 ± 0.2	0.9	2.1 ± 0.1
Zn ZrCC	400.0 ± 0.2	0.9	2.9 ± 0.3
Mg	400.3 ± 0.4	1.2	2.3 ± 0.3
Mg ZrCC	399.8 ± 0.5	0.7	2.8 ± 0.4

Deconvolution of the N 1s XPS peak into its subcomponents has been conducted based on the approach proposed by Barthés-Labrouse and Mercier. [65,66] Since Bronsted interactions result in ionic interfacial bonds, a larger interface dipole will be induced compared to Lewis acid-base interactions, the former results in the largest N 1s peak shift with respect to non-adsorbed N,N'-dimethylscuccinamide. In accordance with literature, Bronsted interactions (N_3) at 401.5 ± 0.2 eV, and Lewis interactions (N_2) at 400.1 ± 0.1 eV and non-interacting N,N'-dimethylsuccinamide (N_1), at 398.8 ± 0.1 eV All subpeaks had a FWHM value of 1.6 eV. An example of the fitting results is presented in figure 4.19.

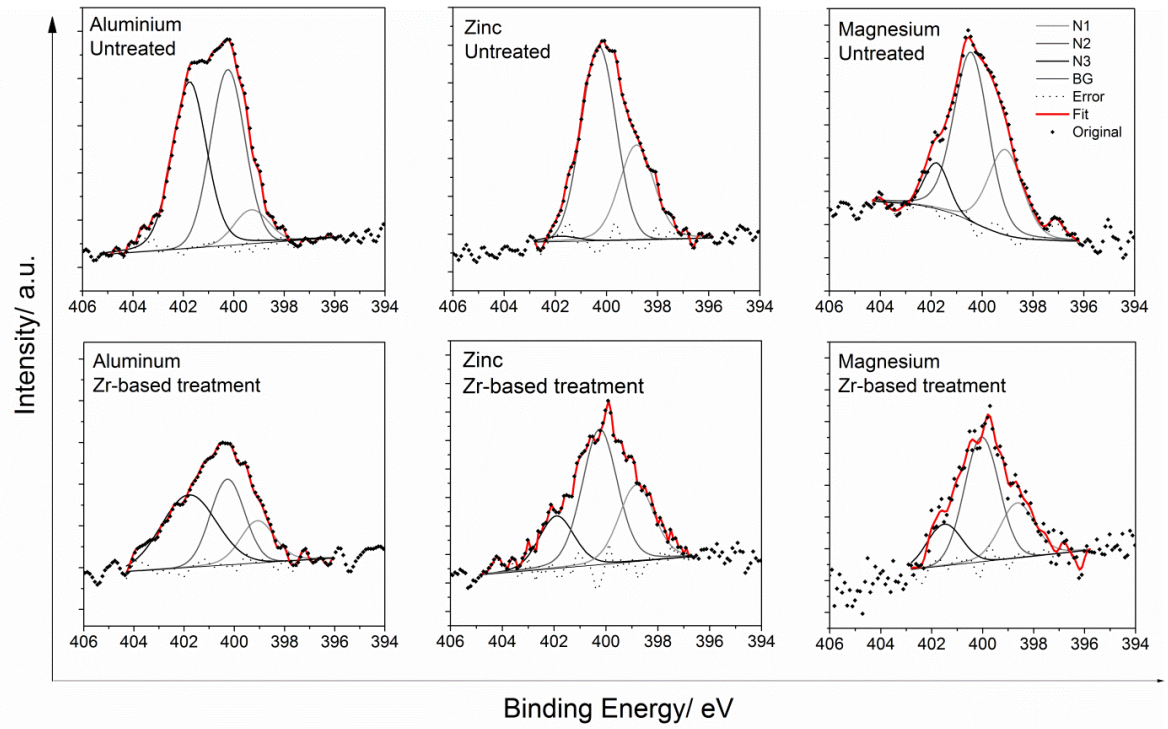

Fig. 4.19: Deconvoluted N 1s High-resoultion XPS peak of native and zirconium-treated magnesium, zinc and aluminium oxides.

The relative contributions of N_1, N_2 and N_3 components to the N 1s peak after adsorption to metal oxide are illustrated in figure 4.19. The fraction unreacted nitrogen approaches 30 % on magnesium and zinc substrates and only about 10 % on aluminium substrates. Fractions of non-reacted nitrogen lower than 50 % suggest that molecules can interact with the metal oxide through both nitrogen atoms within one N,N'-dimethylsuccinamide molecule.

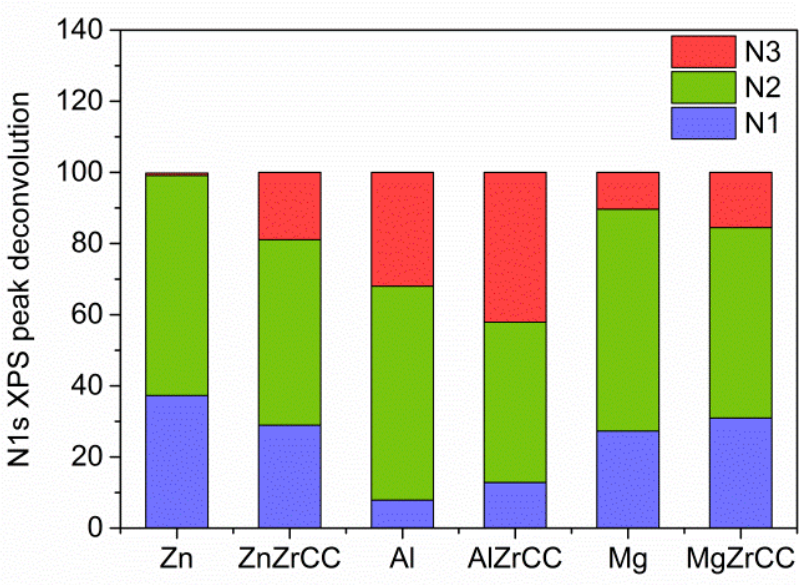

Fig. 4.20: Contribution of N_1, N_2 and N_3 component in N 1s high-resolution XPS peak.

Moreover, figure 4.20 demonstrates a higher contributions of Bronsted acid-base interactions (N_3) upon zirconium- treatment. As illustrated in figure 4.21 Bronsted interactions, also referred to as protonation reactions, require a proton exchange from the metal hydroxide end-group towards the amide oxygen atom. This proton exchange is enhanced with increasing acidic oxide character as this enhances the proton donating capabilities. Contrary, Lewis acid-base interactions result from nucleophilic attack of the partially negatively charged amide oxide atom on the metal cation, thereby substituting a metal hydroxide end-group. In order to favour this reaction pathway, a basic oxide character is preferred as this will promote the leaving character of the metal hydroxide end-group. Both reaction pathways are given in figure 4.21. From figure 4.20, it can be seen that Bronsted acid-base interactions increase upon zirconium-treatment, which can be attributed to the increased acid character of the converted oxide.

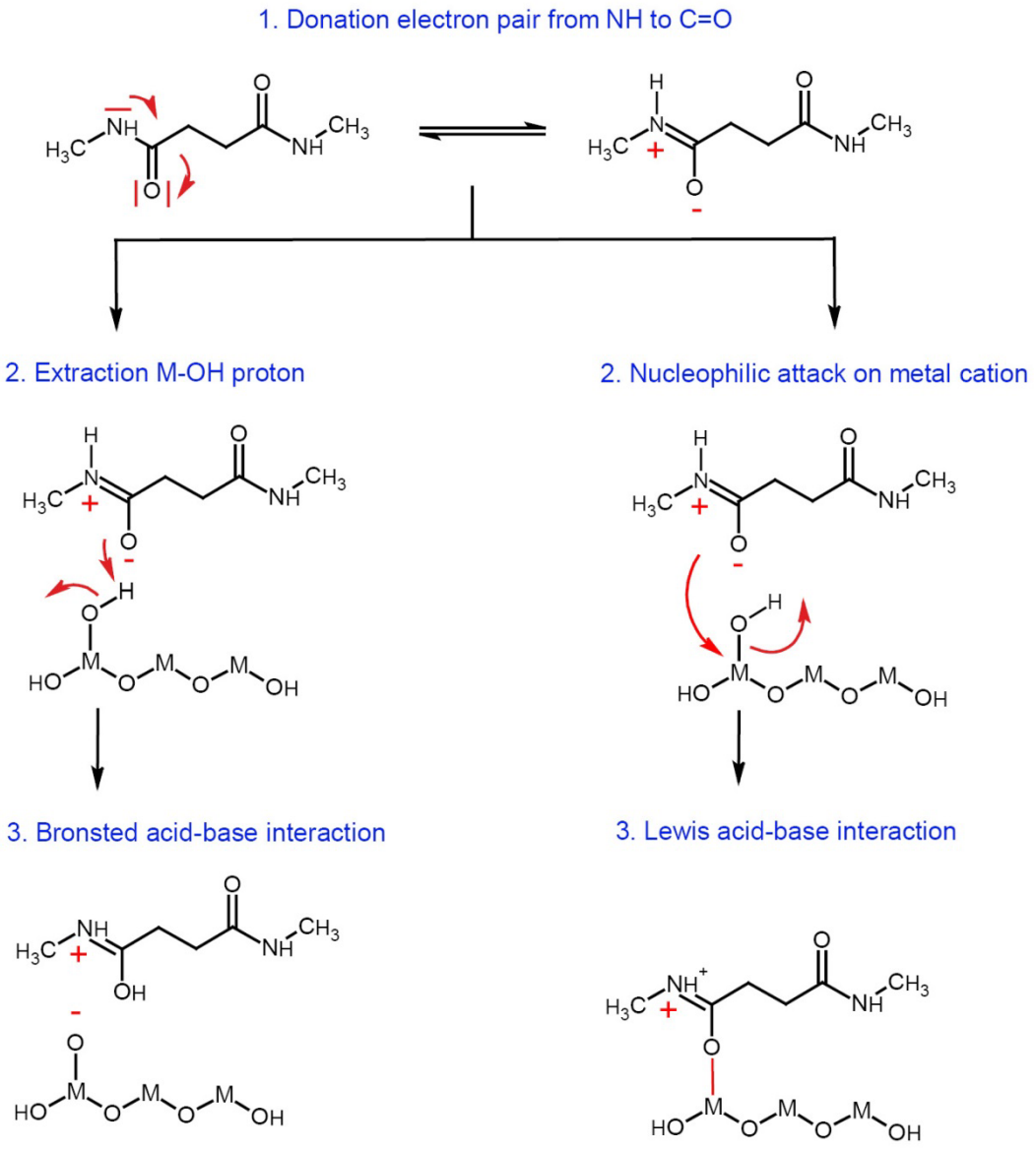

Figure 4.21: Proposed reaction pathways for Bronsted and Lewis acid-base interaction between N,N'-dimethylsuccinamide and metal hydroxide end-groups.

4.4 Conclusions

Both carboxylic acids and ester-functionalized compounds were shown to form interfacial carboxylate bonds upon interaction with multi-metal oxides. Orientation analysis using s-and p-polarized IR-light evidenced that aromatic compounds are oriented in-plane with the surface due to strong π-interactions between the aromatic ring and magnesium oxide. Conversely, carboxylate bonds with aliphatic compounds were shown to orient highly perpendicular to the magnesium surface. This demonstrates that the effect of π-interactions on interfacial bond formation cannot be neglected. In addition, next to carboxylate bond formation, ester-functionalized compounds were

also shown to interact by hydrogen bonding. Both chemisorption mechanisms were shown to depend on the metal-oxide acid-base properties. As such, aluminium oxide demonstrated the highest tendency for hydrogen bonding, which was associated to its more acidic nature as compared to zinc and magnesium oxide. On the other hand, a more alkaline nature of metal cations increases the oxide's ability to donate hydroxide end-groups, favouring ester hydrolysis or carboxylic acid deprotonation reactions. Furthermore, also N,N'-dimethylsuccinamide was shown to chemisorb to metal oxide by two interfacial reaction mechanisms; i.e. Lewis and Bronsted acid-base interactions. Also here, the favoured reaction mechanism was shown to greatly depend on the oxide's acid-base properties. It was suggested that more acidic oxides have increased H-donating capacities, thereby enhancing Bronsted acid-base interactions. Finally, it was shown that a zirconium-treatment increases the acidic oxide properties and thus affects the ratio of competing interface interactions.

Metal-hydroxide end-groups were shown to play a predominant role in all unravelled chemisorption mechanisms. In the case of hydrogen-bonding and Bronsted acid-base interactions metal hydroxides act as a proton donor. For optimal hydrogen donating capacities, acidic metal cations are favourable. This because their high positive charge loosens the O-H bond as shown in figure 4.21. On the other hand, for ester hydrolysis, carboxylic acid deprotonation and Lewis acid-base interactions metal hydroxide end-groups are being substituted by another reactive group. Therefore less positively charged metal cations (with higher alkaline nature) are favourable since this increases the leaving capacity of hydroxide end-groups as shown in figure 4.22.

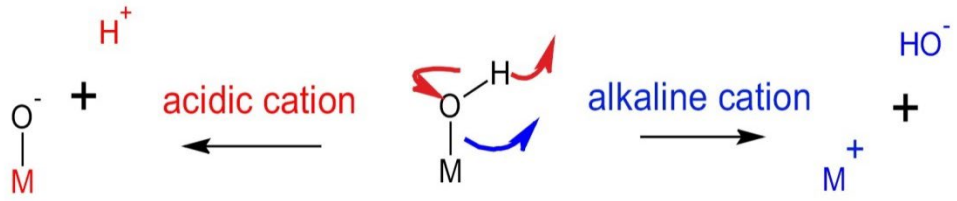

Fig. 4.22: The determining role of metal cation acidity in inducing an interfacial interaction mechanisms

Since, metal-hydroxide end-groups act as bonding site, the amount of surface hydroxides correlates to the amount of established interfacial bonds. However, it has been demonstrated that a saturation of the surface with surface hydroxides reduces interfacial carboxylate bond formation due to sterically and electrostatically hindrance limiting the access of metal cations. Therefore, there should be an optimum of surface hydroxides which does not necessarily equal the maximum of surface hydroxides. In chapter 3, it has been shown that zirconium-treatment greatly affects the surface

hydroxide density. Moreover, the hydroxide fractions at the zirconium-treated surface were shown to correlate to the nature of the initial metal oxide, resulting in different trends for thermally vaporized model substrates and polished metal sheets. However, whereas the amount of interfacial bonds correlates to the surface hydroxide density, the chemisorption mechanism and thus bonding strength is suggested to be determined by the oxide's acid-base properties.

References

(1) Pletincx, S.; Fockaert, L. L. I.; Mol, J. M. C.; Hauffman, T.; Herman, T. Probing the Formation and Degradation of Chemical Interactions from Model Molecule / Metal Oxide to Buried Polymer / Metal Oxide Interfaces. *npj Mater. Degrad.* **2019**, *3* (23), 1–12.

(2) Boiziau, C.; Lecayon, G. Adhesion of Polymers to Metals : A Review of the Results Obtained Studying a Model System. *Surf. Interface Anal.* **1988**, *12*, 475–485.

(3) Marsh, J.; Minel, L.; Barthes-Labrousse, M. G.; Gorse, D. Interaction of Epoxy Model Molecules with Aluminium, Anodised Titanium and Copper Surfaces: An XPS Study. *Appl. Surf. Sci.* **1998**, *133* (4), 270–286.

(4) Wielant, J.; Hauffman, T.; Blajiev, O.; Hausbrand, R.; Terryn, H. Influence of the Iron Oxide Acid-Base Properties on the Chemisorption of Model Epoxy Compounds Studied by XPS. *J. Phys. Chem. C* **2007**, *111* (35), 13177–13184.

(5) Allara, D. L.; Nuzzo, R. G. Spontaneously Organized Molecular Assemblies. 2. Quantitative Infrared Spectroscopic Determination of Equilibrium Structures of Solution-Adsorbed n-Alkanoic Acids on an Oxidized Aluminum Surface. *Langmuir* **1985**, *1* (1), 52–66.

(6) Pletincx, S.; Trotochaud, L.; Fockaert, L.-L.; Mol, J. M. C.; Head, A. R.; Karslıoğlu, O.; Bluhm, H.; Terryn, H.; Hauffman, T. In Situ Characterization of the Initial Effect of Water on Molecular Interactions at the Interface of Organic/Inorganic Hybrid Systems. *Sci. Rep.* **2017**, *7*, 45123.

(7) Brand, J. Van Den; Blajiev, O.; Beentjes, P. C. J.; Terryn, H.; Wit, J. H. W. De. Interaction of Anhydride and Carboxylic Acid Compounds with Aluminum Oxide Surfaces Studied Using Infrared Reflection Absorption Spectroscopy. **2004**, *11* (12), 6308–6317.

(8) Leadley, S. R.; Watts, J. F. The Use of XPS to Examine the Interaction of Poly(Acrylic Acid) with Oxidised Metal Substrates. *J. Electron Spectros. Relat. Phenomena* **1997**, *85* (1–2), 107–121.

(9) Zelenak, V.; Vargova, Z.; Györyova, K. Correlation of Infrared Spectra of Zinc(II) Carboxylates with Their Structures. *Spectrochim. Acta - Part A Mol. Biomol. Spectrosc.* **2007**, *66* (2), 262–272.

(10) Taheri, P.; Wielant, J.; Hauffman, T.; Flores, J. R.; Hannour, F.; Wit, J. H. W. De; Mol, J. M. C.; Terryn, H. A Comparison of the Interfacial Bonding Properties of Carboxylic Acid Functional Groups on Zinc and Iron Substrates. *Electrochim. Acta* **2011**, *56* (4), 1904–1911.

(11) Taheri, P.; Hauffman, T.; Mol, J. M. C.; Flores, J. R.; Hannour, F.; De Wit, J. H. W.; Terryn, H. Molecular Interactions of Electroadsorbed Carboxylic Acid and Succinic Anhydride Monomers on Zinc Surfaces. *J. Phys. Chem. C* **2011**, *115* (34), 17054–17067.

(12) Dobson, K. D.; Mcquillan, A. J. In Situ Infrared Spectroscopic Analysis of the Adsorption of Aliphatic Carboxylic Acids to TiO2, ZrO2, Al2O3, and Ta2O5 from Aqueous Solutions. *Spectrochim. Acta - Part A Mol. Biomol. Spectrosc.* **1999**, *55*, 1395–1405.

(13) Dobson, K. D.; McQuillan, A. J. In Situ Infrared Spectroscopic Analysis of the Adsorption of Aromatic Carboxylic Acids to TiO2, ZrO2, Al2O3, and Ta2O5 from Aqueous Solutions. *Spectrochim. Acta - Part A Mol. Biomol. Spectrosc.* **2000**, *56* (3), 557–565.

(14) Taheri, P.; Lill, K.; De Wit, J. H. W.; Mol, J. M. C.; Terryn, H. Effects of Zinc Surface Acid-Based Properties on Formation Mechanisms and Interfacial Bonding Properties of Zirconium-Based Conversion Layers. *J. Phys. Chem. C* **2012**, *116* (15), 8426–8436.

(15) Cerezo, J.; Taheri, P.; Vandendael, I.; Posner, R.; Lill, K.; de Wit, J. H. W.; Mol, J. M. C.; Terryn, H. Influence of Surface Hydroxyls on the Formation of Zr-Based Conversion Coatings on AA6014 Aluminum Alloy. *Surf. Coatings Technol.* **2014**, *254*, 277–283.

(16) Hu, H.; Saniger, J. M.; Castaño, V. M. Deformation Behavior of Polyacrylic Acid-Metal Oxide Composites in Water. *Mater. Lett.* **1993**, *16* (4), 200–205.

(17) Wit, F. M. De; Mol, J. M. C.; Terryn, H.; Wit, J. H. W. De; Mol, J. M. C.; Terryn, H.; Influence, J. H. W. D. W. T. The Influence of Chemical Pre-Treatment and Magnesium Surface Enrichment on Bonding of Succinic Acid Molecules to Aluminium Alloy The Influence of Chemical Pre-Treatment and Magnesium Surface Enrichment on Bonding of Succinic Acid Molecules. *J. Adhes. Sci. Technol.* **2008**, *22*, 1089–1104.

(18) Mohr, S.; Doepper, T.; Xu, T.; Tariq, Q.; Lytken, O.; Laurin, M.; Steinrueck, H.-P.; Goerling, A.; Libuda, J. Organic Linkers on Oxide Surfaces: Adsorption and Chemical Bonding of Phthalic Anhydride on MgO(100). *Surf. Sci.* **2016**, *646*, 90–100.

(19) Kresse, G.; Hafner, J. Ab Initio Molecular Dynamics for Liquid Metals. *Phys. Rev. B.* **1993**, *47*, 558.

(20) Kresse, G.; Hafner, J. Ab Initio Molecular-Dynamics Simulation of the Liquid-Metal-Amorphous-Semiconductor Transition in Germanium. *Phys. Rev. B.* **1994**, *49*, 14251.

(21) Kresse, G.; Furthmüller, J. Efficient Iterative Schemes for Ab Initio Total-Energy Calculations Using a Plane-Wave Basis Set. *Phys. Rev. B.* **1996**, *54*, 11169–11186.

(22) Kresse, G.; Fürthmüller, J. Efficiency of Ab-Initio Total Energy Calculations for Metals and Semiconductors Using a Plane-Wave Basis Set. *Comput. Mater. Sci.* **1996**, *6*, 15–50.

(23) Heckel, W.; Würger, T.; Müller, S.; Feldbauer, G. Van Der Waals Interaction Really Matters: Energetics of Benzoic Acid on TiO2 Rutile Surfaces. *J. Phys. Chem. C* **2017**, *121*, 17207–17214.

(24) Klimeš, J.; Bowler, D. R.; Michaelides, A. Chemical Accuracy for the van Der Waals Density Functional. *J. Phys. Condens. Matter* **2010**, *22*, 022201.

(25) Klimeš, J.; Bowler, D. R.; Michaelides, A. Van Der Waals Density Functionals Applied to Solids. *Phys. Rev. B.* **2011**, *83*, 195131.

(26) Román-Pérez, G.; Soler, J. M. Efficient Implementation of a van Der Waals Density Functional: Application to Double-Wall Carbon Nanotubes. *Phys. Rev. Lett.* **2009**, *103*, 096102.

(27) Thonhauser, T.; Cooper, V. R.; Li, S.; Puzder, A.; Hyldgaard, P.; Langreth, D. C. Van Der Waals Density Functional: Self-Consistent Potential and the Nature of the van Der Waals Bond. *Phys. Rev. B.* **2007**, *76*, 125112.

(28) Dion, M.; Rydberg, H.; Schröder, E.; Langreth, D. C.; Lundqvist, B. I. Van Der Waals Density Functional for General Geometries. *Phys. Rev. Lett.* **2004**, *92*, 246401.

(29) Graziano, G.; Klimeš, J.; Fernandez-Alonso, F.; Michaelides, A. Improved Description of Soft Layered Materials with van Der Waals Density Functional Theory. *J. Phys. Condens. Matter* **2012**, *24*, 424216.

(30) Bedolla, P. O.; Feldbauer, G.; Wolloch, M.; Gruber, C.; Eder, S. J.; Dörr, N.; Mohn, P.; Redinger, J.; Vernes, A. Density Functional Investigation of the Adsorption of Isooctane, Ethanol, and Acetic Acid on a Water-Covered Fe(100) Surface. *J. Phys. Chem. C* **2014**, *118*, 21428–21437.

(31) Bedolla, P. O.; Feldbauer, G.; Wolloch, M.; Eder, S. J.; Dörr, N.; Mohn, P.; Redinger, J.; Vernes, A. Effects of van Der Waals Interactions in the Adsorption of Isooctane and Ethanol on Fe(100) Surfaces. *J. Phys. Chem. C* **2014**, No. 118, 17608–17615.

(32) Antlanger, M.; Mayr-Schmölzer, W.; Pavelec, J.; Mittendorfer, F.; Redinger, J.; Varga, P.; Diebold, U.; Schmid, M. Pt 3 Zr(0001): A Substrate for Growing Well-Ordered Ultrathin Zirconia Films Byoxidation. *Phys. Rev. B.* **2012**, *86*, 035451.

(33) Choi, J. I. J.; Mayr-Schmölzer, W.; Mittendorfer, F.; Redinger, J.; Diebold, U.; Schmid, M. The Growth of Ultra-Thin Zirconia Films on Pd 3 Zr(0001). *J. Phys. Condens. Matter* **2014**, *26*, 225003.

(34) Carrasco, J.; Liu, W.; Michaelides, A.; Tkatchenko, A. Insight into the Description of van Der Waals Forces for Benzene Adsorption on Transition Metal (111) Surfaces. *J. Chem. Phys.* **2014**, *140*, 084704.

(35) Matos, J.; Yildirim, H.; Kara, A. Insight into the Effect of Long Range Interactions for the Adsorption of Benzene on Transition Metal (110) Surfaces. *J. Phys. Chem. C* **2015**, *119*, 1886–1897.

(36) Würger, T.; Heckel, W.; Sellschopp, K.; Müller, S.; Stierle, A.; Wang, Y.; Noei, H.; Feldbauer, G. Adsorption of Acetone on Rutile TiO2: A DFT and FTIRS Study. *J. Phys. Chem. C* **2018**, *122* (34), 19481–19490.

(37) Mittendorfer, F.; Garhofer, A.; Redinger, J.; Klimeš, J.; Harl, J.; Kresse, G. Graphene on Ni (111): Strong Interaction and Weak Adsorption. *Phys. Rev. B.* **2011**, *84*, 201401.

(38) Liu, W.; Carrasco, J.; Santra, B.; Michaelides, A.; Scheffler, M.; Tkatchenko, A. Benzene Adsorbed on Metals: Concerted Effect of Covalency and van Der Waals Bonding. *Phys. Rev. B.* **2012**, *86*, 245405.

(39) Endlich, M.; Michl, A.; Hildisch, J.; Müller, S.; Kröger, J. Energy and Spectroscopic Line Shape of

the C-O Stretch Mode on Ir (111) in the Presence of Organic Molecules. *J. Phys. Chem. C* **2016**, *120*, 11490–11497.

(40) Monkhorst, H. J.; Pack, J. D. Special Points for Brillouin-Zone Integrations. *Phys. Rev. B.* **1976**, No. 13, 5188.

(41) Blöchl, P.; Jepsen, O.; Andersen, O. Improved Tetrahedron Method for Brillouin-Zone Integrations. *Phys. Rev. B.* **1994**, *49*, 16223–16233.

(42) Oviedo, J.; San, M.; Sanz, J. Oxygen Vacancies on TiO 2 (110) from First Principles Calculations. *J. Chem. Phys.* **2004**, *121*, 7427–7433.

(43) Makov, G.; Payne, M. Periodic Boundary Conditions in Ab Initio Calculations. *Phys. Rev. B.* **1995**, *51*, 4014.

(44) Neugebauer, J.; Scheffler, M. Adsorbate-Substrate and Adsorbate-Adsorbate Interactions of Na and K Adlayers on Al (111). *Phys. Rev. B.* **1992**, *46*, 16067.

(45) Jönsson, M.; Persson, D.; Leygraf, C. Atmospheric Corrosion of Field-Exposed Magnesium Alloy AZ91D. *Corros. Sci.* **2008**, *50*, 1406–1413.

(46) Esmaily, M.; Svensson, J. E.; Fajardo, S.; Birbilis, N.; Frankel, G. S.; Virtanen, S.; Arrabal, R.; Thomas, S.; Johansson, L. G. Fundamentals and Advances in Magnesium Alloy Corrosion. *Prog. Mater. Sci.* **2017**, *89*, 92–193.

(47) Valdez, R.; Manuel, J.; Melgoza, Q. Nanosheets of Co- (Ni and Fe) Layered Double Hydroxides for Electrocatalytic Water Oxidation Reaction. *Int. J. Electrochem. Sci.* **2015**, *10*, 909–918.

(48) Lamaka, S. V.; Gonzalez, J.; Mei, D.; Feyerabend, F.; Willumeit-römer, R.; Zheludkevich, M. L. Local PH and Its Evolution Near Mg Alloy Surfaces Exposed to Simulated Body Fluids. *Adv. Mater. Interfaces* **2018**, *1800169* (5).

(49) Maltseva, A.; Shkirskiy, V.; Lefèvre, G.; Volovitch, P. Effect of PH on Mg(OH)2 Film Evolution on Corroding Mg by in Situ Kinetic Raman Mapping (KRM). *Corros. Sci.* **2019**, *153*, 272–282.

(50) Friedrich, J. *Metal-Polymer Systems: Interface Design and Chemical Bonding*; Wiley-VCH Verlag GmbH & Co., 2018.

(51) George Socrates. *Infrared and Raman Characteristic Group Frequencies*, third edit.; John Wiley & Sons, Inc, 2001.

(52) Brand, J. Van Den; Blajiev, O.; Beentjes, P. C. J.; Terryn, H.; Wit, J. H. W. De. Interaction of Ester Functional Groups with Aluminum Oxide Surfaces Studied Using Infrared Reflection Absorption Spectroscopy. *Langmuir* **2004**, *20*, 6318–6326.

(53) Beentjes, P. C. J.; Van den Brand, J.; De Wit, J. H. W. Interaction of Ester and Acid Groups Containing Organic Compounds with Iron Oxide Surfaces. *J. Adhes. Sci. Technol.*. **2006**, *20* (1), 1–18.

(54) Hu, H.; Saniger, J.; Garcia-Alejandre, J.; Castaño, V. M. Fourier Transform Infrared

Spectroscopy Studies of the Reaction between Polyacrylic Acid and Metal Oxides. *Mater. Lett.* **1991**, *12* (4), 281–285.

(55) Pletincx, S.; Marcoen, K.; Trotochaud, L.; Fockaert, L.-L.; Mol, J. M. C.; Head, A. R.; Karslioğlu, O.; Bluhm, H.; Terryn, H.; Hauffman, T. Unravelling the Chemical Influence of Water on the PMMA/Aluminum Oxide Hybrid Interface In Situ. *Sci. Rep.* **2017**, *7* (1), 13341.

(56) Kosmulski, M. Isoelectric Points and Points of Zero Charge of Metal (Hydr)Oxides: 50 Years after Parks' Review. *Adv. Colloid Interface Sci.* **2016**, *238*, 1–61.

(57) Taheri, P.; Hauffman, T.; Mol, J. M. C.; Flores, J. R.; Hannour, F.; Wit, J. H. W. De; Terryn, H. Electrochemical Analysis of the Adsorption and Desorption Behaviors of Carboxylic Acid and Anhydride Monomers onto Zinc Surfaces. *Electrochim. Acta* **2011**, *56* (25), 9317–9323.

(58) Tao, Y. T. Structural Comparison of Self-Assembled Monolayers of n-Alkanoic Acids on the Surfaces of Silver, Copper, and Aluminum. *J. Am. Chem. Soc.* **1993**, *115* (10), 4350–4358.

(59) Brown, I. D.; Shannon, R. D. Empirical Bond-Strength–Bond-Length Curves for Oxides. *Acta Crystallogr. Sect. A* **1973**, *29* (3), 266–282.

(60) Shannon, B. Y. R. D.; H, M.; Baur, N. H.; Gibbs, O. H.; Eu, M.; Cu, V. Revised Effective Ionic Radii and Systematic Studies of Interatomie Distances in Halides and Chaleogenides. *Acta Crystallogr. Sect. A* **1976**, *32*, 751–767.

(61) Bjelopavlic, M.; Hassan, E.; Moudgill, B. M. *Polymers in Particulate Systems, Chapter 4, Role of Polymer Functionality in Specific Adsorption to Oxides: A Molecular Recognition Approach*; Hackley, V. A., Somasundaran, P., Lewis, J. A., Eds.; New York, Dekker, 2002.

(62) Kassai, M.; Ravi, R. G.; Shealy, S. J.; Grant, K. B.; Box, P. O. Unprecedented Acceleration of Zirconium (IV) -Assisted Peptide Hydrolysis at Neutral PH. *Inorg. Chem.* **2004**, *43* (20), 6130–6132.

(63) EDCt.

(64) Zhao, J.; Wang, J. Understanding the Amide-II Vibrations in β-Peptides. *J. Phys. Chem. B* **2015**, *119* (47), 14831–14839.

(65) Barthés-Labrousse, M. G. Acid-Base Characterisation of Flat Oxide-Covered Metal Surfaces. *Vacuum* **2002**, *67* (3–4), 385–392.

(66) Mercier, D.; Rouchaud, J. C.; Barthés-Labrousse, M. G. Interaction of Amines with Native Aluminium Oxide Layers in Non-Aqueous Environment: Application to the Understanding of the Formation of Epoxy-Amine/Metal Interphases. *Appl. Surf. Sci.* **2008**, *254* (20), 6495–6503.

Chapter 5 : Chemisorption of coil coat primers

This chapter presents in-situ ATR-FTIR in the Kretschmann configuration as interfacial sensitive technique able to probe molecular processes at the interface of an industrial relevant coil coat. The reaction mechanisms elucidated for ester-functionalized molecules were shown to be valid on polyester paint. However, a different coordination was demonstrated compared to monomeric molecules due to steric hindrance of the ester-functionalized groups in the polymer backbone. Moreover, it was evidenced that chemisorption takes place upon immediate contact and thus prior to curing, although curing results in a reorganization of the polymer chains. Furthermore, in addition to interactions with the polyester resin, also interactions with the melamine-based crosslinker were evidenced. Native magnesium oxide and titanium-treated zinc substrates were shown to have the highest affinity for interactions with the melamine-based crosslinker, which was associated to the oxide's physicochemical properties. This highlights the increased complexity of interfacial phenomena at metal–paint interfaces. In accordance to the observations made in chapter 3, it has been demonstrated that zirconium- and titanium-treatments improve the bonding properties of galvanized steel substrates. Yet, these bonding properties were not further enhanced by the addition of organic compounds.

5.1 Introduction

The use of simplified organic compounds has shown to be useful for revealing chemisorption mechanisms.[1] However, hitherto, these insights have not been validated on industrially relevant paints, which typically consist of crosslinkers, curing agents, matting agents, fillers, binders, corrosion-inhibiting pigments, etc. This complex chemistry and constitution of a multicomponent coating is one reason why molecular studies on metal-paint interfaces are limited. Another component that affect the interfacial strength are crosslinkers and more specifically, the degree of crosslinking. Too much crosslinking can make the polymer system too rigid hindering dissipation. On the other hand, less crosslinked polymers are more elastic, so when performing the pull-off test they may deform before the interface breaks.[2] Moreover, in case of a not fully crosslinked polymer system a higher amount of functional groups will be available to interact with the metal substrate.[3] Next to the amount of crosslinkers, also curing is assumed to have an impact on the interfacial properties. Chemical interactions at the metal-polymer interface are expected to take place already before curing.[4] However, curing can change the interface significantly. For instance, it has been reported that curing can relieve polymeric constraints leading to a lower steric hindrance and a stronger metal-polymer bonding.[5] It becomes increasingly clear that adhesion properties are not only a result of resin chemistry. In addition, also disbondment phenomena of painted metal substrates result from an interplay of multiple compounds present in the complex paint formulation.[1,6,7] Moreover, the role of zirconium-based conversion treatments on interfacial bond formation and degradation with industrially relevant paints has not yet been described. The main reason for this is the high complexity of commercial conversion systems containing inorganic and organic additives which increases the surface chemistry complexity. Thus the high share of variables at industrially relevant metal-polymer hybrid systems hinder a straightforward interpretation of bonding properties at these hybrid interfaces.

Due to the well-known difficulties of studying buried metal-polymer interfaces, most interface studies are based on simplification of polymer formulation. Nevertheless, from industrial perspective, there is still a need to obtain reliable molecular information of true metal-paint interfaces. This work attempts to validate the chemisorption mechanisms previously described for ester-functionalized compounds to industrially relevant multicomponent polyester primer formulations using ATR-FTIR in Kretschmann configuration. For ATR-FTIR studies IR-transparent metal substrates are evaporated on internal reflection elements (IRE) on which subsequently a realistic polyester primer is applied (with a thickness within µm-scale). The incident IR-light passes the IRE generating an evanescent wave which penetrates through the thin metal film (20-50 nm). As a consequence, the attenuated reflected IR beam contains molecular information from the metal-

polyester interface. In section 5.3.1 the polyester coil coat has been characterized by means of ATR-FTIR and Raman. Subsequently, section 5.3.2 describes the chemisorption of polyester coil coat on native multi-metal substrates (i.e. zinc, aluminium and magnesium). Subsequently, the effect of zirconium-treatment on the chemisorption of polyester coatings has been investigated in section 5.3.3. To gain fundamental insights on the bonding properties associated by the zirconium conversion oxide layer, there has been opted to use a model conversion solution containing H_2ZrF_6, without organic or inorganic additives. This allows to use study solely the effect of zirconium oxide to the bonding properties of multi-metal substrates . Thereafter, in section 5.3.4 a comparative study has been performed on the role of zirconium and titanium cation in terms of bonding properties of zinc substrates using mode conversion solutions based on H_2ZrF_6 and H_2TiF_6. Finally section 5.3.5 discusses the effect of organic additives is elucidated by polymeric compounds to the model zirconium- and titanium conversion solutions. Three organic additives have been selected based on the polymeric compounds frequently reported in patents being polyacrylic acid (PAA), polyvinyl alcohol (PVA) and polyvinyl pyrrolidone (PVP).

5.2 Experimental

5.2.1 Materials and chemicals.

50 nm zinc (Goodfellow, 99.95%), aluminium (Johnson Matthey, 99.99%) and magnesium (Alfa Aesar, 99.9%) were deposited on germanium internal reflection elements (IRE) by means of a high-vacuum evaporation system (VCM 600 Standard Vacuum Thermal Evaporator, Norm Electronics). To investigate the effect of the cation (Zr vs Ti) and organic additives, model conversion treatments were prepared. Hexafluorozirconic acid, 50 wt% in H_2O (Sigma-Aldrich Chemistry) and hexafluorotitanic acid, 60wt% in H_2O (SigmaAldrich Chemistry) were diluted to 0.01 M. The pH was adjusted to 4 using 1 M NaOH. The polymer additives investigated as potential adhesion enhancers were polyvinyl alcohol (PVA) molecular weight 145 000 (Sigma-Aldrich Chemistry), polyvinylpyrrolidone (PVP) molecular weight 360 000 (Sigma-Aldrich Chemistry) and polyacrylic acid (PAA) molecular weight 150 000 (Sigma-Aldrich Chemistry). They were added to the fluoroacid solutions with a concentration of 0.1 g/L. To dissolve the polymers, stirring at elevated temperatures was required. PVA and PAA were fully dissolved after 30 min stirring at 70°C, PVP required a higher temperature and was dissolved after 12 hours stirring at 80 °C. Aluminium and zinc coated IREs were dipped in conversion solution at room temperature for 60 seconds, whereas the exposure time of magnesium coated IRE to the conversion solution was limited to 10 seconds, due to the high reactivity of the thermally vaporized magnesium film. Subsequently, the samples were generously rinsed with demineralized water and dried with pressurized air. A polymer coating with polyester-based resin, Dynapol LH 820 (Evonik Industries AG) was applied using a 30 µm bar coater. The

resulting polymer film was cured for 15 minutes at 130 °C, which is the maximum operating temperature for germanium IRE. For the studies on multi-metal oxide studies pigmented polyester primer has been used, whereas the comparative zirconium vs titanium studies are conducted using the polyester clear coat formulation. Both the pigmented primer and clear coat formulations can be found in chapter 2, table 2.2.

5.2.2 ATR-FTIR in Kretschmann configuration

The FTIR apparatus was a Thermo-Nicolet Nexus equipped with a liquid-nitrogen cooled mercury-cadmium-telluride (MCT) detector and a nitrogen-purged measurement chamber with a Veemax III single reflection ATR accessory. Germanium IRE (PIKE Technologies) with a fixed face angle of 60 degrees were used. IR-light was configured with an incident set angle of 80 degrees. A precision manual polarizer (PIKE) was mounted on the Veemax III and set to 90° for p-polarized and 0° for s-polarized IR-light. For the chemisorption studies infrared backgrounds were obtained from the metallic coated IRE, after conversion treatment when applicable. Infrared spectra were collected every 300 seconds and averaged from 128 cycles with a resolution of 4 cm^{-1}. The control of the spectra acquisition and incident angles was managed by the OMNIC 8.1 software package (ThermoElectron Corporation, Madison, WI).

5.3 Results

5.3.1 Characterization polyester primer

The ATR-FTIR spectrum of bulk polymer, presented in figure 5.1, was collected on a chemically inert germanium internal reflection element at 80° incidence IR angle. A carbonyl stretching vibration (C=O) appears at 1723 cm^{-1}, together with C-O stretching vibration bands in the region 1100 – 1300 cm^{-1}, with the most intense peak absorption positioned at 1231 cm^{-1} (C-O), which is characteristic for a polyester resin.[8] Peaks in the 3000 – 2800 cm^{-1} region, enlarged in figure 5.1, indicate the presence of CH_2 and CH_3 bonds. Asymmetric and symmetric C-H stretching vibrations specific to CH_3 groups are observed at 2962 and 2890 cm^{-1}, respectively.[8] Shoulders at 2934 and 2876 cm^{-1} relate to asymmetric and symmetric C-H stretching vibrations of CH_2 groups.[8] Whereas, the bands at 1476 and 1374 cm^{-1} are assigned to C-CH_2-C and C-CH_3 bending vibrations, respectively.[8] The occurrence of vibrational bands at 1551 and 815 cm^{-1} can be ascribed to melamine triazine ring (C=N-C) stretching and side chain (C-N) asymmetric stretching vibrations, respectively, specific to the melamine-based crosslinker.[8] The sharp peak observed at 728 cm^{-1} can be assigned to C-H rocking vibrations of the methyl groups, originating from the highly methylated melamine-based crosslinker. The minor sharp peak at 1607 cm^{-1} together with the small signal at 3074 cm^{-1} are indicative for benzene ring vibrations, referring to aromatic structures in the polyester resin.[8] The minor peak at 874 cm^{-1} can be

assigned to $CaCO_3$ that acts as a filler. The assignment of peaks positioned between 1000 – 1200 cm^{-1} is more complex, as different vibrations occur in this region. Examples of possible explanations of peaks in this region are skeletal C-H and C-O rocking vibrations related to the resin and matting agent or Si-O stretching vibration specific to the thickening agent SiO_2.[8]

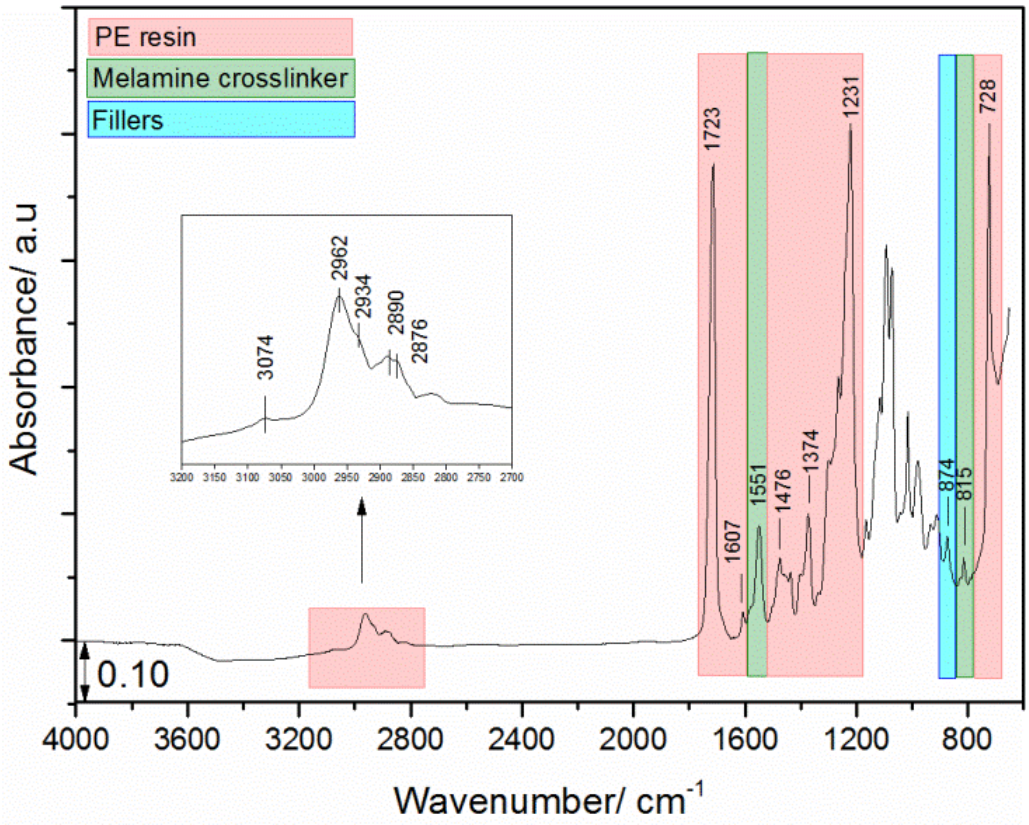

Figure 5.1: ATR-FTIR spectrum of cured polyester coating applied on germanium internal reflection element, collected using non-polarized IR-light at an incident angle of 80 degrees.

Figure 5.2 (a-c) presents Raman spectra of the polyester primer. In the low frequency region, presented in figure 2 (a) the presence of rutile TiO_2 pigment is illustrated at 445 and 609 cm^{-1}. Ma sharp peak at 1002 cm^{-1} may be interpreted as the filler $CaSO_4$. In the mid IR-frequency region, peaks with maximum intensity are observed at 1308 (C-O), 1377 ($C-CH_3$), 1450 ($C-CH_2-C$), 1612 (aromatic ring) and 1724 (C=O) cm^{-1}. When comparing this Raman spectrum with the peaks observed in the mid-IR region, it can be noted that the melamine peak at IR-frequency 1551 cm^{-1}, does not occur in the Raman spectrum. Therefore, the melamine-based crosslinker is suggested to be asymmetric, probably due to its chemical environment. Moreover, the intensity of the Raman peak at 1612 cm^{-1}, specific to aromatic ring vibrations, equals the intensity of the carbonyl peak at 1724 cm^{-1}. Considering the sensitivity of Raman for symmetric bonds this suggests a high concentration of ester-functionalized groups in the polymer.

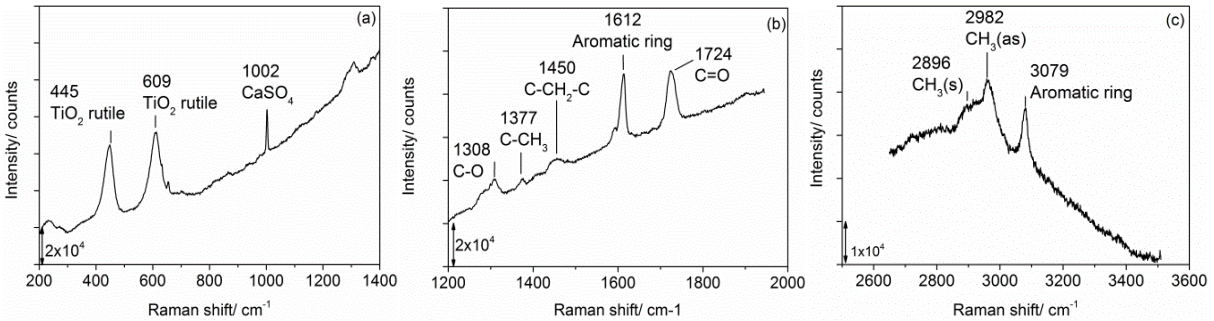

Figure 5.2: Raman spectrum of cured polyester clearcoat applied on CaF_2 window, collected with a 532 nm laser, using 2400 grating, with centre at (a) 850 cm^{-1}, (b) 1400 cm^{-1} and (c) 3100 cm^{-1}.

5.3.2 Chemisorption mechanism polyester coil coat on native multi-metal oxides

ATR-FTIR spectra of the cured polyester coats were obtained after background collection of the metallic coated internal reflection elements. The combination of the high refractive index of germanium with a 80° incident IR angle gives the most interfacial sensitive results. Figure 5.3 (a) demonstrates a clear reduction of OH-stretch vibrations in the FTIR spectra of cured polyester coats applied on native metal oxides. Since the spectra in figure 5.3 were collected using the native oxides as background, this reduction must be related to the disappearance of OH-groups at the oxide surfaces. For aluminium and magnesium a second negative band characteristic of O-H bending vibrations is observed at ca. 1690 cm^{-1} and 1670 cm^{-1}, respectively. The observed intensity reduction of OH stretch vibrations, can be related to chemisorbed water being removed during curing at elevated temperatures (130°C) and/or the consumption of metal hydroxides in interfacial reactions with the polyester coating. After curing of the polyester primer, an intense peak around 1609 cm^{-1} arises in the ATR-FTIR spectra, presented in figure 5.3. The peak positioned at circa 1609 cm^{-1} is positioned at similar wavenumbers as the aromatic ring vibration observed in the cured polyester coat described in figure 5.1. However, aromatic ring vibrations are rather symmetric and thus their infrared vibrations appear as small sharp peaks[9], whereas the peak shapes in figure 5.3 (a) and (b) are broader and more intense. Therefore, the peak is attributed to carboxylate stretching vibrations, which are known to be broad due to interactions with their chemical environment.[10] There are two possible origins for the formed carboxylate species upon interaction with native metal oxides. A first hypothesis relates to the free acid groups present in the polyester resin, as indicated by the acid value in table 5.1. The polyester carbonyl peak in absence of metal substrate, presented in figure 5.1, has shown to be positioned at 1723 cm^{-1}. After interaction with metal oxides, the carbonyl peak shifts to higher wavenumbers, being, 1727 cm^{-1} on native zinc oxide, and at 1731 cm^{-1} on native magnesium and aluminium oxide. Since the carbonyl peak appears symmetric without a distinct shoulder, carbonyl bonds specific to acid and ester groups are expected to occur very close to each

other. Yet, acid carbonyl stretching vibrations are known to appear at lower wavenumbers (1700 - 1725 cm^{-1})[9] compared to ester carbonyl stretching vibrations (1725 – 1750 cm^{-1})[9]. Therefore, the observed shift of the carbonyl peak towards higher wavenumbers upon interaction with metal oxide is interpreted as a reduced contribution of acid groups at the interface. This implies that acid groups at the interface are being deprotonated and form interfacial carboxylate bonds with the metal oxide explaining the appearance of a new peak at 1609 cm^{-1} assigned to asymmetric carboxylate stretch vibration. A second hypothesis relates to the capability of metal oxides to hydrolyse ester-functionalities to more reactive acid groups. The formation of interfacial carboxylate bonds between ester-functionalities and metal oxide surfaces has previously been reported for model compounds.[11,12] The high intensity of the asymmetric carboxylate peak with respect to the carbonyl peak, together with the reduced C-O peak intensities, suggest the consumption of ester groups. Therefore, it is expected that zinc, aluminium and magnesium oxide are capable of hydrolysing ester groups of the polyester resin to form interfacial carboxylate bonds. Consequently, chemical interactions with native zinc, aluminium and magnesium oxide is shown to occur with both acid and ester groups present in the polyester resin.

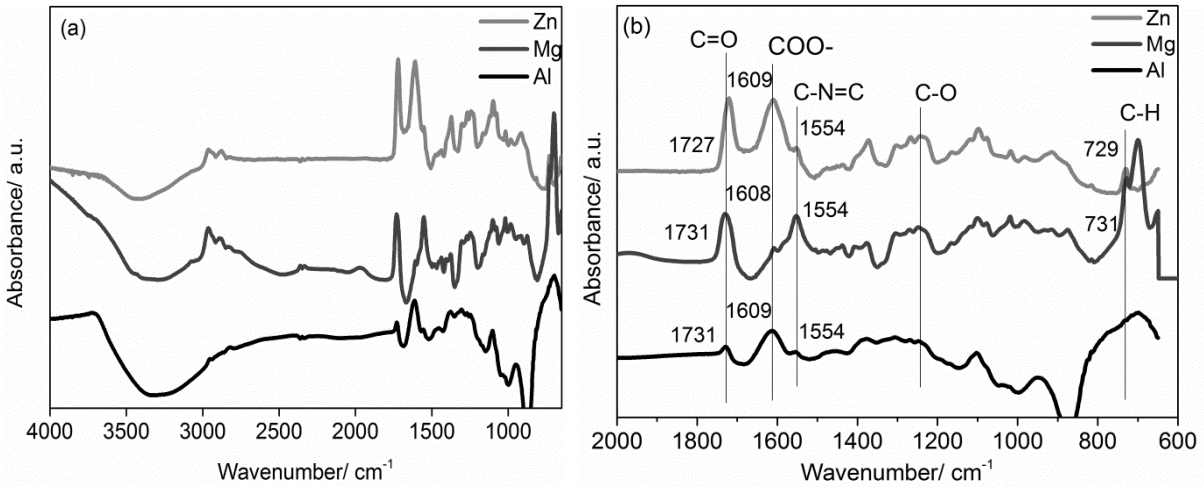

Figure 5.3: ATR-FTIR spectra of cured polyester coating applied on native zinc, magnesium and aluminium oxide, collected using p-polarized IR-light with an incident angle of 80 degrees (a) full scale, (b) head group region.

Furthermore, figure 5.3 (b) demonstrates variations in C-N=C peak intensities. The crosslinking reaction between polyester resin takes place between terminal CH_3 groups of the highly methylated melamine-based crosslinker and OH-groups of the highly hydroxylated polyester[13], as illustrated in figure 2.6. Yet, similar interactions might take place with metal hydroxides, which are also the bonding site for interaction with ester/acid functional groups of the polyester resin. Consequently, competition between chemisorption of melamine-based crosslinker and polyester resin is expected

at the metal oxide surface. The ATR-FTIR spectrum in figure 5.3 (b) demonstrates the highest C-N=C peak intensity as well as the lowest $COO^-_{(as)}$ peak intensity on native magnesium oxide. Therefore, a higher affinity of magnesium oxide to the melamine-based crosslinker is suggested compared to ester/acid groups specific to the polyester resin. A possible explanation for this observation might relate to the ionic nature of magnesium carboxylate complexes, making them less stable compared to zinc- and aluminium carboxylate complexes which bonds have a higher covalent character.[14]

5.3.2.1 Effect of curing

To further investigate whether the established interfacial carboxylate bonds are being formed prior to curing, ATR-FTIR spectra were collected of uncured polyester coat applied on native zinc oxide, as illustrated in figure 5.4. The immediate presence of a strong carboxylate peak at 1609 cm^{-1} verifies that indeed chemical bonds between zinc and polyester are being formed upon immediate contact, even at room temperature. Three vibrational peaks show dynamic behaviour during chemisorption of the polyester coat at room temperatures, being the broad OH-band at 3435 cm^{-1}, which slightly reduces during chemisorption, and the growth of peaks at 1609 cm^{-1} and 1373 cm^{-1}. The reduction of OH stretch vibration can be assigned to hydroxide consumption required for ester hydrolysis. The increase of peak intensities at 1609 cm^{-1} and 1373 cm^{-1} are assigned to asymmetric and symmetric carboxylate stretch vibrations, respectively. This means that the asymmetric and symmetric carboxylate stretching peaks are separated by 236 cm^{-1}, which is too high for bridging bidentate coordination ($\Delta\nu$ 120 - 180)[15] and more in line with monodentate coordination ($\Delta\nu$ > 200)[15]. Comparing the ATR-FTIR spectra of polyester coat before curing, shown in figure 5.4, with those obtained after curing, shown in figure 5.3, a significant reduction of peaks at 1373, 1241, 1110 and 728 cm^{-1} are being observed after curing. The reduction of the sharp peak at 1373 cm^{-1} relates to the disappearance of symmetric carboxylate stretch vibrations using p-polarized light implying a strong orientation of interfacial carboxylate bonds upon curing. More details on orientation are discussed in the following section. Decreased peak intensities at 1241 cm^{-1} and 1110 cm^{-1} refer to reduced C-O bonds as a consequence of the crosslinking reaction illustrated in figure 5.4. Finally, the strong sharp peak at 728 cm^{-1} is assigned to C-H rocking vibrations of terminal CH_3 groups of the melamine crosslinker, which are also being consumed during the curing reaction.

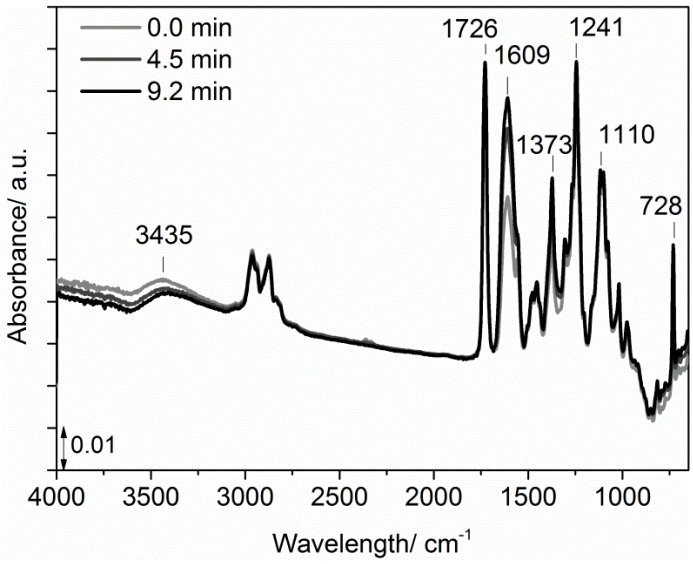

Figure 5.4: Chemisorption kinetics of uncured polyester coat applied on native zinc oxide, collected using p-polarized IR-light.

5.3.2.2 Orientation analysis

Variations in asymmetric and symmetric carboxylate peak intensities before and after curing indicate a reorientation of interfacial carboxylate bonds upon curing. Figure 5.5, compares the ATR-FTIR spectra of polyester coated zinc, collected after curing using p-, s- and non-polarized infrared light. It is evidenced that the asymmetric carboxylate stretch vibration becomes most intense when using p-polarized infrared light. The symmetric carboxylate stretch vibration is not directly evidenced, suggesting strong orientation of interfacial carboxylate bonds upon curing.

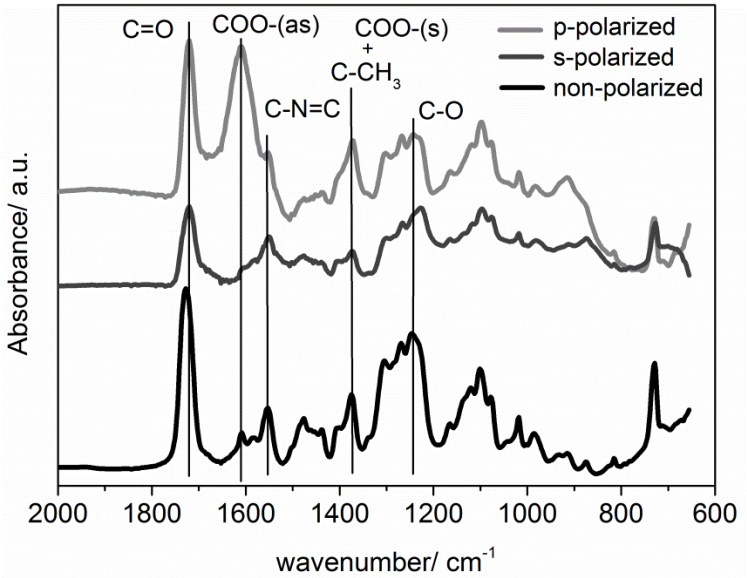

Figure 5.5: ATR-FTIR spectra of cured polyester coating applied on zinc coated germanium internal reflection element, collected using p-polarized, s-polarized and non-polarized IR-light with an incident angle of 80 degrees.

The fact that the asymmetric stretch vibration is strongly enhanced using p-polarized light contradicts the expected bridging bidentate coordination, which has previously been observed for carboxylic compounds.[16–19] For bridging bidentate coordination, asymmetric carboxylate stretch vibrations are expected to be most intense using s-polarized IR-light. This because the dipole moments of asymmetric stretch vibrations are in plane with the substrate in case of bridging bidentate coordination, as illustrated in figure 5.6. On the other hand, in case of monodentate coordination, a dipole moment perpendicular to the surface is expected for asymmetric carboxylate stretch vibrations. Thus, based on the enhancement of asymmetric carboxylate bonds using p-polarized IR-light, as well as the large separation between asymmetric and symmetric carboxylate peaks observed before curing, it can be concluded that interfacial carboxylate bonds are oriented at the interface in a monodentate coordination. Likely, the bridging bidentate coordination mode for monomeric ester-functionalized compounds is not favourable for macromolecular structures due to steric effects.[20]

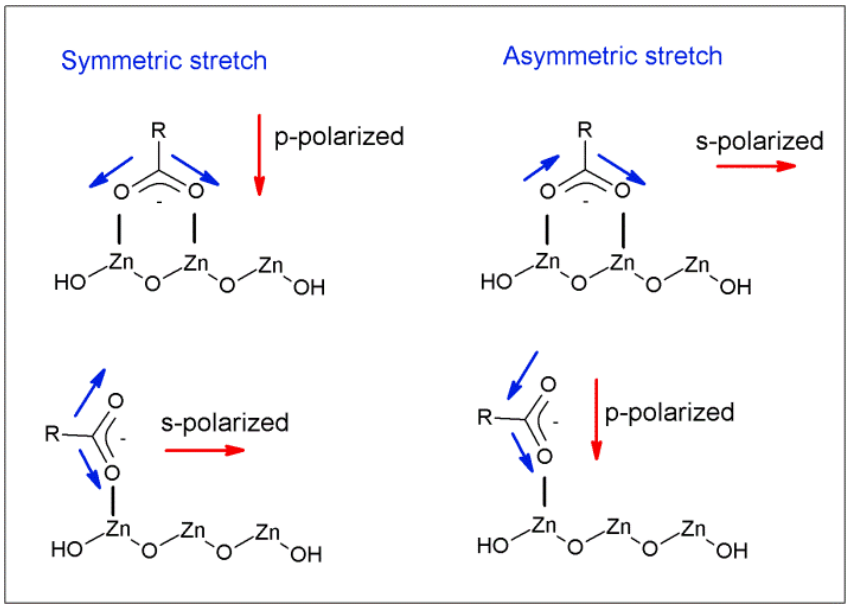

Figure 5.6: Transition dipole moments of asymmetric and symmetric carboxylate stretch vibrations in different coordination modes.

5.3.3 Chemisorption mechanism polyester coil coat on zirconium-treated multi-metal oxides

The ATR-FTIR spectra of cured polyester coating on zirocnium-treated (ZrCC) aluminium, zinc and magnesium, obtained using p-polarized IR-light, are shown in figure 5.7. Asymmetric carboxylate stretch vibrations are revealed on all zirconium-treated susbstrates. Consequently, it can be concluded that the bonding mechanism does not alter upon zirconium- treatment. Similar to the ATR-FTIR spectra obtained with native oxides, also on zirconium-treated oxides, the carbonyl peak shifts to higher wavenumbers, indicating the consumption of carboxylic acid groups. On the other

hand, the intensity of both C=O and C-O bonds remains higher than the asymmetric carboxylate (COO^-_{as}) peak characteristic for newly formed carboxylate bonds. Because of this, it is suggested that surface hydroxides at the zirconium-treated oxides less likely hydrolyse ester groups. Probably, increased surface acidity due to the high valency of zirconium reduces the metal hydroxide donating properties required for ester hydrolysis reactions as discussed in chapter 4 and illustrated in figure 4.11.[21]

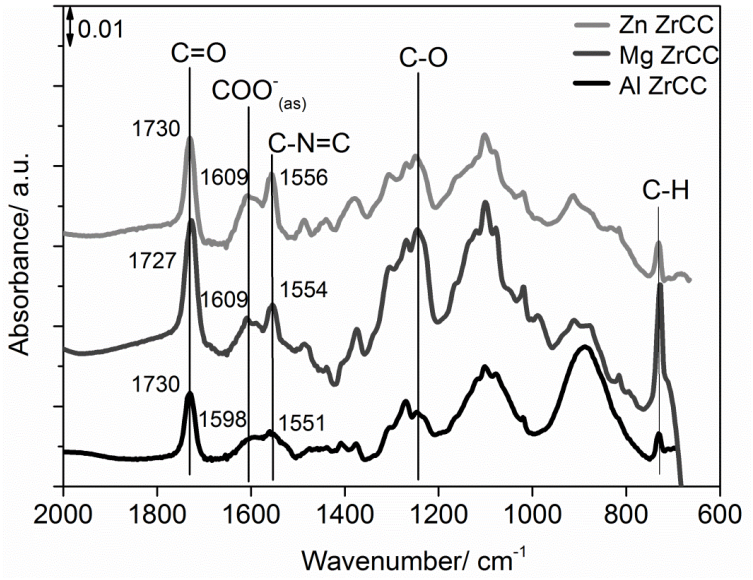

Figure 5.7: ATR-FTIR spectra of cured polyester coating applied on zirconium- treated (ZrCC) zinc, magnesium and aluminium, collected using p-polarized IR-light with an incident angle of 80 degrees.

5.3.4 Chemisorption mechanism polyester coil coat on zirconium- and titanium-treated zinc substrates The effect of chemical conversion treatment on the molecular organisation at the polymer – metal interface is studied using ATR-FTIR in Kretschmann configuration. Figure 5.8 illustrates ATR-FTIR spectra obtained without metallic film (blank), native zinc oxide (Zn), titanium-treated zinc (Zn TiCC) and zirconium-treated zinc (Zn ZrCC). The blank ATR-FTIR spectrum of cured polyester coating is characterized by a strong peak at 1715 cm^{-1} assigned to C=O stretch vibrations, a small sharp peak at 1605 cm^{-1} attributed to aromatic ring stretching vibrations and a peak at 1550 cm^{-1} assigned to ring vibrations specific to the melamine-based crosslinker.[8] Additional peaks in the lower wavenumber region are attributed to the polymer backbone of both the polyester resin and the melamine-based crosslinker, as well as fillers present in the paint formulation.[8] It can be seen that upon interaction with variously treated zinc substrates the peak at 1605 cm^{-1} appear more broad and intense. Since aromatic ring vibrations do not broaden in FTIR spectra, this band is ascribed to asymmetric carboxylate (COO^-_{as}) stretching vibrations associated to the formation of a newly formed interfacial bond.[8] Furthermore, the carbonyl peaks observed on zirconium- and titanium-treated zinc are positioned at higher wavenumbers (1726 and 1729 cm^{-1}, respectively) compared to untreated

zinc (1714 cm^{-1}). From the coil coat formulation it is known that the polyester resin contains both acid and ester functional groups, which leads to two contributions at the carbonyl peak. Since ester carbonyl bonds vibrate at higher wavenumbers (> 1720 cm^{-1})[9] compared to acid carbonyl bonds (< 1720 cm^{-1}),[9] this shift towards higher wavenumbers indicates a reduced fraction of acid carbonyl bonds at the conversion treated zinc interface. Consequently, protonated acid groups (COOH) are being converted to deprotonated carboxylate groups (COO^-) at the zinc surface forming interfacial carboxylate bonds, which is in accordance with the appearance of a broad carboxylate peak at 1605 cm^{-1}. A similar bonding mechanism, i.e. interfacial carboxylate bond formation with carboxylic groups specific to the polyester resin, is thus revealed on both the native zinc oxide surface as well as the zirconium- and titanium-treated zinc surfaces. Yet, a lower carbonyl (C=O) and higher carboxylate (COO^-_{as}) peak intensity can be observed for zirconium-treated compared to titanium-treated substrates. This demonstrates a higher affinity of zirconium oxide for carboxylates bond formation with the polyester resin. On the other hand, the shoulder attributed to C-N=C bonds of the melamine-based crosslinker is more pronounced at titanium-treated zinc substrates suggesting a higher bonding affinity of titanium oxide to the melamine-based crosslinker.

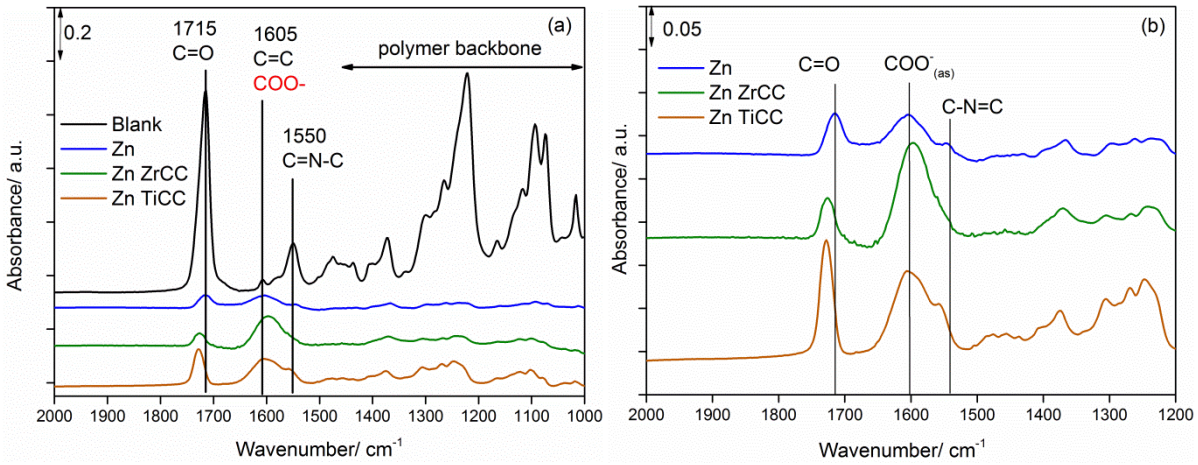

Figure 5.8: (a) ATR-FTIR spectra of cured polyester coating applied on blank IRE (without zinc film) and variously treated zinc substrates (b) zoom in polyester coating interaction with variously treated zinc substrates.

5.3.5 Chemisorption mechanism polyester coil coat on zinc substrates treated with zirconium- and titanium conversion solutions containing organic additives

Figures 5.9 (a) and (b) show the obtained interfacial chemistry between variously treated zinc substrates and the polyester coating upon adding the polymeric compounds of interest (PAA, PVA and PVP) to the zirconium- and titanium--treatments respectively. It should be noted that these spectra were collected using the conversion treated zinc substrates as a background, which means

that the chemical structures associated with the polymeric compounds are also included in the background. Despite the inclusion of organic additives in the background, it can be seen from figure 5.9 (a) that the carbonyl (C=O) peak intensity of polyester coated zinc increases for zirconium-treatments containing organic additives. This increase in carbonyl (C=O) bonds indicates the presence of more carboxylic groups (COOH or COOR) at the converted oxide interface which are not involved in interfacial carboxylate bond formation (COO^-). Consequently, the presence of organic additives does not further improve the bonding properties of zirconium oxide, which is in line with the similar or lowered polar component of the surface free energies illustrated in chapter 3, figure 3.22. Figure 5.9 (b) shows more variations in the respective peak intensities. Similar to the ATR-FTIR spectra in figure 5.8, a higher C-N=C peak area, assigned to the melamine-based crosslinker is demonstrated for titanium-treated zinc substrates, shown in figure 5.9 (b). To verify the degree of interfacial bond formation the COO^-_{as}/C=O peak area ratio is calculated, which requires deconvolution of the carboxylate peak into its two components, being COO^-_{as} and C-N=C. This was done using the following fitting parameters: COO^-_{as} 1595 ± 6 cm^{-1}, FWHM of 56 ± 4 cm^{-1} and C-N=C 1552 ± 10 cm^{-1}, FWHM of 25 ± 3 cm^{-1}. From the obtained peak areas for COO^- and C-N=C bonds, competitive interfacial interactions with polyester resin and melamine-based crosslinker were verified using the COO^-_{as}/C=O and COO^-_{as}/C-N=C peak area ratios, respectively presented in figure 5.10 (a) and (b).

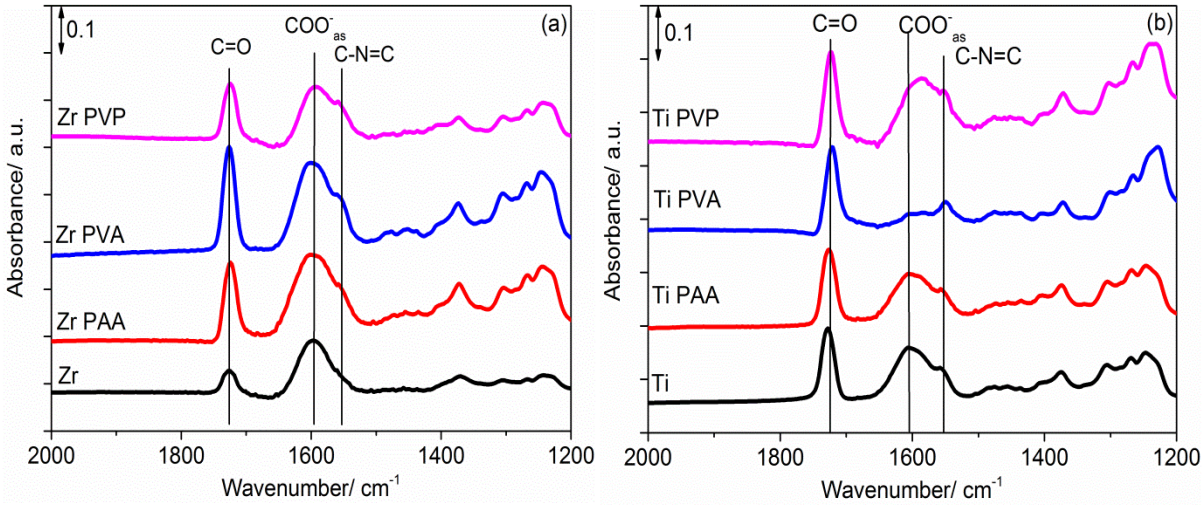

Figure 5.9: ATR-FTIR spectra of cured polyester coating applied on (a) zirconium-treated zinc and (b) titanium-treated zinc substrates.

Figure 5.10 (a) shows the resulting COO^-_{as}/C=O peak area ratios. The higher this ratio, the more carboxylate bonds are being formed at the respective oxide surface. This confirms the higher affinity for carboxylate bond formation of zirconium-treatment compared to titanium-treatment. The presence of organic additives does not further enhance carboxylate bond formation, but in case of

PAA and PVA rather reduces the chemical reactivity of zirconium oxide. This observation is likely associated to the crosslinking of the respective polymeric compounds into the zirconium oxide structure, thereby reducing available bonding sites. Furthermore, figure 5.10 (b) shows the COO^-_{as}/C-N=C peak area ratios. The lower values obtained for titanium-treated zinc substrates confirm their higher affinity for the melamine-based crosslinker. It is well-known that titanium, due to its small ionic radius, is even more acidic than zirconium. Consequently, its high positive partial charge leads to a lower tendency to donate hydroxide ions. Because of this, electrostatic interactions with the highly polarized titanium oxide structure and electron-rich nitrogen ring structures are hypothesized as favoured interaction mechanism. The carboxylic acid study, presented in chapter 4, indicated that electrostatic interactions between metal oxides and electron-rich ring structures can play a predominant role in interfacial metal-molecule interactions, as they were held responsible for the in-plane orientation of aromatic compounds. A comparable interaction mechanism is proposed between titanium-treated zinc substrates and the electron-rich ring structures of the melamine-based crosslinker.

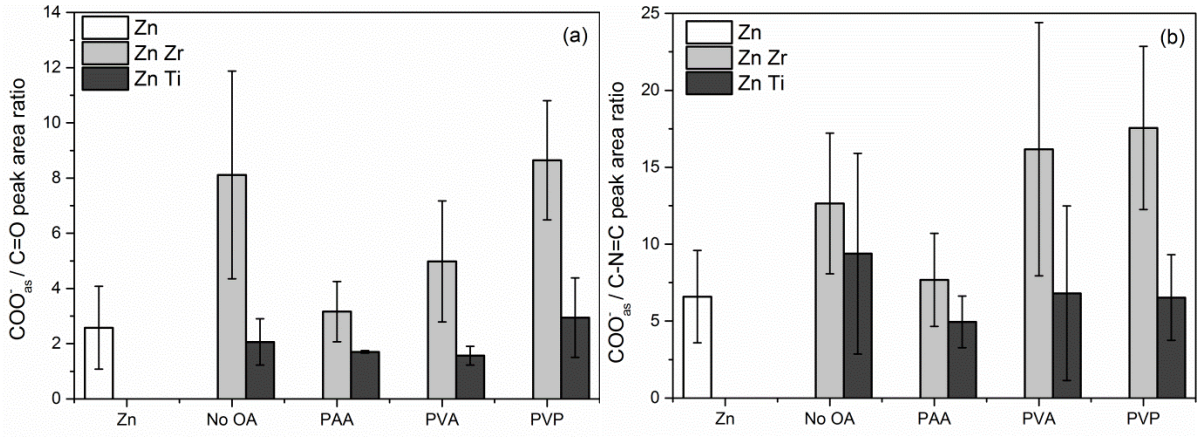

Figure 5.10: ATR-FTIR peak area ratio obtained for variously treated zinc substrartes (a) COO^-_{as}/C=O ratio representative for carboxylate bond formation with polyester resin, (b) COO^-_{as}/C=N-C ratio representative for competitve interaction with melamine-based crosslinker.

5.4 Conclusions

The chemisorption of an industrially relevant polyester coil coat was revealed on variously treated multi-metal substrates. The polyester resin was shown to interact with the metal oxide surface forming interfacial monodentate carboxylate bonds. The establishment of carboxylate bonds is thus in line with the observed chemisorption mechanism elucidated using ester-functionalized model compounds as discussed in chapter 4. However, whereas monomeric model compounds were shown to coordinate in a bridging bidentate mode, polyester resin forms monodentate carboxylate

complexes. The formation of a monodentate coordination was attributed to a combination of steric hindrance and a lower mobility of functional groups due to the large polymeric backbone. Interactions between zinc oxide and polyester resin were shown to occur upon immediate contact. Yet, upon curing at elevated temperatures the carboxylate bonds became more strongly oriented at the interface. A higher affinity for carboxylate bond formation was evidenced on zirconium-treated than on titanium-treated zinc substrates. Similar observations have been made in other research fields, such as the development of metal organic frameworks (MOFs)[22,23] and is believed to be associated to the crosslinking abilities of zirconium oxide. The presence of organic additives did not further enhance carboxylate bond formation, but in case of PAA and PVA even reduces the chemical reactivity of zirconium oxide. Furthermore, it was evidenced that metal oxide not only interacts with polyester resin, but also with the electron-rich groups of the melamine-based crosslinker. As such, titanium-treated zinc demonstrated a higher bonding affinity for the melamine-based crosslinker than zirconium-treated zinc substrates. That interactions with the melamine-based crosslinker are more pronounced on titanium-treated zinc substrates might imply that these interactions are electrostatic. It is well-known that titanium due to its small ionic radius is even more acidic than zirconium. Consequently, its tendency to donate hydroxide ions is very low. Because of this, electrostatic interactions with the highly polarized titanium oxide structure and electron-rich nitrogen ring structures are hypothesized as favoured interaction mechanism.

References

(1) Pletincx, S.; Fockaert, L. L. I.; Mol, J. M. C.; Hauffman, T.; Herman, T. Probing the Formation and Degradation of Chemical Interactions from Model Molecule / Metal Oxide to Buried Polymer / Metal Oxide Interfaces. *npj Mater. Degrad.* **2019**, *3* (23), 1–12.

(2) Abbott, S. *Adhesion Science: Principles and Practice*; DEStech Publications, Inc, 2015.

(3) Papaj, E. A.; Mills, D. J.; Jamali, S. S. Effect of Hardener Variation on Protective Properties of Polyurethane Coating. *Prog. Org. Coatings* **2014**, *77* (12), 2086–2090.

(4) Perruchot, C.; Watts, J. F.; Lowe, C.; Beamson, G. Characterisation of the Curing Temperature Effects on Polyester Systems by Angle-Resolved XPS (ARXPS). *Int. J. Adhes. Adhes.* **2003**, *23*, 101–113.

(5) Taheri, P.; Flores, J. R.; Hannour, F.; De Wit, J. H. W.; Terryn, H.; Mol, J. M. C. In Situ Study of Buried Interfacial Bonding Mechanisms of Carboxylic Polymers on Zn Surfaces. *J. Phys. Chem. C* **2013**, *117* (7), 3374–3382.

(6) Öhman, M.; Persson, D. ATR-FTIR Kretschmann Spectroscopy for Interfacial Studies of a Hidden Aluminum Surface Coated with a Silane Film and Epoxy I. Characterization by IRRAS and ATR-FTIR. *Surf. Interface Anal.* **2012**, *44* (2), 133–143.

(7) Taheri, P.; De Wit, J. H. W.; Terryn, H.; Mol, J. M. C. In Situ Study of Buried Metal-Polymer Interfaces Exposed to an Aqueous Solution by an Integrated ATR-FTIR and Electrochemical Impedance Spectroscopy System. *J. Phys. Chem. C* **2013**, *117* (40), 20826–20832.

(8) George Socrates. *Infrared and Raman Characteristic Group Frequencies*, third edit.; John Wiley & Sons, Inc, 2001.

(9) Coates, J. *Encyclopedia of Analytical Chemistry, Interpretation of Infrared Spectra , A Practical Approach*; Meyers, R. A., Ed.; John Wiley & Sons, Ltd.

(10) Tao, Y. T. Structural Comparison of Self-Assembled Monolayers of n-Alkanoic Acids on the Surfaces of Silver, Copper, and Aluminum. *J. Am. Chem. Soc.* **1993**, *115* (10), 4350–4358.

(11) Leadley, S. R.; Watts, J. F. The Use of Monochromated XPS to Evaluate Acid- Base Interactions at the PMMA/Oxidised Metal Interface. *J. Adhes.* **1997**, *60*, 175–196.

(12) Pletincx, S.; Marcoen, K.; Trotochaud, L.; Fockaert, L.-L.; Mol, J. M. C.; Head, A. R.; Karslioğlu, O.; Bluhm, H.; Terryn, H.; Hauffman, T. Unravelling the Chemical Influence of Water on the PMMA/Aluminum Oxide Hybrid Interface In Situ. *Sci. Rep.* **2017**, *7* (1), 13341.

(13) Wilson, R. C.; Pfohl, W. F. Study of Cross-Linking Reactions of Melamine r Formaldehyde Resin with Hydroxyl Functional Polyester by Generalized 2-D Infrared Spectroscopy. *Vib. Spectrosc.* **2000**, *23*, 13–22.

(14) Hu, H.; Saniger, J. M.; Castaño, V. M. Deformation Behavior of Polyacrylic Acid-Metal Oxide

Composites in Water. *Mater. Lett.* **1993**, *16* (4), 200–205.

(15) Zelenak, V.; Vargova, Z.; Györyova, K. Correlation of Infrared Spectra of Zinc(II) Carboxylates with Their Structures. *Spectrochim. Acta - Part A Mol. Biomol. Spectrosc.* **2007**, *66* (2), 262–272.

(16) Dobson, K. D.; McQuillan, A. J. In Situ Infrared Spectroscopic Analysis of the Adsorption of Aromatic Carboxylic Acids to TiO2, ZrO2, Al2O3, and Ta2O5 from Aqueous Solutions. *Spectrochim. Acta - Part A Mol. Biomol. Spectrosc.* **2000**, *56* (3), 557–565.

(17) Dobson, K. D.; McQuillan, a J. An Infrared Spectroscopic Study of Carbonate Adsorption to Zirconium Dioxide Sol-Gel Films from Aqueous Solutions. *Langmuir* **1997**, *7463* (13), 3392–3396.

(18) Taheri, P.; Wielant, J.; Hauffman, T.; Flores, J. R.; Hannour, F.; Wit, J. H. W. De; Mol, J. M. C.; Terryn, H. A Comparison of the Interfacial Bonding Properties of Carboxylic Acid Functional Groups on Zinc and Iron Substrates. *Electrochim. Acta* **2011**, *56* (4), 1904–1911.

(19) van den Brand, J.; Blajiev, O.; Beentjes, P. C. J.; Terryn, H.; de Wit, J. H. W. Interaction of Anhydride and Carboxylic Acid Compounds with Aluminum Oxide Surfaces Studied Using Infrared Reflection Absorption Spectroscopy. *Langmuir* **2004**, *20* (15), 6308–6317.

(20) Alexander, M. R.; Beamson, G.; Blomfield, C. J.; Leggett, G.; Duc, T. M. Interaction of Carboxylic Acids with the Oxyhydroxide Surface of Aluminium: Poly(Acrylic Acid), Acetic Acid and Propionic Acid on Pseudoboehmite. *J. Electron Spectros. Relat. Phenomena* **2001**, *121* (1–3), 19–32.

(21) Fockaert, L. I.; Taheri, P.; Abrahami, S. T.; Boelen, B.; Terryn, H.; Mol, J. M. C. Zirconium-Based Conversion Film Formation on Zinc, Aluminium and Magnesium Oxides and Their Interactions with Functionalized Molecules. *Appl. Surf. Sci.* **2017**, *423*, 817–828.

(22) Assi, H.; Mouchaham, G.; Steunou, N.; Devic, T.; Serre, C. Titanium Coordination Compounds : From Discrete Metal Complexes to Metal – Organic Frameworks. *Chem. Soc. Rev.* **2017**, *46*, 3431–3452.

(23) Bai, Y.; Dou, Y.; Xie, L.; Rutledge, W.; Li, J.; Zhou, H. Zr-Based Metal–Organic Frameworks: Design, Synthesis, Structure, and Applications. *Chem. Soc. Rev.* **2016**, *45*, 2327–2367.

Chapter 6 : Interfacial stability polyester coil coat primers

Zirconium-based conversion treatments are currently being used as Cr(VI)-free pretreatment for multi-metal substrates prior to painting. However, due to well-known difficulties of studying buried metal-polymer interfaces, its effect on the established interface in aqueous solution is far from fully understood. This chapter presents in-situ ATR-FTIR in the Kretschmann configuration as interfacial sensitive technique able to probe interfacial bond formation and degradation in-situ. This demonstrates improved interfacial stability due to zirconium-based treatment in real-time and on a molecular level. It was evidenced in chapter 5 that the presence of organic additives in zirconium- and titanium-treatments did not further improve the bonding properties. Nevertheless, this chapter demonstrates that organic additives are able to improve interfacial stability. Based on the molecular approach, the effect of organic additives on the interfacial stability was most pronounced for titanium-treated substrates, with PAA performing better than PVA, followed by PVP. However, the macroscopic approach conducted upon longer immersion times, demonstrated a reduced adhesion strength due to the presence of organic additives of 40 and 14 % for titanium-treated and zirconium-treated GI, respectively. This adverse effect was attributed to the dissolution of polymeric compounds during immersion.

6.1 Introduction

Zirconium-based conversion treatments are currently being used as Cr(VI)-free pretreatment for multi-metal substrates prior to painting. However, due to well-known difficulties in studying buried metal-polymer interfaces, its effect on the established interface in aqueous solution is far from fully understood. A major reason for this lack of knowledge relates to the well-known difficulties of studying buried interfaces. In addition, the multicomponent composition of both conversion solution and paint formulations hinder a straightforward mechanistic chemisorption study. In the Kretschmann configuration thin metal films (< 80 nm) are deposited on an internal reflection element. The metal film thickness is kept sufficiently low to allow access of infrared light through the metal film, providing interfacial molecular information. The use of such inverted geometry offers the possibility to introduce aqueous media to the metal oxide-polymer interface. Consequently, the stability of the established interface can be evaluated in-situ using ATR-FTIR. There has been opted to use deuterated water (D_2O) because the O-D bending mode is positioned at a lower wavenumber compared to the O-H bending mode (i.e. 1200 vs 1640 cm^{-1}, respectively). This shift allows in-situ study of the evolution of interfacial carboxylate bonds positioned around 1610 cm^{-1} without interference of dominant water signals. The evolving interface chemistry elucidated by ATR-FTIR is subsequently correlated to pull-off adhesion measurements obtained after 24 hours immersion in an aqueous 0.05 M NaCl solution to study its long term stability.

Section 6.3.1 describes in-situ ATR-FTIR in Kretschmann configuration as an interface-sensitive technique to study the interfacial stability of polyester coated metal oxide surface in real time on a molecular level. This has been done on native and zirconium-treated zinc, aluminium and magnesium oxides. In addition, a comparative study on the effect of zirconium-and titanium-treatment and the impact of organic additives on the durability of polyester coated zinc substrates has been elucidated. Subsequently, section 6.3.2 aims to correlate these gained insights to the industrially relevant substrates GI and MZ by pull off adhesion testing, which is indicative for the adhesion strength after immersion in NaCl solution on a macroscopic level.

6.2 Experimental

6.2.1 Materials and chemicals.

Conversion solution: To investigate the effect of the cation (Zr vs Ti) and organic additives, model conversion treatments were prepared. Hexafluorozirconic acid, 50 wt% in H_2O (Sigma-Aldrich Chemistry) and hexafluorotitanic acid, 60wt% in H_2O (SigmaAldrich Chemistry) were diluted to 0.01 M. The pH was adjusted to 4 using 1 M NaOH. The polymer additives investigated as potential adhesion enhancers were polyvinyl alcohol (PVA) molecular weight 145 000 (Sigma-Aldrich

Chemistry), polyvinylpyrrolidone (PVP) molecular weight 360 000 (Sigma-Aldrich Chemistry) and polyacrylic acid (PAA) molecular weight 150 000 (Sigma-Aldrich Chemistry). They were added to the fluoroacid solutions with a concentration of 0.1 g/L. To dissolve the polymers, stirring at elevated temperatures was required. PVA and PAA were fully dissolved after 30 min stirring at 70°C, PVP required a higher temperature and was dissolved after 12 hours stirring at 80 °C.

Pull-off samples: Hot-dip galvanized steel (GI) sheets with a thickness of 0.4 mm were sourced from Tata Steel IJmuiden B. V. They were ultrasonically cleaned in acetone and ethanol both for 10 minutes. This was followed with an alkaline cleaning step at elevated temperature (60 °C) to remove surface aluminium, which results from the galvanizing process.[1] Therefore, the samples (50 x 50 mm) were immersed for 30 seconds in 1 M NaOH adjusted to pH 12 using concentrated phosphoric acid, after which they were rinsed using demineralized water and dried with compressed air. Subsequently, the alkaline cleaned hot-dip galvanized steel substrates chemically treated by submersing them for 90 seconds in the respective conversion solutions followed by a rinsing step with demineralized water. The variously treated substrates were spincoated with a polyester clearcoat (Dynapol LH 820, Evonik Industries AG) at a speed of 1250 rpm for 40 seconds, whereafter they were cured at 225°C for 5 minutes. The dry film thickness (10 ± 2 µm) was measured using an Elcometer® 456 coating thickness gauge. The device was first calibrated on uncoated GI using the 'zero' calibration method, which is ideal for calibrating on uncoated smooth surfaces.

ATR-FTIR samples: 50 nm zinc (Goodfellow, 99.95%), aluminium (Johnson Matthey, 99.99%) and magnesium (Alfa Aesar, 99.9%) were deposited on germanium internal reflection elements (IRE) by means of a high-vacuum evaporation system (VCM 600 Standard Vacuum Thermal Evaporator, Norm Electronics). Aluminium and zinc coated IREs were dipped in conversion solution at room temperature for 60 seconds, whereas the exposure time of magnesium coated IRE to the conversion solution was limited to 10 seconds, due to the high reactivity of the thermally vaporized magnesium film. Subsequently, the samples were generously rinsed with demineralized water and dried with pressurized air. A polymer coating with polyester-based resin (Dynapol LH 820, Evonik Industries AG) was applied using a 30 µm bar coater. The resulting polymer film was cured for 15 minutes at 130 °C, which is the maximum operating temperature for germanium IRE. For the studies on multi-metal oxide studies pigmented polyester primer has been used, whereas the comparative zirconium vs titanium studies are conducted using the polyester clear coat formulation. Both the pigmented primer and clear coat formulations can be found in chapter 2, table 2.2.

6.2.2 ATR-FTIR in Kretschmann configuration

The FTIR apparatus was a Thermo-Nicolet Nexus equipped with a liquid-nitrogen cooled mercury-cadmium-telluride (MCT) detector and a nitrogen-purged measurement chamber with a Veemax III single reflection ATR accessory. Germanium IRE (PIKE Technologies) with a fixed face angle of 60 degrees were used. IR-light was configured with an incident set angle of 80 degrees. A precision manual polarizer (PIKE) was mounted on the Veemax III and set to 90° for p-polarized IR-light. For the chemisorption studies infrared backgrounds were obtained from the metallic coated IRE, after zirconium-based treatment when applicable. The established interfacial chemistry was followed in-situ during exposure to D_2O (99.9 %, Sigma-Aldrich Chemistry). For these in-situ stability studies, infrared backgrounds were obtained after applying the polymer coating on the respective metal oxides. Consequently, as the interfacial chemistry established after curing was involved in the background, the evolution of interfacial bonds may appear positive, when being increased, or negative when being reduced relative to the initial dry (cured) situation. Infrared spectra were collected every 300 seconds and averaged from 128 cycles with a resolution of 4 cm^{-1}. The control of the spectra acquisition and incident angles was managed by the OMNIC 8.1 software package (ThermoElectron Corporation, Madison, WI).

6.2.3 Pull-off adhesion testing

Pull-off adhesion tests, according to the ASTM D4541-17 standard were performed using the Elcometer® 106 Pull-Off Adhesion tester. Prior to the adhesion testing, coil coated samples were submersed in a 0.05 M NaCl solution for 24 hours. Subsequently, 20 mm diameter dollies were attached to each coated sample using SG 300-05 adhesive (SciGrip) and cured for 24 hours at room temperature. Prior to testing each sample was glued to a 4 mm thick carbon steel plate with cyanoacrylate adhesive to prevent deformation of the 0.4 mm thick galvanized steel substrates. Subsequently, the polyester coat was cut around the dolly to avoid shear stresses on the dolly-polyester coat bond. The dollies were pulled off at a rate of 10 mPa per second.

6.3 Results

6.3.1 In-situ ATR-FTIR study revealing molecular disbondment on a molecular scale

The stability of established interfacial carboxylate bonds has been studied using in-situ ATR-FTIR. Cured polymer coatings applied on nano metallic layers thermally vaporized on germanium IRE have been used as background. Therefore, positive peaks are interpreted as gained bonds and negative peaks as lost bonds at the interface with respect to the dry state. Consequently, interfacial bonds established after curing are expected to appear as negative peaks at the onset of delamination.

6.3.1.1 Native and zirconium-treated zinc oxide

Figure 6.1 (a) and (b) presents in-situ ATR-FTIR spectra obtained during submersion of polyester coated zinc oxide in D_2O. O-D stretch vibrations, positioned at 2500 cm^{-1}, are shown to increase with increasing immersion times referring to the migration of D_2O through the polyester coat towards zinc oxide surface. Simultaneously, peaks assigned to the polyester backbone turn negative illustrating the replacement of polyester by D_2O at the zinc oxide interface. Contrary, asymmetric carboxylate (COO^-_{as}) stretching vibrations appear positive, which can be interpreted as an increase of carboxylate bonds with respect to the dry state. Consequently, it is evidenced that D_2O induces ester hydrolysis, resulting in increased interfacial carboxylate bonds. Yet, after 0.9 hour, illustrated by the blue curve in figures 6.1 (a) and (b), the asymmetric carboxylate peak reaches its maximum intensity, where after it gradually shifts towards lower wavenumbers when reducing in intensity. Hence, interfacial bond degradation as a result of D_2O penetration is monitored *in situ*. After 2.1 hours, presented by the red curve in figure 6.1, the asymmetric carboxylate peak turns negative. From this point on, a lower amount of interfacial bonds is observed with respect to the dry state.

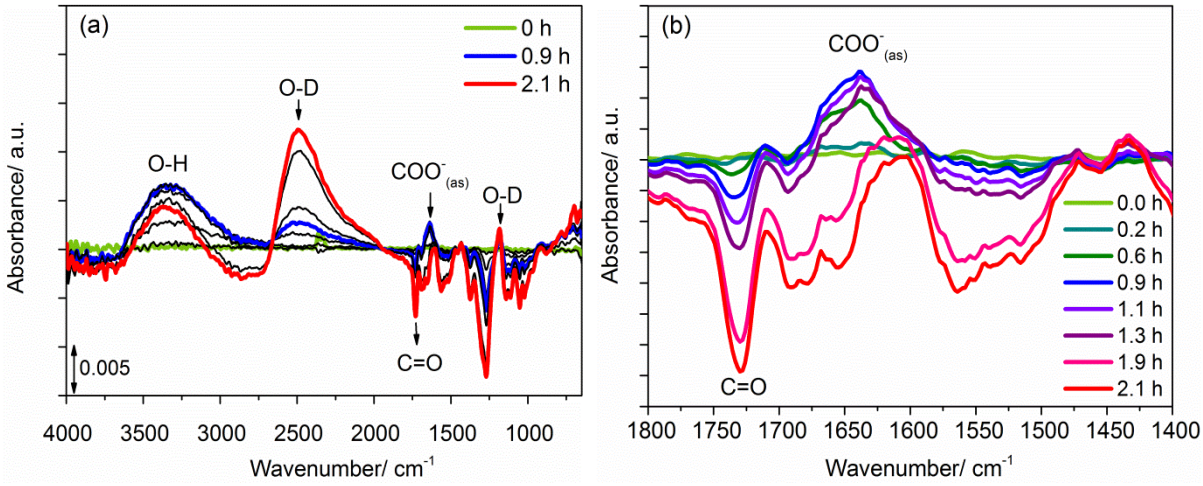

Figure 6.1: ATR-FTIR spectra of D_2O permeation through polyester coating applied on native zinc oxide (a) full scale, (b) enlarged carboxylate region.

A similar evolution of asymmetric carboxylate peak are is observed for zirconium-treated zinc with a maximum of interfacial bonds is observed after 3.6 hours, presented by the blue curve in figure 6.2, followed by interfacial disbondment after 5.5 hours, presented by a red curve. Hence, it is evidenced that the zirconium-treatment of zinc increases the interfacial stability in the presence of D_2O.

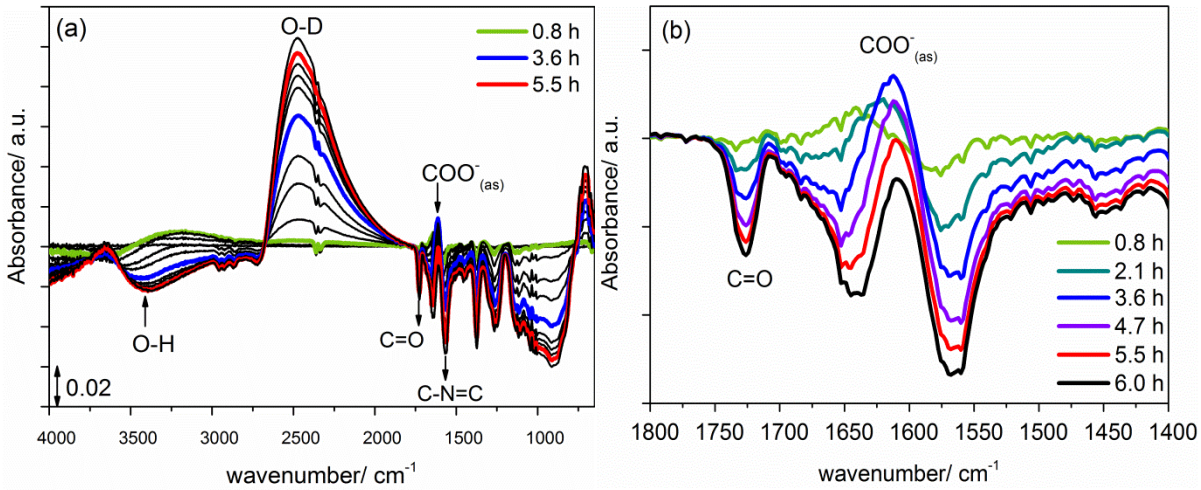

Figure 6.2: ATR-FTIR spectra of D_2O permeation through polyester coating applied on zirconium treated zinc (a) full scale, (b) enlarged carboxylate region.

6.3.1.2 Native and zirconium-treated magnesium oxide

Figure 6.3 demonstrates the interfacial stability of polyester coating applied on native magnesium oxide. An immediate reduction of both carboxylate (COO^-_{as}) and magnesium oxide peaks, suggest that the interface rapidly dissolves upon interaction with D_2O. The high reactivity of magnesium oxide plays a key-role in the instable magnesium-polymer interface.

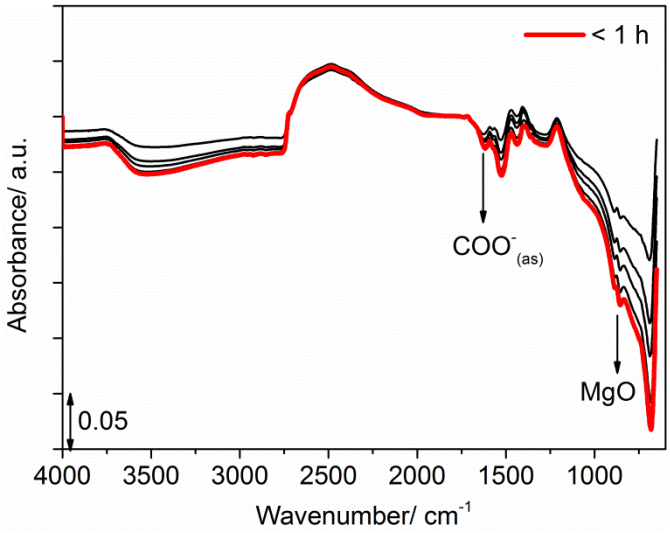

Figure 6.3: ATR-FTIR spectra of D_2O permeation through polyester coating applied on native magnesium oxide.

The interfacial stability of polyester coated zirconium-treated magnesium is presented in figure 6.4 (a) and (b). Peaks at 1595 and 1422 cm^{-1} are assigned to asymmetric and symmetric carboxylate stretching vibrations. Contrary, to native magnesium oxide, carboxylate bonds with zirconium-converted magnesium are shown to increase during initial immersion times in D_2O. The enlarged

carboxylate region, given in figure 6.4 (b), demonstrates maximum carboxylate peak intensity after 3.1 hours where after the asymmetric carboxylate peak gradually reduces. However, disbondment does not occur within the first 19 hours of D_2O accumulation. Large variations in actual disbondment time were observed for zirconium-treated magnesium. The high reactivity of magnesium in the conversion solution resulted in ultrathin converted magnesium films. For this reason, conversion times of 60 seconds as applied on zinc and aluminium were reduced to 10 seconds for magnesium substrates. Yet, due to the high reactivity, the conversion process remains hardly controllable and lead to variations in observed interfacial stability. Nevertheless, the interfacial stability significantly improved due to zirconium-treatment, compared to native magnesium oxide. Moreover, next to the growth of asymmetric carboxylate peaks, positioned at 1595 cm^{-1}, also the growth of C-N=C peak, positioned at 1530 cm^{-1} is demonstrated in figure 6.4 (a) and (b). The simultaneous increase of both carboxylate and melamine peaks confirm the high affinity of magnesium substrates for the melamine-based crosslinker. Therefore, hydroxylation of the zirconium-based converted magnesium surface by D_2O creates increased binding sites for competing interactions with ester groups related to the polyester resin and uncured methyl groups of the melamine-based crosslinker. From the in-situ data presented in figure 6.4 (b), higher interfacial stability is demonstrated for interactions with the melamine, since the asymmetric carboxylate peak reduces more rapidly during immersion in D_2O. Yet, similar to the stability of carboxylate bonds, also variations in stability of melamine-interactions were observed.

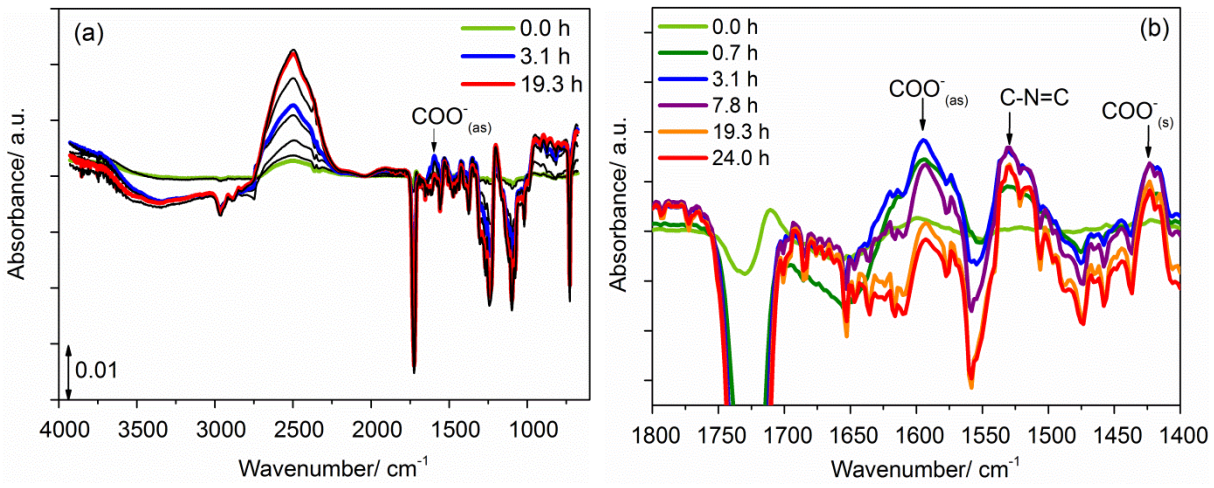

Figure 6.4: ATR-FTIR spectra of D_2O permeation through polyester coating applied on zirconium-treated magnesium oxide (a) full scale, (b) enlarged carboxylate region.

6.3.1.3 Native and zirconium-treated aluminium oxide

Figure 6.5 illustrates the enhancement of interfacial carboxylate bond formation by D_2O on (a) untreated aluminium and (b) zirconium-treated aluminium. The exceptional stability of carboxylate

species adsorbed on both native and zirconium-based converted aluminium oxide (> 24 hours) is related to the stability of aluminium in the presence of D_2O (theoretical pD of D_2O = 7). A broad vibration band at 940 cm^{-1} (Al-O), with a shoulder at 776 cm^{-1} (Al-O-Al) grows at immediate interaction with D_2O. Remarkable is the presence of carbonyl (C=O) stretching vibrations during immersion in D_2O, which appeared to be negative or absent during immersion of zinc and magnesium, respectively. The carbonyl (C=O) peak, positioned at 1723 and 1714 cm^{-1} for untreated and zirconium-treated aluminium, respectively, indicates a shift towards lower wavenumbers with respect to the dry state (1731 and 1730 cm^{-1} for aluminium and zirconium-treated aluminium, as shown in figures 5.3 and 5.7, respectively), indicating its involvement in hydrogen or more correctly deuterium bonds. The higher shift observed in figure 6.5 (b) indicates that deuterium bond interactions are stronger on zirconium-treated aluminium. This is in accordance with the hypothesis that the acid nature of zirconium oxide promotes hydrogen bonding as described for carboxylic monomers in section 4.3.2. The prolonged presence of carbonyl peaks during immersion demonstrate that deuterium bonds formed between both native and zirconium-treated aluminium oxide and polyester carbonyl are stable during immersion in D_2O. Furthermore, peaks attributed to asymmetric carboxylate stretching vibrations appear at 1589 and 1585 cm^{-1} for untreated and zirconium-treated aluminium, respectively. In addition to asymmetric carboxylate peaks also symmetric carboxylate peaks arise upon exposure to deuterated water, positioned at 1408 and 1417 cm^{-1} for untreated and zirconium-treated aluminium, respectively. Consequently, the appearance of a symmetric carboxylate peak indicates an altered orientation of interfacial bonds upon exposure to deuterated water as compared to the dry state, discussed in chapter 5.

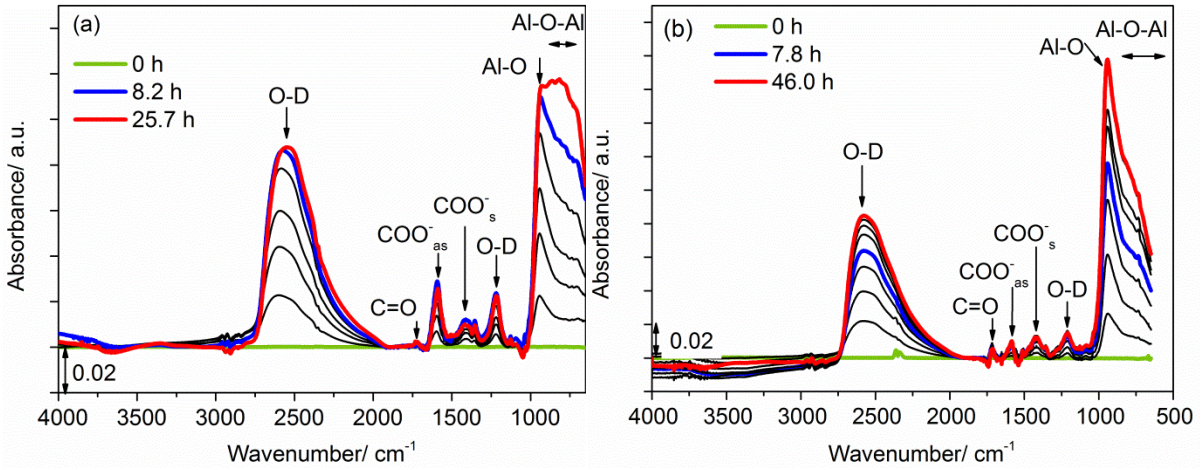

Figure 6.5: ATR-FTIR spectra of D_2O permeation through polyester coating applied on (a) untreated and (b) zirconium- treated aluminium.

6.3.1.4 Quantification of the interfacial stability of zirconium-treated multi-metal oxides

Figure 6.6 presents the quantified carboxylate (COO^-_{as}) peak areas observed on native and zirconium-treated zinc oxide (discussed in 6.3.1.1) versus the immersion time in D_2O. Three stages can be distinguished during the exposure of polyester coated zinc to D_2O. Firstly, carboxylate peaks increase due to hydrolysis reactions induced by D_2O. Secondly, interfacial carboxylate bonds reach a maximum peak area, whereafter their portion gradually decreases, which can be interpreted as the real onset of disbondement. Finally, the carboxylate peak area turns negative, indicating the third stage, which is the defined onset of disbondment. Since the delay time required to reach the defined onset of disbondment is more straightforward to determine than the real onset of disbondment, the former will be used as a reference to quantify the interfacial stability of polymer coated metal substrates.

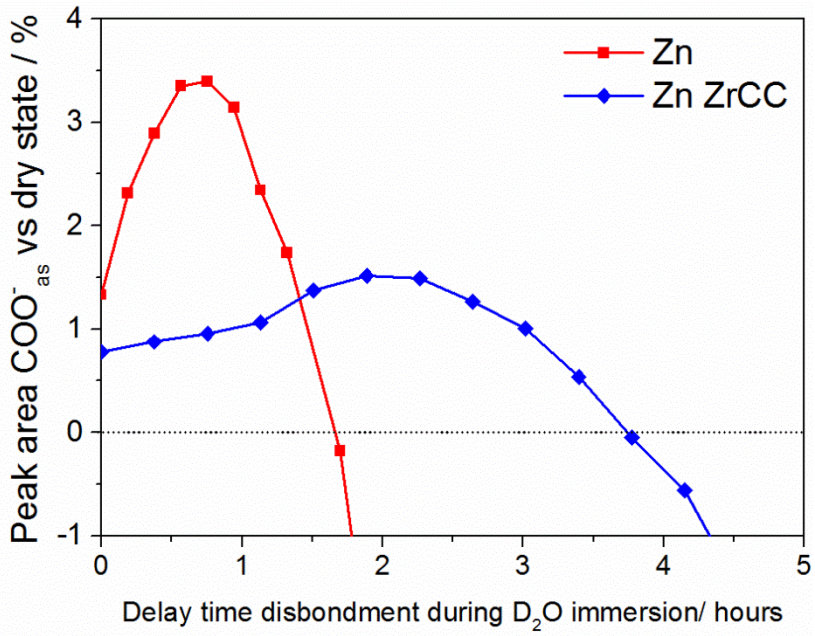

Figure 6.6: Peak area dynamics of polyester coated zinc as a function of exposure time to D_2O.

Figure 6.7 summarizes the defined onsets of delamination during exposure to D_2O, calculated using the approach presented in figure 6.6. On native zinc and magnesium, chemical disbonding is observed rapidly, within less than 2 hours. On the other hand, it is shown that zirconium-treatment successfully passivates the zinc and magnesium oxide surfaces resulting in prolonged interfacial stability. Furthermore, it is clear that the competitive chemisorption of polyester resin and melamine-based crosslinker, as demonstrated on magnesium substrates is not detrimental for the interfacial stability. The highest interfacial stability is demonstrated for aluminium. Interfacial carboxylate bonds established at both untreated, as well as zirconium-treated aluminium remain stable for more than 40 hours. This exceptional durability of the aluminium-polyester interface relates to the stability of aluminium oxide in solutions at neutral pH, or more correct in this case

neutral pD values[2]. Whereas, according to the Pourbaix diagrams, zinc and magnesium are known to be unstable at neutral pH values.[2] zirconium-treatment of zinc and magnesium has shown to passivate these oxides successfully. Further improvement is expected to be possible as a model conversion solution has been used. Optimization of the passivation performance to increase interfacial stability can be done, by adjusting conversion bath concentration and conversion time, as well as by adding organic and/or inorganic additives.

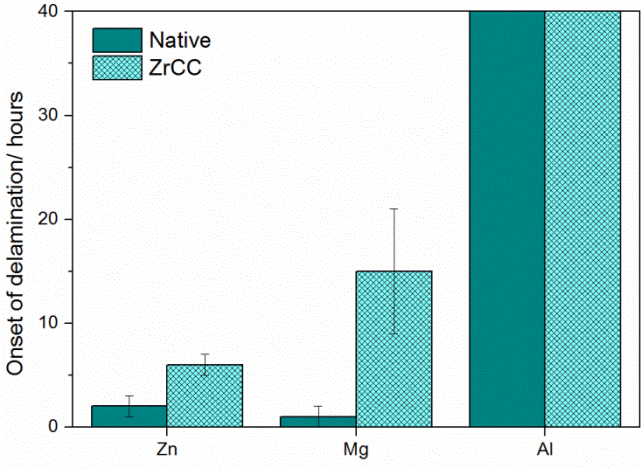

Figure 6.7: Onset of delamination based on infrared peak area of asymmetric carboxylate stretching vibration followed in-situ during exposure to D_2O.

6.3.1.5 Quantification of the interfacial stability of zirconium- and titanium-treated zinc substrates and the effect of organic additives

A similar approach as those discussed in 6.3.1.4 has been used to quantify the interfacial stability of zirconium- and titanium-treated zinc substrates and the effect of organic additives. The required delay times to reach the defined onset of disbanding are summarized in figure 6.8. This evidences a higher interfacial stability for zirconium-treated zinc compared to titanium-treated zinc. On the other hand, the effect of organic additives added to zirconium-treatments is less pronounced than when these are added to titanium-treatments. Comparing the three additives, PAA yields the best performance in stabilizing the zinc-polyester interface in presence of D_2O. On the other hand, PVA and PVP are shown to improve interfacial stability only when added to the titanium-treatment.

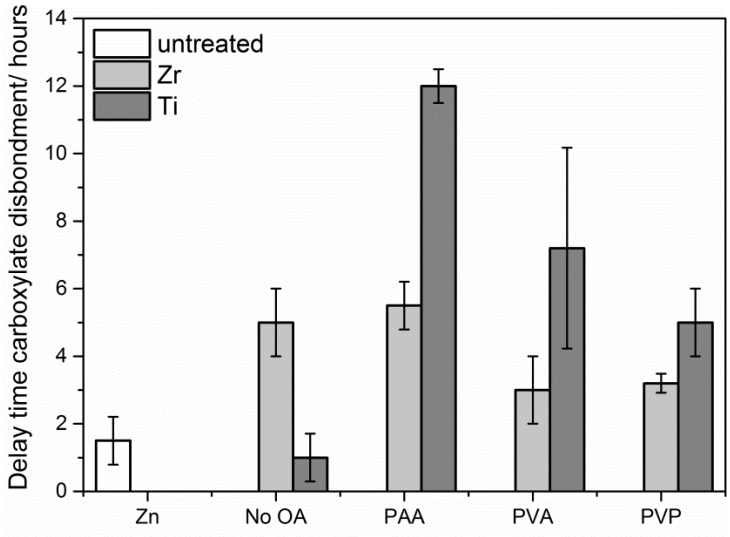

Figure 6.8: Delay time for carboxylate disbondment during immersion in D_2O, observed using in-situ ATR-FTIR.

6.3.2 Pull-off adhesion testing of variously treated GI and MZ revealing interfacial stability on a macroscopic scale

Pull-off adhesion tests have been performed after 24 hours immersion of polyester coated GI substrates in 0.05 M NaCl solution, which results are given in figure 6.9 (a). A pull-off failure stress of 7.2 ± 1.6 MPa was noted for untreated GI. After zirconium- and titanium-treatment the pull-off failure stress increased to 9.3 ± 1.6 MPa and 8.6 ± 1.3 MPa, respectively. The larger increase in adhesion strength in the case of zirconium-treatment (± 30 %) compared to titanium-treatment (± 20 %) is in line with the results presented in chapter 3, evidencing higher polar forces and elemental concentration on zirconium-treated GI compared to titanium-treated GI, as shown in table 3.1 and figure 3.16, respectively. Adding polymeric compounds to both zirconium- and titanium-treatment reduces the adhesion strength. This is most obvious for for the titanium-treatment of GI which gives an adhesion strength of 8.6 ± 1.3 MPa without organic additives and 5.0 ± 0.8 MPa with organic additives. Consequently, the adhesion strength reduced 40 % upon the addition of organic additives after 24 hours of immersion in aqueous environment. In contrast to the initial advantageous effect of the polymeric compounds added to the titanium-treatment, as demonstrated by ATR-FTIR in figure 6.8, the final adhesion strength after longer immersion times becomes thus even worse than untreated GI. The lack of crosslinking ability of titanium oxide is expected to result in more discrete layers of polymeric compounds and titanium oxide, as described in figure 3.23, making them more susceptible to dissolution in aqueous environments. Therefore, the dissolution of the organic additives at the titanium-based conversion coatings is suggested to detoriate the metal-polyester

interface (reduced adhesion strength of 40 %), whereas the impact of organic additives at the zirconium-converted surfaces appears to be more limited (reduced adhesion strength of 14 %).

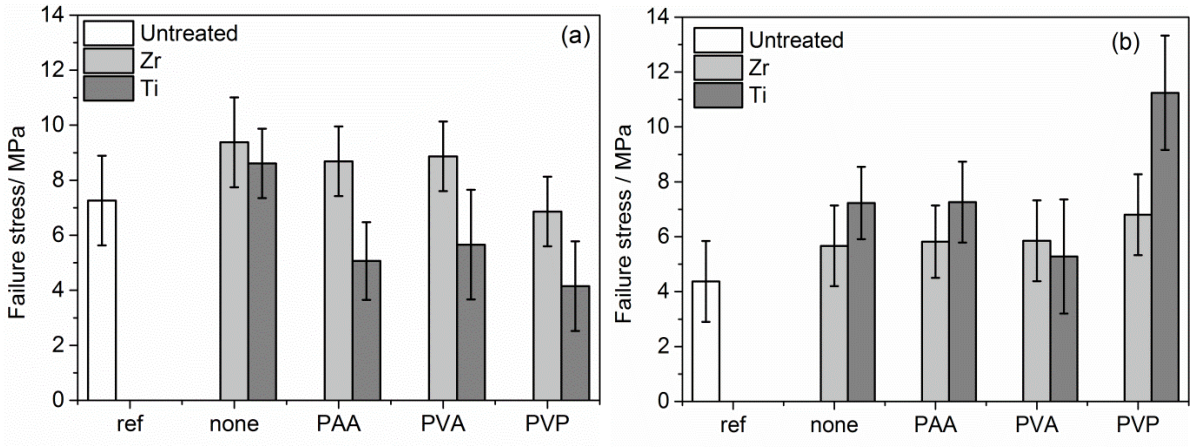

Figure 6.9: Pull-off adhesion strength of variously treated (a) GI and (b) MZ substrates.

The pull-off faillure stresses obtained on variously treated MZ are presented in figure 6.9 (b). Similar to GI, both zirconium-and titanium-treatment improve the adhesion strength of MZ, increasing the failure stresses from 4.3 ± 1.5 MPa to 5.7 ± 1.5 (± 30 %) and 7.2 ± 1.3 MPa (± 65 %), respectively. However, contrary to GI, titanium-treatment of MZ is shown to be more efficient than zirconium-treatment. This is in line with the elemental surface concentrations evidenced by XPS measurements shown in figure 3.1, showing higher titanium compared to zirconium concentrations on conversion treated MZ. Furthermore, in accordance to the observation with GI, organic additives added to the zirconium-treatment of MZ does not significantly alter the adhesion strength, i.e. 6.2 ± 0.6 MPa, which is associated to the crosslinking abilities of zirconium oxide. However, contrary to GI, also the effect of organic additives added to titanium-treatment is shown to be more limited, i.e. 7.9 ± 0.3 MPa. This might be associated to the stable oxides at the MZ surface compared to GI which is benedicial for the interfacial stability. Only PVP is shown to significantly alter the adhesion strength, where it in particular increases the adhesion strength of titanium-treated MZ (± 56 %). Since this beneficial effect of PVP is specific to MZ substrates, it is suggested that the polymeric PVP film is not only concentrated at the outer surface of titanium oxide, but possibly also underneath the titanium oxide at the MZ surface, presented as interface 1 in figure 6.10 (a). As a consequence PVP might anchor both oxide layers by inducing chemical interactions with both magnesium oxide and titanium oxide. Since PVP, which is characterized by a nitrogen containing ring structure has some similarities with melamine, this hypothesis is in accordance with the observations in chapter 5, demonstrating a higher bonding affinity of titanium-treated zinc and native magnesium oxide for the melamine-based crosslinker than for the polyester resin. To confirm this theory, it is recommended to characterize the remainings of both substrate and dolly to gain more insights on the failing interface as illustrated in

figure 6.10 (b). Moreover, although it is expected to be experimentally challenging to study the position of polymeric compounds in the conversion oxide a better understanding of the converison oxide layer-build up with organic additives would give more insights on its effect on interfacial bonding and stability.

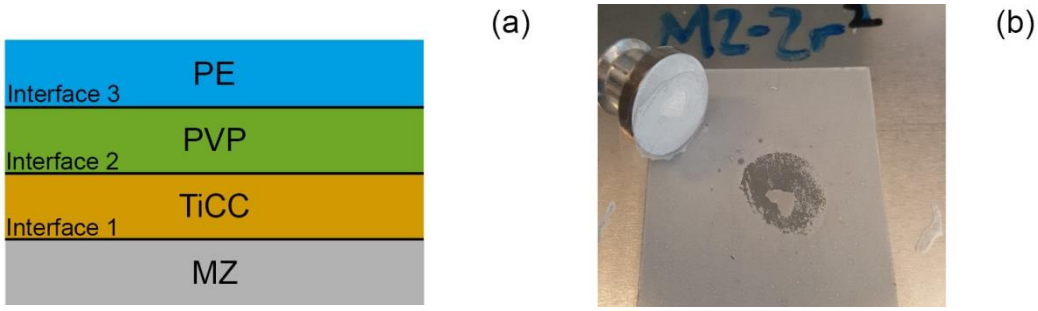

Figure 6.10: (a) Multi-layer polyester coated MZ system, (b) image of resulting pull-off test of zirconium-treated MZ substrate.

6.4 Conclusions

ATR-FTIR in the Kretschmann geometry has shown to be a valuable tool to evaluate the performance of chemical conversion coatings in–situ and on an interfacial level. A molecular approach was proposed to quantify the interfacial stability of polyester coated metal substrates exposed to an aqueous environment. As such, D_2O was chosen as aqueous solution to avoid interference with the asymmetric carboxylate stretch vibrations indicative for interfacial bonding. Three different stages were evidenced when D_2O was introduced at the metal oxide-polyester interface. Initially, enhanced ester hydrolysis reactions lead to increased carboxylate bond formation. Subsequently, the amount of interfacial carboxylate bonds declined, suggesting their replacement by deuterated water. Finally, the asymmetric carboxylate peak area turned negative, indicative for a lower portion of carboxylate bonds with respect to the dry state. Due to their tendency to corrode in neutral aqueous environments, carboxylate disbondment was shown to occur rather rapidly during immersion of polyester coated zinc- and magnesium oxide. However, zirconium-treatment efficiently passivates unstable zinc and magnesium oxide, thereby significantly improving the stability of interfacial carboxylate bonds in aqueous environment. On the other hand, aluminium, which has a stable native oxide layer in neutral aqueous environments performed best regarding interfacial durability. Because of its high stability in aqueous environment, further enhancement of the interfacial stability by zirconium-treatment of aluminium was shown to be limited. Therefore, in addition to the type of interfacial bonds, also the nature of metal oxide is shown to have a predominant role on interfacial stability.

It was demonstrated in chapter 5 that the presence of organic additives in zirconium- and titanium-treatments did not further improve the bonding properties. Yet, in-situ ATR-FTIR measurements presented in this chapter point out that organic additives are able to improve interfacial stability. Based on the molecular approach, the effect of organic additives on the interfacial stability was most pronounced for titanium-treated substrates, with PAA performing better than PVA, followed by PVP. However, the macroscopic approach conducted upon longer immersion times, demonstrated a reduced adhesion strength due to the presence of organic additives of 40 and 14 % for titanium-treated and zirconium-treated GI, respectively. This adverse effect was attributed to the dissolution of polymeric compounds during immersion.

Furthermore, it was demonstrated that zirconium-treatment was more beneficial for the adhesion of polyester coating on GI, whereas the adhesion of polyester on MZ benefits more from the titanium-based treatment. The adhesion strength of titanium-treated MZ could be further improved due to the addition of PVP. It was hypothesized that a PVP film anchors the oxides specific to MZ to titanium oxide thereby improving the adhesion strengths. Yet, more research is required to fully understand the role of the various interfaces at the multi-layer hybrid systems.

References

(1) Fink, N.; Wilson, B.; Grundmeier, G. Formation of Ultra-Thin Amorphous Conversion Films on Zinc Alloy Coatings: Part 1. Composition and Reactivity of Native Oxides on ZnAl (0.05%) Coatings. *Electrochim. Acta* **2006**, *51* (14), 2956–2963.

(2) Pourbaix, M. *Atlas of Electrochemical Equilibria in Aqueous Solutions*; Houston: Nace International 1974, 1974.

(3) Pletincx, S.; Trotochaud, L.; Fockaert, L.-L.; Mol, J. M. C.; Head, A. R.; Karslıoğlu, O.; Bluhm, H.; Terryn, H.; Hauffman, T. In Situ Characterization of the Initial Effect of Water on Molecular Interactions at the Interface of Organic/Inorganic Hybrid Systems. *Sci. Rep.* **2017**, *7*, 45123.

(4) Pletincx, S.; Marcoen, K.; Trotochaud, L.; Fockaert, L.-L.; Mol, J. M. C.; Head, A. R.; Karslioğlu, O.; Bluhm, H.; Terryn, H.; Hauffman, T. Unravelling the Chemical Influence of Water on the PMMA/Aluminum Oxide Hybrid Interface In Situ. *Sci. Rep.* **2017**, *7* (1), 13341.

(5) Pletincx, S.; Mol, J. M. C.; Terryn, H.; Hubin, A.; Hauffman, T. An in Situ Spectro-Electrochemical Monitoring of Aqueous Effects on Polymer / Metal Oxide Interfaces. *J. Electroanal. Chem.* **2019**, *848*, 113311-.

(6) Tao, Y. T. Structural Comparison of Self-Assembled Monolayers of n-Alkanoic Acids on the Surfaces of Silver, Copper, and Aluminum. *J. Am. Chem. Soc.* **1993**, *115* (10), 4350–4358.

Chapter 7 : Validation ATR-FTIR in Kretschmann geometry as in-situ interfacial sensitive technique

Until today in-situ studies of metal-electrolyte interfaces remain experimentally challenging. For this reason most mechanistic studies on corrosion inhibitors are limited to ex-situ studies. Integrating an electrochemical cell in the ATR-FTIR setup creates the opportunity to monitor molecular phenomena at the metal-electrolyte interface in-situ, while simultaneously probing electrochemical properties such as oxide resistance and barrier properties. However, the potentially unique capabilities of such integrated setup have remained underexplored so far, among others due to the high sensitivity of ATR-FTIR for water, which may mask the interface signal of interest. Moreover, ATR-FTIR is limited to thin model metal substrates (<80 nm), which is challenging for highly active substrates such as magnesium in aqueous environment. This work demonstrates the ability of ATR-FTIR to monitor oxide growth and dissolution as well as chemisorption mechanisms of organic inhibiting compounds while simultaneously probing oxide resistances giving unique mechanistic insights in the working principles and performance of corrosion inhibitors for magnesium substrates.

Moreover, there is an ongoing debate on the interfacial sensitivity of ATR-FTIR. This interfacial sensitivity becomes increasingly important when studying industrially relevant paints, studies which are until now rather limited. Due to its selection rules, SFG is an inherently surface sensitive technique. However, likely because of its complexity, rarely used to study metal-polymer hybrid systems. This manuscript presents a comparative interface study of polyester coated zinc using both ATR-FTIR and SFG. This is the first time that SFG studies are being performed on industrially relevant polymer coatings with an applied thickness in the µm-range. Complementary use of both techniques show that the carbonyl and carboxylic acid groups near the interface with zinc/zinc oxide are much more stable than those in the bulk.

7.1 Introduction

ATR-FTIR in the Kretschmann geometry is presumably the most accessible and user-friendly spectroscopic tool to elucidate molecular interactions at the buried polymer-metal (oxide) interfaces. .[1–3] In the Kretschmann geometry, a nanolayered metal (oxide) film, transparent for the IR-beam, is brought in direct contact with an internal reflection element (IRE). Upon reflection from the internal surface of the IRE, an evanescent wave is created and projected orthogonally into the sample. This electromagnetic field, referred to as evanescent wave, extends into the sample and decays exponentially with distance from the IRE interface.[4] The charges in this electromagnetic field polarize the polymer coating, thereby generating a second wave, also known as surface plasmons or the polariton. It is because of this phenomenon, which reduces the intensity of the reflected light, that the technique has obtained its name, attenuated total reflection infrared spectroscopy.[4] The depth of this evanescent wave passing the nanolayered metal film into the polymer coating is a subject of ongoing debate.[5] Typical reported probing depths of ATR-FTIR range from 100 nm to several µm should, implying that it cannot be considered as a surface sensitive technique.[6,7] Nevertheless, ATR-FTIR measurements are frequently used to extract metal-polymer interfacial information.[1–3,8–10] Conversely, visible-infrared sum-frequency generation spectroscopy (SFG) is a second order non-linear technique requiring symmetry breaking and thus a truly interface-sensitive and selective technique. Since, the SFG signal generation is absent in the centrosymmetric media, which is the case for most bulk materials, only molecular bonds at surfaces and interfaces where the symmetry is broken contribute to the SFG signal. Section 7.3.1 presents a comparative ATR-FTIR vs SFG study, to reveal to what extent ATR-FTIR in a Kretschmann configuration represents the interfacial properties of polyester coated zinc oxide. This comparative study has been conducted in the dry state, thus focussing on chemisorption, as well as during immersion in an aqueous environment, focussing on the stability of interfacial bonds. The strengths and limitations of both spectroscopic techniques are being compared to illustrate the complementarity of the two techniques.

The second section 7.3.2, focusses on the integration of an electrochemical cell in the ATR-FTIR setup. This allows monitoring molecular phenomena at the surface, while simultaneously probing electrochemical properties such as oxide resistance and barrier properties.[8,11,12] Consequently, such an integrated setup is very useful to gain fundamental insights in the chemisorption mechanisms of organic compounds (i.e. coatings or corrosion inhibitors), while simultaneously evaluating their performance.[8,13] Nevertheless, until today, most chemisorption studies are limited to ex-situ ATR-FTIR.[14–16] The main reason for the limited use of in-situ ATR-FTIR relates to its high sensitivity for water. As a consequence strong OH-stretch and bending bands might mask IR-signals related to the organic compounds of interest. An additional difficulty of ATR-FTIR relates to its requirement for thin

model substrates, which is especially challenging for active substrates such as magnesium. Magnesium is a lightweight material that is gaining more attention from industry. Its high abundancy together with its high-strength-to-weight ratio and ease of machining and recycling offers a wide range of applications.[17,18] However, its high intrinsic and galvanic corrosion susceptibility remains a major drawback limiting its implementation in industrial engineering. One of the most practical and economical ways to improve corrosion resistance concerns the introduction of corrosion inhibitors. Typically, corrosion inhibitors are small chemical compounds which promote the formation of an insoluble and stable layer at the surface.[19] However, due to its high activity, such effective compounds are limited for magnesium.[20] Section 7.3.2 aims to investigate the capabilities of the integrated ATR-FTIR-EIS setup as spectro-electrochemical tool to in-situ study inhibition mechanism on high purity (HP) magnesium in aqueous environments. In addition to molecular information, unravelling an adsorption mechanism, complementary EIS measurements were performed to measure oxide film resistances indicating the inhibiting performance.

7.2 Experimental

7.2.1 Materials and chemicals

ATR-FTIR-samples: 50 nm zinc (Goodfellow, 99.95%) was deposited on germanium internal reflection elements (IRE) by means of a high-vacuum evaporation system (VCM 600 Standard Vacuum Thermal Evaporator, Norm Electronics). A polymer coating with polyester-based resin, Dynapol LH 820 (Evonik Industries AG) was applied using a 30 µm bar coater. The resulting polymer film was cured for 15 minutes at 130 °C, which is the maximum operating temperature for germanium IRE. The polyester primer formulation can be found in table 2.2 of chapter 2.

SFG-samples: 6 nm zinc films were sputtered on CaF_2 windows (Ø 25 mm, thickness 2 mm, Crystal-GmbH) by means of a LEICA SCD 500 sputter coater using a zinc target (99.9 %, Chempur GmbH) at a argon pressure of 10-2 mbar. A polyester clear coat was applied on both clear CaF_2 and zinc coated CaF_2 windows by spincoating using a rotation speed of 2500 rpm during 1 minute resulting in a final coating thickness of 10 µm.

Samples integrated ATR-FTIR- EIS setup: Magnesium films with a thickness of approximately 20 nm were thermally vaporized (PVD) on germanium internal reflection elements (PIKE Technologies, 60°) by means of a high-vacuum evaporation system (VCM 600 Standard Vacuum Thermal Evaporator, Norm Electronics). The source material for the PVD substrates was resublimed pure Mg (a by-product during Mg sintering process), which composition is shown in table 4.1 of chapter 4. The high purity of the magnesium source used together with the low melting point of magnesium compared to the

impurities present in the source material are expected to result in magnesium films with a level of impurities significantly lower than that in the source material. Inhibitor solutions containing 0.05 M 2,5-pyridinedicarboxylic acid (>98%, Sigma-Aldrich Chemie GmbH),3-methylsalicylic acid (99%, Sigma-Aldrich Chemie GmbH), sodium salicylate (> 99.5 %, Sigma-Aldrich Chemie GmbH) and fumaric acid (98%, Alfa Aesar) were prepared in demineralized water. The pH of the inhibitor solutions was adjusted to pH 7 +/- 0.3 using 1 M NaOH.

7.2.1 ATR-FTIR in Kretschmann configuration

The FTIR apparatus was a Thermo-Nicolet Nexus equipped with a liquid-nitrogen cooled mercury-cadmium-telluride (MCT-A) detector and a nitrogen-purged measurement chamber with a Veemax III single reflection ATR accessory. Germanium IRE (PIKE Technologies) with a fixed face angle of 60 degrees were used. IR-light was configured with an incident set angle of 80 degrees. A precision manual polarizer (PIKE) was mounted on the Veemax III and set to 90° for p-polarized and 0° for s-polarized IR-light. For the chemisorption studies infrared backgrounds were obtained from the metallic coated IRE. The established interfacial chemistry was followed in-situ in aqueous environment using D_2O (99.9 %, Sigma-Aldrich Chemistry). D_2O was chosen instead of H_2O because of the shift of the bending vibrations towards lower wavenumbers (1200 cm-1 for O-D versus 1640 cm-1 for O-H). This shift allows us to probe the asymmetric carboxylate stretching vibrations established at the zinc oxide surface. For these in-situ stability studies, infrared backgrounds were obtained after applying the polymer coating on the respective metal oxides. Consequently, as the interfacial chemistry established after curing was involved in the background, the evolution of interfacial bonds may appear positive, when being increased, or negative when being reduced relative to the initial dry (cured) situation. Infrared spectra were collected every 300 seconds and averaged from 128 cycles with a resolution of 4 cm^{-1}. The control of the spectra acquisition and incident angles was managed by the OMNIC 8.1 software package (ThermoElectron Corporation, Madison, WI).

7.2.2 Attenuated total reflection – Fourier transform infrared spectroscopy (ATR-FTIR) with integrated electrochemical cell for electrochemical impedance spectroscopy measurements (EIS)

The FTIR apparatus was a Thermo-Nicolet Nexus equipped with a liquid-nitrogen cooled mercury-cadmium-telluride (MCT-A) detector and a nitrogen-purged measurement chamber with a Veemax III single reflection ATR accessory. IR-light was configured with an incident set angle of 80 degrees. A precision manual polarizer (PIKE) was mounted on the Veemax III and set to 90° for p-polarized and 0° for s-polarized IR-light. Prior to the in-situ chemisorption studies, infrared backgrounds were obtained of magnesium coated germanium internal reflection elements immersed in demineralized water. Subsequently, demineralized water was quickly replaced by the inhibitor-containing solution for in-situ ATR-FTIR – EIS measurements. Infrared spectra were collected every 3 seconds and

averaged from 16 cycles with a resolution of 4 cm^{-1}. The control of the spectra acquisition and incident angles was managed by the OMNIC 8.1 software package (ThermoElectron Corporation, Madison, WI). Electrochemical impedance (EIS) measurements were performed using a SI1286 electrochemical interface Solartron potentiostat over a frequency range from 10^5 to 10^{-1} Hz, 7 points per decade and a sinusoidal amplitude of 10 mV. This gives an analysis time of ca. 1.7 minutes per EIS cycle. On the other hand, ATR-FTIR data has been averaged from 16 spectra collected every 3 seconds, giving an intermediate time of 27 seconds. Time acquisition occurred upon immediate contact of magnesium substrate with solution. EIS measurements were conducted in the electrochemical cell of PIKE Technology designed for the Veemax III accessory, which has been in-house modified to reduce the exposed contact area to 1 cm^2, allowing the application of an electric connection outside the exposed contact area. in a conventional three-electrode setup, with a platina mesh as counter electrode and Ag/AgCl/sat. KCl (+0.197 V vs standard hydrogen electrode) as reference electrode. Impedance plots were recorded on at least three samples for each inhibitor solution and processed using Zview from Scribner Associates Inc.

7.2.3 Surface sum-frequency generation (SFG) spectroscopy

The laser source used is a Ti:sapphire laser system which consist of an oscillator (Coherent Mantis) and an amplifier (Coherent Legend Duo) generating 35 fs pulses of a broadband beam with a wavelength of 795 nm, a 6.5 mJ pulse energy and repetition rate of 1 kHz. The VIS pulse is prepared by transmitting approximately 20% of the amplifier output through an pulse shaper/monochromator to reduce its spectral bandwidth, yielding a 15 µJ pulse with a FWHM of 15 cm-1. The remaining amplifier output passes through an optical Parametric Amplification (OPA) process (Light Conversion HE-TOPAS) to generate mid-IR broadband pulses tunable in the range of 1200 – 4000 cm-1 with a FWHM of ~400 cm-1. The mid IR broadband pulse is subsequently sent through a long-wave pass filter to filter out the signal and idler beams. The VIS beam is guided through a delay stage to adjust the travel time to that of the IR-beam in the OPA. Thereby temporal overlap of the beams is achieved which is a prerequisite for SFG. The intensity of the beams was controlled with a halfwave plate and a polarizer in the beam paths and by adjusting the apertures of the IR- and VIS-beam. Final intensities were 10 mW for the IR-beam and 3.8 mW for the VIS-beam which were focused on the sample to generate SFG upon spatial and temporal overlap. The reflected SFG beam passes two notch filters to filter out the residual VIS light and a polarizer to select the SFG polarization. Finally, SFG signal obtained with an SSP polarization configuration (SFG=s-polarized, vis=s-polarized, IR=p-polarized) is focused on the detector slit (PIXIS 100B camera with an SP-2-300i Spectrograph). For measurements in the frequency region of the carbonyl and carboxylate stretch vibrations (1300-1900 cm-1) the setup was purged with nitrogen to avoid environmental interference. SFG measurements in the 3000

– 2400 cm-1 region were performed without nitrogen flushing. Due to the low damage threshold of the samples, integration times were limited to maximum 300 seconds. To normalize the SFG signal and to monitor the stability of the laser, an SFG spectrum of a quartz plate was taken regularly, with an integration time of 10 seconds. The measured SFG
spectra were corrected for the background and normalized with a corresponding spectrum of quarts.

SFG-samples: 6 nm zinc films were sputtered on CaF2 windows (Ø 25 mm, thickness 2 mm, Crystal-GmbH) by means of a LEICA SCD 500 sputter coater using a zinc target (99.9 %, Chempur GmbH) at a argon pressure of 10-2 mbar. A polyester clear coat was applied on both clear CaF2 and zinc coated CaF2 windows by spincoating using a rotation speed of 2500 rpm during 1 minute resulting in a final coating thickness of 10 µm.

7.3 Results

7.3.1 Comparative study ATR-FTIR in Kretchmann geometry and SFG

7.3.1.1 Attenuated Total Reflection – Fourier transform infrared spectroscopy (ATR-FTIR)

ATR-FTIR was performed on two-layered (Ge – polyester coating) and three-layered (Ge – zinc/zinc oxide – polyester coating) systems whose configurations are illustrated in figure 7.1.

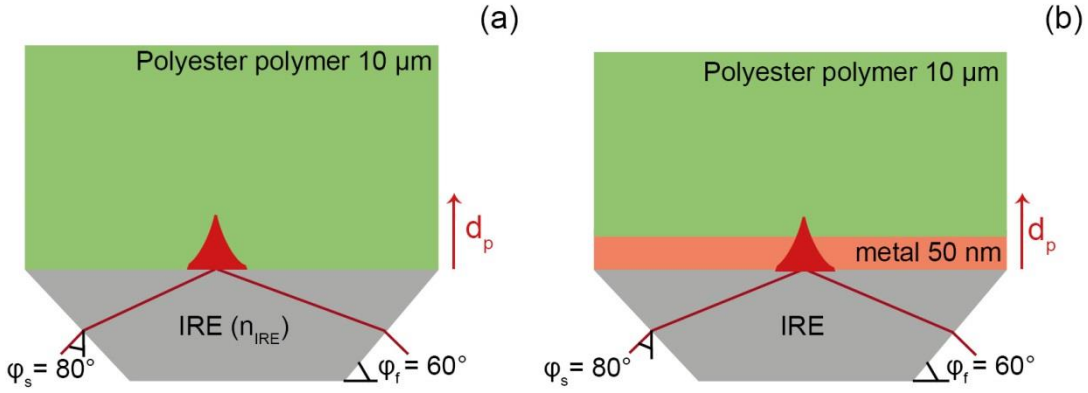

Figure 7.1: (a) Polyester coated IRE (two-layered system) and (b) polyester coated zinc deposited on internal reflection element (three-layered system).

From Harrick's equations[5,6] (equation 1-4) it can be seen that the depth of penetration (d_p) varies with the incident IR angle (φ_{eff}), frequency of the IR beam (λ), and the refractive indexes of the germanium reflection element (n_{IRE} = 4), zinc (n_{Zn}) and polyester coating (n_{PE} = 1.5). The effective incident IR angle (φ_{eff}) results from equation 3, which takes into account the face angle of the germanium IRE (φ_f), fixed at 60°, and the set angle for the incident IR beam (φ_s) set at 80° as illustrated in figure 7.1.

$$d_{p-2} = \frac{\lambda}{2\pi(n_{IRE}^2 sin^2\varphi_{eff} - n_{PE}^2)^{1/2}} \quad (1)$$

$$d_{p-3} = \frac{\lambda}{2\pi n_m (sin^2\varphi_2 - (\frac{n_{PE}}{n_{Zn}})^2)^{1/2}} \quad (2)$$

$$\varphi_{eff} = \varphi_f + sin^{-1}(\frac{\sin(\varphi_s - \varphi_f)}{n_{IRE}}) \quad (3)$$

$$\varphi_2 = sin^{-1}(sin\varphi_{eff}\frac{n_{IRE}}{n_{Zn(\lambda)}}) \quad (4)$$

The refractive index of the polyester coating and germanium IRE, are considered to be constant over the studied IR-frequency range, being 1.5 and 4 respectively. Conversely, metals are characterized by a complex refractive index N, expressed as N = n + iκ, with n, being the magnitude of the refractive index, which is equal to the ratio of phase velocity of light in vacuum to those in medium. The imaginary part of the refractive index, corresponds to the extinction coefficient κ, which expresses the exponential decay of the electromagnetic wave when propagating through a medium.[44] Both values highly depend on the IR-frequency, as shown by the values reported by Querry et al.[21], given in table 7.1. However, the depth of penetration in metals (referred to as skin depth) depends rather weakly on the wavelength, while that in dielectrics increases fast and nonlinearly with the wavelength (typically on the order of λ/2).[22] The depth of penetration into the metal (skin depth) gives a measure on the coupling strength between the evanescent wave induced during internal reflection and the propagating surface plasmons polariton and is directly related to the extinction coefficient. Meanwhile, the depth of penetration is majorly determined by the real part of the refraction index.[5] Strictly speaking one should differentiate between zinc and zinc oxide, considering a four-layered system instead of three-layered system. However, the refractive index of monoclinic zinc oxide is close to that of the polyester coating (i.e. 1.5). Therefore, because of the experimental difficulties on obtaining reliable refractive index values for metal oxides as well as the their close approximation to the refractive index of polyester, the contribution of the zinc oxide layer to the estimated depth of penetration is assumed to be negligible.

Table 7.1: Real and Imaginary parts of the complex refractive index of zinc according to Querry et al.[21]

ν /cm^{-1}	λ /μm	n_{Zn}	κ_{Zn}
4000	2.50	6.3	26.5
1700	5.88	21.4	57.7
600	16.67	58.1	100.9

The estimated values for the depth of penetration for a two- and three-layered system (d_{p-2} and d_{p-3}) are illustrated in figure 7.2. It can be seen that the Harrick's equations, give similar outcomes for a configuration with and without metallic film (three- and two-layered system respectively). On the other hand, the IR-wavenumber is shown to play a predominant role on the depth of penetration. The maximum incident set angle of 80 degrees, considered as most interfacial sensitive, results in an estimated depth of penetration of 250-400 nm in the IR-frequency region of interest, which is the head group region between 1200 and 2000 cm^{-1}.

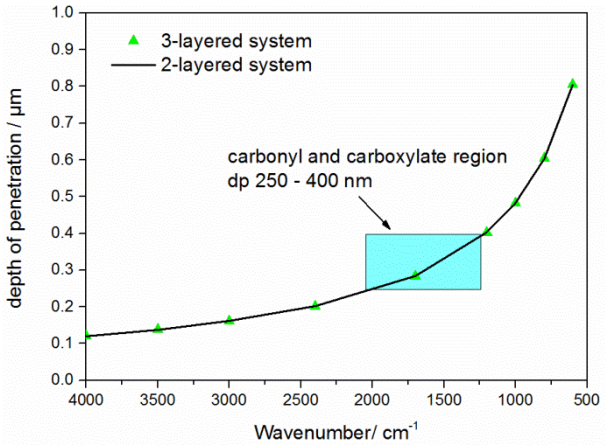

Figure 7.2: Depth of penetration calculated according to Harrick's equations.

Based on Harrick's equations, the probing depth of ATR-FTIR is thus considered to be equal with and without a metallic film. However, the sensitivity of ATR-FTIR can be limited to the first monolayer when the metallic film introduces a surface enhancement effect.

Figure 7.3 presents ATR-FTIR spectra for a two- and three-layered system collected with p- and s-polarized IR-light. Since the ATR-FTIR spectra are expressed in common scale, the magnitude of the spectral peaks in absence and presence of a metallic film can be compared. The presence of the metallic layer does not lead to a significant enhancement of the absorption. Hence, there appears to be no chemical enhancement effect due to chemisorption of functional groups at the zinc oxide surface, nor an electromagnetic enhancement effect. The lack of an electromagnetic effect is explained by relatively large film thickness (50 nm) resulting in a continuous zinc film. Consequently, as no enhancement effects occur, ATR-FTIR interface studies on zinc-polyester hybrid systems cover an interface region 250-400 nm in the carboxylate region, as illustrated in figure 7.2. This means that the ATR-FTIR measurements should be considered as an interphase-sensitive tool, rather than an interface-sensitive tool. Whereas interfaces are characterized by their two-dimensional properties, interphases have a significant additional dimension in depth.

Figure 7.3 illustrates the p-polarized ATR-FTIR spectrum of polyester coated zinc (Zn PE p-pol) with a strong spectral feature positioned at 1605 cm^{-1} which is not shown in the p-polarized ATR-FTIR spectrum of the polyester coating without zinc (PE p-pol). This additional peak is once again assigned to the asymmetric carboxylate stretch vibrations demonstrating the establishment of interfacial carboxylate bonds at the zinc oxide-polyester interface.[23] That this peak is much more intense when using p-polarized IR-light and practically absent when using s-polarized IR-light indicates that the transition dipole moment of asymmetric stretch vibrations occurs highly perpendicular to the surface. In chapter 5, we attributed this to a monodentate zinc-carboxylate coordination.[24]

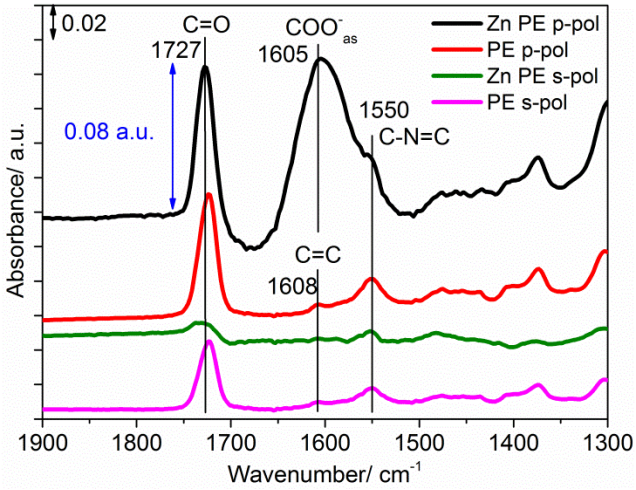

Figure 7.3: ATR-FTIR spectra of polymer-coated zinc on germanium IRE obtained using s- and p-polarized IR-light, and ATR-FTIR spectra of polymer coated germanium IRE obtained using s- and p-polarized IR-light.

7.3.1.2 Sum frequency generation spectroscopy (SFG)

The majority of SFG studies on metal-polymer interfaces are conducted in a top configuration [25–28], meaning that the laser beams reach the interface from the polymer side, as illustrated in figure 7.4 (A-B).

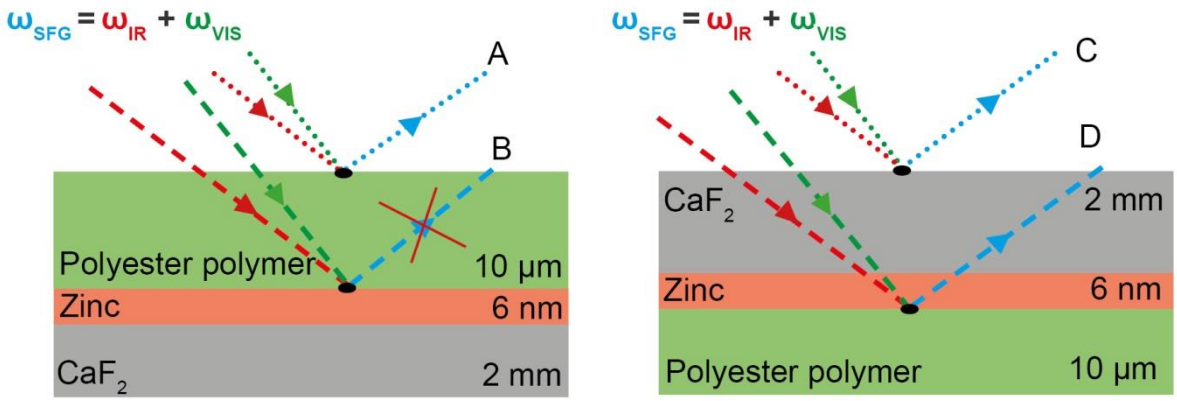

Figure 7.4: Laser beam configuration used to study metal-polymer interfaces, A: top configuration, polyester-air interface, B: top configuration, polyester-zinc/zinc oxide interface, C: inverse configuration, CaF_2-air interface, D: inverse configuration, zinc/zinc oxide-polyester interface.

This top configuration is a useful lay-out when the photons of the incident beams are hardly adsorbed by the polymer layer, which assumption is met in case the polymer film is sufficiently thin, i.e. nanometer scale.[25] For such thin polymer films the interfaces A and B are measured simultaneously and thus additional efforts have to be taken to separate the SFG signals from the respective interfaces.[25,26,29] In this work polyester coatings with a thickness of 10 µm are being studied, which transmission FTIR spectrum is shown in figure 7.5. The molecular bonds given in blue are associated to components present in the polyester resin, whereas the green coloured ring structure, positioned at 1552 cm^{-1}, is assigned to the melamine-rings originating from the crosslinker. The saturated peaks positioned at 1728 and 1244 cm^{-1}, shown in red, evidence that highly polar C=O and C-O bonds fully absorb incident IR-light. Conversely, no or limited IR-absorption is shown to take place in the IR-frequency region ranging from 2000-2700 cm^{-1}, indicated in green. This because of the absence of molecular bonds that vibrate in this specific region. Consequently, the top configuration is not ideal for studying buried metal-paint interfaces in the IR-frequency region of interest. An alternative is the inverse configuration demonstrated in figure 7.4 (C-D). In this configuration the metal-polymer interface is reached from the metal side. This requires the metal film to be sufficiently thin to be transparent for both IR- and VIS-light.

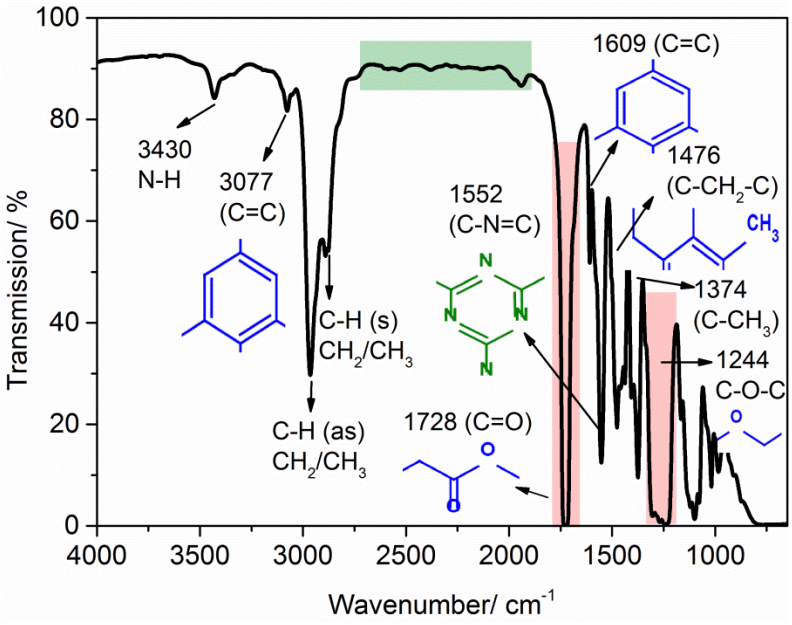

Figure 7.5: Transmission FTIR spectrum of 10 µm polyester coating.

In figures 7.6 (a,b) we present SFG spectra measured for CaF_2-polyester and CaF_2-zinc/zinc oxide-polyester samples in top configuration. The SFG spectrum shown in figure 7.6 (a) is dominated by the response of the polyester-air interface (interface A). Only one peak positioned at 1720 cm^{-1} appears in the carbonyl/carboxylate region (1900-1300 cm^{-1}) that can be assigned to carbonyl (C=O) stretching vibrations. A comparison of this SFG spectrum with the ATR-FTIR spectrum of polyester in absence of zinc/zinc oxide, shown in figure 7.3, shows that remarkably less vibrations are SFG active than IR active. The SFG spectrum of the CaF_2-zinc/zinc oxide-polyester sample in top configuration, shown in figure 7.6 (b) is much more complex. Such significant variations between SFG spectra obtained at interface A and B are unexpected since it concerns the same polymer layer with a similar chemical composition. The only chemical difference that is expected to occur between both interfaces is the establishment of interfacial carboxylate bonds at the zinc-polyester interface as shown by ATR-FTIR in figure 7.3. Furthermore, it is noted that the spectrum shown in figure 7.6 (b) coexists of positive and negative peak intensities. The occurrence of dips in the spectrum are associated to a combination of the broad non-resonant SFG response of the zinc oxide and IR-absorption effects of the polyester layer absorption of IR-light by the 10 µm thick polyester coating. The presence of positive peaks imply that the non-resonant signal of zinc oxide is not very strong. Nonetheless, the complex response of interface B confirms that the top configuration is not a suitable approach for studying buried interfaces covered with macro-coatings.

The SFG spectra of CaF_2-polyester and CaF_2-zinc/zinc oxide-polyester samples measured in the inverse configuration are shown in figure 7.6 (c) and (d). In this configuration the response of the CaF_2-air interface C can be spatially distinguished from that of the zinc/zinc oxide-polymester interface D, thanks to the fact that the CaF_2 has a thickness of 2 mm.

The spectrum of interface C, given in figure 7.6 (c), shows a single peak at 1466 cm^{-1} that can be assigned to symmetric carboxylate (COO^-_s) stretching vibrations.[30] This band shows the adsorption of carboxylate species to the CaF_2 surface and originates from ambient carbon contaminants. The presence of this band illustrates that CaF_2 is not as chemically inert as germanium. The SFG spectrum shown in figure 7.6 (d) represents the spectrum of the zinc/zinc oxide-polymer interface and it is interesting to compare this spectrum with of the non-reacted polyester of figure 7.6 (a). It is seen that the carbonyl peaks consist of two contributions, i.e. a major peak at 1723 cm^{-1} representative for carbonyl bonds specific to ester groups, and a shoulder at 1710 cm^{-1} attributed to carbonyl bonds of acid groups.[31] The increased carbonyl peak intensity in the presence of zinc (0.075 a.u.) versus non-reacted polyester (0.030 a.u.) refers to an increased fraction of strongly oriented ester and acid carbonyl groups near the zinc and zinc oxide. Interestingly, the SFG spectrum only shows the

presence of acid groups (COOH) and not of deprotonated carboxylate (COO^-) at the zinc oxide interface. One possible explanation for this difference is that the SFG spectrum only represents the response of the carboxylic acid groups in molecular proximity of the zinc and zinc oxide surface, whereas the ATR-FTIR spectrum represents the properties of the full bulk-like polyester phase. It could be that the nearby presence of zinc and zinc oxide stabilizes the COOH groups. In addition, the physicochemical properties of the zinc/zinc oxide film may differ due to the different deposition techniques (sputtering vs PVD) as well as the different applied thicknesses (50 vs 6 nm). A detailed surface study on the physicochemical/acid-base properties might give more insights on the observed differences in (de)protonation equilibrium.

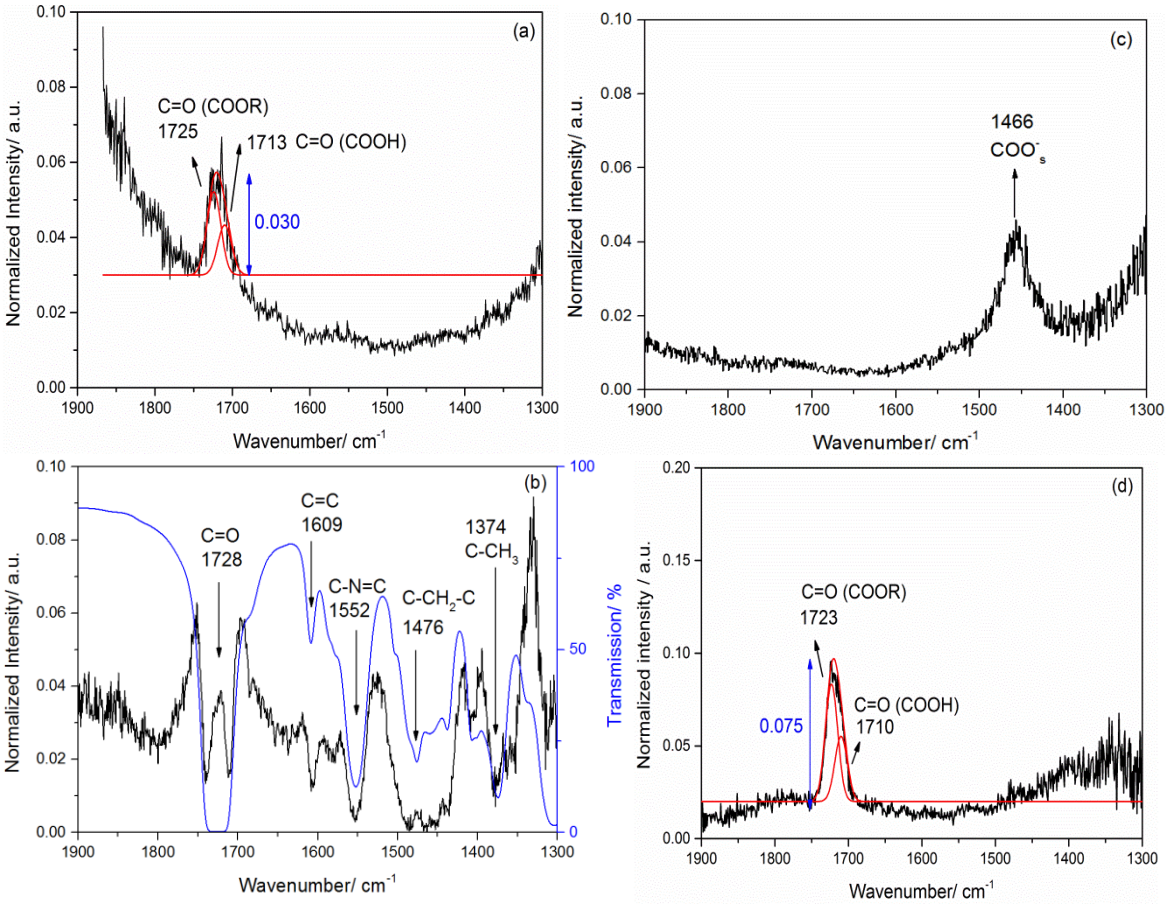

Figure 7.6: (a) SFG spectrum of the polyester-air interface collected using the top configuration (b) spectrum polyester-zinc interface collected using top configuration, with transmission FTIR spectrum shown in blue on the secondary y-axes, (c) SFG spectrum CaF_2-air interface obtained in inverse configuration and (d) SFG zinc-polyester interface obtained in inverse configuration. The ester- and acid carbonyl subpeaks have been fitted using a FWHM of 18 cm^{-1}.

7.3.1.3 In-situ ATR-FTIR and SFG measurements in aqueous environment (D_2O)

It has been demonstrated that for studying buried metal-paint interfaces the use of model metal substrates is a necessity to avoid experimental artefacts. The setups for in-situ ATR-FTIR and SFG measurements during immersion of the zinc/zinc oxide-polyester system in D_2O are depicted in figure 7.7. The inverse configuration for the SFG experiments has as an additional advantage that it can easily be combined with a liquid cell suitable for D_2O exposure measurements.

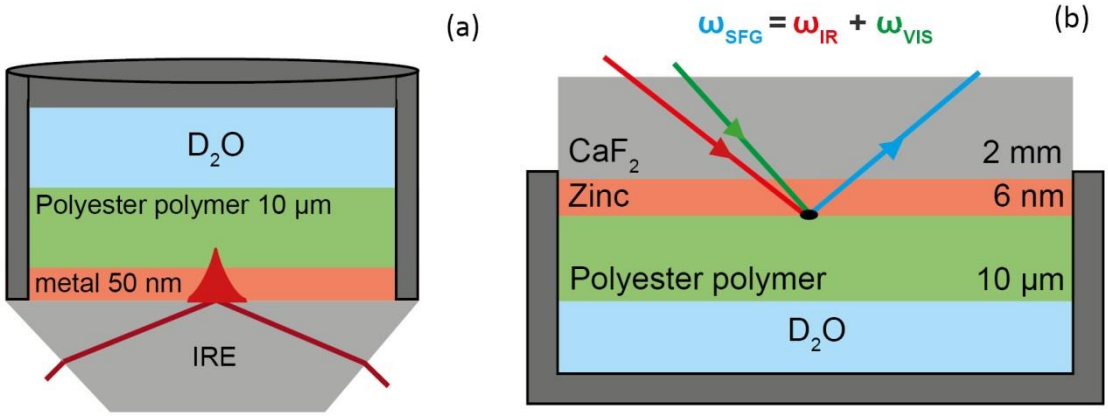

Figure 7.7: (a) ATR-FTIR and (b) SFG configuration for in-situ measurements during immersion in D_2O

Figure 7.8 (a) presents the ATR-FTIR spectra in the frequency region 2000-4000 cm^{-1} at different time intervals after exposing the system to D_2O. The spectra illustrate an increasing O-D stretch band intensity (2473 cm^{-1}) with immersion time, indicative for D_2O uptake by the polyester coating. Meanwhile, C-H stretch vibrations at 2956, 2926 and 2859 cm^{-1} immediately appear as negative peaks. Since the in-situ ATR-FTIR spectra are relative to the dry state, their negative intensity represents the replacement of CH_2 and CH_3 groups in the polyester interphase due to polymer swelling and D_2O accumulation at the interphase during submersion in D_2O. Furthermore, the O-H stretch vibration band at 3394 cm^{-1} also rapidly turns negative illustrating interphase equilibrium reactions where hydrogen atoms are being exchanged by deuterium. Figure 7.8 (b) demonstrates the kinetics of D_2O obtained by SFG during 90 minutes of immersion. Two spectral features are immediately present, the C-H stretch vibrations at 2934 and 2832 cm^{-1} and the O-D stretch band at 2475 cm^{-1}. The C-H stretch vibrations can be assigned to CH_2 groups specific to the polyester resin. Yet, their signal is small en invariable during immersion. For the O-D stretch band a slight reduction can be noted during immersion. This can be explained by the lack of absorbance by the polymer coating in this wavenumber region as demonstrated in the transmission FTIR spectrum in figure 7.5. Because the IR and VIS light beams are not being absorbed by the polyester coat in this frequency region, SFG signal can be generated at the polyester-D_2O interface. Increased absorption of incident IR-light due to D_2O uptake by the coating, is responsible for the reduced SFG signal at the polyester-D_2O interface upon immersion.

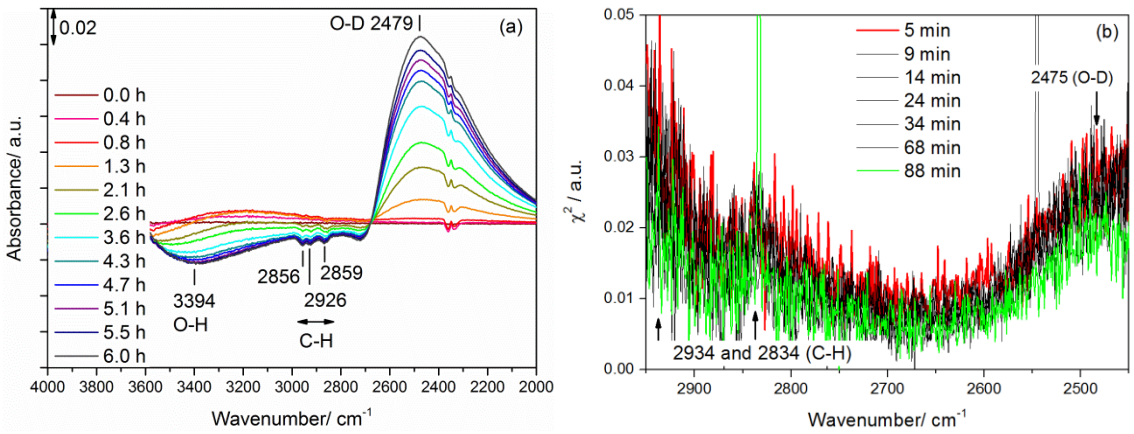

Figure 7.8: In-situ (a) ATR-FTIR and (b) SFG spectra of polyester coated zinc substrates during immersion in D_2O.

Figure 7.9 (a) illustrates carbonyl and carboxylate region of the in-situ ATR-FTIR spectra obtained during initial immersion of the zinc/zinc oxide-polyester system in D_2O. The illustrated spectra are relative to the dry state, given in figure 3. It is noted that the ester carbonyl peak, positioned at 1729 cm^{-1} has a negative peak area intensity, which further declines during prolonged immersion. On the other hand, asymmetric and symmetric carboxylate peaks, positioned at 1638 cm^{-1} and 1471 cm^{-1}, respectively, appear positive and thus refer to an increased carboxylate fraction relative to the dry state. Because of this, it is inferred that ester groups are being hydrolysed due to the migration of D_2O through the polyester coating. The hydrolysis of ester groups results in the formation of carboxylic acids, as indicated by the initial increase of the carbonyl peak at 1710 cm^{-1} during early immersion times. However, prolonged immersion times also turn the acid carbonyl peak negative, which can be attributed to their deprotonation forming carboxylate anions. As a result, the peak area intensity assigned to asymmetric carboxylate stretch vibrations increases with immersion time, attributed to the increased fraction of zinc-carboxylate complexes. However, after 1.1 hours, a maximum carboxylate peak area has been reached, whereafter the peak area intensity declines again. It is thus shown that the formation of zinc-carboxylate complexes at the zinc oxide – polyester interphase occurs fast (i.e. within 1.1 hours), but reduces equally as fast upon prolonged submersion in D2O. Therefore, it is expected that the zinc-carboxylate are highly susceptible to bond degradation in aqueous media, which can be attributed to their ionic character. To quantify the altered bonding density, the maximum peak areas shown in figure 7.9 (a) can be compared to those shown in figure 7.3 representing the dry state. For the carboxyl peak a negative peak intensity of 0.006 a.u. and positive asymmetric carboxylate peak intensity of 0.003 a.u. has been observed after 2.5 and 1.1 h of immersion respectively. On the other hand, in the dry state as shown in figure 3, the carbonyl (C=O) and asymmetric carboxylate (COO-as) peak intensity equals to 0.08 a.u. Expressed in percentage

relative to the dry state this corresponds to a reduction of interphase C=O bonds of 7.5 % after 2.5 h and a maximum increase of 3.8 % carboxylate bonds after 1.1 h of immersion.

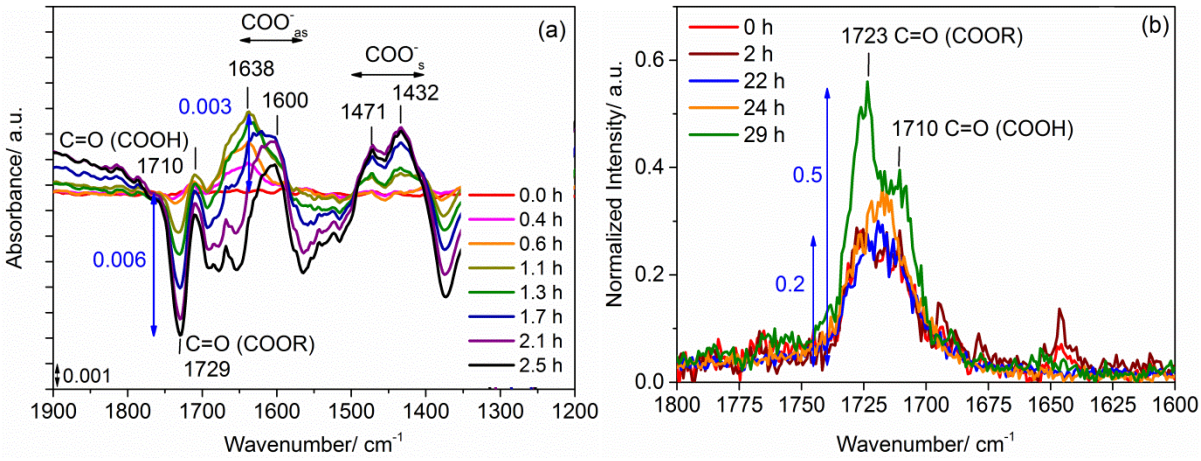

Figure 7.9: Evolution of polyester coated zinc during exposure to D_2O obtained by (a) ATR-FTIR measurements, collected using polyester coated zinc prior to immersion as background; (b) SFG measurements.

In figure 7.9 (b) the SFG response is shown at different delay times after exposure to D_2O. Similar to the measurements under dry conditions, deprotonated acid species at the zinc/zinc oxide surface are not being formed within 30 hours of exposure to D_2O. Nonetheless, a significant increase in carbonyl SFG peak intensity (from 0.075 to 0.2 a.u) is noted. This increase is observed for both the major peak at 1723 cm^{-1} representative for ester groups, as well as its shoulder at 1710 cm^{-1} representative for acid-groups and can be attributed to a higher density of these groups near the zinc/zinc oxide surface and/or an increase in orientation upon exposure to D_2O. It is conceivable that the presence of D_2O increases the mobility of the polyester carbonyl and carboxylic acid groups leading to a better orientation towards zinc oxide and a higher SFG signal. This explanation would also explain the lag time that is observed in the rise of the SFG signal, the SFG signal only starts to rise after a sufficient amount of D_2O has diffuses through the polyester layer and has reached the interface with zinc/zinc oxide. Additional experiments using different polarization modes, such as PPP and SPS polarization combinations might provide additional information in changes in orientation.

Figure 7.10 (a) and (b) demonstrate SFG spectra obtained upon prolonged immersion times (> 3 weeks) of submersed 2-layered and 3-layered system, i.e. without and with zinc, respectively. It can be seen that the carbonyl (C=O) peak position shifts towards lower wavenumbers, i.e. 1712 and 1717 cm^{-1} compared to those obtained in the dry state, 1723 cm^{-1}, as illustrated in figure 7.6 (d). The carbonyl shift indicates the hydrolytic degradation of ester groups forming carboxylic acids. Even

more striking is the appearance of a second peak at 1453 and 1541 cm^{-1} at the polyester-CaF_2 and polyester-zinc oxide interface, respectively. Because asymmetric carboxylate stretch vibrations are expected to be far less SFG active in SSP polarization mode, this additional peak must be assigned to symmetric carboxylate (COO-s) stretch vibrations.[32,33] The eventual deprotonation of acid groups implies that prolonged immersion times cause a near surface pH increase. However, this is suggested to be a very slow process. The considerable difference in symmetric carboxylate peak position shown in figure 7.10 (a) and (b), indicates that different metal cations are involved in the formed metal-carboxylate complexes and thus evidences that a zinc layer still exists upon prolonged immersion. Although, it is known that the IR-frequency of carboxylate stretch vibrations depends on the interacting cation,[34] it is noted that the observed wavenumber for zinc-carboxylate bonds are rather high for symmetric carboxylate stretch vibrations. This high IR-frequency of symmetric carboxylate (COO-s) stretch vibrations shown in figure 7.10 (b) can be associated to loosely bounded ionic zinc-carboxylate bonds, whereas the lower IR-frequency, shown in figure 7.10 (a), suggests that carboxylate anions are more strongly coordinated on calcium cations.[35]

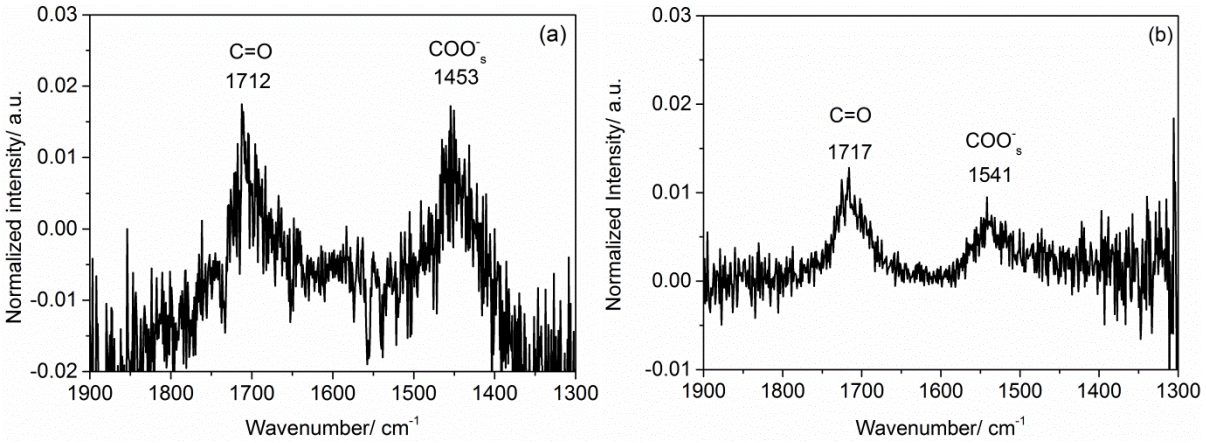

Figure 7.10: SFG spectra of (a) a CaF_2 – polyester and (b) zinc – polyester interface obtained after 3 weeks submersion in D_2O.

7.3.1.4 Strengths, limitations and further perspectives

At this moment two different bonding mechanisms have been elucidated using ATR-FTIR and SFG. Whereas the ATR-FTIR was shown to lead to deprotonation of carboxylic acid groups forming carboxylate species, SFG demonstrated much more stable acid groups, which remained protonated at the zinc oxide surface. It can be expected that different zinc oxide acid-base properties, resulting from the different application process, might shift the equilibrium towards more or less protonation. However, it is highly unlikely that the chemical nature of the zinc layer formed on the SFG samples is that different that it does not introduce any deprotonation reaction. This because isoelectric point

values of zinc are in general situated around 9-10. Consequently, the interfacial sensitivity of the vibrational tools is considered to be majorly responsible for the probed differences in interfacial molecular information.

Nevertheless, further research is strongly recommended to optimize the metal deposition process in such way, that similar films can be applied for ATR-FTIR and SFG measurements. In this way ATR-FTIR and SFG can be used a highly complementary tools. Furthermore, XPS analysis of the metallic zinc films prior to paint application is recommended to correlate observed bonding properties to the oxide's acid-base nature as demonstrated in chapter 4.[36]

Table 7.2 gives an overview of characteristics specific to ATR-FTIR and SFG. Obvious advantages of ATR-FTIR over SFG are its broad IR-frequency region that can be covered during one single measurement. Conversely, using SFG a smaller IR-frequency region has to be defined, with 1200 cm^{-1} being the lower wavenumber limit due to laser limitations. As a consequence spectral features separated by more than 600 cm^{-1} cannot be followed simultaneously during in-situ measurements. On the other hand, advantages of SFG over ATR-FTIR are its monolayer sensitivity and its selectivity for highly ordered/oriented structures as a result of the more strict selection rules of SFG. One of these additional selection rules of SFG compared to ATR-FTIR are the required ordering at the interface inducing symmetry breakage. Because of this requirement, information on orientation can be derived from SFG, which cannot be obtained using ATR-FTIR. This can be even further extended using different polarisation combinations, indicating tilt angles of molecular bonds at the interface. At the expense of these extended selection rules, other spectral information must be obtained using ATR-FTIR. For example, since C-N=C stretch vibrations appear to be SFG inactive, interactions with the melamine-based crosslinker cannot be followed using SFG, although it has been shown in chapter 5 that the melamine-based crosslinker contributes to interfacial bonding.[37] Yet, the information-rich ATR-FTIR spectrum has pros and cons; the high share of vibrational peaks can make the ATR-FTIR very complex and hard to interpret, whereas SFG spectra are generally more straightforward. As an example, spectral interference of asymmetric carboxylate vibrations, by aromatic ring vibrations as well as OH-bending vibrations are not an issue for SFG measurements. Consequently, SFG allows to follow the dynamic behaviour of carboxylate peaks in H_2O, whereas in-situ ATR-FTIR stability studies on carboxylate bonds has to be performed in D_2O. The lack of interference by the O-H bending mode of water in SFG measurements comes with the advantage of controlling the pH of the aqueous solution more easily. Adding chemicals such as NaOH to increase pH or borate salts to buffer the interface pH, introduces H_2O to the solution which might be undesired for in-situ ATR-FTIR measurements. The possibility to use a wide variety of aqueous solutions, the use of SFG can provide more insights in the fundamentals of water and ionic mobility and interfacial bonding properties

metal oxide – polymer hybrid systems. This provides the opportunity to optimize and create new enhanced metallic/organic coating systems that are better resistant to degradation and can lead to an improved lifetime.

Table 7.2: Comparison of the properties specific the spectroscopic techniques; ATR-FTIR and broadband SFG.

Properties	ATR-FTIR	SFG
IR-frequency region	4000-650 cm^{-1}	5000-1000 cm^{-1}
IR-frequency range per single measurement	3350 cm^{-1}	± 600 cm^{-1}(tunable)
Selection rules	Dipole of molecule must change during vibration	Molecular vibrations have to be both IR- and Raman active
	Change of dipole must be the same as the direction of the electric field	The change of dipole must be the same as the direction of the electric field
		SF is selectively generated at surfaces and interfaces where symmetry is broken
		Highly ordered/oriented molecular bonds are SF active
Probing depth	Interphase (100-800 nm)	Interface (one to several monolayers depending on the order in the non-centro-symmetric environment)
Dynamic measurements (in-situ)	Relative to background	Direct
Light source intensity	Low: non-destructive	High: Can induce thermal effects
User-friendliness	Very high	More hands-on

7.3.1.5. Conclusions on the complementarity between SFG and ATR-FTIR

This work elucidated molecular organizations at zinc/zinc oxide polyester coating interfaces using two spectroscopic techniques: attenuated total reflection infrared spectroscopy (ATR-FTIR) and sum frequency generation (SFG). It was shown that ATR-FTIR is an interphase (3D) sensitive technique with probing depths of 250-400 nm in the frequency region of the carbonyl and carboxylate stretch vibrations, i.e. 2000-1200 cm^{-1}. SFG, on the other hand, is an interface (2D) sensitive technique. ATR-FTIR illustrated the formation of carboxylate bonds when zinc oxide was present at the interphase

region of the polyester coating. SFG measurements showed that at the interface with zinc/zinc oxide the carboxylic acid groups are stable and are not converted to carboxylate groups. Exposure of the polymer-zinc/zinc oxide system to D_2O leads to an increase of 3.5 % of carboxylate bonds with respect to the dry state in the polymer phase. This conversion occurs within a few hours. SFG measurements show that the carbonyl and carboxylic acid groups near the interface with zinc/zinc oxide are much more stable and only after days start to be converted to carboxylate groups.

7.3.2 In situ ATR-FTIR-EIS performance study of carboxylic corrosion inhibitors on magnesium

7.3.2.1 In-situ ATR-FTIR chemisorption study

(a) 2,5-Pyridinedicarboxylate (PDC)

Figure 7.11 presents the adsorption kinetics of neutralized PDC from aqueous solution using magnesium immersed in demineralized water as background. The spectrum shown in green illustrates the reference spectrum collected in absence of magnesium. Characteristic peaks at 1577 and 1387 cm^{-1} are attributed to asymmetric and symmetric carboxylate stretching vibrations indicating the deprotonation of 2,5-pyridinedicarboxylic acid at neutral and alkaline pH values (pKa_1 = 2.35, pKa_2 = 4.64 for 2,5-pyridinedicarboxylic acid at 20°C and ionic strength 0.5)[38].

In addition to the reference spectrum, figure 7.11 (a) also illustrates the dynamic behaviour of native magnesium oxide immersed in PDC solution. Similar to the reference, asymmetric and symmetric carboxylate peaks positioned at 1584 and 1384 cm^{-1} appear during submersion of magnesium in PDC solution. Near the asymmetric carboxylate peak at 1584 cm^{-1} a second peak is noted assigned to OH-bending vibrations originating from bulk water. In addition, a new peak positioned at 1249 cm^{-1}, assigned to Mg-OH bonds, appear upon immersion. Similar to the kinetics of magnesium in demineralized water, as discussed in chapter 4, the growth of the Mg-OH peak at 1249 cm^{-1} is associated to the formation of an hydroxylated magnesium oxide ($MgO/Mg(OH)_2$) layer. The quantified peak areas of the magnesium hydroxide (Mg-OH) and asymmetric and symmetric carboxylate (COO^-) peaks are plotted in figure 7.11 (b). After 1.5 minutes the Mg-OH peak area declines, while the carboxylate peak area rapidly increases. This implies that surface hydroxide end-groups are being consumed during the formation of magnesium-carboxylate bonds. After 3 minutes of immersion, both the asymmetric and symmetric carboxylate peaks and the Mg-OH peak reach a plateau. This indicates that chemisorption occurs rapidly, resulting in stable carboxylate bonds, which are able to resist replacement by water.

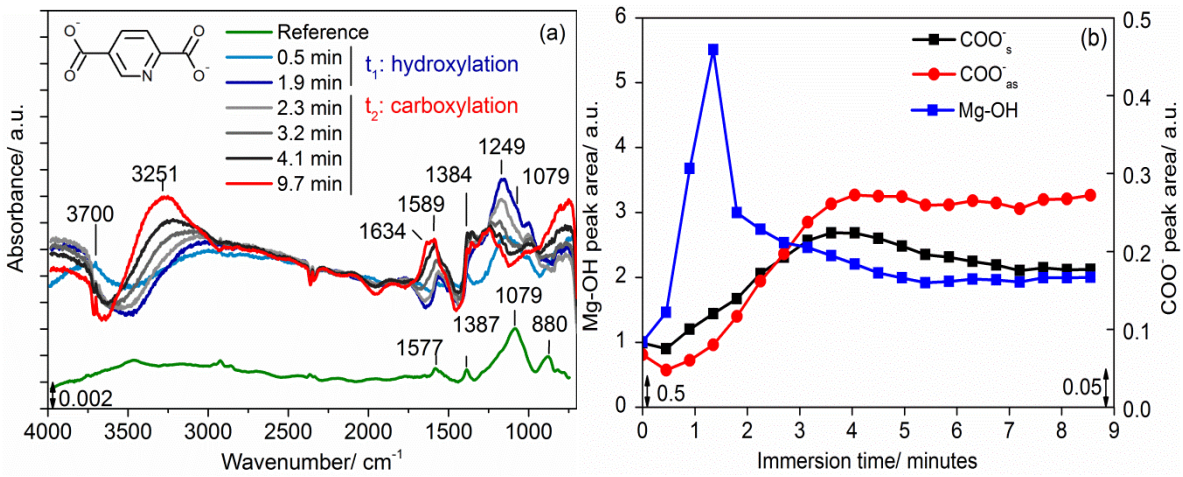

Figure 7.11: (a) in situ ATR-FTIR adsorption spectra, (b) quantified Mg-OH and COO^- peak areas as a function of immersion time in PDC solution.

(b) 3-methylsalicylate (MSA)

The reference ATR-FTIR spectrum of MSA, shown in green in figure 7.12 (a), illustrates peaks at 1597, 1476 and 1395 cm^{-1}, attributed to carbon-carbon stretching vibrations in the aromatic ring, asymmetric and symmetric carboxylate stretching vibrations, respectively. The indication of carboxylate peaks in the reference spectrum again illustrate the deprotonated state of the inhibitor molecules at neutral and alkaline pH values (pKa_1 = 2.82, pKa_2 = 14.6 for 3-methylsalicylic acid at 25°C and ionic strength 0.1 and 0 for Ka_1 and Ka_2, respectively)[42].

During the adsorption of MSA on magnesium, rapid peak formation is observed in the lower IR-frequency region, i.e. 1300-800 cm^{-1}. Similar to previously discussed kinetics of water and 2,5-pyridinedicarboxylate, these broad bands are related to surface hydroxylation reactions. Again a reduction of Mg-OH bonds is noted upon prolonged immersion. Similar to PDC, the reduction of Mg-OH is associated to the consumption of magnesium hydroxide end-groups during the formation of carboxylate bonds with MSA. This is confirmed by the growth of peaks at 1527 and 1476 cm^{-1}, assigned to asymmetric and symmetric carboxylate bond vibrations In addition, a new peak at 1606 cm^{-1} attributed to aromatic ring (C=C) stretching vibrations appears after 8 minutes of immersion in MSA solution. Furthermore, figure 7.12 (b) illustrates that both Mg-OH and COO^- peak areas slowly evolve during prolonged immersion in MSA, whereas during immersion in PDC solution a plateau value was reached after 3 minutes of immersion in PDC solution.

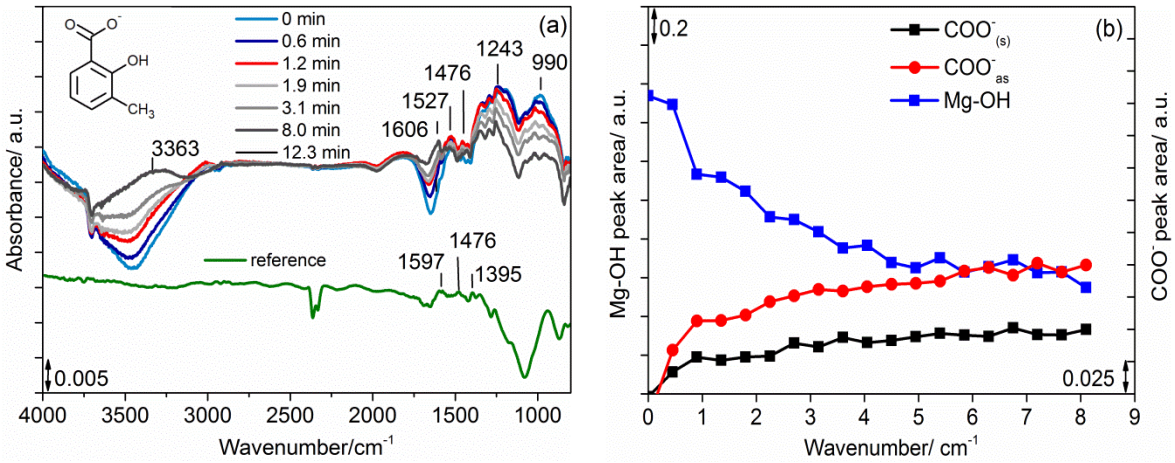

Figure 7.12: (a) in situ ATR-FTIR adsorption spectra, (b) quantified Mg-OH and COO^- peak areas as a function of immersion time in MSA solution.

(c) Sodium salicylate (SS)

Figure 7.13 (a) illustrates the adsorption kinetics of SS (pKa_1 = 2.8, pKa_2 = 13.4 for salicylic acid at 25°C and ionic strength 0.1)[43] on magnesium oxide. Analogous to the reference spectrum, three distinct peaks instantaneously appear at 1607, 1470 and 1370 cm^{-1} attributed to aromatic ring vibrations, asymmetric and symmetric carboxylate stretch vibrations, respectively. The lack of distinct peaks in the lower wavenumber region (1000-1300 cm^{-1}) demonstrates the lack of surface hydroxylation. On the contrary, the negative peak observed at 1097 cm^{-1} refers to $Mg(OH)_2$ layer breakdown. This magnesium hydroxide consumption can be associated to the chelating abilities of SS forming soluble magnesium salicylate complexes (pK = 4.7).[44]

The formation of such magnesium salicylate complexes is evidenced by the growth of asymmetric and symmetric carboxylate peaks at 1470 and 1370 cm^{-1}, respectively. The quantified peak areas of these carboxylate peaks are illustrated in figure 7.13 (b). It can be seen that magnesium-carboxylate complexes are formed rapidly, whereas the Mg-OH bonds associated to the $MgO/Mg(OH)_2$ layer instantaneously decline.

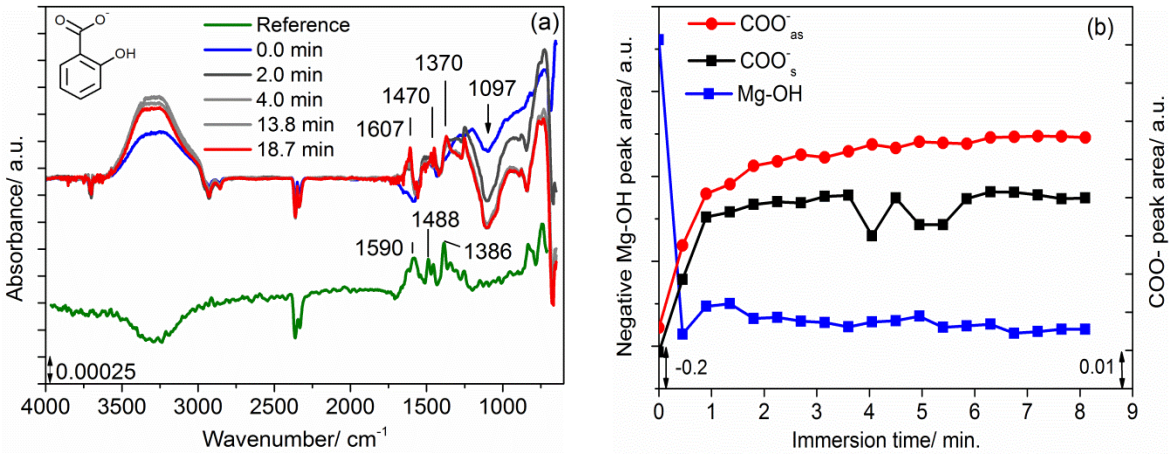

Figure 7.13: (a) in situ ATR-FTIR adsorption spectra, (b) quantified Mg-OH and COO^- peak areas as a function of immersion time in SS solution.

(d) Fumarate (FA)

The green curve in figure 7.14 (a) illustrates the reference ATR-FTIR spectrum of FA in solution in absence of magnesium. Two distinct peaks positioned at 1564 and 1373 cm^{-1} attributed to asymmetric and symmetric carboxylate bonds are noted, which again illustrates its deprotonated state in the respective solution (pKa_1 = 2.85, pKa_2 = 4.1 for fumaric acid at 25°C and ionic strength 0.1)[43]. Similar peaks are revealed during in-situ ATR-FTIR measurements, now positioned at 1578 and 1430 cm^{-1}. The shift of carboxylate peaks towards higher IR-frequencies is associated to the chemisorption of FA. Since, the peak area does not evolve substantially over time, chemisorption of FA is expected to occur immediately upon contact. Meanwhile, broad peaks in the low IR-region continuously increase in peak area indicating the formation of a hydroxylated oxide layer.

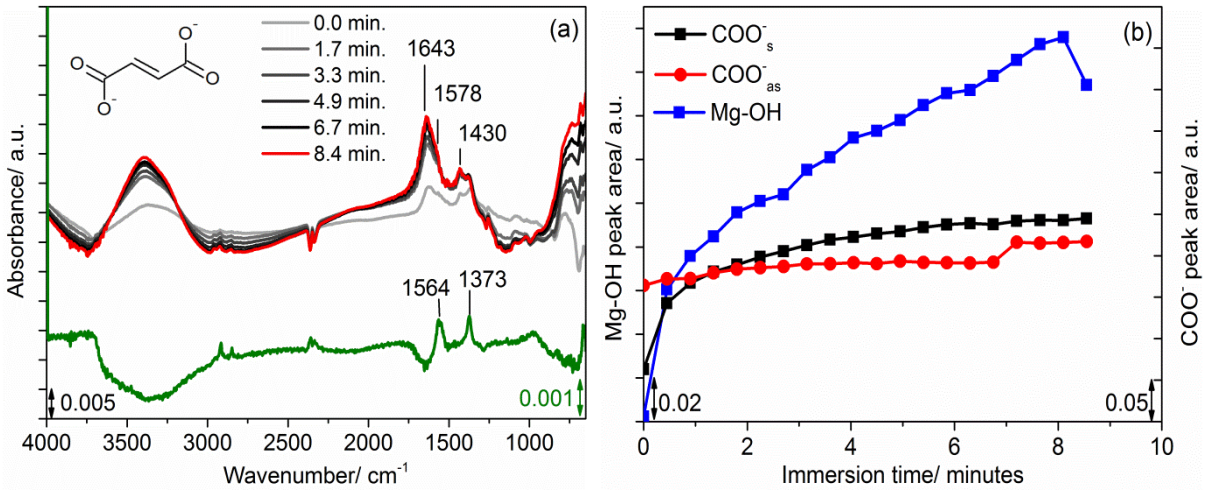

Figure 7.14: (a) in situ ATR-FTIR adsorption spectra, (b) quantified Mg-OH and COO- peak areas as a function of immersion time in FA solution.

7.3.2.2 EIS study of magnesium immersed in carboxylic corrosion inhibitor solutions

The Bode plots shown in figure 7.15, present the EIS data recorded simultanesously with the ATR-FTIR measurements shown in figures 7.11-7.14. It is noted that the impedance modulus increases instantaneously during submersion of magnesium in the inhibitor solutions. Similar also the phase angle increases and broadens during submersion of in the inhibitor solutions, which is associated to the formation of a protective layer, as suggested by the in situ ATR-FTIR measurements.

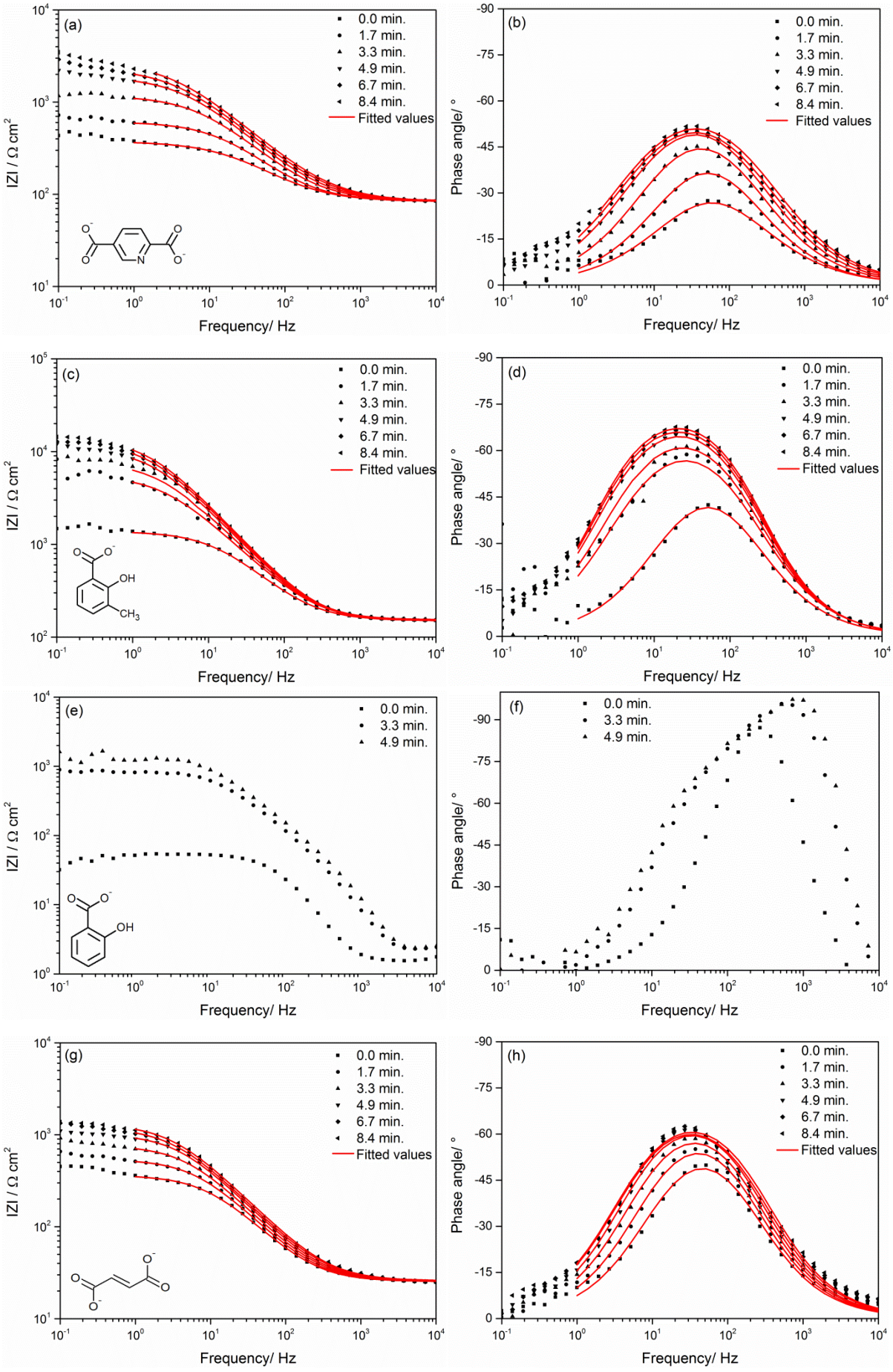
(a)
(b)
(c)
(d)
(e)
(f)
(g)
(h)
0.0 min.
1.7 min.
3.3 min.
4.9 min.
6.7 min.
8.4 min.
Fitted values
|Z| / Ω cm²
Phase angle/ °
Frequency/ Hz
OH
CH3
N

Figure 7.15: Bode modulus of magnesium immersed in (a) PDC, (c) MSA, (e) SS and (g) FA and phase angle plots of magnesium immersed in (b) PDC, (d) MSA, (f) SS and (h) FA.

The EIS data obtained during submersion in PDC, MSA, SS and FA solution are highly scattererd at low frequencies (10^{-1} - 10^{0} Hz) due to fast dissolution of magnesium substrate leading to non-stationarities. Therefore, EIS fitting has been performed in the frequency region 10^{0} – 10^{4} Hz. Within this region one timeconstant can be distinguished from the phase angle plots associated to the formation of a protective film. Consequently, the hydroxylated MgO(/$Mg(OH)_2$ layer and its chemisorbed carboxylate species are considered as one protective film. The protective properties of this dynamic film are being quantified by fitting the EIS data using an electrical equivalent circuit (EEC) containing one timeconstant. This EEC is illustrated in figure 7.16, and is composed of the electrolyte resistance R_{el}, followed by the time-constant associated to the formed protective film (f), with R_f representing the film resistance and CPE_f being the constant phase element describing the capacitance of the film. It is very likely, that a second time-constant representative for electrochemical processes at the MgO/$Mg(OH)_2$ – electrolyte interface exists at lower frequencies. However, due to largely scattered EIS data (caused by non-stationarity) these processes are not quantified by EIS fitting. In the case of sodium salicylate, shown in figure 7.15 (e-f), the phase angle values obtained between 10^{4} - 10^{2} Hz exceeds -90°. Because of this unusual feature, reliable fitting could not be performed in the frequency region of interest. Therefore, no fitting results are displayed in the Bode plots measured during immersion in sodium salicylate, shown in figure 7.15 (e-f). Moreover, the associated decrease of surface area eventually (in ca. 5 min) leads to the loss of magnesium layer, which is in line with the ATR-FTIR – EIS data shown in figure 7.13, where sodium saliclyate was described as a corrosion accelerator rather than a corrosion inhibitor.

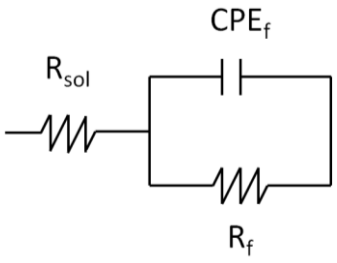

Figure 7.16: proposed equivalent electrical circuits used for fitting EIS spectra obtained in the 10^{0}-10^{4} Hz region during immersion of magnesium in the inhibitor solutions PDC, MSA and FA.

The resulting fitting values associated to the protective properties of the MgO/$Mg(OH)_2$ film and its chemisorbed carboxylate species are given in table 7.3.

Table 7.3: Fitting parameters of EIS spectra obtained in ATR-FTIR electrochemical cell during adsorption of magnesium in the respective inhibitor solutions.

Time/min	R_{sol}/ Ωcm^2	Q (CPE_f)/ μSs^n cm^{-2}	n (CPE_f)	R_f / Ωcm^2	χ^2
2,5-PDC					
0.0	83 ± 0.5	85.6 ± 3.0	0.75 ± 0.01	287 ± 3	1.6×10^{-3}
1.7	85 ± 0.3	50.3 ± 1.4	0.80 ± 0.01	518 ± 4	7.0×10^{-4}
3.3	85 ± 0.6	42.8 ± 1.3	0.79 ± 0.01	1092 ± 17	1.1×10^{-3}
4.9	84 ± 0.6	39.3 ± 0.9	0.77 ± 0.01	1839 ± 23	1.1×10^{-3}
6.7	83 ± 0.6	39.0 ± 0.8	0.76 ± 0.01	2275 ± 27	8.9×10^{-4}
8.4	82 ± 0.5	32.5 ± 0.6	0.75 ± 0.01	3595 ± 67	6.6×10^{-4}
3-MSA					
0.0	150 ± 0.5	20.2 ± 0.4	0.83 ± 0.01	1192 ± 8	1.2×10^{-3}
1.7	150 ± 1.3	16.3 ± 0.5	0.83 ± 0.01	5081 ± 136	2.6×10^{-3}
3.3	150 ± 1.1	13.6 ± 0.3	0.85 ± 0.01	6630 ± 189	3.0×10^{-3}
4.9	151 ± 0.6	11.7 ± 0.1	0.86 ± 0.01	10551 ± 94	4.3×10^{-4}
6.7	153 ± 0.6	10.6 ± 0.1	0.87 ± 0.01	12062 ± 105	3.9×10^{-4}
8.4	153 ± 0.5	9.8 ± 0.1	0.88 ± 0.01	13250 ± 112	3.7×10^{-4}
FA					
0.0	25 ± 0.2	90.1 ± 2.7	0.85 ± 0.01	330 ± 4	1.7×10^{-3}
1.7	26 ± 0.2	80.5 ± 2.9	0.85 ± 0.01	516 ± 11	2.3×10^{-3}
3.3	26 ± 0.3	74.4 ± 2.7	0.85 ± 0.01	754 ± 20	2.8×10^{-3}
4.9	26 ± 0.3	66.8 ± 2.2	0.85 ± 0.01	999 ± 20	3.4×10^{-3}
6.7	26 ± 0.3	66.4 ± 2.2	0.84 ± 0.01	1173 ± 26	3.7×10^{-3}
8.4	26 ± 0.3	62.0 ± 2.0	0.84 ± 0.01	1291 ± 30	3.7×10^{-3}

The evolution of quantified capacitance properties (Q and n) associated to film formation during submersion in inhibitor solution are shown in figure 7.17 (a) and (b), respectively. All carboxylic inhibitor solutions are shown to reduce the film capacitance. These reducing capacitance values imply reduced polarizability of the formed film indicating increased protective properties during prolonged immersion in the respective inhibitor solutions.[79,80] From figure 7.17 (a), reducing capacitance values are noted in the following order: FA > PDCA > MSA. Therefore, the film formed during submersion of magnesium in MSA solution has the lowest polarizability and thus the highest protective properties. In line with these results, figure 7.17 (b) demonstrates increasing n-values during submersion of MSA approaching the ideal capacitor during prolonged immersion of magnesium. Conversely, the n-values are shown to decrease upon immersion of magnesium in FA and PDC. Whereas the values of FA remain close to its initial values, the decrease is highly pronounced in the case of PDC. Therefore, the formed film in PDC solution is suggested to be less homogeneous compared to FA and MSA.

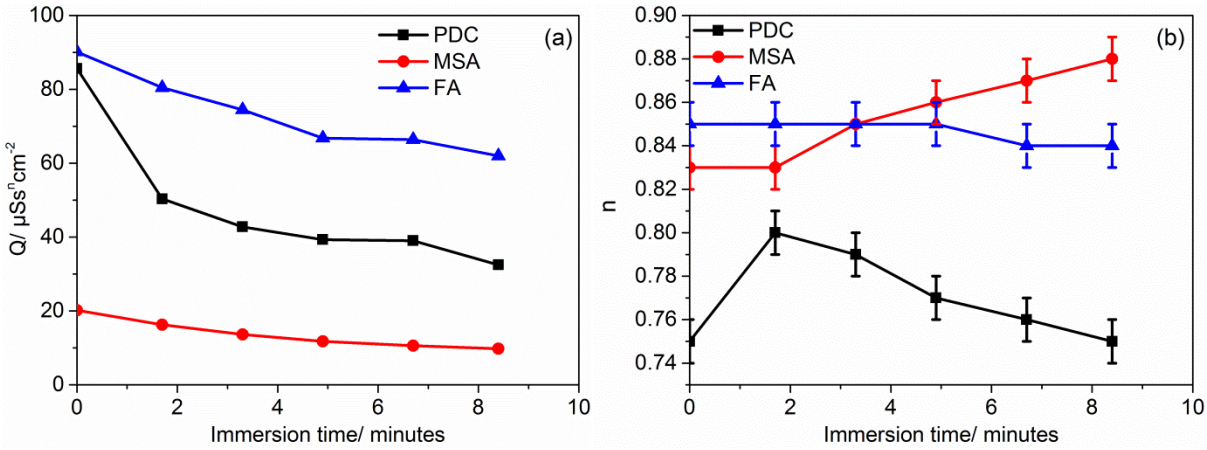

Figure 7.17: Inhibitor film CPE fitting values (a) Q and (b) n.

The resulting film resistance (R_f) of $MgO/Mg(OH)_2$ evolution is shown in figure 7.18. Increasing film resistances with prolonged immersion times are observed in following order: MSA > PDC > FA. These results are in accordance with those reported by Maltseva et al., who attributed the higher barrier properties during immersion in MSA compared to PDC and FA to the formation of a dense and stable $MgO/Mg(OH)_2$ layer.[81,82] PDC gives the second best inhibiting efficiency, although a delay time can be noted. The slightly better performance of PDC compared to FA is expected to relate to additional surface interactions with the pyridine ring electrons (π-interactions) and nitrogen atom. Finally, SS shows the poorest protection capacities which was attributed to the formation of soluble magnesium salicylate complexes. Because of its chelating capacities, salicylate was shown to act as a corrosion accelerator for high purity magnesium, which is reflected in the electrochemical measurements as rapid dissolution of magnesium disconnecting the electrochemical cell. Because of this, film resistance values for magnesium in the presence of SS are not shown in figure 7.18.

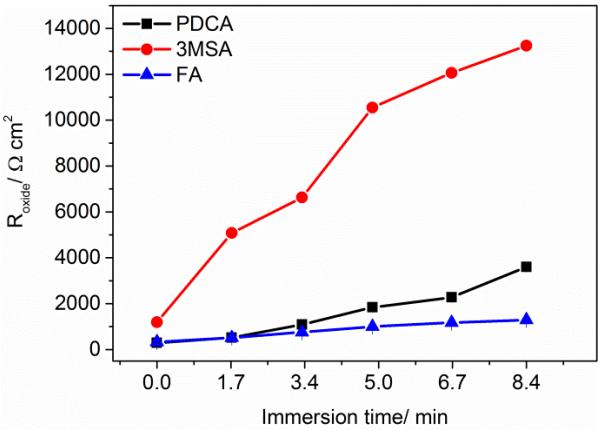

Figure 7.18: Film resistance evolution during immersion in the respective inhibitor solutions.

From figure 7.18, it is inferred that increased film resistance values are noted after a delay time of approximately 3 minutes. The ATR-FTIR results presented in figure 7.19 (a) demonstrate that within

this time lag oxide hydroxylation takes place. The growth of an hydroxylated $MgO/Mg(OH)_2$ layer takes place instantaneously, reaching a maximum intensity within less than 2 minutes. Thereafter, the hydroxide concentration reduces, which is associated to hydroxide consumption required for carboxylate bond formation as indicated by the increasing carboxylate peak areas shown in figure 7.19 (b). The strong Mg-OH peak area decay noted for PDC relates to the deprotonation of the second acid group of PDC.[81,82] This is in line with the higher asymetric carboxylate peak area observed for PDC, referring to a two-end adsorption, where both carboxylate groups coordinate to magnesium cations at the $MgO/Mg(OH)_2$ surface. Therefore, the increased film resistance, shown in figure 7.18 can be attributed to two surface phenomena, being the formation of a $MgO/Mg(OH)_2$ layer, as well as the chemisorption of carboxylic compounds.

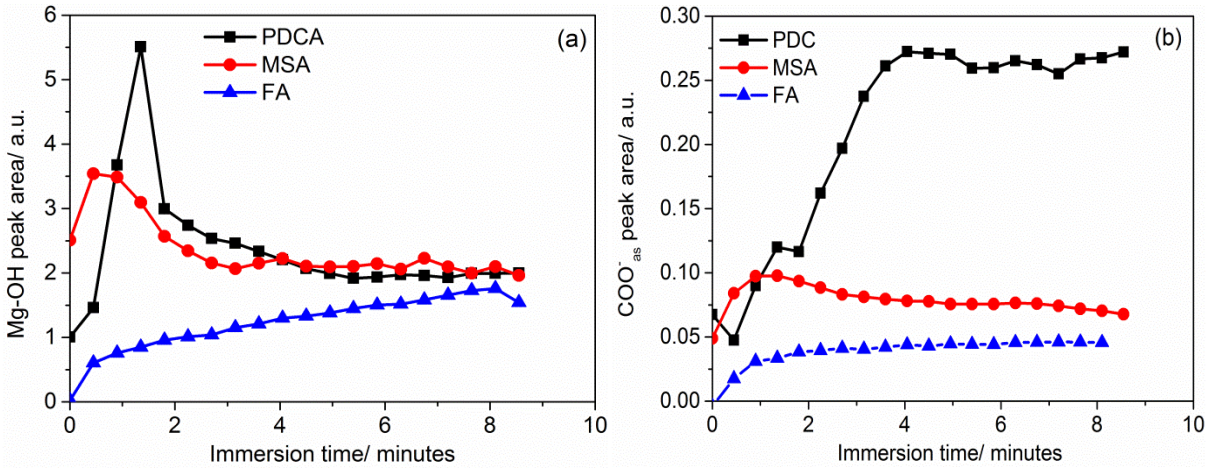

Figure 7.19: in situ ATR-FTIR results (a) Mg-OH peak and (b) asymmetric carboxylate peak area evolution during immersion in PDC, MSA and FA solution.

7.3.2.3. Conclusions on the use of EIS-ATR-FTIR integrated setup for corrosion inhibitor screening

Magnesium oxide evolution, including both hydration and dissolution, as well as inhibitor chemisorption mechanisms were followed in-situ using the integrated ATR-FTIR – EIS setup. Quantification of the oxide resistances at consecutive immersion times gave insights in the protective properties of the formed oxide layers in the presence of adsorbed species. 3-methylsalicylate showed the highest inhibiting performance which was attributed to the stabilization of the $MgO/Mg(OH)_2$ layer. On the other hand, salicylate was shown to act as a corrosion accelerator dissolving the hydrated magnesium oxide surface. Hence, combined use of ATR-FTIR and EIS highlighted the predominant role of the $MgO/Mg(OH)_2$ layer in terms of inhibitor performance. Therefore, the integrated ATR-FTIR – EIS setup is proposed as a highly valuable tool to simultaneously describe inhibiting mechanisms and efficiency.

7.4 Conclusions

ATR-FTIR has shown to be a highly valuable tool for the in-situ study of organic interactions at metal oxide interfaces during immersion in aqueous media. Two different case studies were presented to highlight the strengths and limitations of ATR-FTIR as interface-sensitive tool.

It is known that the introduction of water might disturb ATR-FTIR spectra, due to its high sensitivity for polar bonds. Because the O-H bending modes occur in the same IR-frequency region as the carboxylate bonds of interest, there has been opted to use D_2O, which O-D bending mode shifts to lower IR-frequencies. However, there are cases when you would like to have more freedom in selecting an aqueous media. For example, when pH or conductivity control becomes important. The preparation of aqueous solutions with a defined pH, conductivity are typically prepared by adding inorganic salts, which might contain or in-situ generate water. For SFG studies, the presence of water is not problematic, since OH-bending modes are not active for SFG. ATR-FTIR, on the other hand, requires precautions to deal with dominant water signals. Such an approach is proposed in the second part, where the background of native magnesium oxide immersed in aqueous solution was used as background for the in-situ measurements. This way the chemisorption carboxylic compounds from aqueous solution together with oxide evolutions such as surface (de)hydroxylation was monitored in-situ. In addition, chemisorption and oxide evolution kinetics were correlated to simultaneously collected EIS data.

For the chemisorption studies of organic corrosion inhibitors, the probing depth of ATR-FTIR has no or little impact on the resulting ATR-FTIR spectra. However, in the case of polyester coatings, which have an averaged thickness of 30 µm, determination of the probing depth becomes important to distinguish interface from bulk information. Therefore, the probing depth was calculated using Harrick's equations, which was found to vary between 250 and 400 nm in the frequency region of the carbonyl and carboxylate stretch vibrations, i.e. 2000-1200 cm^{-1}. As a consequence ATR-FTIR is proposed as an interphase (3D) sensitive technique providing molecular information from the near-interface region. SFG, on the other hand, is an inherently interface (2D) sensitive technique.

Similar to the observations in chapter 6, both case-studies demonstrated the key-role of the nature of oxide in aqueous solution (active versus passive) in the stability of interfacial bonds.

References

(1) Taheri, P.; Terryn, H.; Mol, J. M. C. Studying Interfacial Bonding at Buried Polymer–Zinc Interfaces. *Prog. Org. Coatings* **2015**, *89*, 323–331.

(2) Sababi, M.; Terryn, H.; Mol, J. M. C. The Influence of a Zr-Based Conversion Treatment on Interfacial Bonding Strength and Stability of Epoxy Coated Carbon Steel. *Prog. Org. Coatings* **2017**, *105*, 29–36.

(3) Öhman, M.; Persson, D. ATR-FTIR Kretschmann Spectroscopy for Interfacial Studies of a Hidden Aluminum Surface Coated with a Silane Film and Epoxy I. Characterization by IRRAS and ATR-FTIR. *Surf. Interface Anal.* **2012**, *44* (2), 133–143.

(4) Maier, S. A. *Plasmonics: Fundamentals and Applications*; Springer Science & Business Media, 2007.

(5) Mangolini, F.; Rossi, A. *Attenuated Total Reflection-Fourier Transform Infrared Spetroscopy: A Powerful Tool for Investigating Polymer Surfaces and Interfaces*; 2014.

(6) Harrick, N. J. Study of Physics and Chemistry of Surfaces from Frustrated Total Internal Reflections. *Phys. Rev. Lett.* **1960**, *4* (5), 224–226.

(7) Ishida, K. P.; Griffiths, P. R. Theoretical and Experimental Investigation of Internal Reflection at Thin Copper Films Exposed to Aqueous Solutions. *Anal. Chem.* **1994**, *66* (4), 522–530.

(8) Taheri, P.; De Wit, J. H. W.; Terryn, H.; Mol, J. M. C. In Situ Study of Buried Metal-Polymer Interfaces Exposed to an Aqueous Solution by an Integrated ATR-FTIR and Electrochemical Impedance Spectroscopy System. *J. Phys. Chem. C* **2013**, *117* (40), 20826–20832.

(9) Taheri, P.; Flores, J. R.; Hannour, F.; De Wit, J. H. W.; Terryn, H.; Mol, J. M. C. In Situ Study of Buried Interfacial Bonding Mechanisms of Carboxylic Polymers on Zn Surfaces. *J. Phys. Chem. C* **2013**, *117* (7), 3374–3382.

(10) Öhman, M.; Persson, D.; Leygraf, C. In Situ ATR-FTIR Studies of the Aluminium / Polymer Interface upon Exposure to Water and Electrolyte. *Prog. Org. Coatings* **2006**, *57*, 78–88.

(11) Öhman, M.; Persson, D. An Integrated in Situ ATR-FTIR and EIS Set-up to Study Buried Metal – Polymer Interfaces Exposed to an Electrolyte Solution. *Electrochim. Acta* **2007**, *52*, 5159–5171.

(12) Pletincx, S.; Mol, J. M. C.; Terryn, H.; Hubin, A.; Hauffman, T. An in Situ Spectro-Electrochemical Monitoring of Aqueous Effects on Polymer / Metal Oxide Interfaces. *J. Electroanal. Chem.* **2019**, *848*, 113311-.

(13) Snihirova, D.; Lamaka, S. V; Taheri, P.; Mol, J. M. C.; Montemor, M. F. Comparison of the Synergistic Effects of Inhibitor Mixtures Tailored for Enhanced Corrosion Protection of Bare and Coated AA2024-T3. *Surf. Coat. Technol.* **2016**, *303*, 342–351.

(14) Rabizadeh, T.; Asl, S. K. Casein as a Natural Protein to Inhibit the Corrosion of Mild Steel in HCl Solution. *J. Mol. Liq.* **2019**, *276*, 694–704.

(15) Nardeli, J. V; Fugivara, C. S.; Taryba, M.; Pinto, E. R. P.; Montemor, M. F. Tannin : A Natural Corrosion Inhibitor for Aluminum Alloys. *Prog. Org. Coatings* **2019**, *135*, 368–381.

(16) Chauhan, D. S.; Kumar, A. M.; Quraishi, M. A. Hexamethylenediamine Functionalized Glucose as a New and Environmentally Benign Corrosion Inhibitor for Copper. *Chem. Eng. Res. Des.* **2019**, *150*, 99–115.

(17) Esmaily, M.; Svensson, J. E.; Fajardo, S.; Birbilis, N.; Frankel, G. S.; Virtanen, S.; Arrabal, R.; Thomas, S.; Johansson, L. G. Fundamentals and Advances in Magnesium Alloy Corrosion. *Prog. Mater. Sci.* **2017**, *89*, 92–193.

(18) Mordike, B. L.; Ebert, T. Magnesium: Properties - Applications - Potential. *Mater. Sci. Eng. A* **2001**, *302*, 37–45.

(19) Harvey, T. J.; Walsh, F. C.; Nahlé, A. H. A Review of Inhibitors for the Corrosion of Transition Metals in Aqueous Acids. *J. Mol. Liq.* **2018**, *266*, 160–175.

(20) Yang, J.; Blawert, C.; Lamaka, S. V; Yasakau, K. A.; Wang, L.; Laipple, D.; Schieda, M.; Di, S.; Zheludkevich, M. L. Corrosion Inhibition of Pure Mg Containing a High Level of Iron Impurity in PH Neutral NaCl Solution. *Corros. Sci.* **2018**, *142*, 222–237.

(21) M.R. Querry. Optical Constants of Minerals and Other Materials from the Millimeter to the Ultraviolet, Contractor Report CRDEC-CR-88009. 1987.

(22) Barnes, W. L.; Dereux, A.; Ebbesen, T. W. Surface Plasmon Subwavelength Optics. *Nature* **2003**, *424* (6950), 824–830.

(23) Pletincx, S.; Marcoen, K.; Trotochaud, L.; Fockaert, L.-L.; Mol, J. M. C.; Head, A. R.; Karslioğlu, O.; Bluhm, H.; Terryn, H.; Hauffman, T. Unravelling the Chemical Influence of Water on the PMMA/Aluminum Oxide Hybrid Interface In Situ. *Sci. Rep.* **2017**, *7* (1), 13341.

(24) Fockaert, L. I.; Pletincx, S.; Ganzinga-Jurg, D.; Boelen, B.; Hauffman, T.; Terryn, H.; Mol, J. M. C. Chemisorption of Polyester Coatings on Zirconium-Based Conversion Coated Multi-Metal Substrates and Their Stability in Aqueous Environment. *Appl. Surf. Sci.* **2020**, *508*, 144771–144781.

(25) Lu, X.; Shephard, N.; Han, J.; Xue, G.; Chen, Z. Probing Molecular Structures of Polymer/Metal Interfaces by Sum Frequency Generation Vibrational Spectroscopy. *Macromolecules* **2008**, 8770–8777.

(26) Lu, X.; Xue, G.; Wang, X.; Han, J.; Han, X.; Hankett, J.; Li, D.; Chen, Z. Directly Probing Molecular Ordering at the Buried Polymer/Metal Interface 2: Using P-Polarized Input Beams. *Macromolecules* **2012**, *45* (15), 6087–6094.

(27) Myers, J. N.; Chen, Z. Polymer Molecular Behaviors at Buried Polymer/Metal and

Polymer/Polymer Interfaces and Their Relations to Adhesion in Packaging. *J. Adhes.* **2016**, *8464* (July), 1–23.

(28) Lu, X.; Zhang, C.; Ulrich, N.; Xiao, M.; Ma, Y. H.; Chen, Z. Studying Polymer Surfaces and Interfaces with Sum Frequency Generation Vibrational Spectroscopy. *Anal. Chem.* **2017**, *89* (1), 466–489.

(29) Lu, X.; Li, B.; Zhu, P.; Xue, G.; Li, D. Illustrating Consistency of Different Experimental Approaches to Probe the Buried Polymer/Metal Interface Using Sum Frequency Generation Vibrational Spectroscopy. *Soft Matter* **2014**, *10* (29), 5390–5397.

(30) George Socrates. *Infrared and Raman Characteristic Group Frequencies*, third edit.; John Wiley & Sons, Inc, 2001.

(31) Coates, J. *Encyclopedia of Analytical Chemistry, Interpretation of Infrared Spectra , A Practical Approach*; Meyers, R. A., Ed.; John Wiley & Sons, Ltd.

(32) Gan, W.; Wu, D.; Zhang, Z.; Feng, R. R.; Wang, H. F. Polarization and Experimental Configuration Analyses of Sum Frequency Generation Vibrational Spectra, Structure, and Orientational Motion of the Air/Water Interface. *J. Chem. Phys.* **2006**, *124* (11).

(33) Tyrode, E.; Hedberg, J. A Comparative Study of the CD and CH Stretching Spectral Regions of Typical Surfactants Systems Using VSFS: Orientation Analysis of the Terminal CH 3 and CD 3 Groups. *J. Phys. Chem. C* **2012**, *116* (1), 1080–1091.

(34) Tackett, J. E. FT-IR Characterization of Metal Acetates in Aqueous Solution. *Appl. Spectrosc.* **1989**, *43* (3), 483–489.

(35) Tang, C. Y.; Huang, Z.; Allen, H. C. Binding of Mg2+ and Ca2+ to Palmitic Acid and Deprotonation of the Cooh Headgroup Studied by Vibrational Sum Frequency Generation Spectroscopy. *J. Phys. Chem. B* **2010**, *114* (51), 17068–17076.

(36) Fockaert, L. I.; Pletincx, S.; Boelen, B.; Hauffman, T.; Terryn, H.; Mol, J. M. C. Effect of Zirconium-Based Conversion Treatments of Zinc , Aluminium and Magnesium on the Chemisorption of Ester-Functionalized Molecules. *Appl. Surf. Sci.* **2020**, *508*, 145199.

(37) Fockaert, L. .; Pletincx, S.; Ganzinga-Jurg, D.; Boelen, B.; Hauffman, T.; Terryn, H.; Mol, J. M. C. Chemisorption of Polyester Coatings on Zirconium-Based Conversion Coated Multi-Metal Substrates and Their Stability in Aqueous Environment. *Appl. Surf. Sci.* **2019**, Accepted for publication.

(38) Martell, A. E.; Smith, R. M. *Critical Stability Constants, Amino Acids, Vol. 1*; New York: Springer, 1974.

(39) Lamaka, S. V.; Gonzalez, J.; Mei, D.; Feyerabend, F.; Willumeit-römer, R.; Zheludkevich, M. L. Local PH and Its Evolution Near Mg Alloy Surfaces Exposed to Simulated Body Fluids. *Adv. Mater. Interfaces* **2018**, *1800169* (5).

(40) Maltseva, A.; Shkirskiy, V.; Lefèvre, G.; Volovitch, P. Effect of PH on Mg(OH)2 Film Evolution on Corroding Mg by in Situ Kinetic Raman Mapping (KRM). *Corros. Sci.* **2019**, *153*, 272–282.

(41) Leleu, S.; Rives, B.; Bour, J.; Causse, N.; Pébère, N. On the Stability of the Oxides Film Formed on a Magnesium Alloy Containing Rare-Earth Elements. *Electrochim. Acta* **2018**, *290*, 586–594.

(42) Martell, A. E.; Smith, R. M. *Critical Stability Constants, Other Organic Ligands, V. 3*; Springer, New York, 1977.

(43) Martell, A. E.; Smith, R. M. *Critical Stability Constants: Second Supplement, V. 6,*; Springer Science & Business Media, 1989.

(44) Dean, J. A. *Lange's Handbook of Chemistry, New York; London: McGraw-Hill, Inc.*; New york; London: McGraw-Hill, Inc., 1999.

(45) Lamaka, S. V; Vaghefinazari, B.; Mei, D.; Petrauskas, R. P.; Höche, D.; Zheludkevich, M. L. Comprehensive Screening of Mg Corrosion Inhibitors. *Corros. Sci.* **2017**, *128*, 224–240.

(46) Maltseva, A. Evolution de Surface Lors de La Corrosion de Magnésium: Nouvelles Approches Analytiques Pour Comprendre Les Mécanismes de Corrosion et de Protection, ChimieParis/ParisTech, 2018.

Chapter 8: Conclusions and outlook

8.1 Approach

The development of new metal-polymer hybrid systems comes with the need of gaining fundamental insights on the impact of substrate and pretreatment variations on the (chemical) adhesion of coil coat primers. This to guarantee a durable lifetime. Until today, interfacial bonding and disbonding mechanisms at buried metal-polymer interfaces are still far from understood. Moreover, a new generation of Cr(VI)-free surface treatments arises. Fundamental knowledge on the relation of oxide properties and paint adhesion would allow more efficient developments within chemical treatments. It is clear that each separate layer, occurring in metal-polymer hybrid systems is highly complex. Because of this many interface variables are responsible for adhesion, which hinders a straightforward mechanistic study. An additional reason for the existing lack of knowledge on metal-paint interfaces is associated to the difficulty of studying buried interfaces. Different methodologies have been developed in the past to overcome this challenge. For non-destructive research simplification of reality remains a prerequisite. However, with newly developed multi-substrates, as well as multi-component paint systems, there remains a gap between model and industrial systems. This current work aims to reduce this gap, starting with a fundamental interface parameter study using simplified model systems to which complexity is gradually added approaching industrial metal-polymer hybrid systems. This research approach provides the opportunity to optimize and create new enhanced metallic/organic coating systems that are better resistant to degradation and can lead to an improved lifetime. Gained insights on the effect of substrate heterogeneities, conversion bath components and multi-component paint systems on the interfacial chemistry are summarized in section 8.2 – 8.4, respectively. Subsequently, section 8.5 discusses the advantages and limitations of ATR-FTIR in the Kretschmann geometry as an interface-sensitive tool, whereafter the chosen approach and its output are evaluated in section 8.6. Finally section 8.7 reaches suggestions for future research.

8.2 The effect of substrate heterogeneities

8.2.1 What is the effect of substrate heterogeneity on conversion coating formation?

The multi-metal approach, studying pure aluminium, zinc and magnesium substrates, evidenced increased conversion kinetics in the following order aluminium < zinc < magnesium. As a result, a homogeneous zirconium oxide layer fully covering thermally vaporized zinc and magnesium substrates, whereas the thermally vaporized aluminium substrate was only partially covered by zirconium oxide, as illustrated in figure 8.1. The lower activity on aluminium substrates was

attributed to its protective native oxide layer at the conversion conditions used (pH 4). When using a model conversion solution (0.01 M H_2ZrF_6), thin zirconium oxide layers were probed on thermally vaporized zinc and magnesium with a final thickness ranging between 5 and 10 nm. On the other hand, zirconium-treatment of polished bulk substrates with a commercially available conversion solution resulted in pronounced oxide thickness variations, with magnesium forming a conversion oxide layer 10 times thicker than zinc and similarly to the model conversion solution only partially covering aluminium bulk substrates.

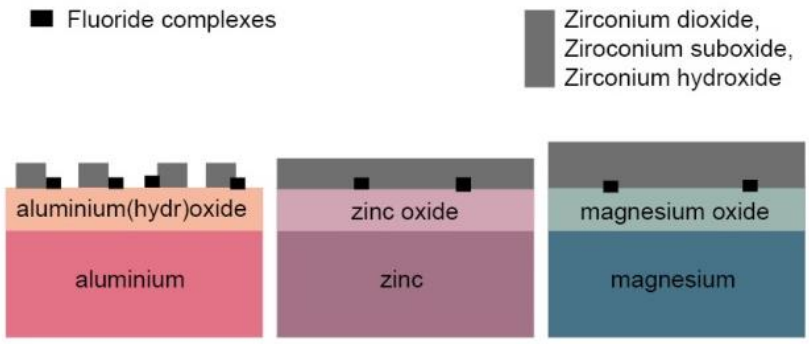

Figure 8.1: Zirconium conversion oxide layer build-up on thermally vaporized aluminium, zinc and magnesium.

Further characterization of zirconium- and titanium conversion oxide layers formed on GI and MZ substrates indicate a homogeneous zirconium oxide coverage of zirconium-treated substrates, while both zinc and titanium coexist at the outer surface of titanium-converted oxides. In addition, it was shown that the fluoride surface concentration was higher on zirconium-treated than on titanium-treated GI and MZ substrates. Consequently, the conversion oxide layer build-up was shown to depend more on the conversion solution (i.e. Zr- or Ti-based), rather than on the base metal substrate (i.e. GI or MZ). The surface free energy of both GI and MZ significantly increased upon conversion. This was attributed to altered polar forces, which increased by a factor ten upon conversion treatment. Consequently, GI and MZ were shown to be equivalent in terms of surface free energy and conversion oxide layer build-up as illustrates in figure 8.2. Therefore, it can be concluded that the variations in conversion oxide precipitation are considerably more pronounced when comparing the separated metal oxides (i.e. high purity zinc, aluminium and magnesium) than when comparing the industrial substrates GI and MZ.

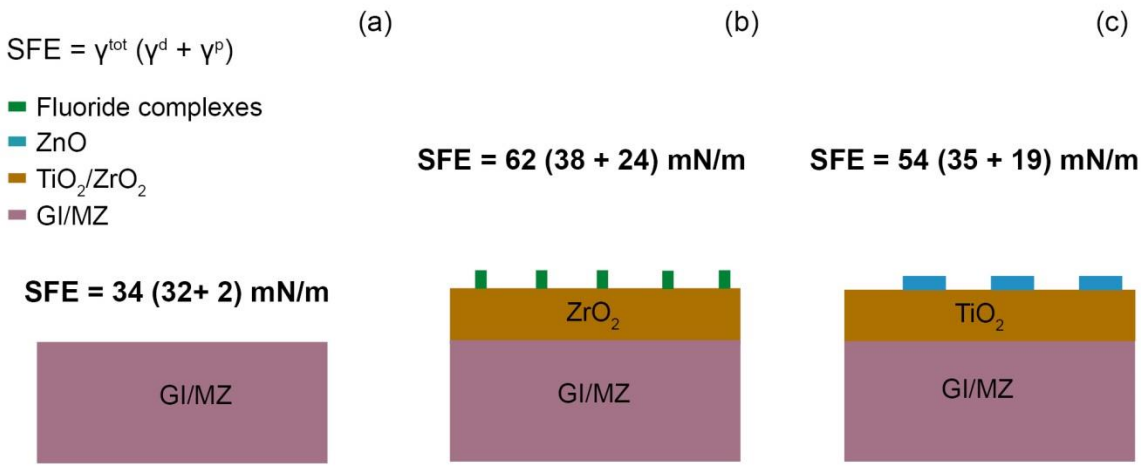

Figure 8.2: zirconium and titanium-based conversion layer build-up on GI/MZ substrates

8.2.2 What is the role of metal oxide acid-base properties on chemisorption mechanisms?

Both carboxylic acid- and ester-functionalized compounds have shown to form interfacial carboxylate bonds upon interaction with multi-metal oxides. In addition, ester-functionalized compounds were also shown to interact by hydrogen bonding. The nature of the established bonds strongly correlates to the metal-oxide acid-base properties. A higher acidic metal oxide character increases the hydrogen bond strength as well as the covalent character of established carboxylate bonds, whereas metal oxides with a highly alkaline character form highly ionic carboxylate bonds as illustrated in figure 8.3.

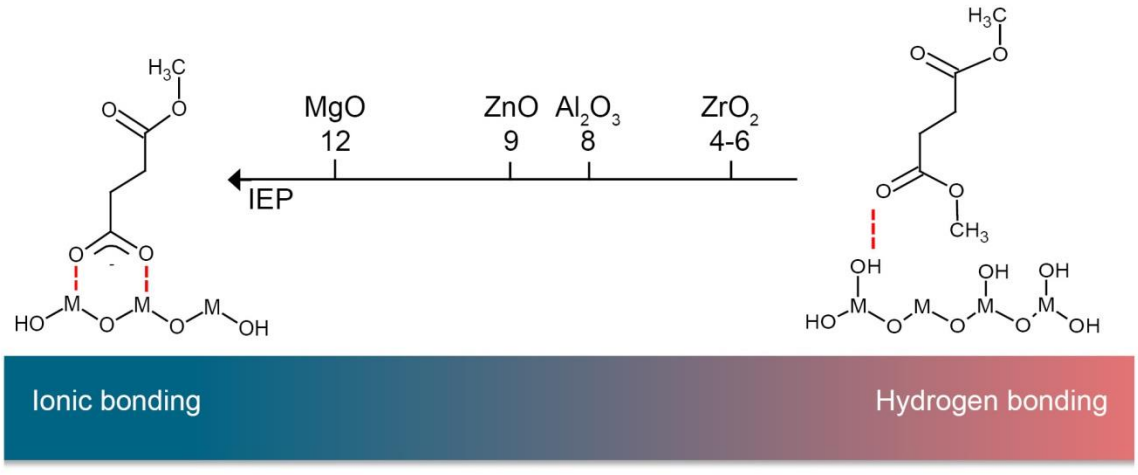

Figure 8.3: Determining role of metal oxide acid-base properties on the preferred interfacial interaction mechanism.

Similarly, N,N'-dimethylsuccinamide was shown to interact by two reaction mechanisms, i.e. Bronsted and Lewis acid-base interactions. Also here metal oxide acid-base properties were shown to play a determining role. As such, the increasing acidic character of zirconium-treated oxides was shown to increase the metal hydroxide's proton donating properties and thus its Bronsted acid nature, whereas the establishment of Lewis acid-base bonds slightly reduced. This minor reduction of Lewis acid-base bonding might be associated to the increased surface hydroxide fraction, sterically hindering the access of metal cations acting as Lewis acid-bonding site. The reaction paths of Bronsted and Lewis acid-base interactions between N,N'-dimethylsuccinamide and metal (hydr)oxides is illustrated in figure 8.4. It is thus shown that zirconium-treatment increases the acidic nature of the oxide, thereby altering the ratio of competitive interfacial interactions. As a result, the impact of zirconium-treatment is most pronounced for base metals with a high IEP and thus increases in following order Al < Zn < Mg.

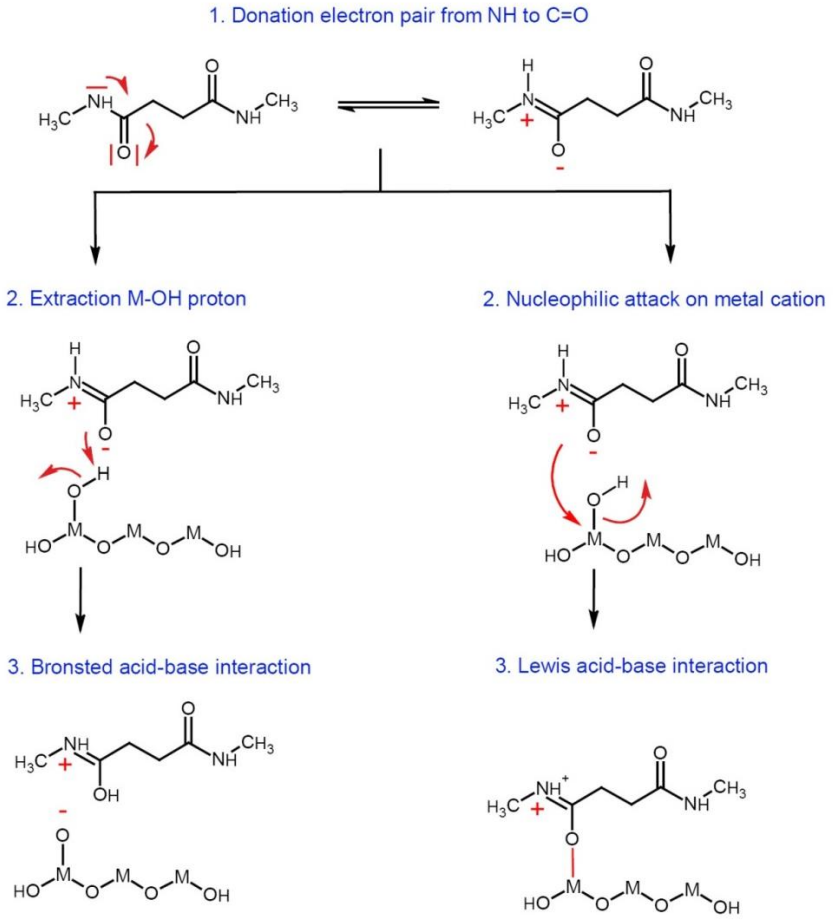

Figure 8.4: Proposed reaction pathways for Bronsted and Lewis acid-base interaction between N,N'-dimethylsuccinamide and metal hydroxide end-groups.

8.2.3 What is the role of surface hydroxides on the chemisorption mechanism?

Metal-hydroxide end-groups were shown to play a predominant role in all unravelled chemisorption mechanisms. In the case of hydrogen-bonding and Bronsted acid-base interactions they act as a bonding site, donating their proton to an electrophilic atom of the organic molecule of interest. For optimal hydrogen donating capacities, acidic metal cations are favourable. This because their high positive charge loosens the O-H bond, as demonstrated at the left side of figure 8.5. On the other hand, for ester hydrolysis and carboxylic acid deprotonation reactions surface hydroxides are being consumed. Therefore less positively charged metal cations (with higher alkaline nature) are favourable since this increases the availability of hydroxide end-groups, as demonstrated by the right side of figure 8.5.

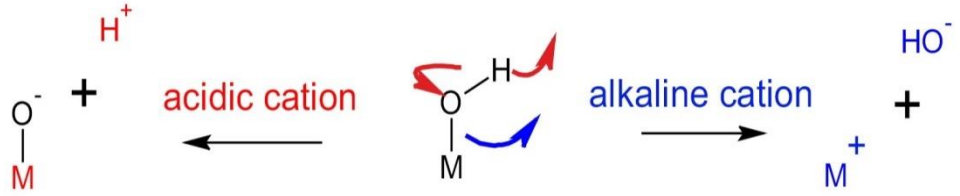

Fig. 8.5: The determining role of metal cation acidity in inducing an interfacial interaction mechanisms

8.2.4 Which interface parameters are responsible for the stability of interfacial bonds established at (conversion treated) metal oxide-paint interfaces exposed to an aqueous environment?

Zirconium-treatment was shown to enhance the interfacial stability when water was introduced at the metal-polyester interface. Two parameters were shown to be associated to this beneficial effect of zirconium-treatment in terms of interfacial stability. The first one relates to the ionic nature of the metal-carboxylate bond. Ionic interfacial interactions are expected to be more sensitive for replacement by water, and the ionic nature of established metal-carboxylate bonds was shown to increase with increasing IEP. Since, zirconium-treatment increases the acid nature of the respective metal oxides, also the covalent nature of the established metal-carboxylate bonds and thus their resistance against water replacement increases. The second explanation of the enhanced interfacial stability upon zirconium-treatment correlates to the oxide's activity in the respective aqueous environment. Carboxylate disbondment was shown to occur rapidly on zinc and magnesium substrates due to their tendency to corrode in neutral aqueous environments. However, zirconium-treatment efficiently passivates these unstable oxides, thereby significantly improving the stability of interfacial carboxylate bonds in aqueous environment. The interfacial durability of aluminium did not increase upon zirconium-treatment within the investigated timeframes, which is associated to its stable native oxide layer in neutral aqueous environments. It is thus both the nature of interfacial

bonds as the metal oxide's tendency to corrode that determines interfacial stability in aqueous environments.

8.2.5 How do thermally vaporized model substrates used for the thin substrate approach correlate to industrial substrates?

The conversion kinetics obtained by in-situ studies of thermally vaporized multi-metal substrates were in accordance with those obtained on high purity polished metal sheets. However, strikingly different surface hydroxide fractions were noted between between converted thermally vaporized model substrates and converted polished bulk substrates. Both ATR-FTIR and XPS analysis evidenced obvious surface hydroxylation in the case of thermally vaporized multi-metal substrates, whereas polished multi-metal sheets were shown to dehydroxylate upon conversion treatment. This was observed for zinc, aluminium and magnesium sheets, as well as for GI and MZ and this upon both zirconium- and titanium-treatment. Different hydroxide equilibria between thermally vaporized and bulk, i.e. high purity metal sheets and industrial substrates, were attributed to the different nature and thus activity of the native oxides in the respective conversion solution.

Since metal-hydroxide end-groups act as bonding site, the amount of surface hydroxides correlates to the amount of established interfacial bonds. However, it has been demonstrated that a saturation of the surface with surface hydroxides reduces interfacial carboxylate bond formation due to sterically and electrostatically hindrance limiting the access of metal cations. Therefore, there should be an optimum of surface hydroxides which does not necessarily equal the maximum of surface hydroxides. However, where the amount of interfacial bonds correlates to the surface hydroxide density, the chemisorption mechanism and thus bonding strength is suggested to be determined by the oxide's acid-base properties, which is comparable for thermally vaporized model substrates and bulk substrates.

8.3 The effect of conversion bath composition

8.3.1 What is the effect of conversion bath composition on the conversion layer build-up?

Both zirconium- and titanium-treatment increase the surface energy of GI and MZ by a factor 10. However, the addition of organic additives to zirconium-treatment does not further improve the surface free energy. Conversely, the addition of PAA to the titanium-treatment slightly increases the surface free energy, whereas PVA and PVP severely reduced the surface free energy. The limited impact of organic additives on the surface free energy of zirconium-treated substrates was associated to its crosslinking capacities resulting in an entanglement of the polymeric compounds in the zirconium oxide structure. On the other hand, titanium does not possesses these crosslinking

capacities, which means that the polymeric compounds form an additional layer on top of the titanium oxide layer, explaining its higher impact on the surface free energy.

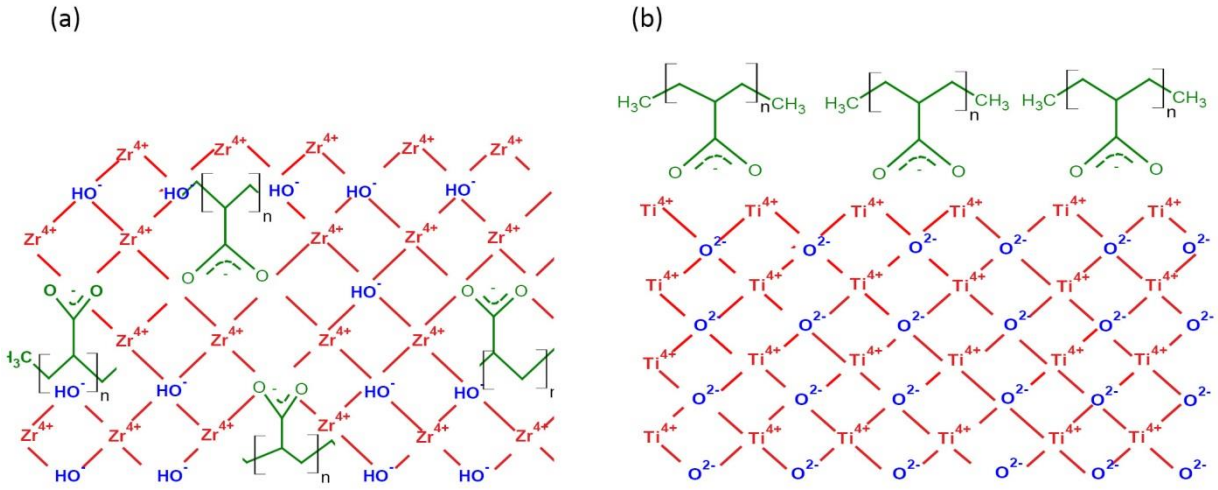

Fig. 8.6: Proposed conversion oxide structures containg PAA as organic additive, (a) PAA crosslinked in amorphous zirconium-oxide strucure, (b) PAA layer positioned on top of titanium oxide.

8.3.2 What is the effect of fluoacid cation (Zr-and Ti) on adhesion performance?

A higher affinity for carboxylate bond formation was evidenced on zirconium-treated than on titanium-treated zinc substrates. Furthermore, it was evidenced that not only carboxylic acid and ester groups specific to the polyester resin, but also the electron-rich groups of the melamine-based crosslinker interacts at the metal oxide surface. As such, titanium-treated zinc demonstrated a higher bonding affinity for the melamine-based crosslinker than zirconium-treated zinc substrates. It is well-known that titanium due to its small ionic radius is even more acidic than zirconium. Consequently, its tendency to donate hydroxide ions is very low, what explains the lower affinity for carboxylate bond formation compared to zirconium. Instead, electrostatic interactions between highly polarized titanium oxide and electron-rich nitrogen ring structures of melamine are hypothesized as favoured interaction mechanism.

In addition, the highest adhesion strength of polyester coil coat was demonstrated on zirconium-treated GI and titanium-treated MZ. This invers relation is in line with the XPS surface analysis, which demonstrated higher atomic concentrations of titanium on MZ and zirconium on GI. This substrate dependency on conversion efficiency might relate to variations in surface alkalinity or electrochemical activity.

8.3.3 What is the effect of organic compounds added to conversion bath to adhesion performance?

The presence of organic additives did not further enhance carboxylate bond formation, but in case of PAA and PVA even reduces the chemical reactivity of zirconium oxide. This suggests that bonding

with PAA and PVA reduces the number of available bonding sites at the zirconium oxide surface, what results in a lower carboxylate formation with the polyester resin. Conversely, the adhesion strength of titanium-treated MZ could be further improved due to the addition of PVP. It was suggested that PVP is not only concentrated at the outer surface of titanium oxide, but possible also underneath the titanium oxide at the MZ surface, where it anchors both oxides forming chemical interaction with both titanium and magnesium oxide. Consequently, it is shown that organic additives do not enhance interactions with the polyester resin. Yet, they are able to improve interfacial stability. Based on the molecular approach using in-situ ATR-FTIR, the effect of organic additives on the interfacial stability was most pronounced for titanium-treated substrates, with PAA performing better than PVA, followed by PVP. However, the macroscopic approach conducted upon longer immersion times, demonstrated a reduced adhesion strength due to the presence of organic additives of 40 and 14 % for titanium-treated and zirconium-treated GI, respectively. This adverse effect was attributed to the dissolution of polymeric compounds during immersion.

8.4 The effect of paint composition and curing

8.4.1 How do model organic components used for the model molecule and thin film approach correlate to industrially relevant paint formulations?

The chemisorption of an industrially relevant polyester coil coat was revealed on variously treated multi-metal substrates. The polyester resin was shown to interact with the metal oxide surface forming interfacial monodentate carboxylate bonds. The establishment of carboxylate bonds is thus in line with the observed chemisorption mechanism elucidated using ester-functionalized model compounds as discussed in chapter 4. Yet, whereas monomeric model compounds were shown to coordinate in a bridging bidentate mode, polyester resin formed monodentate carboxylate complexes. The formation of a monodentate coordination was attributed to a combination of sterical hindrance and a lower mobility of functional groups due to the large polymeric backbone.

Furthermore, it was evidenced that not only carboxylic acid and ester groups specific to the polyester resin, but also the electron-rich groups of the melamine-based crosslinker interacts at the metal oxide surface. As such, titanium-treated zinc demonstrated a higher bonding affinity for the melamine-based crosslinker than zirconium-treated zinc substrates. It is well-known that titanium due to its small ionic radius is even more acidic than zirconium. Consequently, its tendency to donate hydroxide ions is very low. Because of this, titanium is known to have a lower affinity for carboxylate bond formation compared to zirconium. Therefore, electrostatic interactions between the highly polarized titanium oxide structure and electron-rich nitrogen ring structures of melamine are hypothesized as favoured interaction mechanism.

8.4.2 How does curing alter the interfacial properties?

It was shown in chapter 5 of this work that interfacial carboxylate bonds between polyester resin and zinc oxide's hydroxide end-groups are immediately, and thus before curing, being formed. Three FTIR peaks showed dynamic behaviour upon reaction of the polyester coating at the zinc oxide surface at ambient conditions. Reduction of the peak intensity attributed to zinc hydroxide, indicative for their consumption upon interaction, and the growth of an asymmetric and symmetric carboxylate peaks, indicative for their formation. The separation of asymmetric and symmetric carboxylate peak suggest the formation of monodentate coordinated carboxylate bonds. However, upon curing, the symmetric carboxylate peak disappeared when using p-polarized IR-light, which referred to strongly increased orientation of interfacial carboxylate bonds with their transition dipole moment of the asymmetric stretch vibration perpendicular to the surface. Moreover, spectral peaks attributed to methyl groups of the melamine-based crosslinker and C-O ether bonds of the polyester resin strongly reduced indicating that opposite to interfacial bonding, crosslinking only takes place at elevated temperatures.

8.5 The value of ATR-FTIR in Kretschmann configuration as interfacial sensitive tool

8.5.1 On the importance of the use of complementary tools

Two approaches have been used in this work to access buried metal-polymer interfaces, the thin film approach, accessing the buried interface from the polymer side (i.e. top configuration), and the thin substrate approach, accessing the buried metal-polymer interface from the metal-side (i.e. inverse configuration). Both approaches required different analytical tools. As such, measurements in top configuration were mainly performed using XPS, whereas those in the inverse approach were mainly conducted using ATR-FTIR Kretschmann. It was demonstrated in chapters 4 and 5 that ATR-FTIR is a highly suitable tool for studying hydrogen bonding and carboxylate bond formation and might even be indicative for the bonding strength of these interfacial bonds. This because the strength of a hydrogen-bond is reflected in the size of the carbonyl peak shift towards lower wavenumbers. The stronger the hydrogen bond, the larger this shift. Carboxylate bond formation, on the other hand, was evidenced by newly formed FTIR-peaks assigned to asymmetric and symmetric carboxylate stretch vibrations. Their IR-frequency separation is indicative for the coordination mode of the carboxylate bonds. But in addition to that also the ionic nature of the carboxylate bond could be derived. As such it was shown that a higher alkaline nature of metal cation was associated to higher IR-frequency of the asymmetric carboxylate bond, which was attributed to a higher ionic nature of the metal-carboxylate bonds. Furthermore, the use of polarized IR-light has shown to be indicative for the orientation of the carboxylate bonds, which was shown to depend on the molecular backbone. Comparing the chemisorption of aliphatic and aromatic carboxylic acids yielded new

insights on the involvement of aromatic ring structures at interfacial bonding. It was shown that aromatic carboxylic acids were oriented in plane with the surface, which maximizes interfacial interactions between magnesium oxide and π-electrons of the aromatic rings. Conversely, aliphatic carboxylic acids orient with their carboxylate anions perpendicular to the magnesium oxide surface. Moreover, ATR-FTIR has shown to be a highly valuable tool for in-situ chemisorption measurements in aqueous media, even when the metal substrate of interest is highly active, as in the case of magnesium. However, ATR-FTIR is less suitable for determining chemisorption mechanisms involving amide-functionalized molecules. It is known from literature that the C=O stretch (amide I) and C-N/C-H stretch (amide II) peaks are anticorrelated. Yet, such a relation was not shown in this work, which infers a rather complex reaction pathways of amide-functionalized at the metal oxide surfaces. The high complexity most likely results from competitive Lewis- and Bronsted acid-base interactions, which cannot be distinguished using ATR-FTIR Kretschmann. On the other hand, the N 1s XPS peak analysis can provide valuable information on these competitive reaction mechanisms. A correlation between the metal oxide acid-base properties and favoured chemisorption mechanism, i.e. Bronsted or Lewis acid-base interactions has been established. Such correlation, i.e. interfacial bond density versus metal hydroxide fractions was also observed for carboxylic acid and ester-functionalized molecules. Consequently, XPS, can provide highly valuable information regarding the role of surface hydroxide fractions on the interfacial bonding mechanism and resulting bonding density, what makes XPS analysis highly complementary to ATR-FTIR. A limitation of XPS, is the difficulty of performing non-destructive in-situ interfacial analysis during immersion in aqueous media.

Finally, ATR-FTIR and XPS can be used complementary in the way they approach the buried metal-polymer interface. Typically, XPS is used to access the interface from the polymer side, requiring thin organic films, whereas ATR-FTIR Kretschmann accesses the buried interface from the metal substrate, requiring model metal substrates. Their complementary use allows for systematic comparison of model and industrial coatings and metal substrates, gradually reducing the gap between fundamental science and industry. Table 8.1 summarizes the strengths and limitations of both analysis techniques.

Table 8.1: Complementary, strengths and limitations of XPS and ATR-FTIR in studying metal-polymer interfaces.

XPS	ATR-FTIR
• Top con figuration • Thin organic film • Distinguish amide Lewis/Bronsted acid-base interactions from the amide N 1s peak shift • Quantify metal oxide hydroxide fractions	• Inverse configuration • Thin metal substrate • Indicate hydrogen bonds and their bond strength • Indicate carboxylate coordination

• Quantify carboxylate bonds based on C 1s peak fitting • No information on orientation/coordination No in-situ analysis in immersed conditions • Ex-situ determination of lateral and in-depth elemental conversion oxide composition	• Indicate orientation using s- and p-polarized IR-light • Indicate carboxylate bonds and their ioinic/covalent character • Allows in-situ analysis in immersed aqueous conditions • Allows integration of complementary techniques, such as electrochemical impedance spectroscopy • Able to follow zirconium oxide formation in-situ

8.5.2 To which degree can ATR-FTIR in Kretschmann configuration be considered as an interfacial sensitive technique?

In chapter 7 of this work the depth of penetration using ATR-FTIR Kretschmann has been estimated using Harick's equations. These equations relate the depth of penetration correlates to the frequency (ω_{IR}) and incident angle (θ) of the incident IR-light beam, the frequency dependent refraction index of the metal film (n_m) and the refraction indexes of IRE (n_{IRE}) and polymer coating (n_{PE}). Therefore, the depth of penetration obtained by Harrick's equations is considered to be independent of the field strength and thus the thickness of the metal film. Contrary, the amplitude of the electric field significantly reduces in the presence of a metallic film. Therefore, the magnitude of the FTIR signal relates to the thickness and optical properties of the absorbing metal film. Following this model, the penetration depth of zinc/zinc oxide/polyester systems probed using ATR-FTIR Kretschmann on a germanium internal reflection element, was estimated to be around 250-400 nm in the frequency region of the carbonyl and carboxylate stretch vibrations, i.e. 2000-1200 cm^{-1}. This estimated depth of penetration significantly reduces when spectral enhancement effects are being generated, increasing the surface selectivity to the first monolayer (within 5 nm) directly attached to the surface. Such spectral enhancements, also referred to as surface enhanced infrared absorption spectroscopy (SEIRA) – ATR-FTIR, are solely observed in very specific conditions. An electromagnetic enhancement effect can be observed on thin discontinuous metal films, consisting of small metal islands with a size which is smaller than the wavelength of the incident infrared light beam. When the metal islands grow in size, forming a continuous layer, the enhancement effect significantly reduces. Therefore, such electromagnetic enhancement effect is not expected to occur on metal films > 10 nm as in the case of this presented work. Additionally, SEIRA is typically induced on noble metals, such as Ag, Au and Cu, which is another condition that is not fulfilled within this work. Furthermore, a chemical enhancement effect can take place when molecules are being chemisorbed to the thin metal film. This enhancement mechanism is attributed to charge-transfer interactions between adsorbate and metal, which preferentially enhances vibrational modes with dipole changes perpendicular to the

metal surface. To investigate the occurrence of such chemical effects ATR-FTIR measurements have been performed using s- and p-polarized IR-light. Since the intensity of the observed spectral features were shown to be comparable in both polarization modes, no such chemical enhancement effect is expected to occur in the presented work. Finally, polyester coatings were examined directly applied on the IRE in absence of a metal film and when applied on a thin metal film, thermally vaporized on the IRE. Comparison of both measurements demonstrated similar magnitudes of the spectral features, confirming Harrick's equations that the presence of a metallic film does not considerably limit the depth of penetration of the evanescent wave. Yet, the presence of additional features could be observed in presence of a metallic film, indicating the formation of new interfacial bonds. In the case of polyester coatings, the newly formed infrared peak was interpreted as a metal-carboxylate bond. Consequently, although ATR-FTIR Kretschmann is considered to be an interphase (3D) sensitive technique with a penetration depth in the order of hundred nanometers, this technique is able to probe chemical interfacial bonds and has thus interfacial sensitivity.

To compare the spectral features obtained by ATR-FTIR Kretschmann, a second order nonlinear vibrational technique sum frequency generation (SFG) has been used, which due to its selection rules has a inherent (2D) surface selectivity. Whereas ATR-FTIR illustrated the presence of carboxylate anions at the polyester - zinc oxide near-interphase, SFG measurements showed that protonated carboxylic acid groups at the polyester - zinc oxide interface are highly stable and thus not deprotonated to carboxylate groups. In-situ ATR-FTIR measurements during the immersion of polyester coated zinc in D_2O lead to an immediate increase of carboxylate bonds with respect to the dry state in the polymer phase. This conversion occurs within a few hours, after which a rapid reduction of carboxylate bond density has been observed. Contrary, SFG measurements show that the carboxylic acid and ester groups near the zinc oxide interface are much more stable requiring continue immersion for multiple days to convert protonated carboxylic acids to carboxylate anions. These notable spectral differences can be attributed to a higher probing depth specific to ATR-FTIR Kretschmann compared to SFG. Nevertheless, it should be noted that the metal film thickness used for the two spectroscopic techniques vary, using 50 nm zinc layers for ATR-FTIR measurements and 6 nm zinc films for SFG measurements. A current debate, is whether a thicker metal film, lowers the amplitude of the electric field at the zinc oxide-polyester interface, thereby reducing the contribution of bulk chemistry. Additional experimental studies are required to define the effective depth of penetration.

To summarize, different trends in ATR-FTIR and SFG spectra hint towards different probing depths of the respective techniques. Arguments for the occurrence of SEIRA-ATR-FTIR were rejected, leading to estimated probing depths in the order of hundreds of nanometers. Therefore, ATR-FTIR Kretschmann is considered to be rather interphase (3D) than interface (2D) selective. Yet, comparative ATR-FTIR

studies with and without metallic layer, demonstrated the formation of interfacial metal-carboxylate bonds indicating that ATR-FTIR has adequate interface sensitivity to distinguish bulk and interfacial chemical structures.

8.6 Bridging fundamental research and industry

The inevitable need for simplified model systems when studying buried metal-polymer interfaces has been extensively discussed. Direct and non-destructive access to the buried metal-polymer interface requires thinning of at least or the metal substrate or the polymer coating. Both, the thin substrate and thin organic film approach have been used in this current work, as illustrated in figure 8.7.

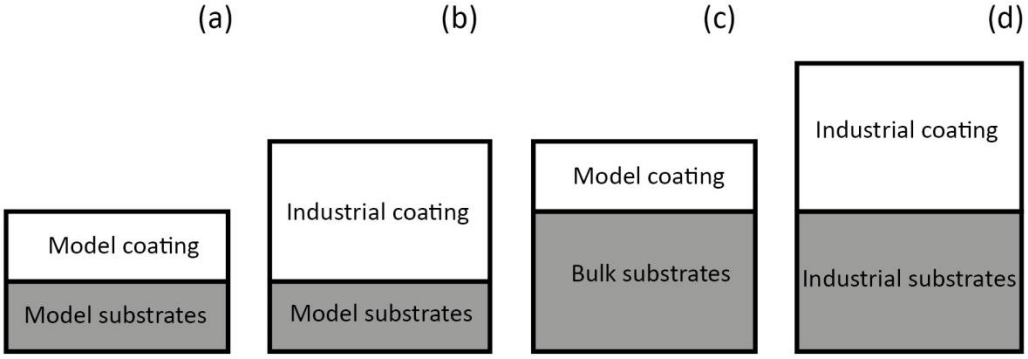

Figure 8.7: Bridging the gap between simplified model systems and industry.

The elucidated bonding mechanisms using model molecules, as illustrated in figure 8.5 (a) were successfully validated on industrially relevant polyester primer, as illustrated in figure 8.5 (b). However, the gained insights regarding the chemisorption of polyester coating could not directly and unambiguously been evidenced without simplifying the organic layer chemistry. This because polyester paint itself has an information rich FTIR-spectrum with aromatic ring stretch and carbon-hydrogen bend vibrations occurring at the same IR-frequency of asymmetric and symmetric carboxylate stretch vibrations, respectively. In addition, decomposition of heterogeneous multi-metal substrates into its pure compounds, i.e. zinc, aluminium and magnesium oxide highlighted the determining role of metal oxide acid-base properties on the chemisorption of organic compounds. These new insights on the importance of the oxide's nature, lead to a fundamental understanding of the bonding properties of zirconium-treated substrates. As such, zirconium-treatment was shown to increase the acidic character of the metal oxide thereby altering the ratio of competitive interfacial interactions. Whereas, the thin substrate approach, shown in figure 8.7 (a) and (b) accesses the interface with realistic paint systems using SFG and ATR-FTIR, the thin organic film approach, shown in figure 8.7 (a) and (c) accesses the interface with realistic metal substrates using XPS and AES. This demonstrated that thermally vaporized metal substrates differ significantly from bulk metal substrate in terms of oxide activity, which was shown to largely affect the conversion film formation.

As a result of variations in oxide nature, highly varying hydroxylation equilibria were evidenced. Nevertheless, this work highlights that whereas the hydroxide fractions are correlated to interfacial bond fractions, the type of established interfacial bonds are predominantly associated to the oxide's acid-base properties. Therefore, the interfacial chemistry obtained on model substrates could be successfully translated to industrial substrates. Furthermore, water was introduced at the interface to determine the stability of established interfacial bonds. For the first time, interfacial bond formation and degradation was monitored in-situ. It was shown that interfacial bond degradation was associated with the metal oxide activity in the respective environment and could thus be delayed by passivating the metal oxide upon conversion treatment. Finally, macroscopic adhesion testing upon introduction of interfacial water, as illustrated in figure 8.7 (d), has been performed to validate the molecular stability study shown in figure 8.7 (b).

Whereas this study started from highly simplified systems in terms of metal substrate, conversion solution and organic layer, the proposed stepwise approach to which complexity is systematically added lead to valuable insights on the effect of zirconium-and titanium-treatments on interfacial bonding and stability proposing them as promising conversion treatments. Despite substrate variations, the impact of conversion treatment was shown to be equivalent for GI and MZ in terms of layer-build up and surface free energy.

8.7 Future research

8.7.1 On the characterization of a new generation chemical conversion coatings

8.7.1.1 Experimental determination of the position of polymeric additives in the conversion oxide layer build-up

It was shown in this work that the addition of organic additives had a different impact when added to zirconium- or titanium-based conversion solutions, which was associated to the different behaviour of zirconium- and titanium cations when forming a solid phase from aqueous solutions. A notable distinction can be made based on the crosslinking ability, a property that has been assigned to zirconium, but not to titanium oxide. Because of their differences in crosslinking ability, it has been hypothesized that polymeric additives are differently incorporated in the respective conversion oxide structures. However, experimental evidence for this hypothesis is missing. The lack of experimental evidence relates to the required surface sensitivity, since it concerns very thin oxide layers. Especially in the case of thermally vaporized metal substrates, the conversion oxide layers were estimated to scale around 5-10 nm. Moreover, for such thin oxide layer, the interpretation of carbon signals is further complicated by ambient contamination.[1,2] Especially, small fatty acids strongly adsorb to metal oxide surfaces upon immediate contact to atmospheric environment, which hinders

unambiguous assignment of carbon signal to the respective organic additives. One way to overcome this difficulty is to grow thicker conversion oxide layers, allowing the generation of sputter profiles. However, it should be kept in mind that mixing effects and preferential sputtering might affect the shape of the depth profile.

8.7.1.2 Determination of oxide surface charge

The key-role of metal oxide's acid-base properties on interfacial bonding and stability has extensively been discussed in this current work. To indicate the multi-metal oxide's acid-base character, there has been frequently referred to isoelectric point (IEP) values. However, reported IEP values are typically obtained using colloidal dispersions instead of solid substrates and may show some scattering depending on the oxide chemistry and measurement conditions. Therefore, it would be highly valuable to experimentally determine the oxide surface charges on the solid metal oxides. In particular zirconium- and titanium conversion oxides are expected to have varying surface charges depending on their formation mechanism. This because the final solid form of a precipitated metal cation (hydroxide, oxyhydroxide or oxide, more or less hydrated) depends on the nature of the cation, mostly its charge, radius and electronegativity.[3] The first step leading to the solid phase is the formation of aquo-hydroxo precursor. The precursors are not stable in their monomeric forms and will form polymeric structures. The second step is condensation of the precursor. For a metal M, it can proceed through an 'oxo' bridge if the precursor is an anion, as illustrated in figure 8.6 (a). When the precursor is positively charged or neutral, the condensation proceeds through an 'hydroxo' intermediate bridge, as illustrated in figure 8.8 (b).[3–5] In the process of forming a solid phase, there is thus a competition between the olation reaction (leading to hydroxo bridged Zr-OH-Zr bonds) and an oxolation reaction (leading to Zr-O-Zr bonds). The orientation of the reaction depends essentially on the pH, the total Zr concentration in solution, temperature and presence of anions.[4] The presence of anions also determine the final chemical composition of the formed species as hydroxyl deficiencies are being compensated by anions in solution.[4] Therefore, the addition of inorganic, but also organic additives is expected to shift the isoelectric point (IEP) at the interface. It would thus be highly valuable to measure the chemically converted metal oxide's IEP prior to organic coating application.

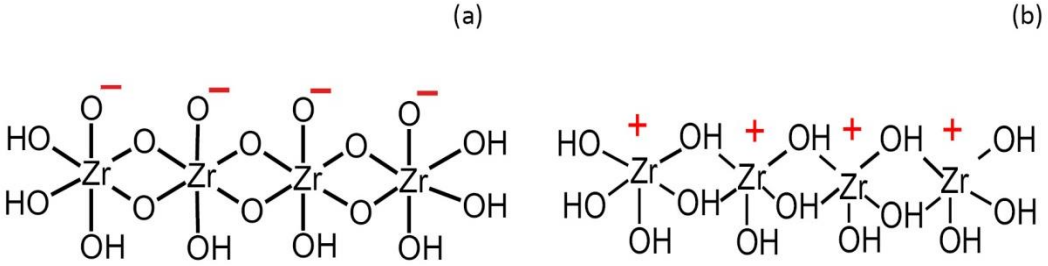

Figure 8.8: (a) oxolation and (b) olation polymeric structure.

One methodology to indicate surface charges on solid surface is by using phase and/or time-resolved SFG. Due to its selection rule, SFG can be used to study interfacial water without any contribution of bulk water. Generally, the frequency-dependent SFG Intensity I(ω) is proportional to the square of the effective second-order nonlinear response, $\chi^{(2)}(\omega)$. The overall effective response $\chi^{(2)}(\omega)$ can contain in addition to resonant terms, $\chi^{R(2)}(\omega)$, also nonresonant terms, $\chi^{NR(2)}(\omega)$, as well as possible contributions from the third-order nonlinear optical response, $\chi^{(3)}(\omega)$. Access to the separate real and imaginary parts of $\chi^{(2)}$, or equivalently; the amplitude and phase of the overall response, is relevant for determining the precise amplitude and sign of the resonant response peak.[6] The imaginary part of the overall $\chi^{R(2)}(\omega)$, $Im[\chi^{R(2)}(\omega)]$, is equivalent to the bulk absorption coefficient and is of particular interest because the sign of the peak reflects the absolute orientation of the transition dipole moments of the studies vibrational transition. In aqueous environments close to the IEP, the SF intensity of the water signals is weak due to random orientation of the water. In contrast, when the pH of the aqueous environment deviates from the IEP, solid surfaces might become charged. Under influence of the charged surface, water molecules orient themselves with the hydrogen atoms towards (negatively charged surface) or away from the solid (positively charged surface). The imaginary part of $\chi^{(2)}$ can thus be used to determine absolute molecular orientation ("down" or "up") at the interface, as illustrated in figure 8.9.[6] Therefore, SFG can be used to reveal the surface charge of solid surfaces in contact with water of different pH.[6–10]

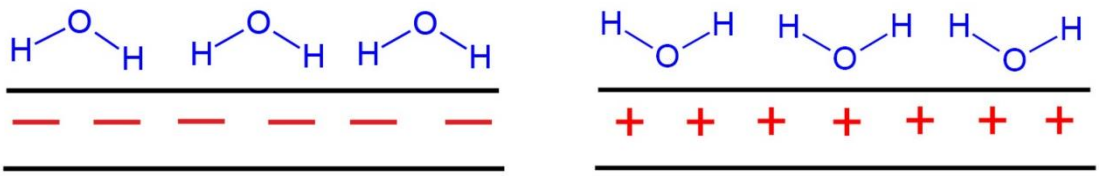

Figure 8.9: down and upward orientation of well-ordered water molecules at a charges surface.

As such, several approaches have been developed to determine the complex $\chi^{(2)}$, rather than $|\chi^{(2)}|^2$. Scanning frequency or "phase-resolved" SFG and broadband SFG provide both the amplitude and phase, or, equivalently, the real and imaginary parts, of $\chi^{(2)}$. Although, phase-resolved SFG allows for determination of the sign of $Im[\chi^{(2)}]$ for dominating spectral features, unambiguous analysis of the spectral shape of $Im[\chi^{(2)}]$ is reported to be challenging.[6] More recently, time-resolved (TR) and two-dimensional (2D) versions of SFG spectroscopy have been developed, including phase-resolved 2D-SFG spectroscopy. Adding an additional pulse to the pulse scheme to excite a significant fraction of oscillators to their first excited vibrational state, providing additional information.[6]

8.7.2 Further development of a non-destructive in-situ interfacial methodology to study metal-polymer interfaces

8.7.2.1 Experimental determination of the effective depth of penetration in ATR-FTIR Kretschmann

The effective depth of penetration using ATR-FTIR Kretschmann is still an ongoing debate due to lack of experimental evidence. In this current work, the depth of penetration has been estimated using Harrick's equations, who states that the presence of a metal film does not considerably alter the electric field strength of the generated evanescent wave, leading to comparable penetration depths with and without a metal layer. Other researchers on the other hand, reason that the presence of a metal film reduces the electric field strength of the evanescent wave, thereby reducing the spectral contributions from the bulk. Following this reasoning, the surface sensitivity of ATR-FTIR Kretschmann can be improved by applying thicker metal films. However, no experimental evidence is provided to validate both models. The generation of a multilayer system, with different discrete ultrathin (preferably monolayers) might allow experimental determination of the effective depth of penetration in the presence of a metallic film. Nevertheless, it should be noted that the development of such multilayer system is experimentally challenging. Moreover, it can be expected that the bulk chemistry of a macroscopic paint layer gives a higher signal than ultrathin stacked monolayers of organic compounds having different functionalities, which means that the proposed model is possibly not fully representative for macroscopic paint layers.

8.7.2.2 Integration of complementary techniques

For the first time, interfacial bond formation of paints and its degradation in an aqueous environment was studied in-situ, which was accomplished using ATR-FTIR in the Kretschmann configuration. For polyester coated zinc substrates, the initial growth of the carboxylate peak and its subsequent degradation in D_2O was shown to correspond to a deviation of 3.5 % compared to the dry state. Nevertheless, the altered bonding density observed on a molecular scale has a rather unknown impact on the macroscopic adhesion. Adhesion pull off-testing after 24 hours of immersion in aqueous media already gave some insights on the macroscopic behaviour of polyester coil coated galvanized steel sheets. However, it would be highly valuable to perform Volta potential measurements by means of scanning Kelvin probe to learn more on the delamination mechanism and kinetics of the variously treated multi-metal substrates.

Combined use of spectroscopic techniques and Volta potential measurements would give more insights on the importance of interfacial bonding and chemical stability under corrosive conditions. The inverse SFG configuration allows the use of a translation stage to move the sample, making it highly compatible with SKP measurements. As a result, the progressive evolution of delamination

fronts observed by SKP might be associated to interfacial disbondment or altered surface charges, determined using SFG. ATR-FTIR, on the other hand, is less suitable for lateral measurements, because the position of the germanium crystal with its fixed angles is more critical for internal reflection generation. Moreover, in-situ ATR-FTIR measurements are restricted to the use of D_2O, when the interfacial bond of interest is positioned in the same IR-frequency region as the OH-bending mode. Since SFG has not this sensitivity for OH-bending modes, a wide variety of aqueous solutions (and thus controlled pH) might be used, providing more insights in the fundamentals of water and ionic mobility and interfacial bonding properties metal oxide – polymer hybrid systems. This provides the opportunity to optimize and create new enhanced metallic/organic coating systems that are better resistant to degradation and can lead to an improved lifetime.

Furthermore, the implementation of an electrochemical cell in the spectroscopic setups would be an undoubted added value, providing insights on bulk coating properties (i.e. swelling and water uptake) and the onset of corrosion reactions. However, quantitative electrochemical analysis requires consistent coating application, which is not evident on IRE. Its small size hinders accurate use of barcoaters, whereas its weight hinders the use of spin coating. In this work, a barcoater of 30 µm has been used to apply polymer coatings on the IRE. For this purpose, the IRE was placed in a mold. However, multiple polishing sessions for cleaning the IRE alters the height of the crystal and thus the applied coating thickness. Hence, further optimizations on reproducible coating application on IRE is required for quantitative use of integrated electrochemical techniques.

References

(1) Baer, D. R.; Engelhard, M. H.; Lea, A. S.; Nachimuthu, P.; Droubay, T. C.; Kim, J.; Lee, B.; Mathews, C.; Opila, R. L.; Saraf, L. V.; et al. Comparison of the Sputter Rates of Oxide Films Relative to the Sputter Rate of SiO2. *J. Vac. Sci. Technol. A Vacuum, Surfaces, Film.* **2010**, *28* (5), 1060.

(2) Hofmann, S.; Zhou, G.; Kovac, J.; Drev, S.; Lian, S. Y.; Lin, B.; Liu, Y.; Wang, J. Y. Preferential Sputtering Effects in Depth Profiling of Multilayers with SIMS, XPS and AES. *Appl. Surf. Sci.* **2019**, *483* (November 2018), 140–155.

(3) Jolivet, J.; Henry, M.; Livage, J.; Bescher, E. *Metal Oxide Chemistry and Synthesis - From Solution to Solid State*, 3th editio.; John Wiley & Sons, Inc, 2000.

(4) Brown, P. L.; Curti, E.; Grambow, B.; Ekberg, C. Chemical Thermodynamics of Zirconium. **2008**, 1–512.

(5) Verdier, S.; Delalande, S.; Van Der Laak, N.; Metson, J.; Dalard, F. Monochromatized X-Ray Photoelectron Spectroscopy of the AM60 Magnesium Alloy Surface after Treatments in Fluoride-Based Ti and Zr Solutions. *Surf. Interface Anal.* **2005**, *37* (5), 509–516.

(6) Backus, E. H. G.; Cyran, J. D.; Grechko, M.; Nagata, Y.; Bonn, M. Time-Resolved Sum Frequency Generation Spectroscopy: A Quantitative Comparison Between Intensity and Phase-Resolved Spectroscopy. *J. Phys. Chem. A* **2018**, *122* (9), 2401–2410.

(7) Hosseinpour, S.; Tang, F.; Wang, F.; Livingstone, R. A.; Schlegel, S. J.; Ohto, T.; Bonn, M.; Nagata, Y.; Backus, E. H. G. Chemisorbed and Physisorbed Water at the TiO2/Water Interface. *J. Phys. Chem. Lett.* **2017**, *8* (10), 2195–2199.

(8) Zhang, L.; Tian, C.; Waychunas, G. A.; Shen, Y. R.; Di, V.; Berkeley, L. Structures and Charging of r -Alumina (0001)/ Water Interfaces Studied by Sum-Frequency Vibrational Spectroscopy. *J. Am. Chem. Soc.* **2008**, *130* (0001), 7686–7694.

(9) Kataoka, S.; Gurau, M. C.; Albertorio, F.; Holden, M. A.; Lim, S. M.; Yang, R. D.; Cremer, P. S. Investigation of Water Structure at the TiO2/Aqueous Interface. *Langmuir* **2004**, *20* (5), 1662–1666.

(10) Khatib, R.; Backus, E. H. G.; Bonn, M.; Perez-Haro, M. J.; Gaigeot, M. P.; Sulpizi, M. Water Orientation and Hydrogen-Bond Structure at the Fluorite/Water Interface. *Sci. Rep.* **2016**, *6* (April), 1–10.

Appendix: Quantification of surface hydroxide fractions

Because metal hydroxides are known to be important binding sites for molecule interactions, their densities are being estimated before and after chemical conversion using the approach proposed by McCafferty and Wightman[68]. This approach represents metal oxide as a multilayer system composed of discrete layers in depth, whereas lateral effects are averaged in the measured spot size of 100 µm. This model, illustrated in figure A.1, assumes homogeneity of the discrete layers. The composition of this multilayer system consists of an overlayer of adsorbed organic contamination (t) covering the converted metal oxide layer. Underneath the contamination layer, an outermost oxide layer with a hydroxylated region of chemisorbed water exists. This outermost oxide layer consist of zirconium oxide in case of hexafluorozirconic acid treated substrates under which a pure innermost metal oxide layer is expected.

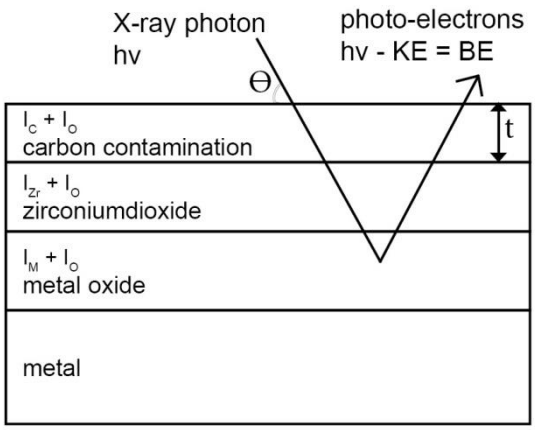

Figure A.1: Model used to describe the oxide composition of zirconium-treated zinc.

The thickness (t), of the carbon contamination layer, illustrated in figure A.1 can be estimated by equation A.1, described by Smith et al.[69]

$$t = -\lambda_{C1s} cos\Theta \ln(1 - C\ 1s/100) \qquad \text{(A.1)}$$

With λ_{C1s} being 2.3 nm, which is the effective electron attenuation length for carbon 1s photoelectrons in the carbon contamination layer, Θ the take-off angle relative to the surface normal. Values for C 1s, being the concentration of carbon expressed in atomic %, are obtained by collecting survey XPS spectra after which the traced elements are converted using the sensitivity factors of the manufacturer.

The measured O 1s signal contains contributions from the oxide matrix and was deconvoluted into three contributions (O^{2-}, OH and H_2O) as illustrated in figure A.2. The O^{2-} component specific to metal oxide, is positioned at 529.9 eV ± 0.3 eV.[70] Similar binding energies are expected in case of ZnO, Al_2O_3, MgO and ZrO_2. Therefore, no distinction can be made between metal and zirconium oxide based on the O 1s XPS peak. A second component, OH^- specific to metal hydroxide contributions is positioned at 531.5 ± 0.2 eV.[70] It is evidenced that the O^{2-} component reduces relative to OH^- component after zirconium-treatment indicating increased hydroxide densities at the metal surface after conversion. A third component assigned to chemisorbed water is positioned at 532.6 ± 0.3 eV.[70]

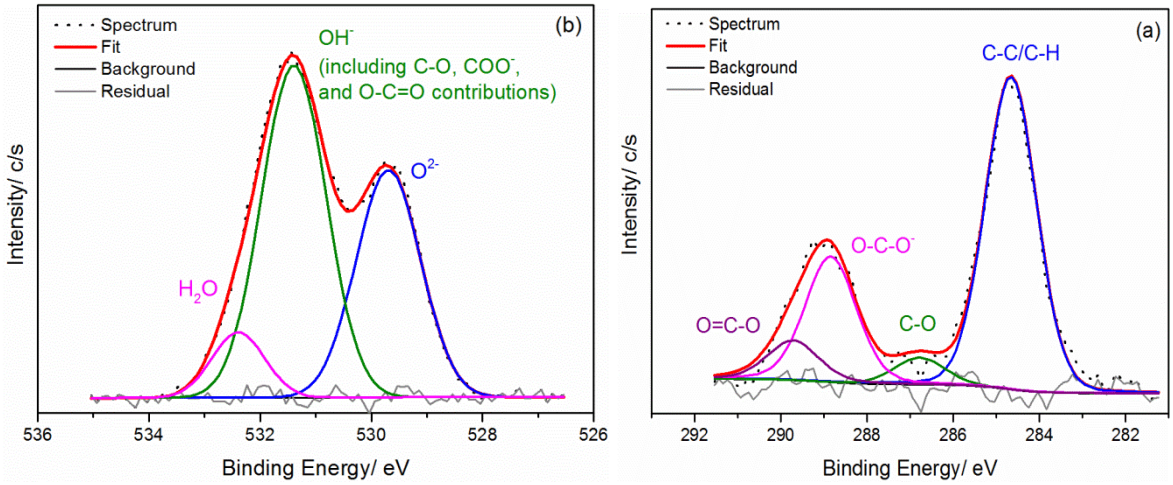

Figure A.2: Curvefit of (a) O 1s high resolution XPS peak and (b) C 1s high resolution XPS peak of a zinc substrate with native oxide.

Next to contributions of the oxide matrix also contributions from the carbon contamination layer (C-O, COO^-, O-C=O) are included in the O 1s peak. Because of the negligible differences in binding energy, OH contributions cannot be differentiated from those contributions specific to carbon contaminations. Therefore, a correction of the OH subpeak has to be made to avoid overestimation of surface hydroxyls due to the presence of organic contaminants. The XPS peak intensities (subpeak areas) of the respective contributions are obtained by C 1s and O 1s high resolution XPS curve fitting, as illustrated in figure A.2 (a) and (b) respectively. From the assessed peak areas for oxygen bonded carbon (C-O, COO^- and O-C=O), a correction can be made for the overestimation of OH^- subpeak area, according to equation A.2.[68]

$$I_{OH}^{*} = \frac{I_{C-O} + I_{COO-} + I_{O-C=O}}{I_{OH}} \qquad \text{(A.2)}$$

The corrected hydroxide sub peak intensity (I_{OH}^{*}) are correlated to the unknown concentrations of OH^- (C_{OH}) and O^{2-} (C_{O2-}) according to equation A.3 and A.4, which have been described extensively in earlier work.[70–72]

$$C_{OH} = \frac{\sigma_C\lambda_C(1-e^{-t/\lambda_C sin\Theta})-I_1\sigma_O\lambda_O(1-e^{-t/\lambda_O sin\Theta})}{I_{OH}^{*}\sigma_O\lambda_O(1-e^{-t/\lambda_O sin\Theta})} \quad (A.3)$$

$$C_{O2-} = \frac{\sigma_C\lambda_C(1-e^{-t/\lambda_C sin\Theta})}{I_{O_2-}\sigma_O\lambda_O(1-e^{-t/\lambda_O sin\Theta})} \quad (A.4)$$

With σ being the photoionization cross-section of the component of interest, λ the inelastic mean free path (IMFP) of electrons specific to the component of interest and t the thickness of the contamination layer. λ, the IMFP describes the mean distance that an electron travels through a solid before losing energy. Consequently, the intensity attenuation of elements in the oxide layer by the covering ambient carbon contamination layer are taken into account when calculating the oxide elemental concentrations. Based on figure A.3, mixed contributions of zirconium and metal oxide are being probed by XPS. Therefore, their properties (σ and λ) are being averaged as illustrated in table A.1.

Table A.1: Photo-ionisation cross-sections (σ) and inelastic mean free paths (IMFP, λ) and used for quantifying surface hydroxide and oxide concentrations (equation 5 and 6)

Element	**Photo-ionization cross-section (σ)**[73]	**Inelastic mean free path (λ)/ nm**[74]
C	0.192	2.583
O (Al_2O_3)	0.523	2.251
O (ZnO)	0.523	1.870
O (MgO)	0.523	2.324
O (ZrO_2)	0.523	1.858
O (average)	0.523	2.076

Finally, solving the above described equations allows the calculation of the surface hydroxide fraction using equation A.5.

$$Hydroxyl\ fraction = \frac{1}{1+\frac{C_{O2-}}{C_{OH}}} \quad (A.5)$$

Acknowledgements

The research presented in this dissertation has been conducted in the framework of the Partnership Program of the Materials innovation institute (M2i) and the Foundation for Fundamental Research on Matter (FOM), which is part of the Netherlands Organisation for Scientific Research (NWO). I would like to thank these partners for the financial support of this project, but also for their support in the track of becoming an independent researcher. It took several years to complete this dissertation, a task which would have been unthinkable without the assistance of many people, to whom I would like to express my gratitude to.

First of all I would like to thank my dedicated promotors Prof. Herman Terryn and Prof. Arjan Mol. You form a strong team, always available for discussions and providing me valuable feedback on the essence and weakness of the presented information when I once again got lost in the details of the conducted research. You both reached me your networks when I moved to the edges of our fields of expertise, giving me the freedom to develop myself without any limitations. Your approachability and sense for humour creates an informal atmosphere where the group greatly benefits from, and this from both scientific and personal perspective.

Furthermore, I would like to thank Dr. Berend Boelen, for always showing interest in the presented work and being constantly supportive along the way. I really enjoyed our close collaboration and the open mind and interest of your research team within TataSteel. For each problem that I faced within my project you were able to connect me to the well-skilled people within your team and beyond. Therefore, I would like to thank Koen Lammers for his support in XPS analysis of the zirconium-and titanium-based conversion oxides and Deborah Ganzinga-Jurg for sharing her passion for molecular spectroscopy with me. It was a great pleasure working with you.

This leads me to the people of the ultrafast spectroscopy group within Amolf. I am grateful to Prof. Huib Bakker for giving me the opportunity of being part of the ultrafast spectroscopy group. Our discussions greatly influenced my vision on interfaces. I would like to thank Dr. Jan Versluis, who gave me the opportunity to gain some independence on handling the SFG setup. In addition I would like to thank the group members for your warm welcome during our stay as guest researchers.

Also other research groups warmly welcomed me during my journey. I greatly acknowledge Dr. Saman Hosseinpour for initiating me into the world of SFG. It was a great experience to visit your lab at Friedrich Alexander University and learn the principles of SFG. There is no doubt that your guidance greatly accelerated the output of my stay at Amolf. I would also like to thank the people from Helmholtz-Zentrum Geesthacht; Reneé Unbehau for your nice company during our long days at

the integrated ATR-FTIR-EIS setup and Dr. Sviatlana Lamaka, Tim Würger and Prof. Mikhail Zheludkevich for their highly appreciated input on the joint work concerning corrosion inhibitors for magnesium.

I would also like to express my gratitude to Prof. Tom Hauffman and Sven Pletincx of the SURF group at Vrije Universiteit Brussel (VUB), for the many fruitful and highly in-depth discussions, which greatly contributed to the quality of this work. Another special thanks goes to Oscar Steenhout and Priya Laha for their support on the XPS, AES and FE-AES. In addition, I would like to thank the entire SURF-team at VUB for the pleasant moments both at the VUB and on conferences.

The majority of this current work has been conducted at the Materials Science and Engineering department of the TUDelft. A great place to perform scientific research where interdisciplinary collaboration is greatly encouraged. I would like to thank all experts and craftsmen for their numerous support in all experimental aspects. A special thanks goes to Kees Kwakernaak for preparing my SFG samples. Finally, I also greatly acknowledge my colleagues from the Corrosion Technology and Engineering (CTE) group, my office mates Shoshan, Mats and Bala, but also Agata, Ali, Aytac, Claire, Emina, Joost, Jose, Majid, Maria, Marta, Peter, Peyman, Prakash, Sajjid, Soheil, Uma, Ursa, Wojciech, Yaiza and finally Maxine, who largely contributed to the study on the effect of organic additives to conversion treatments. A special thanks goes to Agnieszka, for her unlimited support which went much further than solely technical support in the lab.

I would like to thank my friends and family who accurately felt when I had to been dragged away from all my running (work and personal related) projects.

Finally, I would like to express my sincere gratitude to my lovely parents whom were enormously proud of me getting a bit more Dutch mentality, which will likely be more valuable in life than a doctoral degree. My lovely partner Ben, who encouraged me to jump and leave for a 4 years project to Delft. And this at the very same time that we started an intensive renovation project. You never complained and were always supportive, even in my crazy bike rides, where you frequently waited for me at Breda central station to join me on the way back home. And then, last but definitely not least, little Tess. You placed everything in a total different perspective, making science so relative. Thanks for all the laughter, looking forward to the beautiful things left to come.

Peer-reviewed journal articles

L. I. Fockaert, M. V. E. Ankora, J. P. B. Van Dam, S. Pletincx, A. Yilmaz, B. Boelen, T. Hauffman, Y. Garcia-Gonzalez, H. Terryn, J. M. C. Mol, Erratum to 'Effect of organic additives in fluoacid-based Ti and Zr-treatments for galvanized steel on the stability of a polymer coated interface.' *Progress in Organic Coatings*, **(2020)** 105902.

L. I. Fockaert, M. V. E. Ankora, J. P. B. Van Dam, S. Pletincx, A. Yilmaz, B. Boelen, T. Hauffman, Y. Garcia-Gonzalez, H. Terryn, J. M. C. Mol, Effect of organic additives in fluoacid-based Ti and Zr-treatments for galvanized steel on the stability of a polymer coated interface, *Progress in Organic Coatings*, 146 **(2020)** 105738.

L. I. Fockaert, T. Würger, R. Unbehau, B. Boelen, R. H. Meißner, S. V. Lamaka, M. L. Zheludkevich, H. Terryn, J. M. C. Mol, ATR-FTIR in Kretschmann configuration integrated with electrochemical cell as in-situ interfacial sensitive tool to study corrosion inhibitors for magnesium substrates, *Electrochimica Acta,* 345 **(2020)** 136166.

L.I. Fockaert, D. Ganzinga-Jurg, J. Versluis, B. Boelen, H.J. Bakker, H. Terryn, J.M.C. Mol, Studying chemisorption at metal-polymer interfaces by complementary use of attenuated total reflection – Fourier transform infrared spectroscopy (ATR-FTIR) in the Kretschmann geometry and visible-infrared sum-frequency generation spectroscopy (SFG)*, Journal of Physical Chemistry C,* 124, 13 **(2020)** 7127-7138.

L.I. Fockaert, S. Pletincx, B. Boelen, T. Hauffman, H. Terryn, J.M.C. Mol, Effect of zirconium-based conversion treatments of zinc, aluminium and magnesium on the chemisorption of ester-functionalized molecules, *Applied Surface Science,* 508 **(2020)**145199-145210.

L.I. Fockaert, S. Pletincx, D. Ganzinga-Jurg, B. Boelen, T. Hauffman, H. Terryn, J. M. C. Mol, Chemisorption of polyester coatings on zirconium-based conversion coated multi-metal substrates and their stability in aqueous environment, *Applied Surface Science,*508 **(2020)** 144771-144781.

L. I. Fockaert, P. Taheri, S. T. Abrahami, B. Boelen, H. Terryn, J. M. C. Mol, Zirconium-based conversion film formation on zinc, aluminium and magnesium oxides and their interactions with functionalized molecules. *Applied Surface Science*, 423 **(2017)** 817–828.

S. Pletincx, L.I. Fockaert, M. Meeusen, J.M.C. Mol, H. Terryn, T. Hauffman, Probing the formation and degradation of chemical interactions from model molecule/metal oxide to buried polymer/metal oxide interfaces, *npj Materials Degradation*, 3, 23 **(2019)** 1-12.

Y. Li, H. Jahr, K. Lietaert, P. Pavanram, A. Yilmaz, L.I. Fockaert, M.A Leeflang, B. Pouran, Y. Gonzalez-Garcia, H. Weinans, J.M.C. Mol, J. Zhou, A.A. Zadpoor, Additively manufactured biodegradable porous iron, *Acta Biomaterialia*, 77 **(2018)** 380-393.

S. Pletincx, L.I. Fockaert, M. Meeusen, J.M.C. Mol, H. Terryn, T. Hauffman, In situ methanol adsorption on aluminum oxide monitored by a combined ORP-EIS and ATR-FTIR Kretschmann Setup, *Journal of Physical Chemistry C*, 122, 38 **(2018)** 21963-21973.

Y. Li, J. Zhou, P. Pavanram, M. A. Leeflang, L.I. Fockaert, B. Pouran, N. Tümer, K.U. Schröder, J. M. C. Mol, H. Weinans, H. Jahr, A. A. Zadpoor, Additively manufactured biodegradable porous magnesium, *Acta biomaterialia*, 67 **(2018)** 378-392.

S. Pletincx, L. Trotochaud, L. Fockaert, J. M. C. Mol, A. R. Head, O. Karslıoğlu, H. Bluhm, H. Terryn, T. Hauffman, In Situ Characterization of the Initial Effect of Water on Molecular Interactions at the Interface of Organic/Inorganic Hybrid Systems*, Scientific Reports*, 7 **(2017)** 45123.

S. Pletincx, K. Marcoen, L. Trotochaud, L. Fockaert, J. M. C. Mol, A. R. Head, O. Karslioğlu, H. Bluhm, H. Terryn, T. Hauffman, Unravelling the Chemical Influence of Water on the PMMA/Aluminum Oxide Hybrid Interface In Situ, *Scientific Reports*, 7 **(2017)** 13341.

Oral presentations at International conferences

SLIMAIA Conference, Rueil-Malmaison, France **2018**
L. I. Fockaert, S. Pletincx, M. Meeusen, H. Terryn, J. M. C. Mol, In-situ study of interfacial bonding and bond degradation of polyester coating on multi-metal oxides.

AETOC Conference, Billerbeck, Germany **2017**
L.I. Fockaert, P. Taheri, S.T. Abrahami, H. Terryn, J.M.C. Mol, Elucidating bonding mechanisms and stability of galvanized steel-polymer interfaces.

EUROCORR Conference, Prague, Czech Republic **2017**
L.I. Fockaert, P. Taheri, S. Abrahami, S. Pletincx, H. Terryn, J.M.C. Mol, The effect of zirconium-based conversion treatment of zinc-, aluminium- and magnesium oxides on the bonding mechanisms and degradation of ester functionalized molecules.

EUROCORR Conference, Montpellier, France **2016**
L.I. Fockaert, B. Boelen, H. Terryn, J.M.C. Mol, Zr-based conversion film formation on single and multi-metal substrates and their interactions with functionalized molecules.

Curriculum Vitae

Laura-Lynn Irena Fockaert
Born on December 3, 1991
Wilrijk, Belgium

Education

MSc Industrial Engineering Chemistry	University of Antwerp (BE)	2012 - 2014
BSc Chemistry	Plantijn Hogeschool Antwerpen (BE)	2009 - 2012
Technical Secondary Education: Chemistry	Heilig Graf Instituut, Turnhout (BE)	2007 - 2009

Traineeships

Msc. Thesis, Research trainee	Delft University of Technology, (NL)	2014
Bsc Thesis, Research trainee	University-College Bergen, (No)	2012
Laboratory technician	SGS, Antwerp, (BE)	2011
Laboratory technician	EVONIK, Antwerp, (BE)	2010
Research trainee	Mondi Foods, Rijkevorsel, (BE)	2009

Working experience

Catalyst	Catalisti, Antwerp (BE)	2020-present
Ph.D. Industrial Engineering	Delft University of Technology (NL)	2015 - 2019